Mahoney, J.J., Fitton, J.G., Wallace, P.J., et al., 2001
Proceedings of the Ocean Drilling Program, Initial Reports Volume 192

4. SITE 1184[1]

Shipboard Scientific Party[2]

BACKGROUND AND OBJECTIVES

Site 1184 lies at a water depth of 1661.5 m on the unnamed northern ridge of the eastern lobe or salient of the Ontong Java Plateau (Fig. **F1**). The eastern lobe had not been drilled before Leg 192. As with the dome of the high plateau (see **"Background and Objectives,"** p. 1, in the "Site 1183" chapter), we thought that this site near the summit of the ridge might be in an area that originally was at relatively shallow water depths. The site is 570 km from central Malaita, 807 km from Deep Sea Drilling Project (DSDP) Site 289, 907 km from Ocean Drilling Program (ODP) Site 1183, 918 km from ODP Site 803, and 1274 km from ODP Site 807.

The relationship of the eastern lobe to the high plateau is unknown. It could be contemporaneous with the high plateau or be the trace of the postulated plume tail following the emplacement of the high plateau and, specifically, may be the main locus of 90-Ma eruptions (Tejada et al., 1996). Also, the eastern lobe appears to have been rifted into northern and southern portions that were separated by nearly 300 km of seafloor spreading in the Stewart Basin (Kroenke and Mahoney, 1996). The southern portion, known as Stewart Arch, is the proposed conjugate feature to the northern ridge. Lavas associated with this poorly understood rifting event may have been preserved along both the northern and southern rift-facing sides of the salient. Furthermore, this part of the plateau passed over the estimated position of the Samoan hotspot ~35–40 Ma (Yan and Kroenke, 1993), and volcanic evidence of this passage might be present.

Site 1184 is on the faulted crest of the northern ridge, which trends northwest-southeast, as does a corresponding free-air gravity high (Figs. **F1, F2**). The ridge's southwestern flank is cut by numerous normal faults that are likely to be related to the opening of the Stewart Basin. The ends of four northeast-southwest trending seamount chains inter-

F1. Predicted bathymetry of Ontong Java Plateau, with site locations, p. 29.

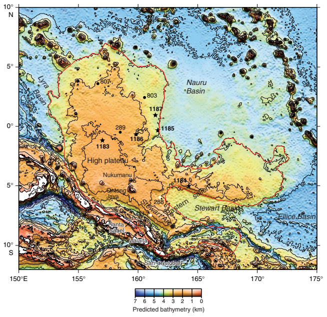

F2. Free-air gravity map of the Ontong Java Plateau region, p. 30.

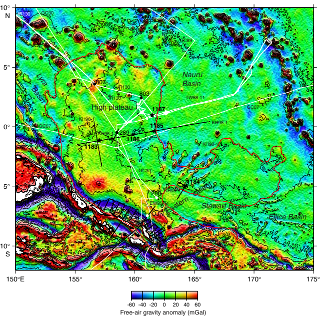

---

[1] **Examples of how to reference the whole or part of this volume.**
[2] **Shipboard Scientific Party addresses.**

sect the ridge, one in the vicinity of Site 1184. Several distinct, semicircular bathymetric and free-air gravity highs, possibly related to these chains, are evident along the ridge; three lie within 35 km of Site 1184, and the closest is 15 km west of the site (Fig. F3).

Geophysical Background

Site 1184 is located at a water depth of ~1662 m (drill pipe measurement) on multichannel seismic (MCS)–reflection Line 101 of Leg 2, cruise KH98-1 of the *Hakuho Maru,* ~2.5 km southwest of the intersection with Line 102 (Figs. F2, F3). The site is ~2.5 km north-northeast of the bounding fault of a ≥15-km-wide graben (Figs. F4, F5). As seen on the Line 101 profile, this graben contains >1.0 s two-way traveltime (TWT) of sediment, which, assuming an average *P*-wave velocity of 2000 m/s for the entire sediment package, corresponds to a thickness of 1000 m. The upper surface of the fault block on which Site 1184 is located has an apparent dip of 4° in the direction of 32° (using a sediment velocity of 1650 m/s for the portion of the sediment package cored; see **"Physical Properties,"** p. 24). On the intersecting Line 102 profile, the upper surface of the block has an apparent dip of 1° in the direction of 302° (Fig. F6). We calculate the true dip of this surface to be 4° in the direction of 18°. Approximately 10 km southeast of Site 1184, a major fault offsets the seafloor downward to the southeast by ~85 m (Fig. F7). The nature and orientation of the fault cannot be determined from the single existing MCS-reflection line.

A sedimentary megasequence onlaps the medium-amplitude, medium-frequency continuous reflection that marks the upper surface of the fault block at this site (Figs. F8, F9). Onlap is evident in both of the intersecting MCS-reflection profiles (Figs. F4, F6, F7, F8, F9) and suggests deposition of the megasequence by dominantly downslope processes rather than by pelagic sedimentation. A plausible source for the onlapping sediments is one or both of the bathymetric highs to the west and north-northwest. At Site 1184, the thickness of the sedimentary megasequence is 0.225 s TWT, thinning to the southwest and thickening to the northeast. Parallel to subparallel reflections are of low to medium amplitude, medium to high frequency, and low to medium continuity. In places, the reflection character is chaotic.

Reflection character within the fault block in the vicinity of Site 1184 differs from that of basaltic basement on the main plateau. Within the block, basement reflection character varies considerably, but some parallel-to-subparallel, high-frequency reflections of limited and variable continuity persist to depths as great as 1.0 s TWT (1625 m at a velocity of 3250 m/s) beneath the surface of the block. Coherent reflections within the fault block (Fig. F4) have an apparent dip of 8° in the direction of 32° (assuming a velocity of 3250 m/s). On the intersecting profile, coherent reflections within the fault block have an apparent dip of 5° in the direction of 302° (Fig. F6). We calculate the true dip of the reflections to be 9° in the direction of 0°.

Summary of Objectives

The main objectives at this site were to determine

1. Compositions of rocks within the fault block, for comparison with those of lavas exposed in Malaita, Santa Isabel, and San

F3. Location and site-survey data, Site 1184, p. 31.

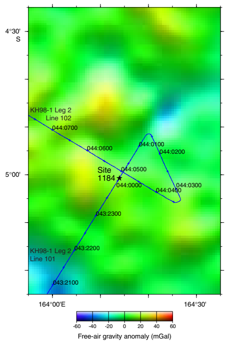

F4. Line 101 MCS reflection profile across Site 1184, p. 32.

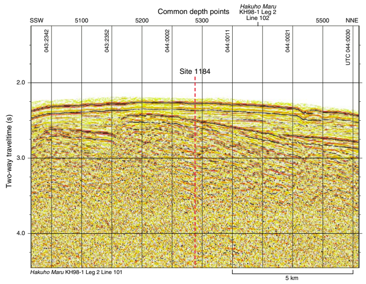

F5. Line 101 MCS reflection profile near Site 1184, p. 33.

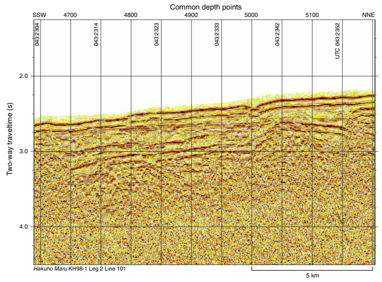

F6. Line 102 MCS reflection profile near Site 1184 (Line 101 intersects Line 102), p. 34.

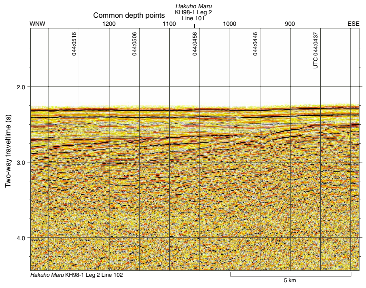

Cristobal, and drilled at DSDP Site 289, ODP Sites 803 and 807, and the other Leg 192 sites;

2. Ages of rocks within the fault block and of sedimentary rocks overlying it to help test the hypothesis that the eastern lobe was an important site of 90-Ma magmatism; alternatively, to ascertain whether this part of the plateau was affected by the later volcanic events recorded in Malaita (Tejada et al., 1996; Neal et al., 1997) and San Cristobal (Birkhold-VanDyke et al., 1996);
3. Physical volcanology of rocks in the fault block and the nature of possible sedimentary interbeds, in order to deduce the eruptive environment (type of eruption and approximate water depths);
4. Early subsidence history, as recorded in the rocks of the fault block and the overlying sedimentary succession; and
5. Ages of sequence boundaries observed in the seismic record.

OPERATIONS

Transit to Site 1184

As we were unable to obtain clearance from the Solomon Islands to drill at the second site planned for Leg 192 (prospectus Site OJ-7D), we proceeded to prospectus Site OJ-6D to drill Site 1184. We accomplished the 911-km transit in 47 hr at an average speed of 10.5 kt. The vessel proceeded directly to the GPS coordinates of the site, and at 1346 hr on 1 October 2000 we deployed a beacon.

Hole 1184A

We spudded Hole 1184A with the rotary core barrel (RCB) at 2000 hr on 1 October. The bit tagged the seafloor at a depth of 1661.5 mbsl. We drilled ahead without coring to 134.4 meters below seafloor (mbsf) at an average rate of penetration of 67 m/hr. After retrieving the wash barrel, we dropped another core barrel and began rotary coring. Hole 1184A was rotary cored from 134.4 to 326.6 mbsf with an average recovery of 76.3%. We contacted a volcaniclastic sequence at 201 mbsf. The average recovery in this sequence was 77.1% (96.4 m recovery); the average penetration rate was 2.5 m/hr.

After coring to 326.6 mbsf, the bit had accumulated 54 rotating hours, and we decided to change the bit. A 50-bbl sepiolite mud flush was circulated in the hole and the bit pulled back to 142 mbsf. Following the successful deployment of the second free-fall funnel (FFF) of the leg, we observed the withdrawal of the bit from the top of the FFF with the vibration-isolated subsea television camera. Most of the FFF was covered by sediment, but the three glass floats were clearly visible. The used bit cleared the rotary table at 0800 hr on 5 October. An inspection of the bit found that it was, remarkably, in nearly pristine condition with no visible wear evident except a slight rounding of the chisel inserts on the cones. The crew removed the old bit and mechanical bit release and replaced these with a new RBI C-7 harder-formation bit and a new mechanical bit release.

We successfully reentered Hole 1184A at 1400 hr on 5 October after a 30-min search. The drill string was run in to 238 mbsf, where the driller observed 20,000–30,000 lb of drag. After the top drive was picked up, the drill string became stuck in the formation. Fortunately, circulation

F7. Line 102 MCS reflection profile near Site 1184, p. 35.

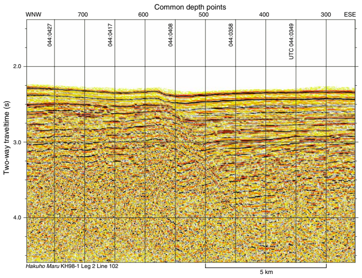

F8. Line 101 MCS reflection profile across Site 1184 (Line 102 intersects Line 101), p. 36.

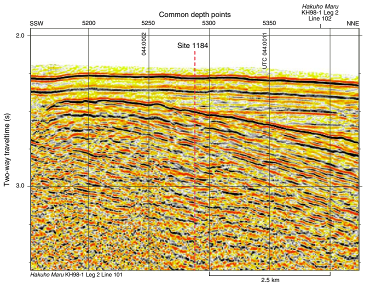

F9. Line 101 MCS reflection profile across Site 1184, p. 37.

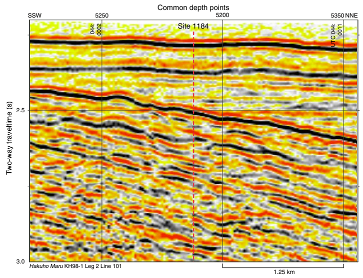

was never lost, and the pipe came free after applying 200,000 lb of overpull above the weight of the drill string. Routine hole maintenance was conducted by washing and reaming the hole from 238 to 326 mbsf. We resumed coring operations in Hole 1184A at 1730 hr on 5 October. The interval from 326.2 mbsf to 538.8 mbsf was cored at an average rate of penetration of 4 m/hr and 86% average recovery. We terminated operations in Hole 1184A when the time allocated for this site had expired. After the crew retrieved the drill string, recovered the beacon, and retracted the thrusters and hydrophones, we began the transit to Site 1185 at 0530 hr on 9 October 2000.

The cored interval in Hole 1184A was 404.4 m (Tables **T1, T2**) with 328.8 m recovered (81.3%) and an average penetration rate of 3.8 m/hr. Apart from the momentary sticking of the drill string following the bit change, we encountered no hole problems.

T1. Coring summary, p. 107.

T2. Expanded coring summary, p. 108.

LITHOSTRATIGRAPHY

Overview

Hole 1184A was washed to 134.4 mbsf, then continuously cored to 538.8 mbsf. Recovery was excellent. We divided the recovered sequence into two units: calcareous ooze above 201.1 mbsf and generally coarse-grained volcaniclastic rocks below. An ~1-cm-thick ferromanganese crust separates the two units. Seismic reflection data show that the boundary between these two units dips 4° to the north-northeast (18°). Reflectors within Unit II dip ~9° in about the same direction (0°), whereas reflectors within Unit I are horizontal and onlap the surface between the units (see **"Background and Objectives,"** p. 1). Paleontological results suggest that most of the volcaniclastic rocks were deposited during the middle Eocene and that the ~65 m of ooze recovered was deposited during the early Miocene. The sedimentary record of the ~20 m.y. between the middle Eocene volcaniclastic phase and the early Miocene pelagic phase of deposition is missing or represented by the ferromanganese crust.

F10. Lithostratigraphic summary, p. 38.

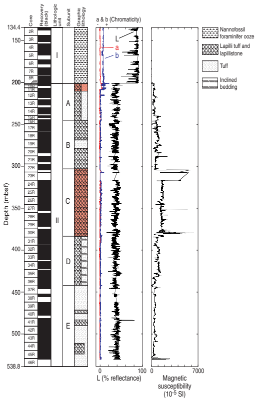

Unit Descriptions

Sedimentary intervals recovered from Hole 1184A are composed of an upper interval of calcareous ooze (Unit I) overlying a lower interval of volcaniclastic rocks (Unit II). The volcaniclastic rocks are divided into five subunits (Fig. **F10**).

Unit I

Interval: 192-1184A-2R-1, 0 cm, to 8R-CC, 10 cm
Depth: 134.4–201.1 mbsf
Age: early Miocene
Lithology: nannofossil foraminifer ooze

F11. Magnetic susceptibility spikes in carbonate ooze, Unit I, p. 39.

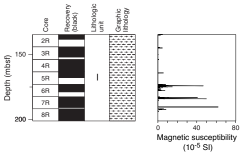

Unit I (Fig. **F11**) is composed predominantly of white, homogeneous, nannofossil foraminifer ooze to foraminifer nannofossil ooze (95 wt% $CaCO_3$; Table **T3**) and contains ≤10% siliceous microfossils. Coring began in this unit at 134.4 mbsf (Section 192-1184A-2R-1, 0 cm). The calcareous ooze probably extends up to the seafloor. The recovered interval contains early Miocene microfossils (see **"Biostratigraphy,"**

T3. Inorganic carbon, carbonate, and XRD analyses of Unit I samples, p. 116.

p. 11). In Core 192-1184A-8R, the ooze is broken into 10- to 20-cm-long pieces (biscuits) set in a slurry of material disturbed by drilling. This type of recovery is common in ooze near the chalk–ooze transition, but no chalk was recovered from Hole 1184A. Thus, Unit I in Hole 1184A corresponds to Subunit IA (Neogene ooze) at those other sites drilled on the Ontong Java Plateau in which the sedimentary sequence was divided into units (e.g., Andrews, Packham, et al., 1975; Kroenke, Berger, Janecek, et al., 1991; see **"Lithostratigraphy,"** p. 4, in the "Site 1183" chapter). The base of Unit I is placed at 201.1 mbsf between the ooze and a ferromanganese crust on top of volcaniclastic Unit II. The unit boundary occurs between Cores 192-1184A-8R and 9R. The unit boundary shows up as a step in color and magnetic susceptibility traces (Fig. **F10**), but, because the unit boundary is between cores, the sharpness of the contact is unknown.

F12. Lithologic characteristics of Unit II, p. 40.

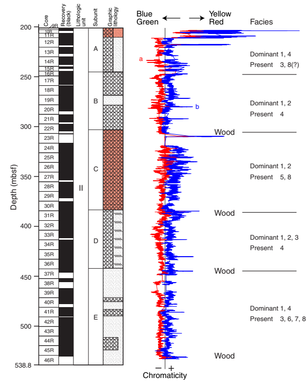

Variations in color and texture within Unit I are generally very subtle. The white ooze has a slight greenish tinge in Cores 192-1184A-2R and 4R, and the greenish intervals seem to contain a slightly higher abundance of siliceous microfossils and foraminifers than the whiter intervals. Faint burrow mottling and discrete burrows are present where color varies. We observed no other trace fossils or physical sedimentary structures.

Volcanic ash is a minor component of the sediment in Cores 192-1184A-4R through 7R. Ash-rich layers are present in Cores 192-1184A-4R, 5R, and 7R and show up as small spikes in the magnetic susceptibility record (Fig. **F11**). In addition, isolated burrows in Cores 192-1184A-4R to 7R are filled by a light gray mixture of ash and ooze, suggesting additional eruptive events.

Very faint, 1- to 2-cm-thick, subhorizontal color bands are present in Cores 192-1184A-6R and 7R. These bands are broader and fainter than, but otherwise similar to, the Liesegang banding within the calcareous ooze and chalk of Hole 1183A (see **"Lithostratigraphy,"** p. 4, in the "Site 1183" chapter). Rare dark flecks throughout Unit I may represent authigenic pyrite or ferromanganese oxide grains.

F13. Whole and fragmented accretionary lapilli, p. 41.

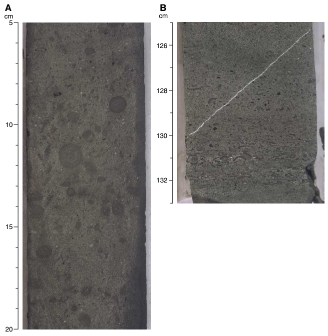

Unit II

Interval: 192-1184A-9R-1, 0 cm, to 46R-1, 132 cm
Depth: 201.1–538.8 mbsf
Age: middle Eocene
Lithology: tuff, lapilli tuff, and lapillistone

Unit II represents a succession of >330 m of volcaniclastic rocks. The most common lithologies are tuff, lapilli tuff, and lapillistone containing lithic and vitric clasts (Fig. **F12**). The tuff is dominated by sand-size volcaniclastic material, whereas the lapilli tuff and lapillistones are characterized by pebble-size volcaniclastic material in a sand-size matrix (see **"Lithostratigraphy,"** p. 6, in the "Explanatory Notes" chapter). Accretionary and armored lapilli are present throughout most of Unit II (Fig. **F13**). We interpret most of the unit as redeposited material derived from primary deposits of explosive hydroclastic volcanic eruptions (see **"Igneous Petrology,"** p. 13). Rare ash-fall layers, wood, and organic-rich intervals are also present.

F14. Ferromanganese crust on volcaniclastic rocks, p. 42.

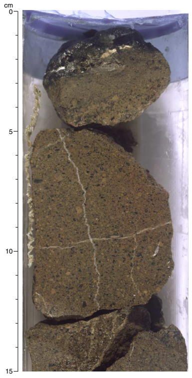

Nannofossils are present in >75% of the tuffs examined, suggesting that most of Unit II is marine; the nannofossils suggest deposition during the middle Eocene (see **"Biostratigraphy,"** p. 11). The top of Unit II is an ~1-cm-thick ferromanganese crust (Fig. **F14**) at the top of interval

192-1184A-9R-1, 0–1 cm (201.1 mbsf). We did not reach the base of Unit II; however, using the velocity data obtained from the volcaniclastic rocks (see **"Physical Properties,"** p. 24) to convert seismic travel times to depth, Unit II could be 1500–2000 m thick. Similar volcaniclastic units have not been encountered previously on the Ontong Java Plateau.

Rocks in Unit II can be grouped into eight facies types (Table **T4**). We used changes in the abundance and color of these lithologies to divide Unit II into five subunits. Interpretations in the following subunit descriptions are discussed further in **"Interpretation of the Sedimentary Record at Site 1184,"** p. 9, in this chapter.

T4. Characteristics of Unit II lithologic facies, p. 117.

Subunit IIA

Interval: 192-1184A-9R-1, 0 cm, to 16R-1, 81 cm
Depth: 201.1–245.21 mbsf
Age: middle Eocene
Lithology: vitric lithic tuff and vitric lithic lapilli tuff

F15. Whole, broken, and armored accretionary lapilli, p. 43.

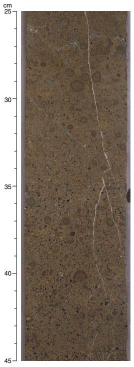

Subunit IIA is 44 m thick. The top of the subunit is placed at the ferromanganese crust at 201.1 mbsf (interval 192-1184A-9R-1, 0–1 cm). The base of the subunit is placed at the base of 3.5 m of massive, fine- to medium-grained, thin- to medium-bedded vitric lithic tuff, which overlies an ~25-m-thick bed of massive vitric lithic lapilli tuff of uppermost Subunit IIB (245.21 mbsf; Section 192-1184A-16R-1, 81 cm).

Subunit IIA is characterized by a succession of thin- to medium-bedded vitric lithic tuff and vitric lithic lapilli tuff. Cores 192-1184A-9R through 11R and interval 12R-4, 10–75 cm, are very pale brown to yellowish red (Fig. **F15**); the rest of Subunit IIA is greenish gray. Some beds are massive, but beds with slightly inclined layers, normal grading, and reverse grading, are common. We tentatively interpret beds containing grading and parallel laminations as turbidity-current deposits. Massive beds within Subunit IIA are interpreted as debris-flow deposits. This subunit shows an overall fining-upward trend.

F16. Massive lapillistone, Subunit IIB, p. 44.

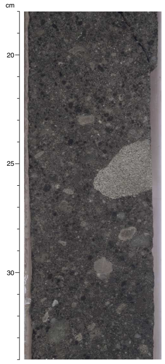

Subunit IIB

Interval: 192-1184A-16R-1, 81 cm, to 22R-6, 93 cm
Depth: 245.21–304.21 mbsf
Age: middle Eocene
Lithology: lithic vitric lapilli tuff and lithic vitric tuff

Subunit IIB is 59 m thick and composed of greenish gray to reddish brown, coarse-grained lithic vitric tuff and lithic vitric lapilli tuff. The top of the subunit is placed at 245.21 mbsf (Section 192-1184A-16R-1, 81 cm) at the top of an ~25-m-thick massive lapilli tuff. The base of the subunit is placed at the top of a tachylitic lapillistone at 304.21 mbsf (Section 192-1184A-22R-6, 93 cm).

F17. Inverse-graded bed, Subunit IIB, p. 45.

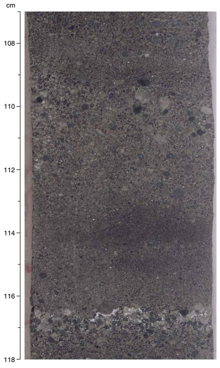

Most beds in Subunit IIB are massive and very poorly sorted. They range in thickness from 5 cm to >25 m (Fig. **F16**). Grain size ranges from very fine sand to coarse pebble. Grading is absent to very subtle within most beds, but some beds show distinct inverse grading (Fig. **F17**). We interpret most of the beds of Subunit IIB as debris flows. Four relatively thin intervals of fine- to medium-grained tuff are present (192-1184A-18R-5, 110 cm, to 19R-1, 75 cm; 19R-8, 0–40 cm; 20R-2, 40–55 cm; 21R-2, 15–80 cm). There is a slight fining-upward trend through this subunit.

Subunit IIC

Interval: 192-1184A-22R-6, 93 cm, to 30R-5, 15 cm
Depth: 304.21–380.52 mbsf
Age: middle Eocene
Lithology: vitric lithic lapilli tuff and vitric lithic lapillistone

Subunit IIC is 76 m thick and composed of red, vitric lithic lapilli tuff (Fig. **F18**) and vitric lithic lapillistone bounded by tachylitic lapillistone (Fig. **F19**). The upper tachylitic lapillistone varies from reddish gray to weak red, and its top defines the top of Subunit IIC at 304.21 mbsf (192-1184A-22R-6, 93 cm). This bed spans the interval from Sections 192-1184A-22R-6, 93 cm, to 24R-1, 17 cm (304.21–316.60 mbsf). However, only ~2 m of rock was recovered in that >12-m interval, so bedding thickness is uncertain and the possibility of unrecovered interbeds cannot be ruled out. The lower tachylitic lapillistone is gray to dark gray; its base falls at 380.52 mbsf (Section 192-1184A-30R-5, 15 cm). It grades upward over 2 m into the vitric lithic lapillistone that makes up the main body of Subunit IIC.

The dominant lithologies (vitric lithic lapilli tuff and vitric lithic lapillistone) of Subunit IIC are very thick bedded and massive. They contain a high proportion of red clasts and a generally red matrix (Fig. **F18**). The proportion of lithic clasts is higher, and that of accretionary lapilli is lower, in Subunit IIC than in the rest of Unit II (Fig. **F20**). Magnetic susceptibility is higher in Subunit IIC than in the rest of Unit II and is particularly high in the tachylitic lapillistone at the top and bottom of the subunit (Fig. **F10**). Tachylite is indicative of subaerial cooling (see **"Igneous Petrology,"** p. 13) and the abundant red clasts in Subunit IIC are consistent with prior subaerial weathering of these clasts. A thin-bedded, fine-grained tuff layer in interval 192-1184A-27R-5, 30–35 cm, appears to be a primary ash-fall deposit.

Subunit IID

Interval: 192-1184A-30R-5, 15 cm, to 36R-4, 50 cm
Depth: 380.52–437.39 mbsf
Age: middle Eocene
Lithology: vitric lithic tuff to vitric lithic lapilli tuff

Subunit IID comprises 57 m of vitric lithic tuff and vitric lithic lapilli tuff. The top of the subunit is placed at the base of the lower tachylitic lapillistone of Subunit IIC at 380.52 mbsf (Section 192-1184A-30R-5, 15 cm). The base of Subunit IID is placed at the base of a 50-cm-thick, horizontally layered interval at 437.39 mbsf (Section 192-1184A-36R-4, 50 cm). Both contacts are gradational. Near the contacts, lithologies typical of Subunit IID are interbedded with lithologies typical of the subjacent and superjacent subunits over 5–10 m of the section.

Subunit IID is characterized by relatively well defined bedding, and inclined layers are common (Fig. **F21**). The top ~17 m of the subunit (interval 192-1184A-30R-5, 15 cm, to 32R-3, 150 cm) are heterogeneous. The interval includes fine to medium sand-size, medium-bedded, dark gray and greenish gray vitric lithic tuff containing accretionary lapilli and wood; inclined granule-rich layers in beds of vitric lapilli tuff; and a 1.24-m-thick bed of massive pebble-rich lapilli tuff typical of Subunit IIC (interval 192-1184A-30R-7, 10–134 cm). This heterogeneous interval is underlain by ~35 m (interval 192-1184A-32R-4, 0 cm, to 35R-8, 75 cm) of interbedded, massive, greenish gray lapillistones and lapilli tuffs with inclined layers. The lower ~5 m of the sub-

F18. Lapilli tuff with rip-up clast, p. 46.

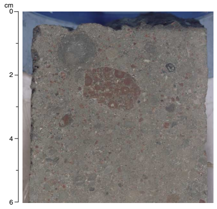

F19. Lapillistone that forms upper boundary, Subunit IIC, p. 47.

F20. Lapilli, lithic clasts, and wood, p. 48.

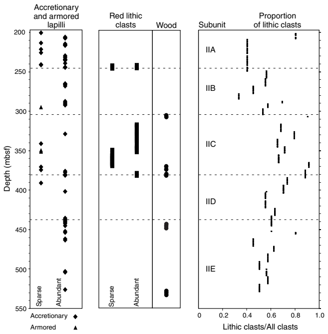

F21. Inclined layering, Subunit IID, p. 49.

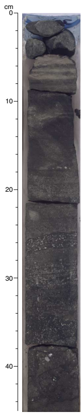

unit (interval 192-1184A-36R-1, 0 cm, to 36R-4, 50 cm) is composed of fine- to medium-sand–size, normally and inversely bedded vitric lithic tuff with common inclined layers of coarse sand and granules. Intercalation of internally layered beds and massive beds suggests that more than one major depositional process was active. Possibilities include current or wave reworking between deposition of massive mass flows and of debris eroded from more proximal deposits.

Subunit IIE

Interval: 192-1184A-36R-4, 50 cm, to 46R-1, 132 cm
Depth: 437.39–538.8 mbsf
Age: middle Eocene
Lithology: lithic vitric tuff to lithic vitric lapilli tuff

Subunit IIE is at least 101 m thick. The top of Subunit IIE is placed below a 50-cm-thick bed of internally layered lapilli tuff typical of Subunit IID at 437.39 mbsf (Section 192-1184A-36R-4, 50 cm), but the transition is gradational. Subunit IIE extends to the base of Hole 1184A.

Subunit IIE is dominated by massive lithic vitric tuff and lithic vitric lapilli tuff. Wood-bearing intervals are present near the top of the subunit and at the base of the cored section (Fig. F22). The subunit exhibits an overall fining-upward trend and grain-size oscillations on scales from centimeters to meters. The upper ~30 m of Subunit IIE (interval 192-1184A-36R-4, 50 cm, to 39R-7, 105 cm) consists of fine to medium sand–size tuff containing accretionary lapilli and of inclined layers composed of granule and coarse sand–size grains. The underlying ~70 m (interval 192-1184A-39R-7, 105 cm, to 45R-6, 105 cm) contains interbedded lithic vitric lapilli tuff and fine to medium grained tuff with rare granule- to pebble-size clasts. Changes in grain size are gradual. Individual beds are up to 6 m thick, but bedding is generally indistinct. Finer-grained beds contain well-preserved accretionary lapilli (Fig. F13A), horizontal granular stringers, and ~10-cm-thick intervals of massive lapilli tuff. Chaotic bedding suggestive of synsedimentary slumping is present in interval 192-1184A-45R-6, 105 cm, to 45R-7, 130 cm (Fig. F23). The chaotic bed also contains wood at eight different levels (Fig. F22). One of these wood pieces displays *Teredo*-like mollusk borings (Fig. F24). The basal 1.3 m of Subunit IIE (Section 192-1184A-46R-1) contains three inversely graded beds, one of which is overlain by fine-grained sand and clay. Wood pieces are present, and the clay contains small black particles, which may be organic.

F22. Wood and organic-carbon-rich layers, Subunit IIE, p. 50.

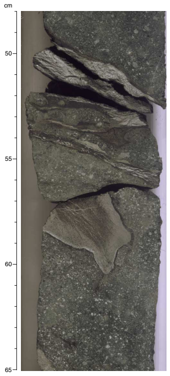

F23. Deformed bedding, Subunit IIE, p. 51.

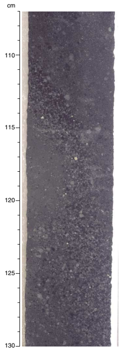

F24. Wood showing *Teredo*-like borings, Subunit IIE, p. 52.

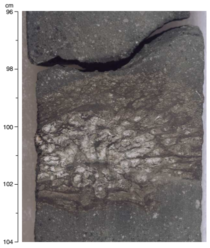

Dip and Direction of Inclined Layers

Inclined layers are present throughout Unit II. They are most abundant in Subunit IID and are rare in Subunit IIC (Fig. F25). We combined the dip and dip direction of 82 laminae with paleomagnetic declinations in order to orient the dip directions relative to magnetic north (see **"Paleomagnetism,"** p. 19). Dips within Subunit IIA are generally <15°, whereas in Subunit IID dips >25° are common. Layers in the other three subunits show a range of inclinations. Throughout Unit II, the dip of the inclined layers is predominantly toward the north-northwest.

F25. Orientation of inclined layers, p. 53.

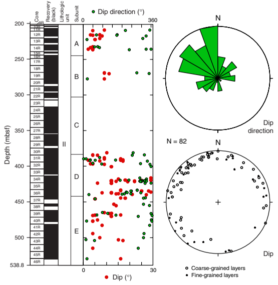

Interpretation of the Sedimentary Record at Site 1184

Middle Eocene: Hydroclastic Volcanism

The middle Eocene volcaniclastic beds (Unit II) at Site 1184 preserve the record of nearby hydroclastic volcanism. Characteristics of the clasts in Unit II that support a dominantly hydroclastic source are presented in **"Igneous Petrology,"** p. 13. Volcaniclastic grains make up virtually 100% of the rock, but we suggest that most beds are redeposited sediment (i.e., rocks in Unit II are not generally interpreted as primary pyroclastic fall or flow deposits). Most of the sedimentary features in Unit II are consistent with a model in which sediments were derived from primary deposits near the vent and then were redeposited on the flanks of the volcano at depths at or below wave base (Fig. **F26**).

F26. Inferred depositional setting at Site 1184, p. 54.

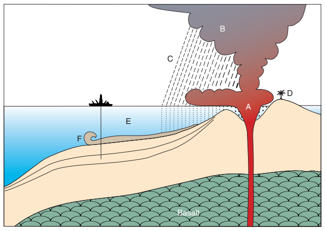

Source Area(s)

Sediments preserved in Unit II were derived from a volcanically active island. Most eruptions were submarine, as demonstrated by the abundance of vitric clasts, but the eruption column often reached the atmosphere, as indicated by the presence of accretionary and armored lapilli (see **"Igneous Petrology,"** p. 13). The presence of wood and other organic material at several intervals (Figs. **F12, F22**) suggests that the upper portion of the volcanic edifice became subaerial long enough to become vegetated.

One or more of the three bathymetric and free-air gravity highs within 35 km of Site 1184 may mark the location of a volcano active during the middle Eocene (Fig. **F3**) (see **"Background and Objectives,"** p. 1). The preferred north to northwest dips of inclined layers in Unit II (Fig. **F25**) and the regional dip of ~9° to the north (see **"Background and Objectives,"** p. 1) may indicate transport from the south-southeast. However, if the regional dip is to the north, many of the low-angle inclined layers in the core could be subparallel to bedding and thus not provide independent estimates of transport direction (see **"Paleomagnetism,"** p. 19).

Depositional Setting and Paleobathymetry

Coarse, massive beds composed almost exclusively of volcaniclastic material dominate Unit II. No pelagic interbeds were observed, but nannofossils are present throughout the unit, indicating submarine deposition. The nannofossil assemblages suggest most of Unit II was deposited in ~3 m.y. or less (see **"Biostratigraphy,"** p. 11). The short time interval represented by Unit II and the paucity of nonvolcaniclastic material argue for rapid deposition proximal to the source. The presence of relatively delicate accretionary lapilli and angular vitric clasts is consistent with short transport distances. Close to the vent, however, we would expect to find a significant number of large (>2 cm), dense clasts (e.g., blocks and spindle bombs), which we did not observe. Therefore, the rocks cored from Site 1184 were probably not the most proximal primary deposits, and we infer that Site 1184 was located on the flanks of the volcano (Fig. **F26**).

Gravity flows should be common on a rapidly aggrading sedimentary apron around a volcano. Features typical of volcaniclastic debris flow deposits (massive, poorly sorted, or coarse) are abundant in Unit II. Other volcanic processes can produce massive beds, but they are usually subaerial and occur in association with internal and/or interbedded, layered deposits (e.g., Fischer and Schmincke, 1984). The presence of nannofossils throughout Unit II (see **"Biostratigraphy,"** p. 11) is consistent with submarine mass-flow deposits. Similarly, the majority of internally stratified beds in Hole 1184A do not appear to represent primary volcanic layering. Fine-grained material that may be air-fall ash is present rarely, but we did not observe layering typical of coarser material that has settled through the water column. Rather, the graded beds, parallel-laminated intervals, and subhorizontal coarse sand and granule layers in Unit II are consistent with deposition from high-concentration turbidity currents. Steeply inclined layers in Subunit IID suggest sediment transport with a unidirectional component and could be crossbedding formed by currents.

As with our conclusions regarding distance to the vent, paleobathymetric inferences are based largely on negative data. Debris flow deposits provide no depth information, and high sedimentation rates (estimated to be >100 m/m.y.), coupled with possible uplift or subsidence pulses associated with the nearby active volcanism, may imply significant paleodepth changes during deposition of Unit II. With these caveats, we propose that Subunits IIA, IIB, and IIE probably accumulated below the storm-wave base (≳50 m) but shallower than the present-day water depth of Unit II (~2000 m). The upper depth limit is based on the scarcity of sedimentary structures indicative of reworking or winnowing by waves or currents after each debris flow was deposited. Shallow-water bioclasts are absent, but there is also a lack of fine-grained and/or pelagic interbeds. If inclined layers (Fig. **F21**), which are most common in Subunit IID, reflect transport by storm-wave-generated currents, they indicate deposition near the storm-wave base.

Subunit IIC is coarse grained throughout, contains abundant red lithic clasts, and is bounded by tachylitic lapillistone (Fig. **F19**). The tachylitic clasts formed during subaerial eruptions (see **"Igneous Petrology,"** p. 13). The red clasts (Fig. **F18**) and some aspects of alteration suggest subaerial weathering (see **"Alteration,"** p. 17). Together, these observations suggest a significant subaerial component within the sediments of Subunit IIC, but we have little sedimentological control on the final depth of deposition.

Depositional Trends in Unit II

Debris flow deposits dominate the volcaniclastic rocks of Unit II. There is a general increase in the thickness, coarseness, and abundance of these deposits from Subunit IIE to IIC and a decrease from Subunit IIC to IIA. If the tachylite and the high proportion of red lithic clasts in Subunit IIC indicate a proximal, shallow to subaerial setting, then the trends through Unit II can be interpreted as progressive shallowing from Subunit IIE to IIC and deepening from Subunit IIC to IIA. Conversely, differences among subunits might reflect variability within a submarine facies characterized by a mosaic of depositional styles that vary as a function of sediment input (e.g., changes in debris flow frequency or clast composition caused by variations in volcanic activity).

Early Miocene: Pelagic Deposition

In the early Miocene, pelagic ooze began to accumulate at Site 1184. The ooze is typical of pelagic deposition above the calcite compensation depth (CCD) under an oxygenated water column and contains rare volcanic ash layers. Similar ash layers were found in coeval deposits from Site 1183 (see **"Lithostratigraphy,"** p. 4, in the "Site 1183" chapter). The ooze contains a bathyal to abyssal benthic foraminifer assemblage (see **"Biostratigraphy,"** p. 11). Seismic stratigraphy shows that a thick accumulation of horizontally layered sediments in this area is currently present below the level of the oldest ooze at Site 1184 (Fig. F4). However, at Site 1184, a ferromanganese crust formed between the termination of volcaniclastic deposition during the middle Eocene and the initiation of pelagic accumulation ~20 m.y. later during the early Miocene. Ferromanganese crusts and nodules typically grow at a rate of a few millimeters per million years. The crust between Units I and II may record nondeposition during much of the middle Eocene through early Miocene hiatus. The pervasive alteration and reddish orange color of the upper 8 m of Unit II and the capping ferromanganese crust are consistent with a hiatus (Figs. F14, F15). Why the pelagic sediments onlap rather than drape the volcaniclastic surface is unresolved.

BIOSTRATIGRAPHY

Overview

Sixty-seven meters of lowermost Miocene (Fig. F27) calcareous ooze (Cores 192-1184A-2R through 8R) was drilled at Site 1184. Integrated calcareous microfossil biostratigraphy demonstrates that a hiatus of nearly 1 m.y. duration (Fig. F28) is present between Core 192-1184A-4R and 5R. The poorly consolidated sediment recovered from Core 192-1184A-8R came from upsection. Nannofossil assemblages place most of the volcaniclastic material (Cores 192-1184A-13R through 45R) within the middle Eocene Zone NP16 of Martini (1971).

F27. Calcareous microfossil biostratigraphy of Unit I, p. 55.

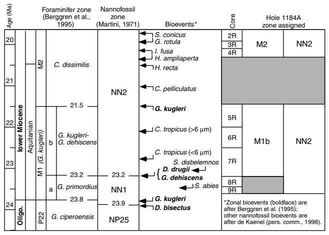

F28. Age vs. depth plot, p. 56.

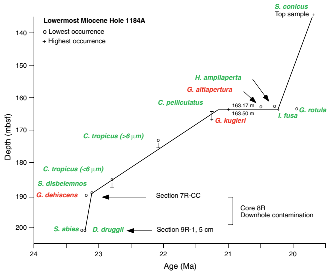

T5. Planktonic foraminifer and calcareous nannofossil HO and LO, p. 118.

Unit I: Lower Miocene Calcareous Ooze

All samples examined contain abundant and well-preserved calcareous nannofossils and planktonic foraminifers. The calcareous microfossil biozonations used and our zonal assignments are illustrated in Figure F27. Table T5 is a summary of the main biostratigraphic events identified in Unit I, and Figure F28 (Ma values are from Berggren et al., 1995, and E. de Kaenel, pers. comm., 1998) is a time-depth plot.

Calcareous Nannofossils

All assemblages recovered from Unit I are from Zone NN2 of Martini (1971); *Triquetrorhabdulus carinatus* is present in the topmost sample examined (Sample 192-1184A-2R-1, 20–21 cm), and *Discoaster druggii* ranges to the base of Unit I. Additional nannofossil events can be used to subdivide Zone NN2 (Table T5; Fig. F27).

Planktonic Foraminifers

The boundary between Zones M1b and M2 of Berggren et al. (1995) is contained within the lowermost Miocene sediments. The two uppermost cores (Cores 192-1184A-2R to 3R) contain an assemblage typical of Zone M2 and are characterized by abundant species of *Globoquadrina, Globigerinoides,* and *Dentoglobigerina,* as well as the taxa *Catapsydrax dissimilis, Jenkinsella siakensis, Globigerina venezuelana,* and *Globorotalia mendacis.* Several appearances that have been placed near the base of Zone M2 (Kennett and Srinivasan, 1983; Bolli and Saunders, 1985) occur in Cores 192-1184A-4R and 5R (Table T5), indicating that this zone may be relatively complete. Zone M1b (Samples 192-1184A-5R-3, 20–21 cm, to 7R-CC, 0–10 cm) is marked by abundant *Globorotalia kugleri, G. mendacis, Globigerina ciperoensis,* and *G. fariasi,* as well as rare *Globoquadrina dehiscens* and *G. praedehiscens*. Sample 192-1184A-5R-3, 20–21 cm, marks the highest occurrences of both *Globorotalia kugleri* and *Globigerina ciperoensis;* the former species defines the M1b/M2 boundary.

Globally, the appearance of *Globigerinoides* species is variable and has been tied to the influx of warm, tropical water masses (Stainforth and Lamb, 1981; Bolli and Saunders, 1985). Its appearance at Site 1184 is relatively high in the section, in the lower part of Zone M2, where the genus is rare (i.e., the lowest occurrences of *Globigerinoides primordius* and *G. parawoodi* are in Sample 192-1184A-5R-1, 20–21 cm). A more common and diverse *Globigerinoides* assemblage is present at and above Section 192-1184A-3R-CC, where *G. trilobus, G. quadrilobatus,* and *G. sacculifer* enter the section. The reason for this delayed entry is unclear. *Globoquadrina dehiscens* is rare below the main *Globigerinoides* influx, possibly indicating a late entry of the tropical water mass typical of the Neogene Ontong Java Plateau region after cooling in the Oligocene. However, *Globigerina venezuelana* is common throughout the entire recovered lower Miocene interval and is a warm-water-mass indicator (e.g., Kennett and Srinavasan, 1983). Thus, either some unknown paleoecologic factor affected this site or the tropical preference of *G. venezuelana* has been overestimated.

Unit II: Volcaniclastic Sandstones and Conglomerates

Calcareous Nannofossils

We applied the Martini (1971) zonation to the rare and poorly preserved assemblages recovered throughout the volcaniclastic sequence in Cores 192-1184A-9R through 46R. We assume these assemblages are in situ. A sample from a thin chalk-filled fracture (Sample 192-1184A-9R-1, 5 cm) near the top of Unit II contains an early Miocene assemblage from Zone NN2, with *Discoaster druggii*. However, the characteristics of the assemblage (e.g., very high number of nannoliths) are very unlike those of any assemblage recovered from the overlying chalks. A sample from Core 192-1184A-10R yielded a single specimen of *Ericsonia formosa* and is no younger than earliest Oligocene (Zone NP21). *Discoaster barbadiensis* is present in Cores 192-1184A-11R and 12R, indicating an age no younger than latest Eocene (Zone NP20). *Reticulofenestra umbilica* ranges downward to near the base of the recovered section (Sample 192-1184A-45R-5, 12 cm), which indicates an age no older than the middle Eocene Zone NP16. Single specimens of *Chiasmolithus minimus* and *Discoaster bifax* recovered from Sample 192-1184A-13R-1, 59–60 cm, may indicate that nearly the entire volcaniclastic sequence belongs within the same nannofossil zone (NP16). Single specimens of *Sphenolithus furcatolithoides* in Sample 192-1184A-18R-6, 28–29 cm, and *Discoaster gemmeus* in Sample 192-1184A-25R-5, 68 cm, also were observed; both these species also went extinct within Zone NP16 (Perch-Nielsen, 1985). Although the total thickness of the volcaniclastic sediments is unknown, the deposition of >300 m of section within a single nannofossil zone implies a very rapid rate of deposition. It is therefore likely that much of the unit was deposited under comparatively deep-water conditions to provide the needed accommodation space. Cores 192-1184A-9R through 12R should be examined in more detail to determine if any of the volcaniclastic sediment is actually post–middle Eocene.

Planktonic Foraminifers

Unit II is barren of foraminifers.

Paleoenvironment

Well-preserved benthic foraminifers recovered from the lower Mio-cene section represent two distinct assemblages. Intervals 192-1184A-2R-CC, 0–10 cm, to 3R-CC, 14–19 cm, may have been deposited at middle-slope depths. This possibility is indicated by the near absence of *Bulimina jarvisi* and the presence of *Gyroidinoides soldanii, G. altispira, Hoeglundina elegans,* and *Sphaeroidina bulloides* (Van Morkhoven et al., 1986). Samples 192-1184A-4R-CC, 0–5 cm, through 5R-3, 20–21 cm, contain a marked increase in benthic foraminifer diversity and abundance over those recovered from the underlying section. *Globocassidulina moluccensis, Bulimina jarvisi, B. mexicana, Planulina rugosa,* and *Karreriella chapapotensis* characterize the assemblage from this interval. In the absence of abyssal species, *Bulimina jarvisi* is an excellent lower-slope indicator (van Morkhoven et al., 1986); the other species present are consistent with this interpretation. The section below Sample 192-1184A-5R-3, 20–21 cm, contains rare benthic foraminifers, dominated by *Stilostomella gracillima, Uvigerina senticosa,* and *Vulvulina spinosa,* indicating a transition from the lower slope to an abyssal paleoenvironment. The uppermost 8 m of volcaniclastic rock is completely altered to pale brown Fe oxyhydroxide and clay, indicating weathering in an oxidizing (possibly subaerial) environment (see **"Site 1184,"** p. 14, in "Principal Results" in the "Leg Summary" chapter). Therefore, the overlying deep-water pelagic ooze indicates very rapid subsidence to near-abyssal water depths after the end of volcanism.

IGNEOUS PETROLOGY

Introduction

We recovered a 337.7-m-thick sequence of volcaniclastic rocks from Hole 1184A with an average recovery of 82.6%. We defined this sequence as Unit II and divided it into five subunits on the basis of changes in sedimentary structures, clast types, and characteristic grain size (see **"Lithostratigraphy,"** p. 4). Because of the high proportion of volcanic glass shards, we assigned lithologic names for pyroclastic deposits as defined by Fisher and Schmincke (1984) (see **"Igneous Petrology,"** p. 12, in the "Explanatory Notes" chapter). Using this nomenclature, Unit II consists of a sequence of poorly sorted vitric and lithic tuffs, lapilli tuffs, and lapillistones.

Vitric and lithic clasts and armored and accretionary lapilli are present throughout Unit II, and coarse tachylite-rich layers form the upper and lower parts of Subunit IIC. The morphology and relative proportion of lithic to vitric clasts (ash to lapilli size) show systematic downhole variation (Fig. **F20**).

Macroscopic Description and Petrography

The volcaniclastic rocks consist of six principal components: ash- to lapilli-size lithic clasts and vitric shards, accretionary lapilli, armored lapilli, crystal fragments (plagioclase and clinopyroxene), and matrix and/or cement (Figs. **F29, F30**). Carbonized wood fragments are a minor component (Fig. **F20**). Thin section observations (summarized in Table **T6**) show that the matrix consists of fine-grained vitric and lithic ash, clay, and other alteration minerals cemented by zeolite or calcite. Titanomagnetite and, rarely, minor amounts of sulfide are also found within the matrix. The plagioclase and clinopyroxene crystal fragments are generally unaltered, but the titanomagnetite grains in the matrix show evidence of alteration to maghemite (Fig. **F31**). Some discrete plagioclase crystals exhibit irregular oscillatory zoning. Glass inclusions are found in the clinopyroxene and plagioclase crystals (Figs. **F32, F33**).

The lithic clasts in all five subunits of Unit II are composed of basalt, reworked volcaniclastic rock or diabase. They range in size from <1 to ~65 mm and are generally subangular to subround. The largest clasts are reworked volcaniclastic rocks, generally rip-up clasts of tuff and lapilli tuff (Fig. **F18**). Some rip-up clasts contain red, clay-coated accretionary and armored lapilli (Figs. **F18, F34**). Some moderately to highly vesicular lithic clasts contain smaller clasts of nonvesicular, aphyric basalt (Fig. **F35**).

The basalt clasts are predominantly nonvesicular to moderately vesicular and aphyric to sparsely plagioclase and/or clinopyroxene phyric (see Table **T6**). Scoriaceous basaltic clasts containing plagioclase and clinopyroxene are also present. Thin section examination demonstrates that some of the highly altered basaltic clasts have visible igneous textures, including intersertal, subtrachytic, and subophitic (Figs. **F36, F37, F38**). Several aphanitic basalt clasts contain clinopyroxene and plagioclase glomerocrysts. Rounded clasts of apparently more evolved basalt (Fig. **F39**) are distinguished by a greater abundance of plagioclase and titanomagnetite relative to clinopyroxene. In contrast to the aphanitic basalt, the diabase clasts contain unaltered plagioclase, clinopyroxene and titanomagnetite (Figs. **F40, F41**).

Armored and accretionary lapilli, though generally sparse, are often concentrated in layers ≤5 cm thick (e.g., Figs. **F42, F43**). Layers with concentrations of broken armored and accretionary lapilli grade into layers in which these lapilli are unbroken (Fig. **F44**). Where the armored and accretionary lapilli are broken, they are commonly found in a hydrodynamically stable, convex-upward orientation (Fig. **F45**), which suggests some reworking (see **"Lithostratigraphy,"** p. 4). Both armored and accretionary lapilli have red (oxidized) margins in Subunits IIA and IIC (Fig. **F15**). Thin sections show that the armored lapilli have nuclei of vesicular basalt, aphanitic basalt, or altered glass (Figs. **F46, F47**).

The majority of vitric clasts are subangular to angular glass shards, <10 mm in size. The glass is generally blocky and nonvesicular, but minor amounts of sparsely to highly vesicular shards (some with scalloped edges or internal flow textures) are present (Figs. **F48, F49, F50**). In the upper 250 m of the cored section, glass shards are highly altered and commonly replaced by concentric layers of smectite, celadonite, and zeolite (see **"Alteration,"** p. 17; Fig. **F49**). Unaltered glass is generally present below Core 192-1184A-38R. Some glass shards contain small euhedral crystals of plagioclase and clinopyroxene (Fig. **F51**).

A highly altered, highly vesicular scoria clast type is also present and may represent devitrifed vesicular glass shards. The high degree of alteration gives these clasts the appearance of lithic fragments; as a result, the proportion of vitric to lithic clasts may be underestimated.

The lapillistones forming the upper and lower parts of Subunit IIC have a more compacted texture than the rest of Unit II (Fig. **F19**). In thin section, the lapillistones contain large amounts of tachylite (glass

F29. Lithic and vitric clast types, p. 57.

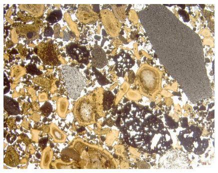

F30. Lapilli tuff with basaltic clasts, glass, and lapilli, p. 58.

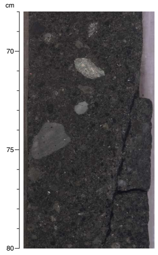

T6. Thin section descriptions for Unit II volcaniclastic rocks, p. 119.

F31. Titanomagnetite to maghemite alteration, p. 59.

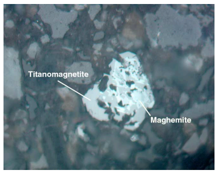

F32. Glass inclusions in plagioclase crystal, p. 60.

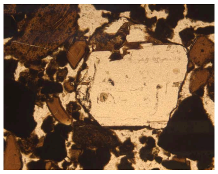

F33. Glass inclusions in clinopyroxene, p. 61.

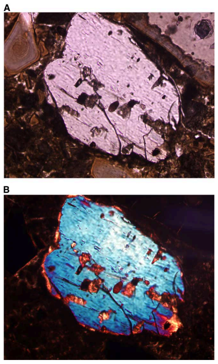

made nearly opaque by the presence of Fe-Ti oxide microlites) (Fig. F52). Plagioclase laths within the tachylite define a subtrachytic-to-trachytic texture around flattened or elongated lithic clasts (Figs. F53, F54).

Geochemistry

We selected six samples of tuff for whole-rock analysis by inductively coupled plasma–atomic emission spectrometry (ICP-AES). The samples fall into two compositional groups on the basis of position in the cored section and the presence or absence of unaltered glass. Unaltered glass is rare above Core 192-1184A-39R but is present from Section 39R-1 to the bottom of the hole. The three samples from above Core 192-1184A-39R (192-1184A-18R-6, 43–45 cm; 31R-1, 140–142 cm; 36R-7, 74–76 cm) have higher total alkali contents than do the other three samples (Fig. F55). The apparent alkalic character of the upper three samples is probably a result of alteration rather than an original magmatic signature, because their incompatible element abundances are low (Table T7) compared to abundances in alkalic basalts on Malaita and Santa Isabel (Tejada et al., 1996). All six samples have relatively high weight loss on ignition (5.8–7.4 wt%) (Table T7).

Downhole Summary

We find no downhole change in the types of vitric and lithic clasts that are present throughout Unit II, except that tachylite and red, oxidized lithic clasts are much more abundant in Subunit IIC. Differences in the relative abundance of lithic to vitric clasts correlate broadly with the subunit boundaries (Fig. F20), and there is a peak in the proportion of lithic clasts within Subunit IIC. Armored and accretionary lapilli are also present throughout Unit II but are generally least abundant in Subunit IID. This subunit comprises vitric lithic tuffs with inclined layers, suggesting current reworking, perhaps above storm-wave base (see **"Lithostratigraphy,"** p. 4). Reworking of these tuffs could have destroyed accretionary lapilli that may originally have been present. The upper 20 m of Subunit IIA may have been extensively reworked (see **"Biostratigraphy,"** p. 11). However, Subunit IIA contains the highest abundance of accretionary lapilli and the highest proportion of angular vitric clasts, indicating that little reworking occurred during deposition of the lower part of this subunit.

Subunit IIC is defined by the presence of compacted tachylite-rich layers, a higher ratio of lithic to vitric clasts, abundant red (oxidized) clasts, and high magnetic susceptibility and paleomagnetic intensity (see **"Paleomagnetism,"** p. 19, and **"Physical Properties,"** p. 24).

Environment of Eruption

The volcaniclastic sequence recovered from Hole 1184A represents several broadly similar eruptive events. Significantly, several features of the volcaniclastic rocks are consistent with eruption in a shallow-water to emergent setting.

The abundance of blocky glass shards suggests that the volcaniclastic sequence formed through the explosive interaction of basaltic magma with water in hydroclastic eruptions. The accretionary and armored lapilli indicate the presence of steam-rich subaerial eruption columns. Such eruption columns are typical of hydroclastic volcanic activity and

F34. Lapilli tuff with clast of tuff, p. 62.

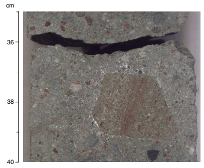

F35. Altered aphyric basalt within vesicular basalt clast, p. 63.

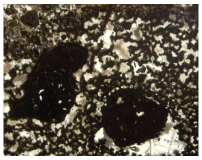

F36. Subtrachytic texture in basalt clast, p. 64.

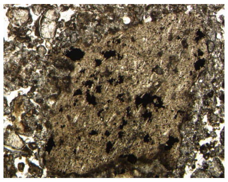

F37. Large rounded basalt clast, p. 65.

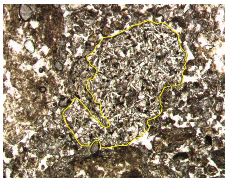

F38. Phenocrysts in a titanomagnetite-rich basalt clast, p. 66.

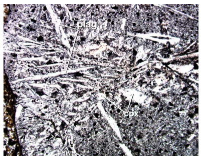

F39. Titanomagnetite-rich basalt clast, p. 67.

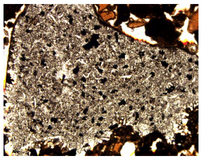

generally originate from vents at water depths of <300 m (e.g., Fisher and Schmincke, 1984). Alternatively, the eruption could have occurred on land, with ground or surface water providing the moisture necessary for formation of accretionary lapilli.

The presence of tachylite clasts and red (oxidized) lithic clasts in the volcaniclastic succession strongly suggests a subaerial setting for at least some of the eruptions. Tachylite clasts are most abundant in Subunit IIC, but vesicular tachylite clasts are sparse throughout the succession. Tachylite is generally thought to form by rapid cooling of basaltic magma droplets in air or in littoral environments where subaerial lava flows quench and fragment as they enter the sea (e.g., Fisher and Schmincke, 1984). The local existence of land is supported by the presence of carbonized wood fragments at several intervals that coincide with subunit boundaries (see **"Lithostratigraphy,"** p. 4), suggesting that the wood fragments accumulated at the sites of deposition between major depositional and/or eruptive events.

The presence of rip-up clasts and bands of convex-upward accretionary lapilli fragments (e.g., Fig. **F45**) suggests some reworking of the volcaniclastic sediments, which is consistent with the sedimentological observations for Unit II (see **"Lithostratigraphy,"** p. 4). The absence of blocks and bombs suggests that the sequence did not originate close to the eruptive center, but the fact that accretionary lapilli are abundant suggests relatively short transport distances during reworking. Estimating with any certainty the distance to the eruptive vent(s) is impossible, but the small positive free-air gravity anomalies and bathymetric highs around Site 1184 suggest three possible sources (see Fig. **F3**; also see **"Background and Objectives,"** p. 1).

Comparison with Other Parts of the Ontong Java Plateau

One of the objectives for Site 1184 was to determine the nature of the basement on the eastern salient of the Ontong Java Plateau (see **"Background and Objectives,"** p. 1). The recovery of a sequence of volcaniclastic sediments containing a high proportion of vitric clasts and accretionary and armored lapilli indicates that the eastern salient was the site of explosive hydroclastic eruptions in a shallow marine to emergent environment. The presence of volcaniclastic rocks with intercalated wood fragments at Site 1184 provides the first clear evidence of emergent, explosive volcanism on the plateau. The inferred middle Eocene age for the volcaniclastic sequence (see **"Biostratigraphy,"** p. 11) is nearly the same as that of the 44-Ma alkalic Maramasike Formation on the island of Malaita (Tejada et al., 1996) and broadly comparable to that of the most recent eruptive event producing tholeiitic basalts on the island of San Cristobal (Makira) at 36 ± 3 Ma (Birkhold-VanDyke et al., 1996).

Immobile-element abundances in the six samples analyzed by ICP-AES are similar to those of basalt from Site 1185 (lower group), Site 1186, and Units C–G at Site 807. One sample from Hole 1184A plots on the border of the Singgalo Formation field, defined by basalt flows from Malaita (Fig. **F56**), and is similar to some 90-Ma Site 803 basalts. This pattern is less clear on a plot of TiO$_2$ vs. Mg# (Fig. **F57**), but the MgO contents may have been affected by alteration. The three samples from below Core 192-1184A-39R have similar TiO$_2$ contents to those of the Kwaimbaita Formation basalts, Units C–G from Site 807, and the lavas

F40. Diabase clast, p. 68.

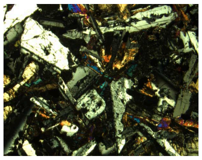

F41. Skeletal titanomagnetite in diabase clast, p. 69.

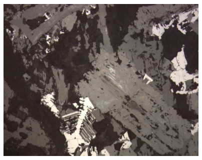

F42. Tuff with accretionary lapilli bands, p. 70.

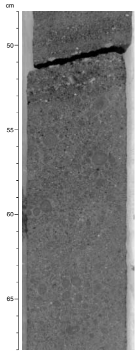

F43. Accretionary lapilli in lapilli tuff, p. 71.

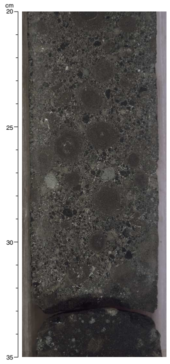

F44. Tuff with accretionary lapilli, p. 72.

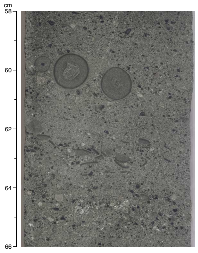

from Sites 1183, 1185 (lower group), and 1186, but Cr (and Ni) abundances are higher (Fig. F58).

The inferred middle Eocene age of eruption for volcaniclastic rocks at Site 1184, coupled with magmatism of a broadly similar age on Malaita and San Cristobal, suggests that magmatic activity was widespread on the Ontong Java Plateau during the Paleogene. The fact that the Site 1184 Unit II bulk samples are tholeiitic and have incompatible element abundances similar to Ontong Java Plateau basalts erupted at ~122 Ma implies that similar mantle sources, melting to similarly high degrees (Neal et al., 1997), were available as long as 80 m.y. after the initial plateau magmatism.

ALTERATION

Introduction

The entire 337.7-m-long sequence of lithic vitric tuff, lapilli tuff, and lapillistone cored at Site 1184 has undergone low-temperature alteration. The top of Core 192-1184A-9R is capped by a thin (3–7 mm) black ferromanganese crust. The upper 8 m (Cores 192-1184A-9R through 11R) is completely altered to red, tan, and pale brown iron oxyhydroxides and clay minerals, indicative of highly oxidizing conditions. Color changes in this oxidized zone are commonly gradational and do not seem to correspond to alteration fronts. Red to bright brick-red zones commonly occur in fine-grained areas; however, we observed no correlation between alteration and primary sedimentary structures. Background alteration in the remainder of the hole has imparted a greenish gray color to the rocks because of alteration of individual clasts and matrix to smectite. Toward the bottom of the hole, red or reddish brown lithic fragments and accretionary and armored lapilli are commonly intermixed with less altered clasts and/or surrounded by greenish gray matrix. This intermixture suggests that variable conditions were operating, possibly before deposition in a marine environment. The rocks are cemented with smectite, analcime, calcite, rare celadonite, and several zeolites, including gmelinite, chabazite, levyne, and clinoptilolite (identified by X-ray diffraction [XRD]). Several generations of late, white crosscutting veins contain calcite, analcime, apophylite, natrolite, and mordenite (identified by XRD). For a complete list of secondary minerals identified by XRD, see Table T8.

Clasts

The volcaniclastic rocks are made up of the following types of clasts in decreasing order of abundance: basaltic glass shards, dark tachylitic clasts, various gray lithic clasts, and diabase clasts (see "Igneous Petrology," p. 13). The basaltic glass shards are generally nonvesicular and angular to subangular. They are most commonly totally replaced by secondary minerals, mainly yellowish brown to orange-brown, submicroscopic to scaly smectite (Fig. F59). Zeolites and/or analcime replace the centers of a few glass shards (Figs. F60, F61, F62). The most commonly observed assemblage of secondary minerals filling vesicles in individual glass fragments follows the depositional sequence (from rim to center): smectite, analcime and/or zeolites, calcite. Celadonite was tentatively identified as rare, thin rims on individual fragments (Fig. F63), participating in the replacement of basaltic glass with smectite (Fig. F64) and

F45. Tuff with convex-upward accretionary lapilli fragments, p. 73.

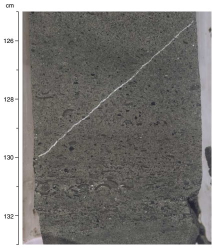

F46. Armored lapillus, p. 74.

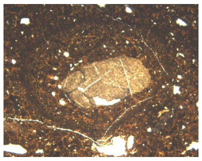

F47. Altered glass shard armored by ash, p. 75.

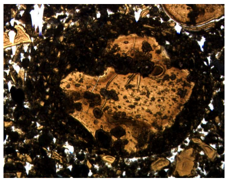

F48. Unaltered glass in interiors of vitric clasts, p. 76.

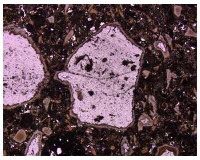

F49. Lithic vitric tuff with alteration bands, p. 77.

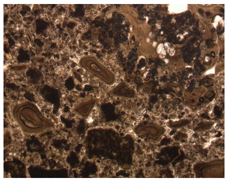

F50. Flow banding in fresh glass clast, p. 78.

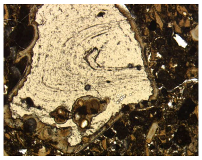

filling vesicles in glass (Fig. F65). Celadonite spherules displaying well-developed Liesegang banding were observed in association with fine-grained celadonite filling vesicles (Fig. F66).

Unaltered basaltic glass is present in Cores 192-1184A-11R through 13R, Core 31R, and Cores 39R through 45R. A thin layer of brown to yellowish brown smectite commonly rims individual shards of unaltered glass (Fig. F67). An interesting feature in several shards is the presence of dark, tubular to vermicular, commonly fibril-like features at the interface between the alteration rim and unaltered glass (Fig. F68). These types of features have previously been ascribed to microbially mediated alteration of basaltic glass (e.g., Fisk et al., 1998; Torsvik et al., 1998). Vesicles in unaltered glass are either empty or, more commonly, completely filled by smectite (Figs. F68, F69).

The dark brown to black tachylite clasts are commonly highly vesicular and scoriaceous. We could not determine the extent of alteration of the matrix of tachylitic clasts because the matrix is almost totally opaque in thin section. Vesicle fillings in the tachylite clasts are similar to those in vesicles within glass fragments. The lithic clasts we observed in thin section are rarely altered; however, the matrix of one diabase clast was totally replaced by smectite.

Cement

The cement between individual clasts is predominantly composed of the same minerals as those replacing glass fragments and filling cavities. The assemblage of secondary minerals is significant because the zeolites we identified commonly form as the result of low-temperature alteration of basaltic rocks in subaerial environments (e.g., Coombs et al., 1959; Walker, 1951, 1959, 1960a, 1960b) and are uncommon in oceanic basalts or sediments (Kastner, 1979; Honnorez, 1981). Coarser grained intervals commonly display patchy filling of pore spaces with calcite, analcime, and zeolites. A few occurrences of milky white to bluish chalcedony filling pore spaces were also observed (e.g., Cores 192-1184A-36R through 38R). Rare pleochroic celadonite has also been identified tentatively in the cement (Fig. F70). In two thin sections (192-1184A-42R-1, 147–150 cm, and 42R-6, 82–85 cm), we observed that the clasts were cemented by a matrix made up of fine-grained ash completely altered to smectite, and that the intergranular zeolite cement was relatively rare.

Veins

Several generations of white, hairline to >5-mm-wide veins crosscut the cores. The veins are filled with analcime ± zeolites (natrolite or mordenite) ± calcite and are lined with minor smectite and/or celadonite (identified by XRD) at the vein margins. Several of the larger (2- to >5-mm-thick) veins contain prismatic crystals formed during symmetrical open-space infilling of fractures with minor or no replacement of the wall rock; empty pore space is still present in some fractures. Pyrite is observed in a large (~1 cm thick) calcite + analcime + quartz + mordenite vein at the bottom of Section 192-1184A-46R-1. The abundance of veins appears to decrease downhole, although we did not carry out a statistical study of the veins at this site.

F51. Plagioclase-clinopyroxene-phyric glass clast, p. 79.

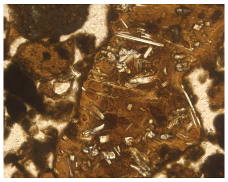

F52. Disseminated titanomagnetite in tachylitic lapillistone, p. 80.

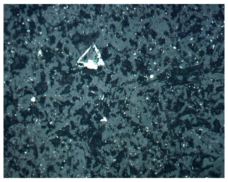

F53. Tachylite with plagioclase microlites, p. 81.

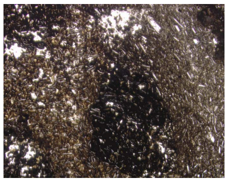

F54. Tachylite clasts with plagioclase microlites, p. 82.

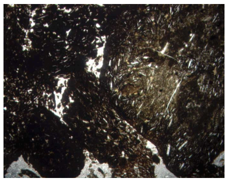

F55. Total alkalies vs. silica, p. 83.

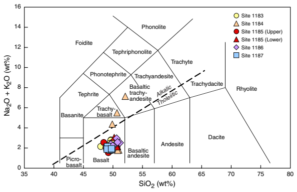

T7. Geochemical data for rock samples, Hole 1184A, p. 120.

Halos

Halos in the groundmass adjacent to the veins are rare, diffuse, and poorly developed. If present, they commonly extend <1 cm into the groundmass and contain celadonite or Fe oxyhydroxides.

Magnetic Minerals

Magnetite and hematite were identified on the basis of bulk-rock XRD analysis in Sections 192-1184A-28R-4 and 29R-3, respectively. These core intervals fall within Subunit IIC, which has high magnetic susceptibility (see **"Paleomagnetism,"** p. 19). Further work is necessary to determine where these minerals reside (i.e., clasts or matrix).

Summary

The highly oxidized nature of the upper 8 m of the basement section, along with the presence of a predominantly nonmarine zeolite assemblage in the cement and veins, suggests this sequence of rocks underwent low-temperature alteration in a subaerial environment. This type of alteration is in contrast to the low-temperature alteration commonly observed in seafloor basalts, which results from interaction between the basalts and circulating bottom seawater. The mixture of oxidized and unoxidized lithic fragments and accretionary and armored lapilli present in several sections of the core suggests they were derived from different source regions in which different alteration processes were operating. Some of the highly oxidizing alteration may have occurred before deposition in a marine environment, possibly soon after eruption.

PALEOMAGNETISM

Introduction

Pass-through magnetometer measurements were taken on all split-core archive sections at 5-cm intervals. Pass-through magnetic susceptibility measurements were taken on all unsplit core sections at 4-cm intervals. In addition, we subjected several discrete samples to detailed thermal and alternating-field (AF) demagnetization as well as isothermal remanent magnetization (IRM) experiments.

To isolate the characteristic remanent magnetization (ChRM), cores were subjected to AF cleaning. The number of AF demagnetization steps and the peak-field intensity varied depending on the lithology, the natural remanent magnetization (NRM) intensity, and the amount of time available. In general, following the measurement of their NRM, the calcareous ooze split–cores were demagnetized using three AF steps up to 15 mT. The volcaniclastic split cores were demagnetized using a minimum of six AF steps. The maximum applied field ranged between 30 and 80 mT. We analyzed the results in Zijderveld and stereoplot diagrams and, where possible, calculated the ChRM direction using principal component analysis (Kirschvink, 1980). Examples of good-quality demagnetization results are shown in Figure **F71.**

F56. Zr vs. TiO_2, p. 84.

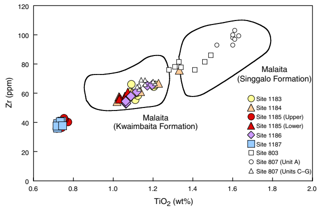

F57. TiO_2 vs. Mg#, p. 85.

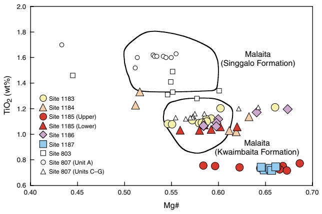

F58. Cr vs. TiO_2, p. 86.

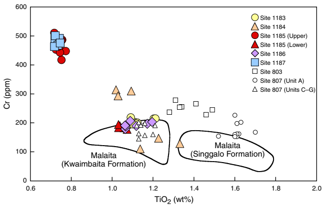

T8. Mineral distribution in bulk rock and vein samples, p. 121.

F59. Glass fragments replaced by smectite, p. 87.

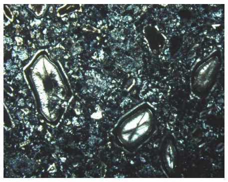

F60. Glass fragment replaced by smectite and zeolite, p. 88.

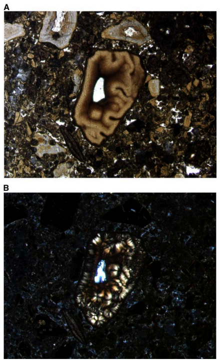

Rock-Magnetic Properties

We found the NRM intensities of sediments at Hole 1184A to be extremely variable, ranging over five orders of magnitude from <5 × 10^{-5} to >5 A/m. The lower Miocene (see **"Biostratigraphy,"** p. 11) ooze (Cores 192-1184A-2R through 8R) is weakly magnetic with a mean NRM intensity of 3 × 10^{-4} A/m and negative susceptibility values, reflecting the dominance of diamagnetic calcite. The ooze was disturbed by drilling, rendering NRM related measurements unreliable (see also **"Paleomagnetic Directions,"** p. 21).

The middle Eocene (see **"Biostratigraphy,"** p. 11) volcaniclastic rocks (Cores 192-1184A-9R to 46R), in contrast, are strongly magnetic (Fig. **F72**). Susceptibility values range from 10^{-3} to 5 × 10^{-2} SI, which is higher than the bulk susceptibility of common, weakly magnetic minerals (e.g., goethite and hematite). Hence, the magnetic signal is carried by more strongly magnetic minerals (e.g., titanomagnetite, maghemite, or pyrrhotite). This conclusion agrees well with the few IRM acquisition experiments we carried out, in which we did not detect hematite, goethite or other high-coercivity magnetic minerals. Although hematite and goethite may be present, they do not contribute significantly to the magnetic properties of the volcaniclastic rocks. Thermal demagnetization on discrete specimens often showed a decrease in NRM intensity and a small increase in susceptibility after heating to 350°C (Fig. **F71C**). We interpret this behavior to be the result of the breakdown of maghemite to magnetite, a process that typically takes place at ~300°C.

In conclusion, the preliminary rock-magnetic observations point to a magnetic mineralogy dominated by magnetite (possibly titanomagnetite) that, to a variable degree, has undergone low-temperature hydrothermal oxidation to maghemite. These rock-magnetic observations agree well with the finding of maghemitized titanomagnetite in polished thin sections (see **"Igneous Petrology,"** p. 13) and the detection of magnetite in XRD studies (see **"Alteration,"** p. 17). Simple calculations suggest that as much as 1.5% of a magnetite-type mineral is required to explain the observed susceptibility values.

NRM intensity, magnetic susceptibility, Koenigsberger ratio, and the percentage of NRM removed after AF demagnetization to 20 mT for the volcaniclastic rocks are shown in Figure **F72.** In a gross sense, the downhole variations in magnetic properties reflect the presence of three major layers: 201.1–304.2 mbsf, 304.2–442.5 mbsf, and 442.5 mbsf to the bottom of the hole. The boundaries between these magnetic layers coincide with lithologic boundaries (see **"Lithostratigraphy,"** p. 4), but not all lithologic boundaries are associated with major changes in magnetic properties. For example, there is no significant difference in the NRM intensities between Subunits IIA and IIB nor between Subunits IIC and IID. Below we describe the variations in magnetic properties for each lithostratigraphic unit of the volcaniclastic rocks:

1. Subunit IIA. The NRM intensities are somewhat variable throughout this interval, ranging from 0.03 to 1.0 A/m. In general, the increases and decreases in NRM intensity with depth match the corresponding changes in susceptibility, and we interpret this to signify that the concentration, rather than the nature, of the magnetic minerals is changing.
2. Subunit IIB. The upper and lower portions of this subunit differ in their NRM intensity and in the way in which it changes with depth. In the upper 25 m, the NRM intensity is rather uniform,

F61. Altered glass fragment replaced by smectite and zeolite, p. 89.

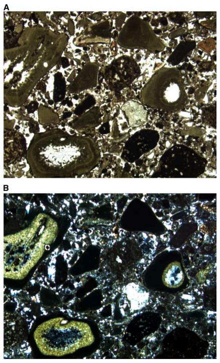

F62. Altered glass fragment rimmed by smectite with zeolite in center, p. 90.

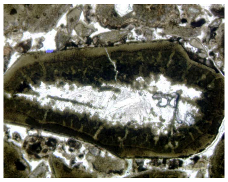

F63. Altered glass replaced by smectite with inner rim of celadonite, p. 91.

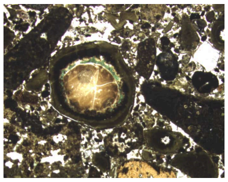

F64. Altered glass replaced by smectite and celadonite, p. 92.

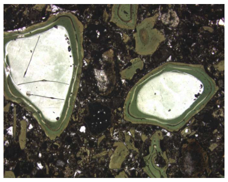

F65. Altered vesicular glass replaced by celadonite, p. 93.

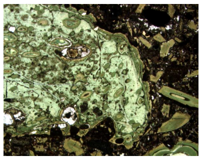

with a mean value of 0.38 A/m. Susceptibilities in this interval are also remarkably uniform. In contrast, in the lower half of Subunit IIB, from 268 to 304 mbsf, the NRM intensity is quite variable, decreasing downward with a mean intensity lower than that in the upper portion (Fig. F72). The Koenigsberger ratio decreases, and the proportion of NRM removed at 20 mT increases downward. We interpret this result to indicate a gradual downward increase in magnetic grain size.

3. Subunit IIC. We observed a substantial increase in NRM intensity across the Subunit IIB/IIC boundary. The mean NRM intensity in Subunit IIC is high (average = 1.8 A/m). We observed several variations in Subunit IIC that are characterized by a gradual increase of NRM intensity and Koenigsberger ratio with depth and a decrease in the proportion of NRM removed at 20 mT (Fig. F73). We noted such features between 316 and 328 mbsf, 328 and 342 mbsf, and 342 mbsf and the base of the subunit and speculate that these variations may correspond to changes in grain size that reflect depositional patterns. Detailed shore-based magnetic mineral analyses will help us better address the question of whether the magnetic variations are caused by grain size changes, mineralogical changes, or both.
4. Subunit IID. At the boundary between Subunits IIC and IID, we observed an abrupt decrease in NRM intensity followed by a downward intensity increase (Fig. F72). The mean intensities above and below this boundary, however, are essentially equal. NRM variations with depth in Subunit IID are somewhat similar to those in Subunit IIC, and we attribute both to a similar process. For example, we observed a gradual increase in NRM intensity between 387 and 395 mbsf that has the same pattern as the features shown in Figure F73. The susceptibility remains high in Subunit IID but, on average, is less than that in Subunit IIC above. Susceptibility varies with depth more in this subunit than in Subunit IIC. In the lower 20 m of Subunit IID we documented an overall decrease in NRM intensity that closely matches corresponding changes in the susceptibility. The magnetic properties of the lower 10 m of this subunit do not differ appreciably from those of the underlying subunit.
5. Subunit IIE. The mean NRM intensity of Subunit IIE (0.24 A/m) approximately equals that of Subunit IIA and the lower part of Subunit IIB. An increase in intensity near 480 mbsf, followed downhole by a decrease, corresponds with a coarser layer identified within Core 192-1184A-41R (see **"Lithostratigraphy,"** p. 4). Other than this interval, the NRM intensity remains fairly consistent throughout the subunit to a depth of 525 mbsf. From this level to the base of the hole, intensity variations are large.

Paleomagnetic Directions

The Miocene oozes were badly disturbed by drilling. For this reason, we were unable to obtain reliable paleomagnetic directions from Cores 192-1184A-2R to 8R. In contrast, the volcaniclastic rocks were largely undisturbed by drilling, and relatively long, continuous pieces were recovered. The demagnetization data from Cores 192-1184A-20R through 22R were scattered, and interpreting them using principal component analysis (PCA) was impossible. The scatter may be caused by the presence of many large clasts in this interval. The AF demagnetization of

F66. Liesegang rings in celadonite spheres, p. 94.

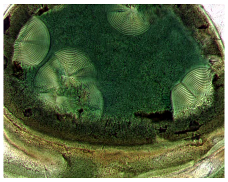

F67. Altered glass fragment rimmed by smectite, p. 95.

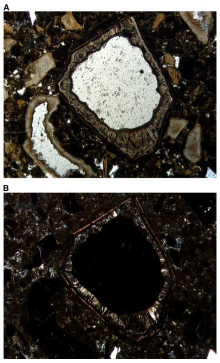

F68. Altered glass, p. 96.

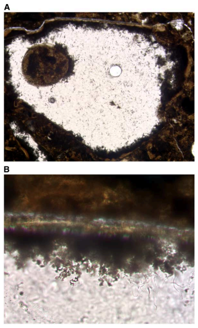

F69. Vesicular glass fragments with smectite-filled vesicles, p. 97.

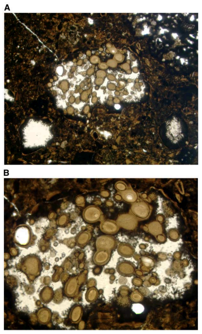

the remaining volcaniclastic rocks produced straightforward results, and we could define the ChRM direction precisely (e.g., Fig. **F71**). We used PCA to calculate the ChRM direction for ~2200 points, corresponding to roughly every 10–15 cm of recovered core (i.e., every second to third measurement point). In order to better represent the large amount of data, we have used the method of Kono (1980) to calculate the mean magnetic inclination and associated alpha-95 value for 5-m intervals (Fig. **F74**). The inclination values used are those we determined from PCA, and each value in Figure **F74** therefore represents the mean of ~25–30 estimates.

The mean inclination for all intervals, –54.4°, is significantly steeper than the ~–30° value predicted for Eocene age rocks at Site 1184 (see, for example, Sager, 1987; Petronotis and Gordon, 1999). We were therefore concerned that it might be an artificial remanence acquired in the recovery process. The inclination is shallower than that expected for a drilling overprint, which is commonly close to 90° (see "Paleomagnetism" in the "Site 717" chapter of the Leg 116 *Initial Reports* volume [Shipboard Scientific Party, 1988]). In addition, drilling overprints are usually "soft" and can be reduced significantly or eliminated entirely by low-field AF demagnetization. However, we were able to document the –54° direction in core sections that had been routinely demagnetized at fields of 40 mT and, in some cases, in fields as high as 80 mT. Another explanation for the –54° inclination is that it is an artifact of the core-splitting process. To eliminate this as a possible source of the magnetization, we performed pass-through magnetometer measurements on a whole core section (Section 192-1184A-34R-4) and compared the results with those obtained from the corresponding split-core section. We observed the same inclination in both the whole and split-core sections. To further investigate the nature of this magnetization, we selected several discrete samples for demagnetization. Five discrete samples were AF demagnetized in small steps up to 80mT, and six samples were subjected to thermal demagnetization up to 600°C. In neither the AF nor the thermal demagnetization experiments did we find evidence for magnetic directions other than the dominant –54° inclination direction. Because many core sections contained long, continuous pieces, we were able to successfully compare the discrete sample AF demagnetization results with those of the pass-through measurements. We found good correlations between these two data sets, demonstrating that the pass-through measurements reliably isolated the dominant remanence. A few pass-through measurements suggested the presence of an additional, lower-coercivity component, but such intervals were rare, and we were unable to firmly document this component. Detailed shore-based measurements on discrete samples will allow us to investigate such components further.

On the basis of the tests described above, the results of the discrete sample demagnetization and the relationship of the magnetic directions to sedimentary features (see immediately below), we tentatively conclude that the –54° direction is a natural rather than an artificial magnetization. Consequently, we interpret the negative inclination to be that produced by magnetization at a southerly latitude during a period of normal field polarity.

We are currently unable to provide a satisfactory explanation for the steepness of this component. Without any tilting of the sediments, the –54° inclination corresponds to a latitude of ~35°S, which is considerably farther south than predicted for the site in the Eocene by other authors (e.g., Sager, 1987; Yan and Kroenke, 1993) and also

F70. Altered glassy to tachylitic shards, p. 98.

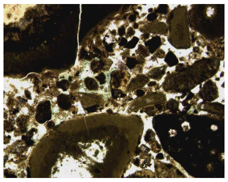

F71. Zijderveld diagrams for volcaniclastic rock samples, p. 99.

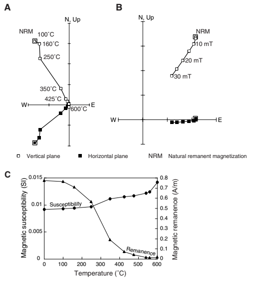

F72. Downhole variations, p. 100.

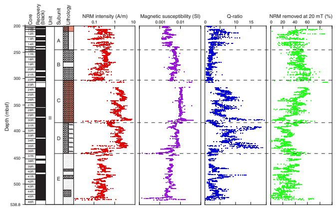

F73. NRM intensity and NRM intensity removed by AF demagnetization, p. 101.

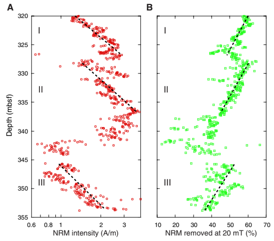

F74. Mean paleomagnetic inclinations of the ChRM, p. 102.

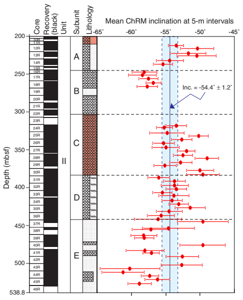

by our own results from Eocene cores from Site 1183 (see **"Paleomagnetism,"** p. 32, in the "Site 1183" chapter), which suggest that Site 1184 was located near 15°–20°S. Because regional tilting of the beds is generally to the north, correction for this tilting produces an even more steeply inclined magnetization vector. To obtain a magnetic inclination that corresponds to the predicted Eocene latitude, the sedimentary rocks would have to acquire their magnetization on a more steeply inclined surface whose angle was later reduced. We have considered a number of other possible factors to help explain the steep inclination, including local tilting of the beds not apparent in the available seismic reflection data, deviation of the drill hole from vertical, abnormal secular variation, a geomagnetic excursion, and a significantly more southerly Eocene position for the eastern salient than for other parts of the Ontong Java Plateau. None of these appears to be a likely candidate to explain the steep inclination that corresponds more closely to the inclinations observed at Site 1183 (see **"Paleomagnetism,"** p. 32, in the "Site 1183" chapter) in 100- to 120-m.y.-old rocks. We conclude that the magnetic inclinations at Site 1184 are inconsistent with the Eocene age assigned, based upon the biostratigraphic analysis (see **"Biostratigraphy,"** p. 11).

The dominant –54° inclination component appears to vary somewhat systematically with depth in the section. This variation has an amplitude of ~5°, varying between –50° and –60°, and is observed over depth intervals of ~150–200 m. The variation is greater than the uncertainty in the individual mean values; we infer that the variation corresponds to changes in the geomagnetic field as the sediments were magnetized. Because the variations at Site 1184 are similar to secular variations of the field observed in modern lake sediments, we speculate that they may reflect processes occurring over intervals of hundreds to thousands of years. Whether such changes took place during the accumulation of the sediments or were postdepositional is unknown.

Relationship between Magnetic Directions and Sedimentary Features

We measured the dip angle and downdip direction of all clearly distinguishable inclined layers found in the volcaniclastic rocks. Omitting features we suspected to be related to erosion rather than deposition, we measured 82 planar features. Their dip angles and downdip directions, measured in core coordinates, are shown in Figure **F75A** (core coordinates are defined in **"Sampling Coordinates,"** p. 20, in "Paleomagnetism" in the "Explanatory Notes" chapter). The apparent grouping of down-dip directions parallel to the splitting-surface (y-z plane) is an artifact, caused by the fact that it is much easier to estimate the dip in this plane than in the x-z plane. In cases where we were unsure of the x-z plane dip, we tended to underestimate this dip.

F75. Dip angle and down-dip directions of inclined layers, p. 103.

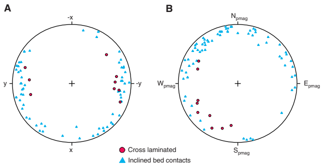

Using the declination of the ChRM for the continuous core pieces that contain the inclined layers, we reoriented each individual feature in paleomagnetic coordinates (Fig. **F75B**). Defining the ChRM direction for two data points was impossible, so these were discarded. The dip directions are more tightly grouped after reorientation, providing independent support to our conclusion that the ChRM was acquired by the sediments while they were in place and does not relate to drilling or laboratory artifacts. Furthermore, the dip angles and dip directions of the inclined layers, in paleomagnetic coordinates, agree fairly well with the estimated dip of intravolcaniclastic seismic reflections (i.e., dip angle ~9°, downdip direction ~0°, see **"Background and Objectives,"** p. 1). We interpreted nine steeply (>20°) inclined layers of Subunit IID, dipping toward the southwest (Fig. **F75B**), to reflect cross-bedding, possibly indicating the sediment transport direction (for further discussion, see **"Lithostratigraphy,"** p. 4).

PHYSICAL PROPERTIES

Introduction

Index properties, including wet bulk density, grain density, dry bulk density, water content, void ratio, and porosity, were measured on discrete samples taken from each core recovered at Site 1184. We made physical properties measurements on whole-core sections of all cores with the multisensor track (MST), including magnetic susceptibility, gamma ray attenuation (GRA) bulk density, and natural gamma radiation (NGR). Sonic compressional (*P*-wave) velocities were measured on cut samples and, where possible, in more than one direction on oriented cubes to investigate velocity anisotropy. Thermal conductivity was measured in unsplit sediment sections and on split rock samples from each core.

Index Properties

The general trend exhibited by the index properties data (Table **T9**) reflects downhole variations in lithology (Fig. **F76**). In Unit I (134.4–201.1 mbsf), bulk densities lie between 1.4 and 1.8 g/cm^3, grain densities range from 2.4 to 2.6 g/cm^3, and porosity fluctuates between 53% and 72%. Sediments in this interval consist of early Miocene foraminifer nannofossil ooze (see **"Lithostratigraphy,"** p. 4). Below 201.1 mbsf, in the volcaniclastic sequence of Unit II, bulk density increases (Fig. **F76**). Both the water content and porosity (Table **T10;** Fig. **F76**) also begin to decrease below this depth. The mean bulk densities are 1.8 g/cm^3 in Subunit IIA, 1.9 g/cm^3 in Subunit IIB, 2.0 g/cm^3 in Subunit IIC, 2.1 g/cm^3 in Subunit IID, and 2.0 g/cm^3 in Subunit IIE. Mean values of grain density in these same intervals are 2.2, 2.3, 2.4, 2.6, and 2.4 g/cm^3, respectively. Porosity varies only slightly within Unit II, from a mean of 37.2% in Subunit IIA to 33.0% in Subunit IIB, 31.0% in Subunit IIC, 32.1% in Subunit IID, and 31.2% in Subunit IIE.

Although values are rather variable in the lower part of Subunit IIE, the slopes of all index properties data change noticeably, albeit slightly, at the boundary between Subunits IID and IIE (~437 mbsf). The mean bulk and grain densities in Subunit IIE are 2.0 and 2.4 g/cm^3, respectively (Fig. **F76**), slightly less than those of Subunit IID.

Multisensor Track Measurements

Magnetic Susceptibility

We determined magnetic susceptibility with the Bartington meter at 4-cm intervals along whole-core sections of all cores. The results are shown in Figures **F77** and **F78.** Magnetic susceptibility was also measured independently every 2 cm with the point-susceptibility meter on the archive multisensor track (AMST). The two magnetic-susceptibility data sets compare well with each other (Fig. **F77**). Susceptibility peaks

T9. Index properties data, p. 122.

F76. Index properties and thermal conductivity vs. depth, p. 104.

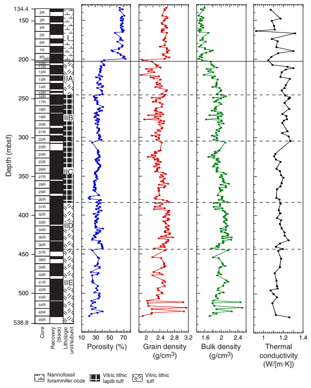

T10. *P*-wave velocity, p. 126.

F77. Magnetic susceptibility profiles, p. 105.

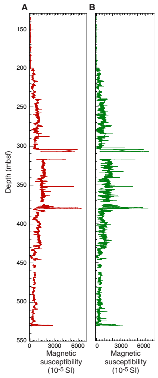

F78. *P*-wave velocity and whole-core measurements vs. depth, p. 106.

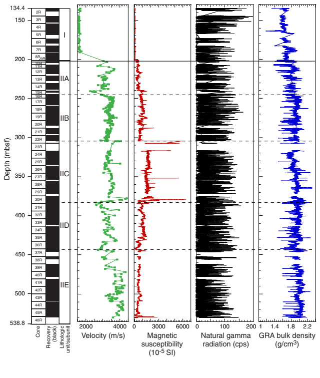

in lithologic units commonly correlate with lithologic changes, such as from the lithic vitric lapilli tuff of Subunit IIB to the lithic lapillistone layers of Subunit IIC (Fig. F78). Detailed results are discussed in "Paleomagnetism," p. 19, in conjunction with the NRM pass-through paleomagnetic measurements.

Gamma Ray Attenuation Bulk Density

We estimated bulk densities from whole-core GRA measurements in all sections (Fig. F78). Although the GRA downhole bulk density profile (Fig. F78) consistently shows lower values than the data obtained from discrete samples (Fig. F76), the downhole trends exhibited by the two different data sets correlate well. In the foraminifer nannofossil ooze of Unit I, the average bulk density is 1.5 g/cm^3. Below 201.1 mbsf, which is the boundary between Units I and II (see "Lithostratigraphy," p. 4), the bulk density gradually increases to an average of 1.8 g/cm^3 in Subunit IIA, 1.9 g/cm^3 in Subunits IIB and IIC, and 2.0 g/cm^3 in Subunits IID and IIE.

Natural Gamma Radiation

NGR measurements on sections of the foraminifer-bearing white ooze near the top of Unit I (Fig. F78) in Cores 192-1184A-2R and 3R show peaks of >150 counts per second (cps) that probably reflect an increase in clay content between ~135 and ~150 mbsf. Below this interval, NGR values for the most part fluctuate between 0 and 150 cps, with a mean value of 28 cps, probably reflecting a relatively constant fluid content and an absence of significant voids in the cored sediments.

P-Wave Velocity

We determined *P*-wave velocity from discrete measurements on both split-core sections and cut samples (Table T10). *P*-wave velocities in Unit I range from 1562 to 1721 m/s, with a mean of 1589 m/s (Fig. F78). A marked velocity increase occurs in Unit II at ~200 mbsf, at the boundary between the foraminifer nannofossil ooze of Unit I and the lithic vitric tuff of Subunit IIA. Below 202 mbsf, velocities are typically >3000 m/s (Fig. F78), with a mean value of 3007 m/s in Subunit IIA, 3365 m/s in Subunit IIB, 3438 m/s in Subunit IIC, 3219 m/s in Subunit IID, and 3721 m/s in Subunit IIE. *P*-wave velocity abruptly increases at ~304 mbsf, where the lithologic change from Subunit IIB to Subunit IIC occurs. Magnetic susceptibility also increases at this depth (Fig. F78). *P*-wave velocities in Subunit IIC range from 3017 to 4408 m/s, with a mean value of 3438 m/s. Below 380 mbsf, the upper boundary of Unit IID, both magnetic susceptibility and velocity decrease. The high *P*-wave velocities (>3500 m/s) in the lithic vitric tuff and lithic vitric lapilli tuff of Subunit IIE are probably associated with high bulk and grain densities (Fig. F76).

Thermal Conductivity

We determined thermal conductivity in unsplit soft-sediment cores and in selected samples of lithified sediments (Table T11). Thermal conductivity values, commonly between 0.9 and 1.3 W/(m·K), exhibit little scatter in either Units I or II. Interestingly, the mean thermal conductivity value for the depth interval from ~320 to 397 mbsf, which en-

T11. Thermal conductivity values, p. 131.

compasses Subunit IIC (where both magnetic susceptibility and velocity show major increases), is slightly but noticeably lower than that above this interval (Fig. F76).

REFERENCES

Andrews, J.E., Packham, G., et al., 1975. *Init. Repts. DSDP,* 30: Washington (U.S. Govt. Printing Office).

Berggren, W.A., Kent, D.V., Swisher, C.C., III, and Aubry, M.-P., 1995. A revised Cenozoic geochronology and chronostratigraphy. *In* Berggren, W.A., Kent, D.V., Aubry, M.-P., and Hardenbol, J. (Eds.), *Geochronology, Time Scales and Global Stratigraphic Correlation.* Spec. Publ.—Soc. Econ. Paleontol. Mineral. (Soc. Sediment. Geol.), 54:129–212.

Birkhold-VanDyke, A.L., Neal, C.R., Jain, J.C., Mahoney, J.J., and Duncan, R.A., 1996. Multi-stage growth of the Ontong Java Plateau (OJP)? A progress report from San Cristobal (Makira), Solomon Islands. *Eos, Trans. Am. Geophys. Union,*77F:714.

Bolli, H.M., and Saunders, J.B., 1985. Oligocene to Holocene low latitude planktic foraminifera. *In* Bolli, H.M., Saunders, J.B., and Perch-Nielsen, K. (Eds.), *Plankton Stratigraphy:* Cambridge (Cambridge Univ. Press), 155–262.

Coombs, D.S., Ellis, A.J., Fyfe, W.S., and Taylor, A.M., 1959. The zeolite facies, with comments on the interpretation of hydrothermal syntheses. *Geochim. Cosmochim. Acta,* 17:53–107.

Fisher, R.F., and Schmincke, H.-U., 1984. *Pyroclastic Rocks:* New York (Springer Verlag).

Fisk, M.R., Giovannoni, S.J., and Thorseth, I.H., 1998. Alteration of oceanic volcanic glass: textural evidence of microbial activity. *Science,* 281:978–980.

Honnorez, J., 1981. The aging of the oceanic crust at low temperature. *In* Emiliani, C. (Ed.), *The Sea* (Vol. 7): *The Oceanic Lithosphere:* New York (Wiley), 525–587.

International Hydrographic Organization/Intergovernmental Oceanographic Commission (IHO/IOC), 1997. *General Bathymetric Chart of the Ocean (GEBCO) Digital Atlas:* London (British Oceanographic Data Centre).

Kastner, M., 1979. Zeolites. *In* Burns, R.G. (Ed.), *Marine Minerals.* Mineral. Soc. Am., Rev. Mineral., 6:111–123.

Kennett, J.P., and Srinivasan, M.S., 1983. *Neogene Planktonic Foraminifera: A Phylogenetic Atlas:* Stroudsburg, PA (Hutchinson Ross).

Kirschvink, J.L., 1980. The least-squares line and plane and the analysis of palaeomagnetic data. *Geophys. J. R. Astron. Soc.,* 62:699–718.

Kono, M., 1980, Statistics of paleomagnetic inclination data. *J. Geophys. Res.,* 85:3878–3882.

Kroenke, L.W., Berger, W.H., Janecek, T.R., et al., 1991. *Proc. ODP, Init. Repts.,* 130: College Station, TX (Ocean Drilling Program).

Kroenke, L.W., and Mahoney, J.J., 1996. Rifting of the Ontong Java Plateau's eastern salient and seafloor spreading in the Ellice Basin: relation to the 90 Myr eruptive episode on the plateau. *Eos, Trans. Am. Geophys. Union,* 77F:713.

Le Bas, M.J., Le Maitre, R.W., Streckeisen, A., and Zanettin, B., 1986. A chemical classification of volcanic rocks based on the total alkali-silica diagram. *J. Petrol.,* 27:745–750.

Macdonald, G.A., and Katsura, T., 1964. Chemical composition of Hawaiian lavas. *J. Petrol.,* 5:82–133.

Mahoney, J.J., Storey, M., Duncan, R.A., Spencer, K.J., and Pringle, M.S., 1993. Geochemistry and age of the Ontong Java Plateau. *In* Pringle, M.S., Sager, W.W., Sliter, W.V., and Stein, S. (Eds.), *The Mesozoic Pacific: Geology, Tectonics, and Volcanism.* Geophys. Monogr., Am. Geophys. Union, 77:233–262.

Martini, E., 1971. Standard Tertiary and Quaternary calcareous nannoplankton zonation. *In* Farinacci, A. (Ed.), *Proc. 2nd Int. Conf. Planktonic Microfossils Roma:* Rome (Ed. Tecnosci.), 2:739–785.

Neal, C.R., Mahoney, J.J., Kroenke, L.W., Duncan, R.A., and Petterson, M.G., 1997. The Ontong Java Plateau. *In* Mahoney, J.J., and Coffin, M.J. (Eds.), *Large Igneous Provinces: Continental, Oceanic, and Planetary Flood Volcanism.* Am. Geophys. Union, Geophys. Monogr., 100:183–216.

Perch-Nielsen, K., 1985. Mesozoic calcareous nannofossils. *In* Bolli, H.M., Saunders, J.B., and Perch-Nielsen, K. (Eds.), *Plankton Stratigraphy:* Cambridge (Cambridge Univ. Press), 329–426.

Petronotis, K.E., and Gordon, R.G., 1999. A Maastrichtian palaeomagnetic pole for the Pacific plate from a skewness analysis of marine magnetic anomaly 32. *Geophys. J. Int.,* 139:227–247.

Sager, W.W., 1987. Late Eocene and Maastrichtian paleomagnetic poles for the Pacific plate: implications for the validity of seamount paleomagnetic data. *Tectonophysics,* 144:301–314.

Sandwell, D.T., and Smith, W.H.F., 1997. Marine gravity anomaly from Geosat and ERS-1 satellite altimetry. *J. Geophys. Res.,* 102:10039–10054.

Shipboard Scientific Party, 1988. Site 717. *In* Cochran, J.R., Stow, D.A.V., et al., *Proc. ODP, Init. Repts.,* 116: College Station, TX (Ocean Drilling Program), 45–90.

Smith, W.H.F., and Sandwell, D.T., 1997. Global seafloor topography from satellite altimetry and ship depth soundings. *Science,* 277:1956–1962.

Stainforth, R.M., and Lamb, J.L., 1981. An evaluation of planktonic foraminiferal zonation of the Oligocene. *Univ. Kansas Paleontol. Contrib.,* 104:1–42.

Tejada, M.L.G., Mahoney, J.J., Duncan, R.A., and Hawkins, M.P., 1996. Age and geochemistry of basement and alkalic rocks of Malaita and Santa Isabel, Solomon Islands, southern margin of the Ontong Java Plateau. *J. Petrol.* 37:361–394.

Tejada, M.L.J., Mahoney, J.J., Neal, C.R., Duncan, R.A., and Petterson, M.G., in press. Basement geochemistry and geochronology of central Malaita, Solomon Islands, with implications for the origin and evolution of the Ontong Java Plateau. *J. Petrol.*

Torsvik, T., Furnes, H., Muehlenbachs, K., Thorseth, I.H., and Tumyr, O., 1998. Evidence for microbial activity at the glass-alteration interface in oceanic basalts. *Earth Planet. Sci. Lett.,* 162:165–176.

van Morkhoven, F.P.C.M., Berggren, W.A., and Edwards, A.S., 1986. Cenozoic cosmopolitan deep-water benthic foraminifera. *Bull. Cent. Rech. Explor.—Prod. Elf-Aquitaine,* 11.

Walker, G.P.L., 1951. The amygdale minerals in the Tertiary lavas of Ireland. I. The distribution of chabazite habits and zeolites in the Garron plateau area, County Antrim. *Min. Mag.,* 29:773–791.

————, 1959. The amygdale minerals in the Tertiary lavas of Ireland. II. The distribution of gmelinite. *Min. Mag.,* 32:202–217.

————, 1960a. The amygdale minerals in the Tertiary lavas of Ireland. III. Regional distribution. *Min. Mag.,* 32:503–527.

————, 1960b. Zeolite zones and dike distribution in relation to the structure of the basalts in eastern Iceland. *J. Geol.,* 68:515–528.

Yan, C.Y., and Kroenke, L.W., 1993. A plate tectonic reconstruction of the southwest Pacific, 0–100 Ma. *In* Berger, W.H., Kroenke, L.W., Mayer, L.A., et al., *Proc. ODP, Sci. Results,* 130: College Station, TX (Ocean Drilling Program), 697–709.

Figure F1. Predicted bathymetry (after Smith and Sandwell, 1997) of the Ontong Java Plateau showing the locations of Site 1184 and other sites drilled during Leg 192 (stars). The plateau is outlined. Black dots = previous ODP and DSDP drill sites that reached basement; white dots = Site 288, which did not reach basement but bottomed in Aptian limestone, and Site OJ-7, which was proposed for Leg 192 but not drilled. The bathymetric contour interval is 1000 m (IHO/IOC, 1997).

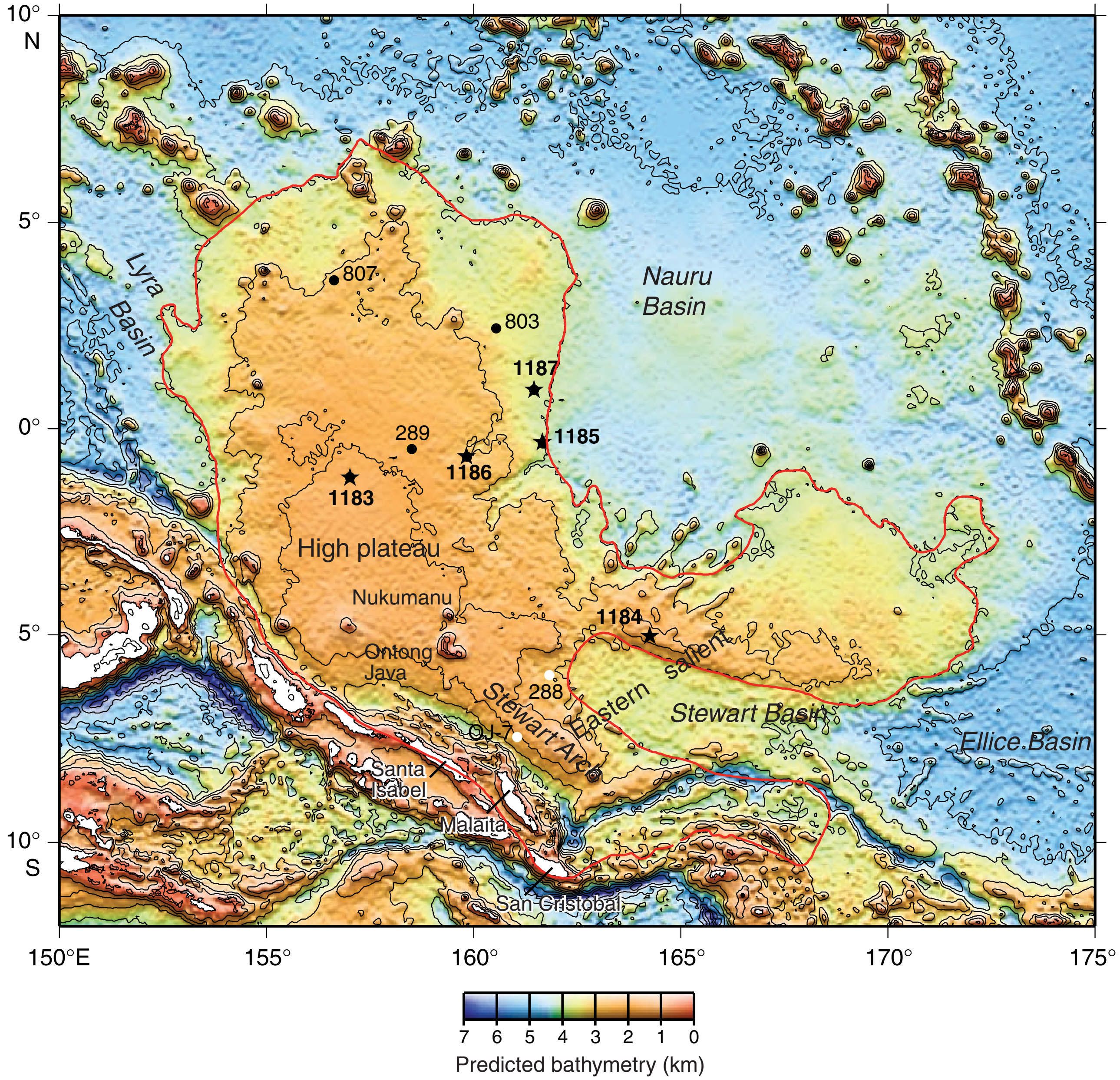

Figure F2. Satellite-derived free-air gravity map of the Ontong Java Plateau region (after Sandwell and Smith, 1997). Stars = locations of basement sites drilled during Leg 192. Black dots = previous ODP and DSDP drill sites that reached basement; white dots = Site 288, which did not reach basement but bottomed in Aptian limestone, and Site OJ-7, which was proposed for Leg 192 but not drilled. Black lines = surveys providing multichannel seismic control: *Hakuho Maru* KH98-1 Leg 2 (1998) and *Maurice Ewing* EW95-11 (1995). White lines = surveys providing single-channel seismic control: *Glomar Challenger* Leg 7 GC07 (1969), *Glomar Challenger* Leg 30 GC30 (1973), *Glomar Challenger* Leg 89 GC89 (1982), *Thomas Washington* TW-11 (1988), and *JOIDES Resolution* Leg 130 JR130 (1990). The bathymetric contour interval is 1000 m (IHO/IOC, 1997).

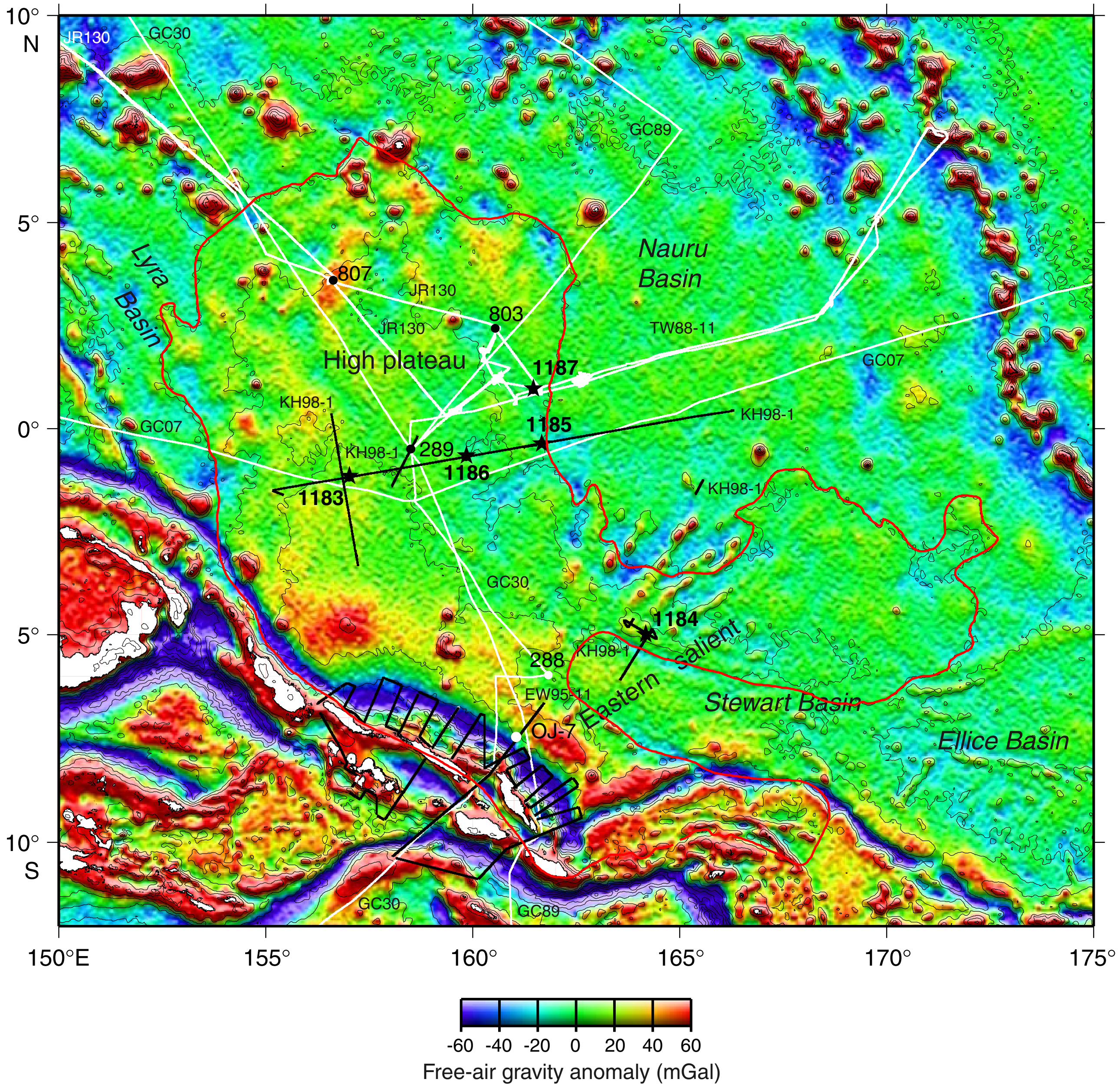

Figure F3. Location of Site 1184 and site-survey data on satellite-derived free-air gravity map (after Sandwell and Smith, 1997). Navigation for *Hakuho Maru* KH98-1 Leg 2 survey, Lines 101 and 102, is shown in Julian-day time. Water depths in the survey area are between 1500 and 2000 m (IHO/IOC, 1997).

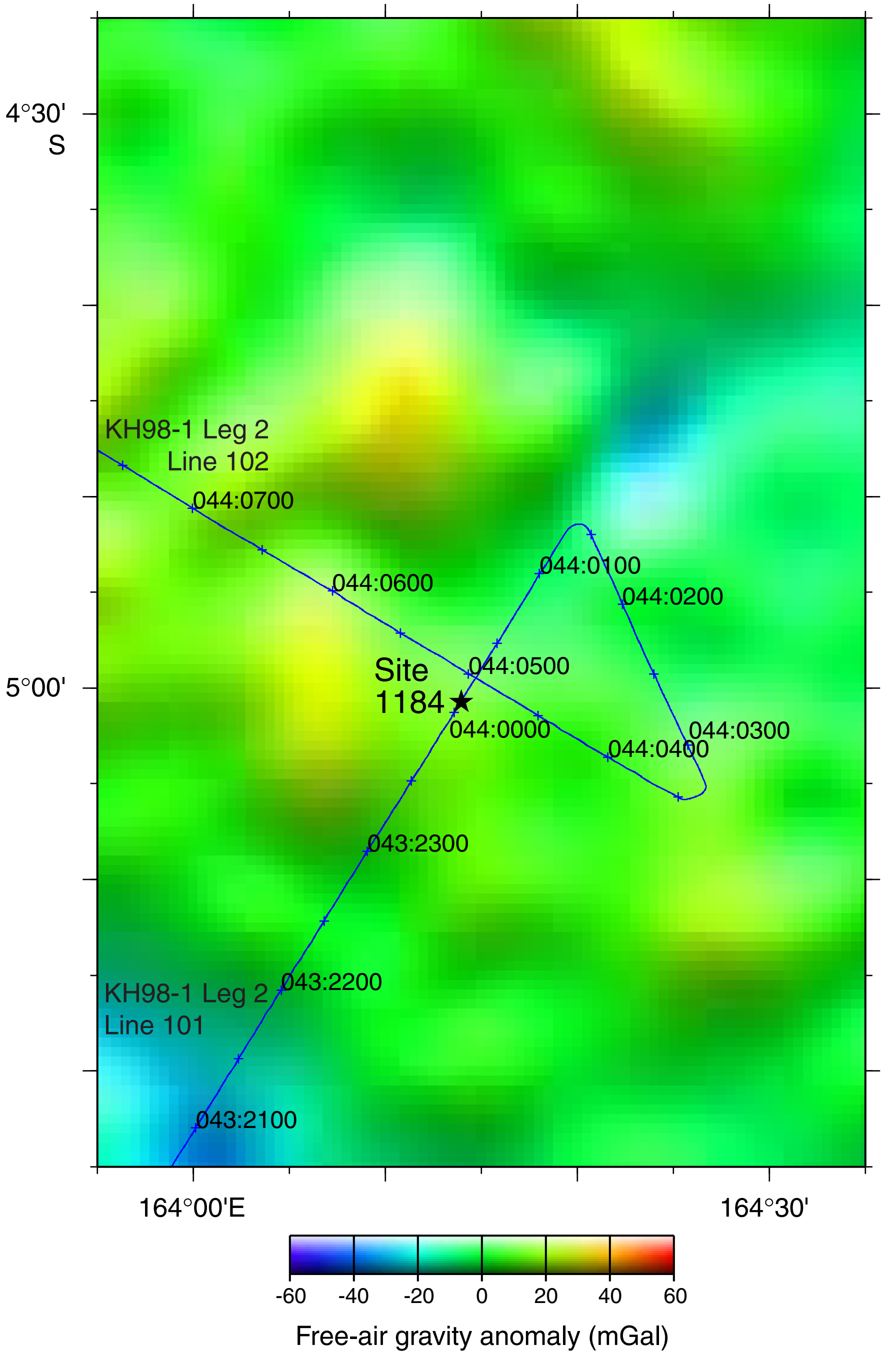

Figure F4. Multichannel seismic reflection profile across Site 1184 (see Fig. F3, p. 31, for location). Line 101 intersects Line 102 north-northwest of Site 1184. The vertical exaggeration is ~4.2 at seafloor. UTC = Universal Time Coordinated.

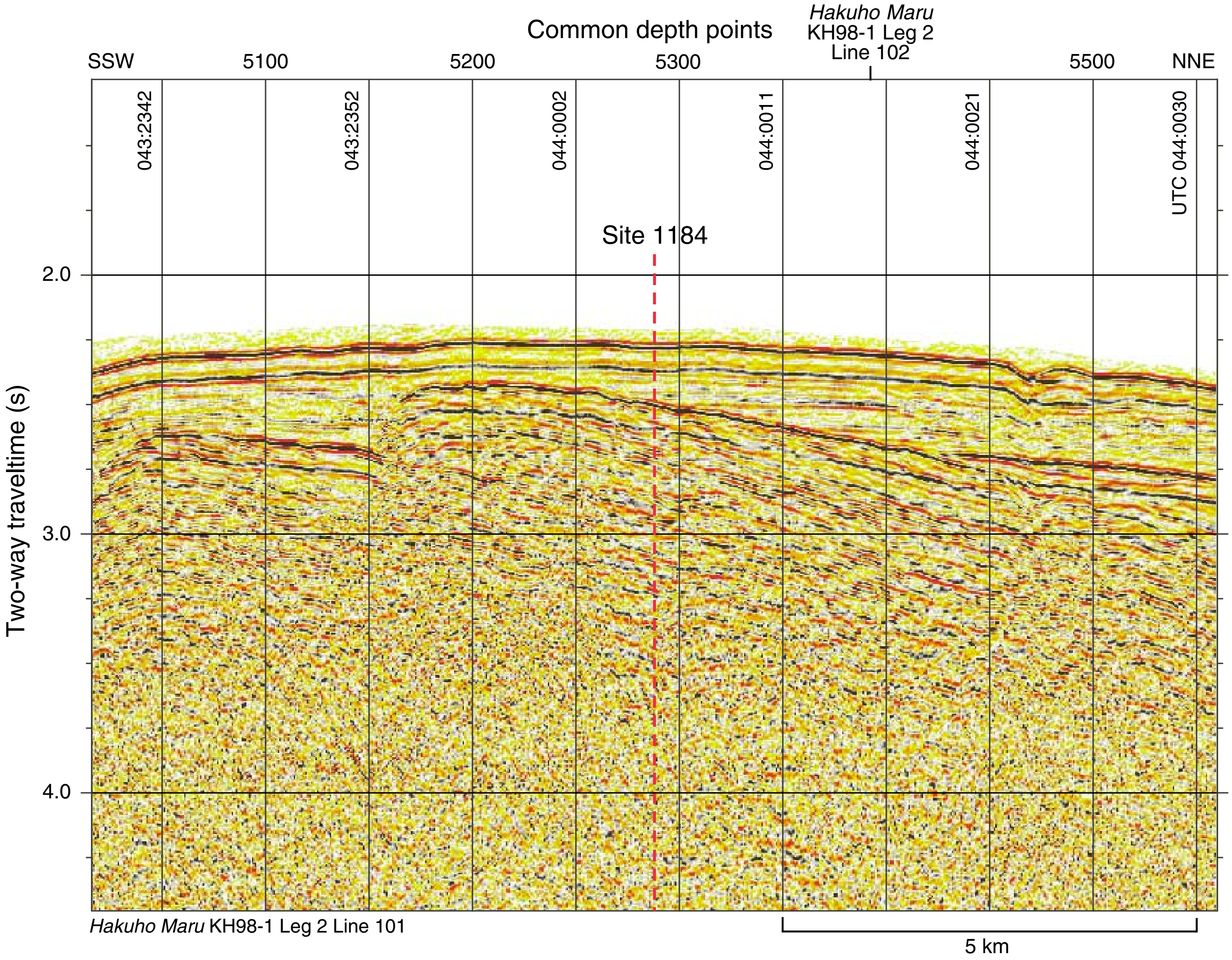

Figure F5. Multichannel seismic reflection profile near Site 1184 (see Fig. F3, p. 31, for location). The vertical exaggeration is ~4.2 at seafloor. UTC = Universal Time Coordinated.

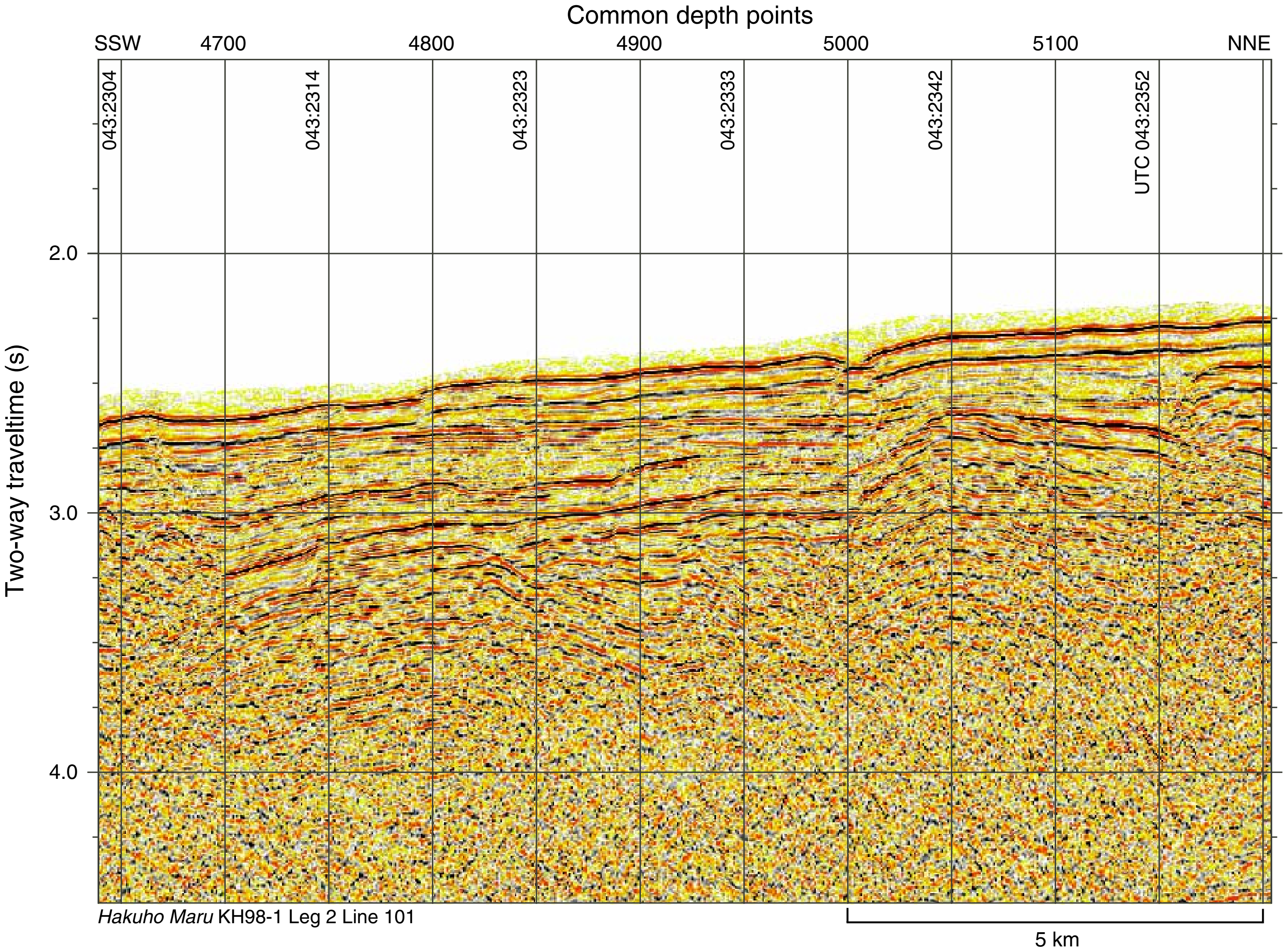

Figure F6. Multichannel seismic reflection profile near Site 1184 (see Fig. F3, p. 31, for location). Line 101 intersects Line 102 near the center of the profile. The vertical exaggeration is ~4.2 at seafloor. UTC = Universal Time Coordinated.

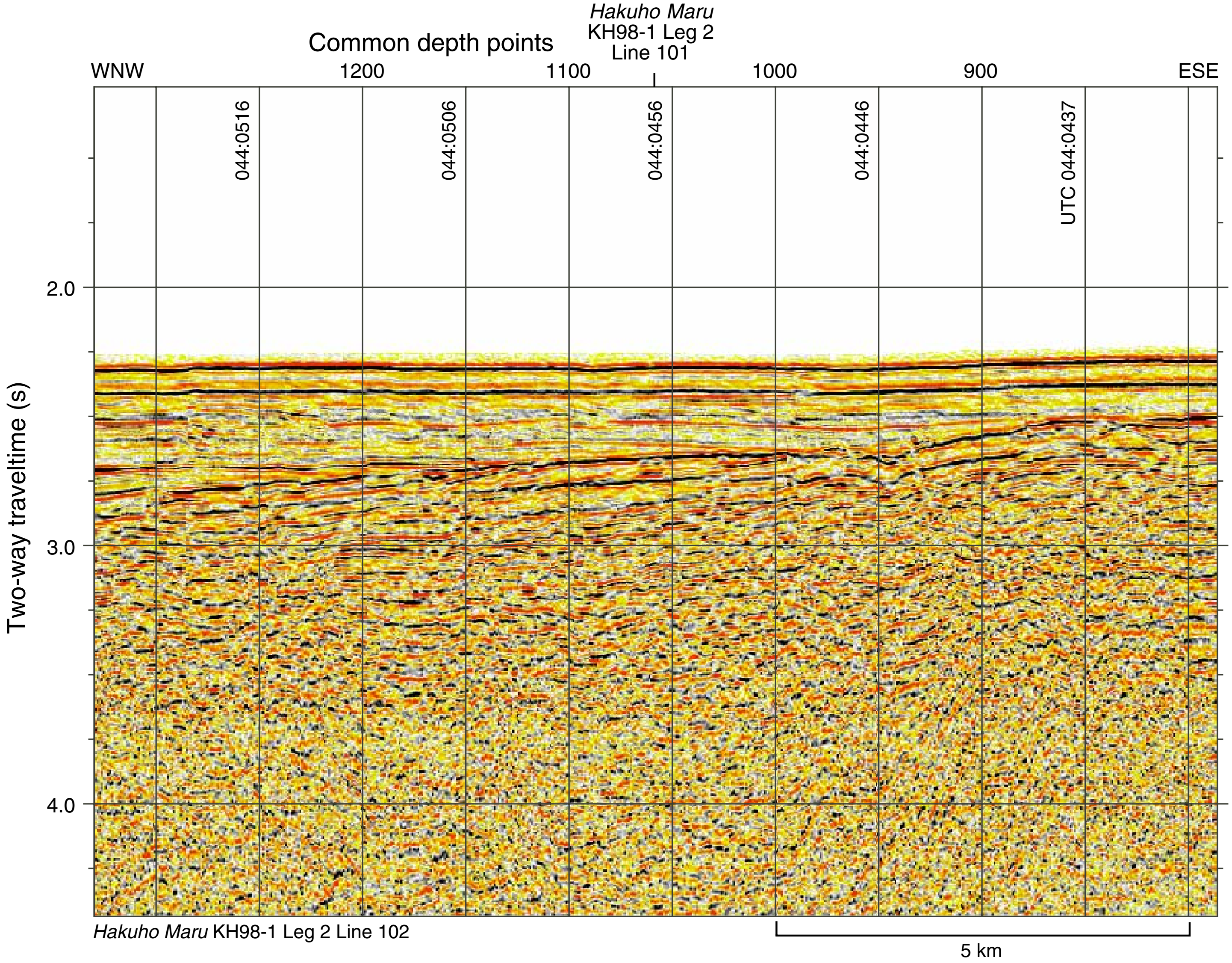

Figure F7. Multichannel seismic reflection profile near Site 1184 (see Fig. F3, p. 31, for location). The vertical exaggeration is ~4.2 at seafloor. UTC = Universal Time Coordinated.

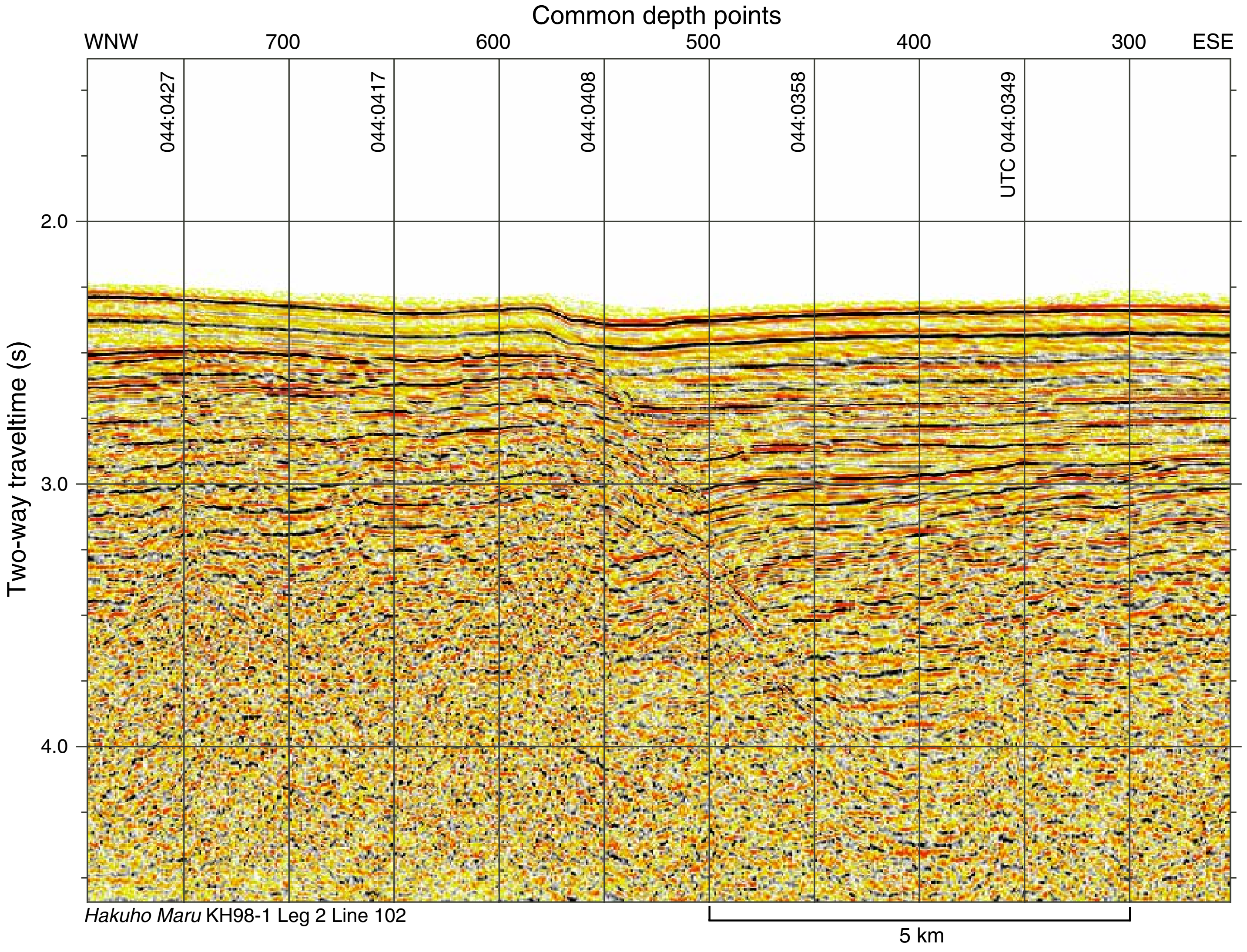

Figure F8. Multichannel seismic reflection profile across Site 1184 (see Fig. F3, p. 31, for location). Line 102 intersects Line 101 north-northeast of Site 1184. The vertical exaggeration is ~4.2 at seafloor. UTC = Universal Time Coordinated.

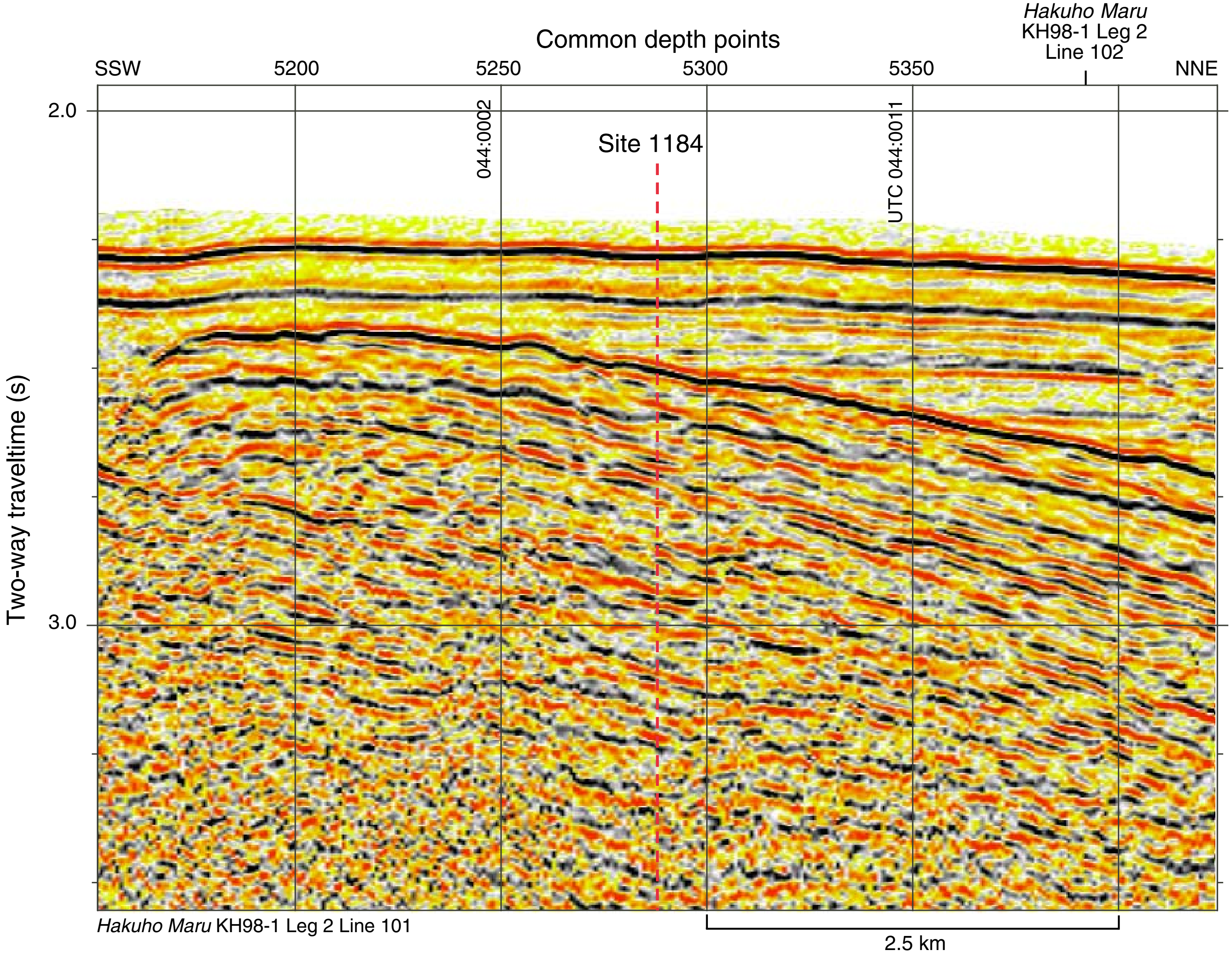

Figure F9. Multichannel seismic reflection profile across Site 1184 (see Fig. F3, p. 31, for location). The vertical exaggeration is ~4.2 at seafloor. UTC = Universal Time Coordinated.

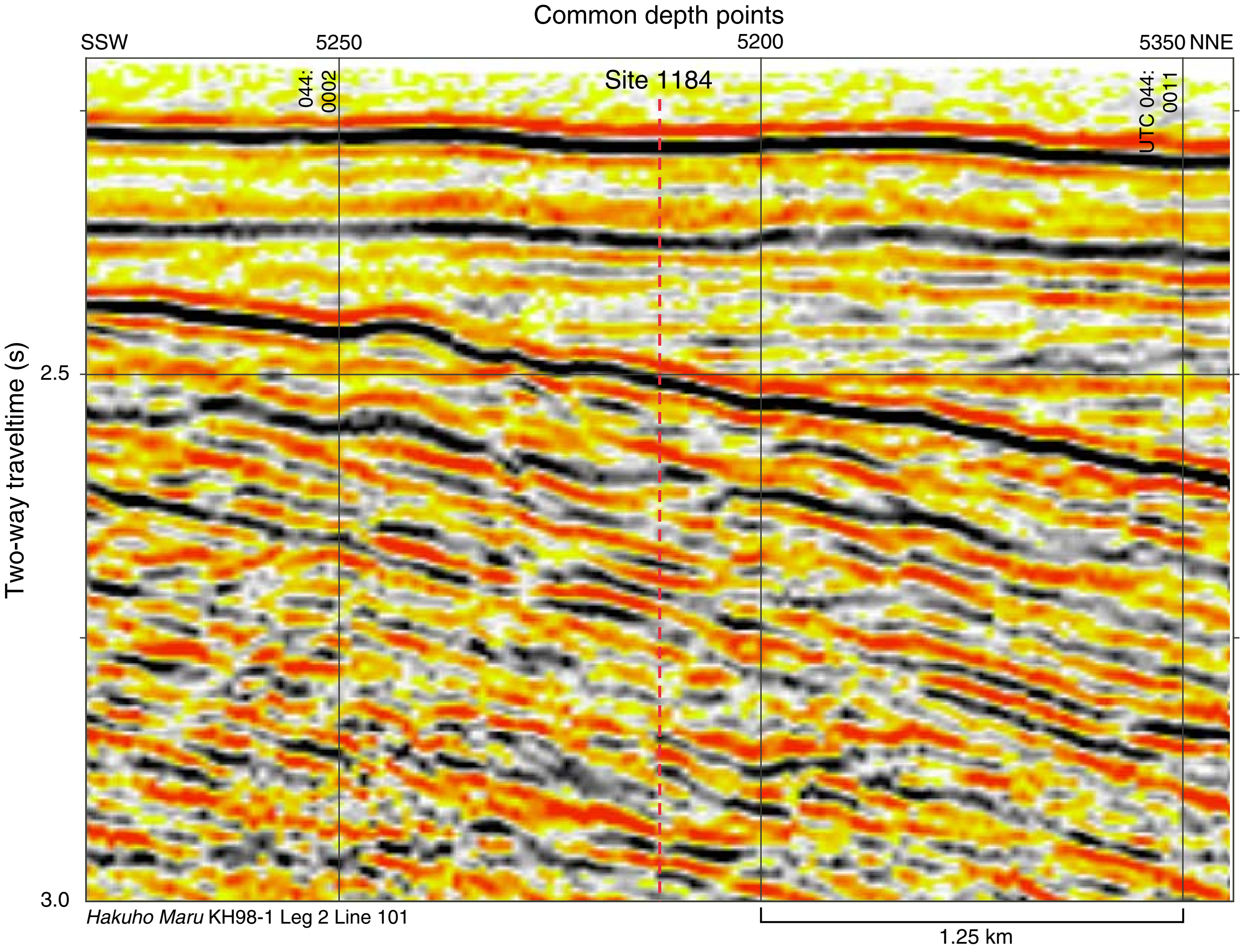

Figure F10. Core recovery (in black), lithostratigraphic divisions, schematic lithology, color, and magnetic susceptibility from Hole 1184A. For color, L is the total reflectance and indicates lighter shades to the right; a and b quantify the hue as chromaticity, where the a-axis shows variation between green (negative) and red (positive) and the b-axis shows variation between blue (negative) and yellow (positive). Red shading in the Graphic lithology column indicates red or yellow oxidized intervals.

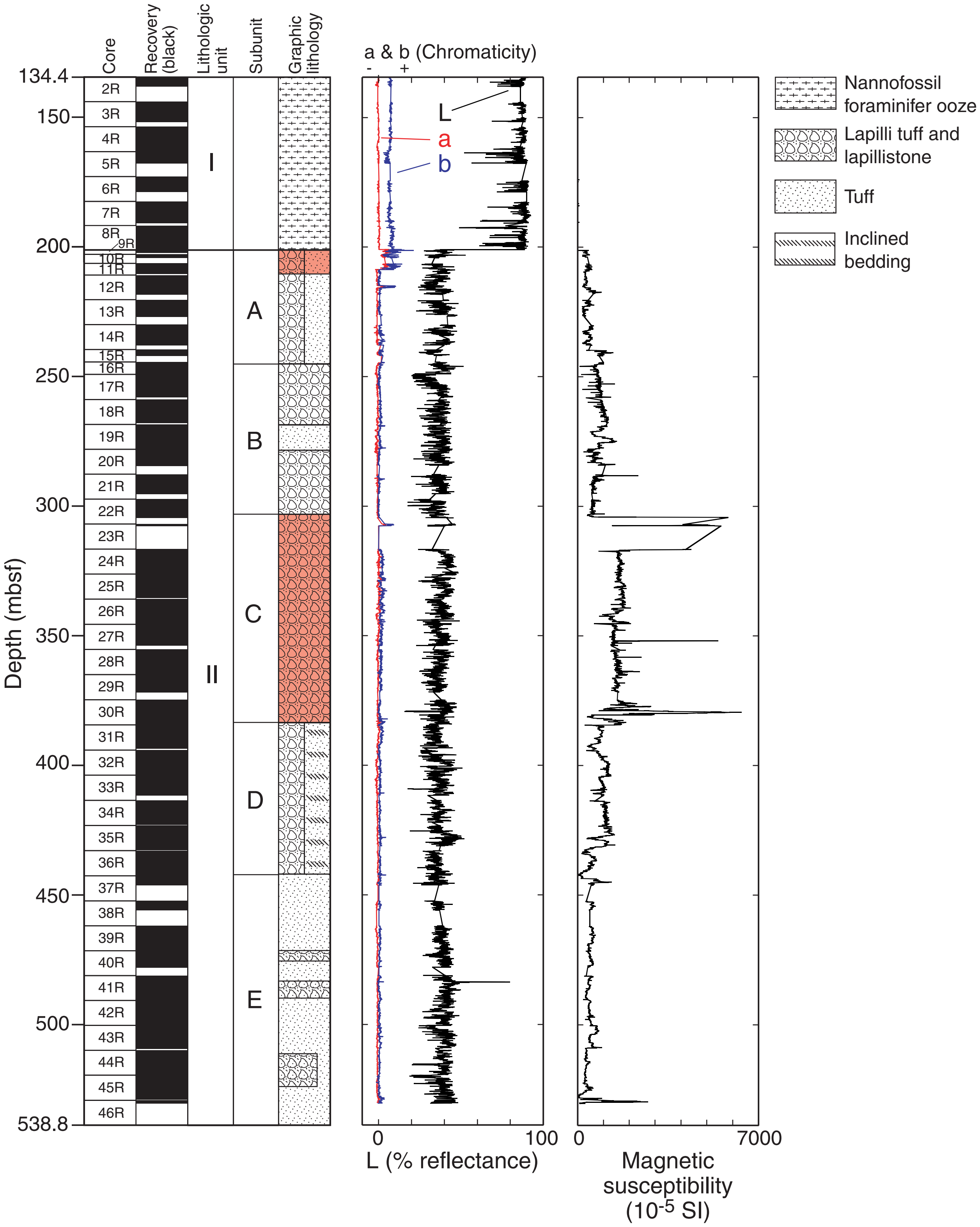

Figure F11. Spikes in magnetic susceptibility in carbonate ooze of Unit I, Hole 1184A. Most spikes correspond to intervals containing abundant volcanic glass shards. Similar shards are rare in the rest of Unit I. The small increases in susceptibility in the tops of Cores 192-1184A-2R and 3R may be caused by contamination. See legend in Figure F10, p. 38.

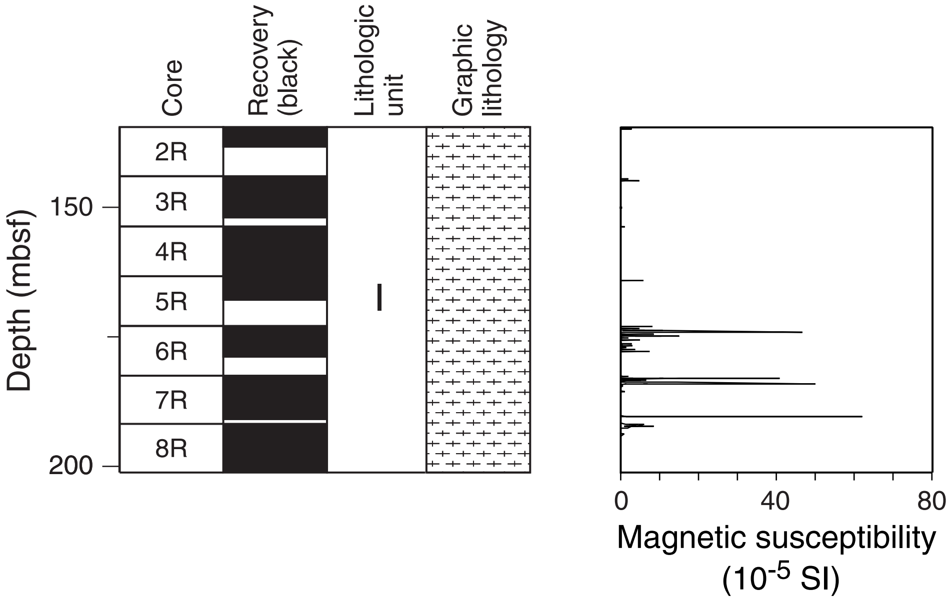

Figure F12. Lithologic characteristics in the subunits of Unit II from Hole 1184A using the lithologic facies defined in Table T4, p. 117. "Wood" indicates approximate intervals in which pieces of wood were found. The uppermost interval is represented by two pieces 1–2 cm across and <2 mm thick. At the other three wood-bearing levels, wood pieces are up to 6 cm across and 4–6 cm long. Red shading in the Graphic lithology column indicates red or yellow oxidized intervals. See legend in Figure F10, p. 38.

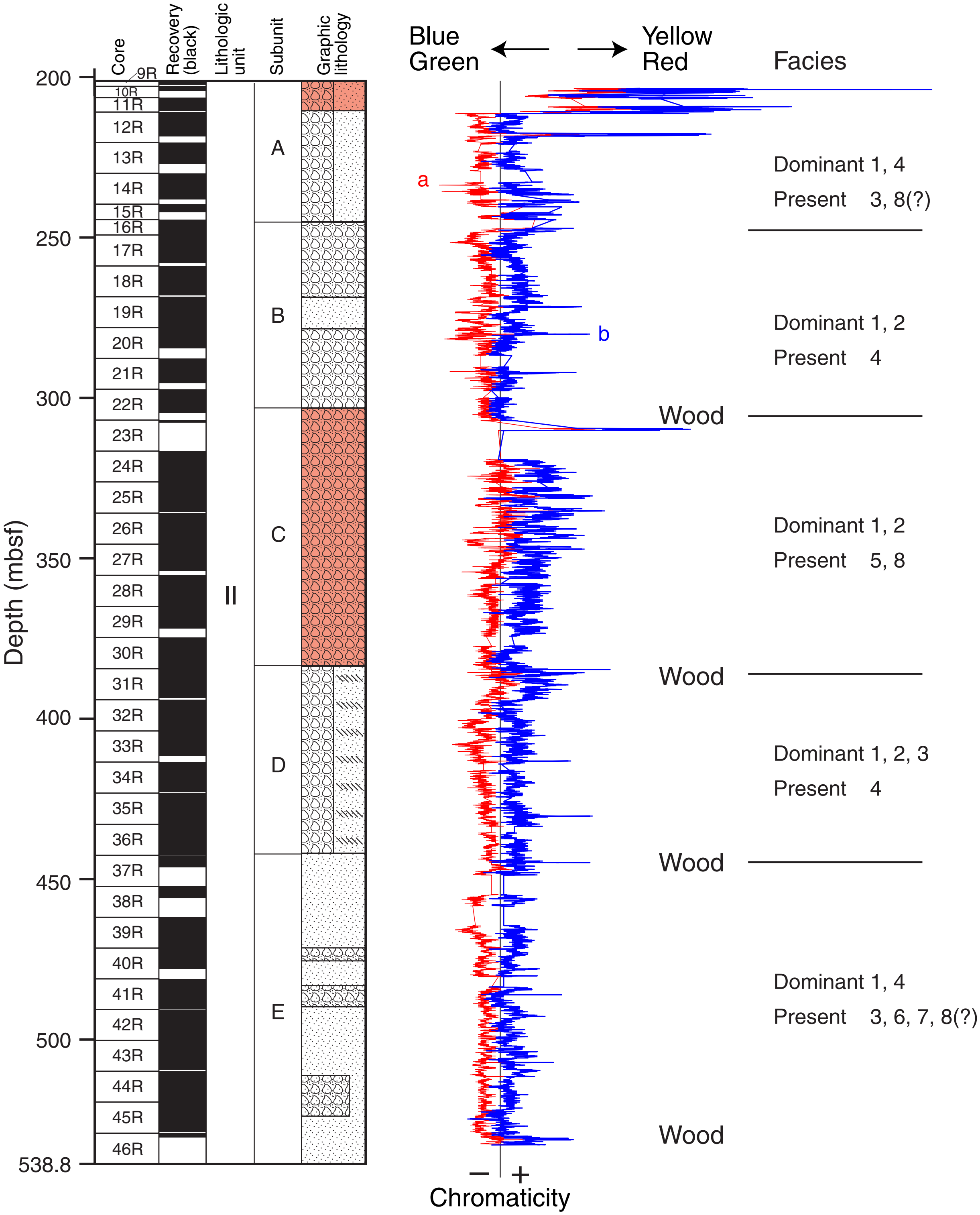

Figure F13. (**A**) Whole (round) accretionary lapilli (interval 192-1184A-43R-3, 5–20 cm) and (**B**) fragmented accretionary lapilli (interval 192-1184A-12R-4, 125–133 cm) are present throughout most of Unit II.

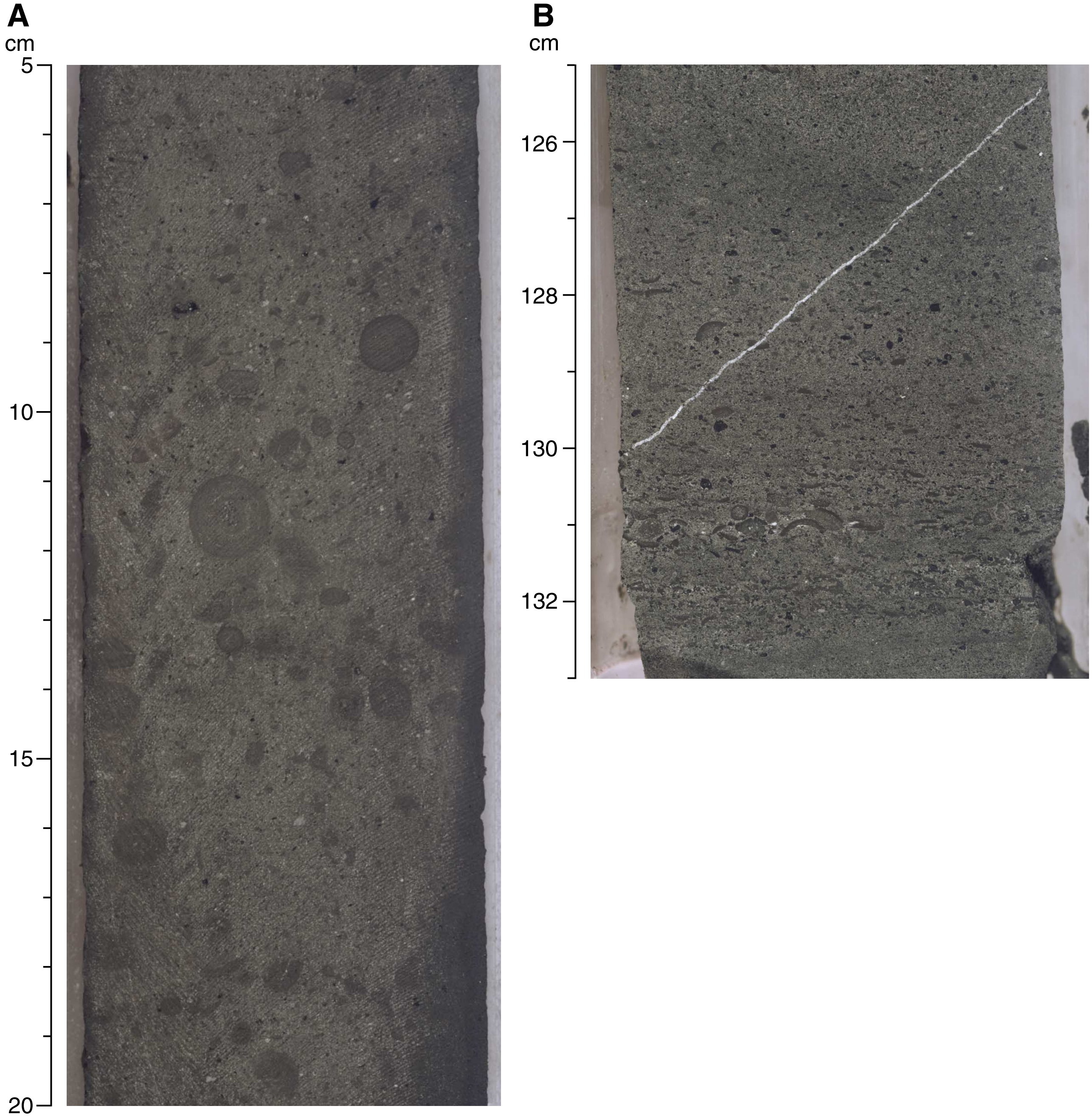

Figure F14. Ferromanganese crust on top of light orange volcaniclastic rocks at the top of Unit II (interval 192-1184A-9R-1, 0–15 cm). The crust is at 1–2 cm.

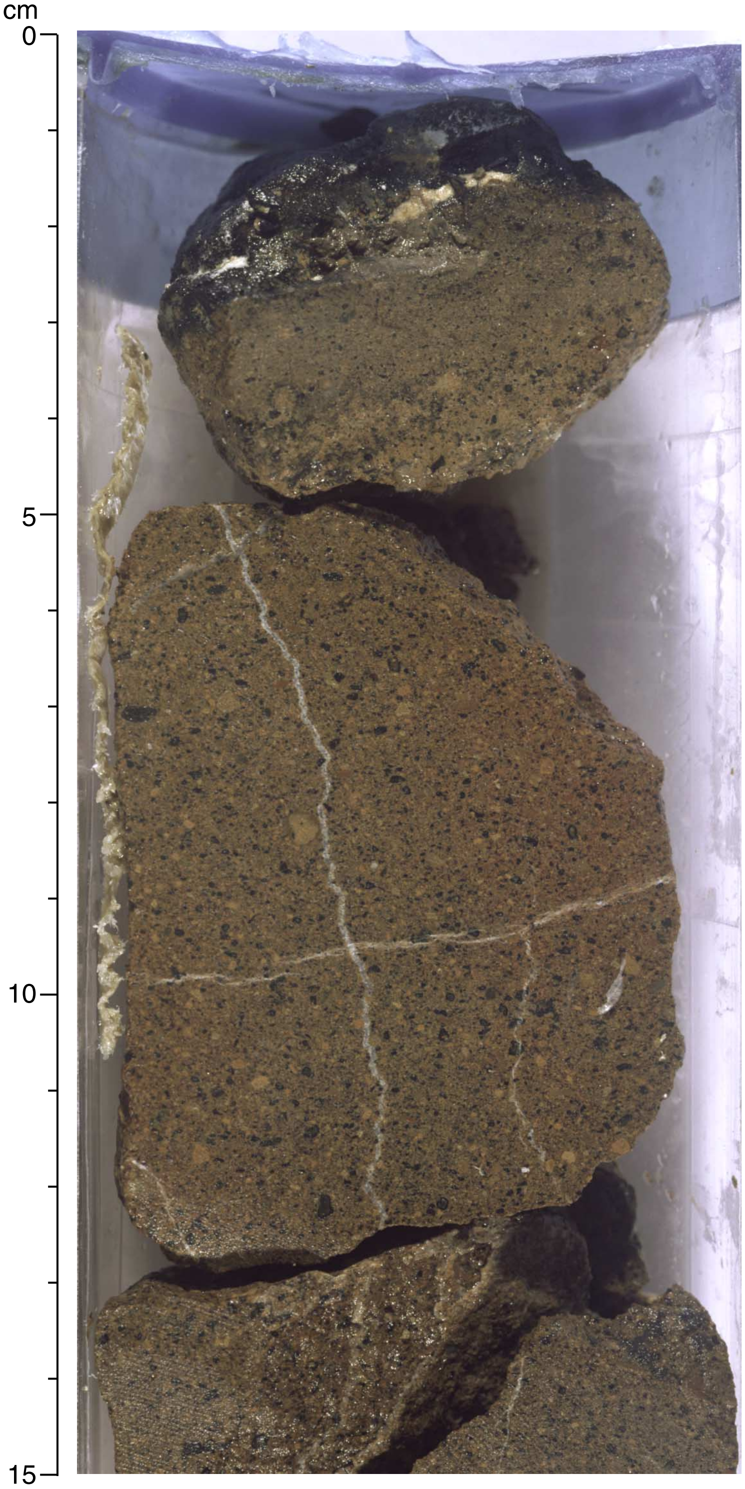

Figure F15. Interval 192-1184A-11R-2, 25–45 cm, showing whole, broken, and armored accretionary lapilli in a tuff with a brown altered matrix. The brown to yellowish red colors are typical of the upper portion of Subunit IIA.

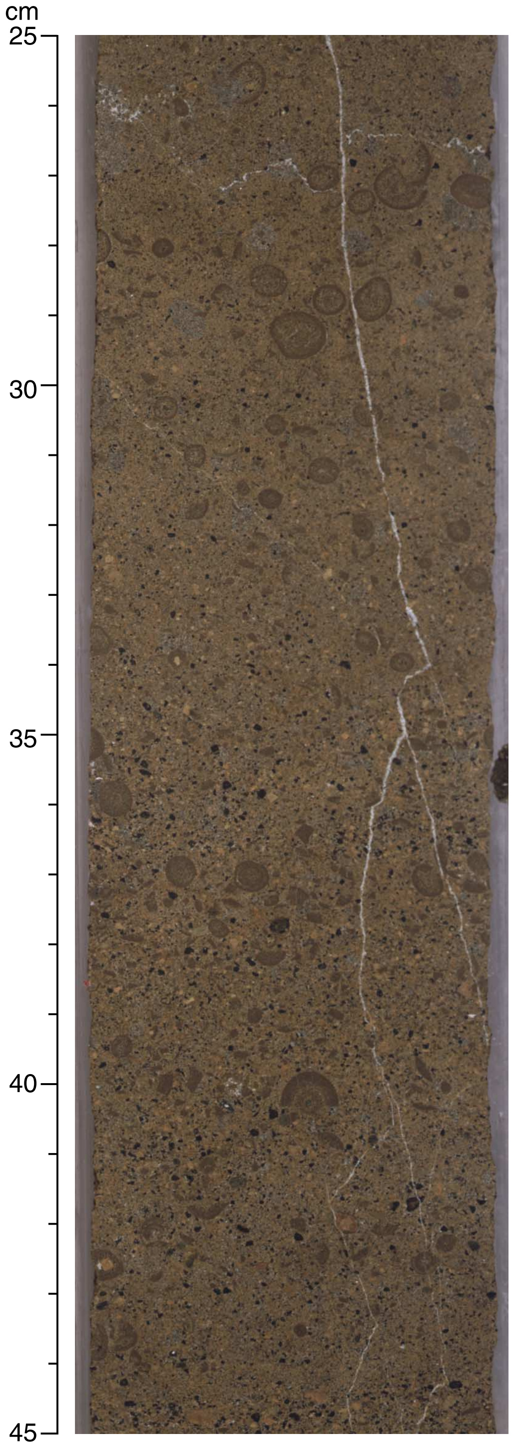

Figure F16. Massive lithic vitric lapilli tuff typical of Subunit IIB (interval 192-1184A-22R-1, 18–34 cm).

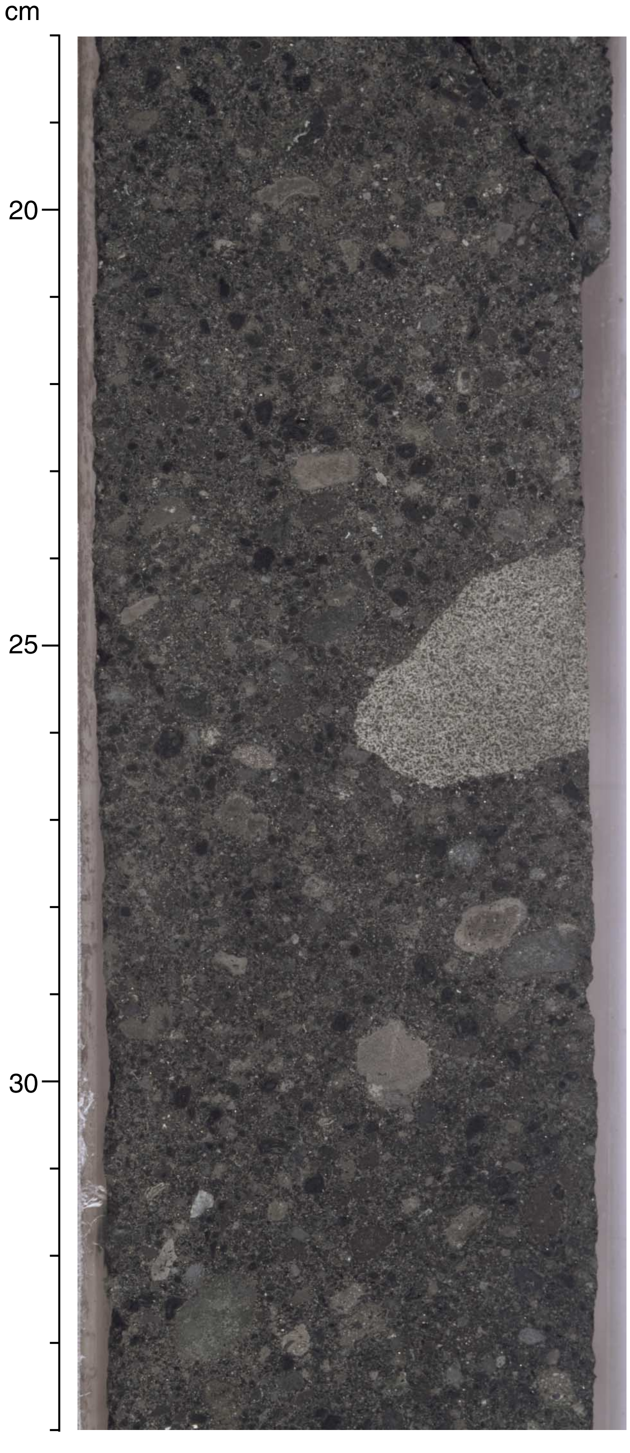

Figure F17. Inverse-graded bed within dominantly massive Subunit IIB (interval 192-1184A-19R-2, 107–118 cm).

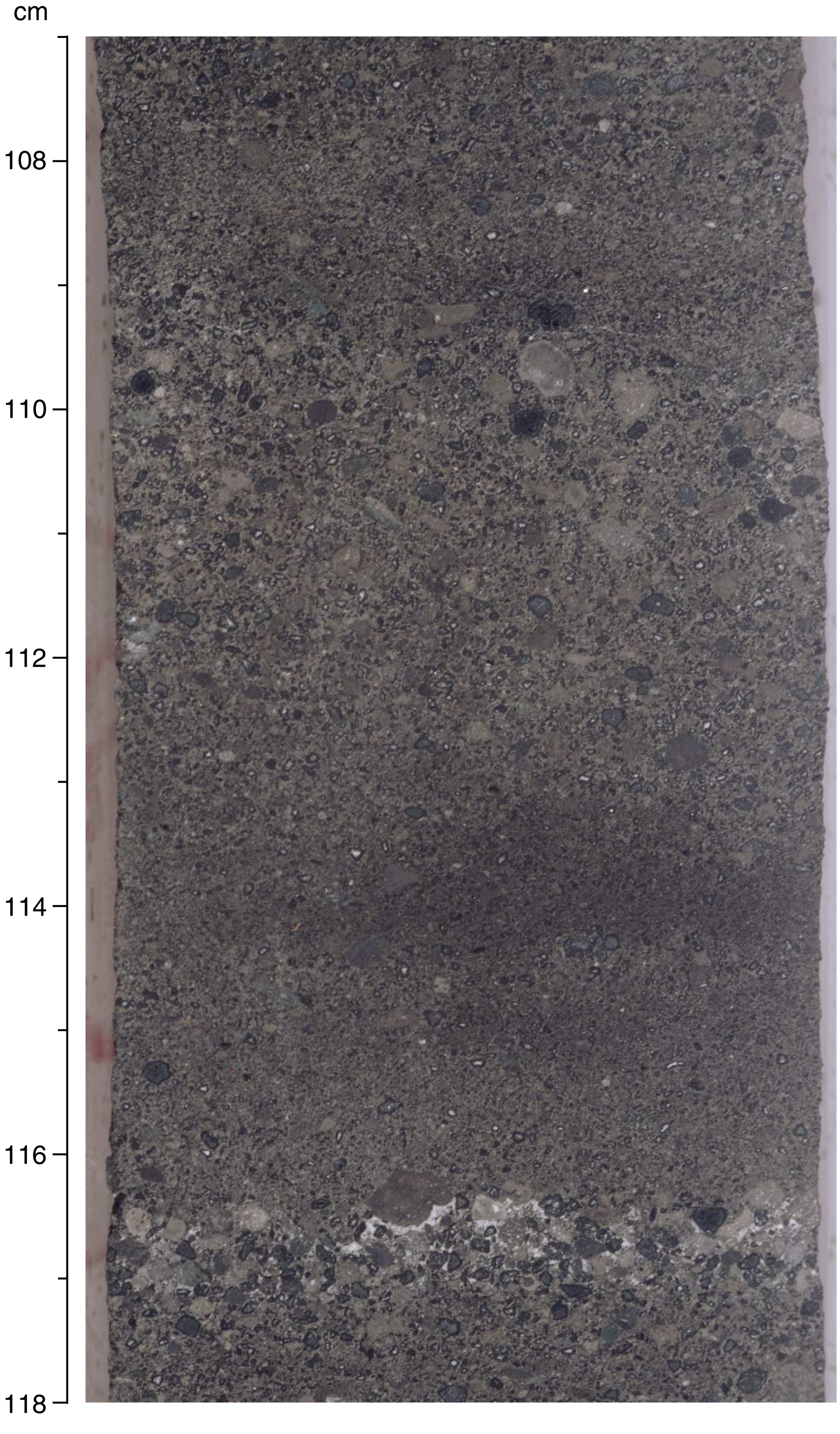

Figure F18. Interval 192-1184A-24R-7, 0–6 cm (working half of core), showing lapilli tuff with a rip-up clast of lapilli tuff containing accretionary lapilli. The accretionary lapilli are oxidized.

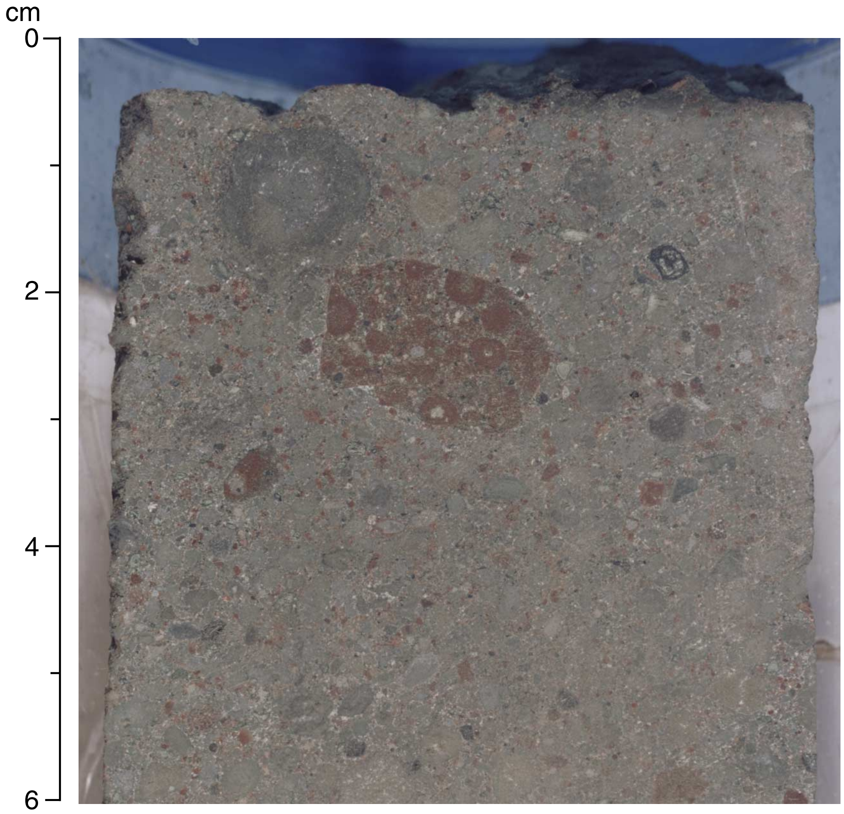

Figure F19. Interval 192-1184A-22R-6, 93–113 cm, showing tachylite-rich lapilli-stone that forms the upper bounding bed of Subunit IIC.

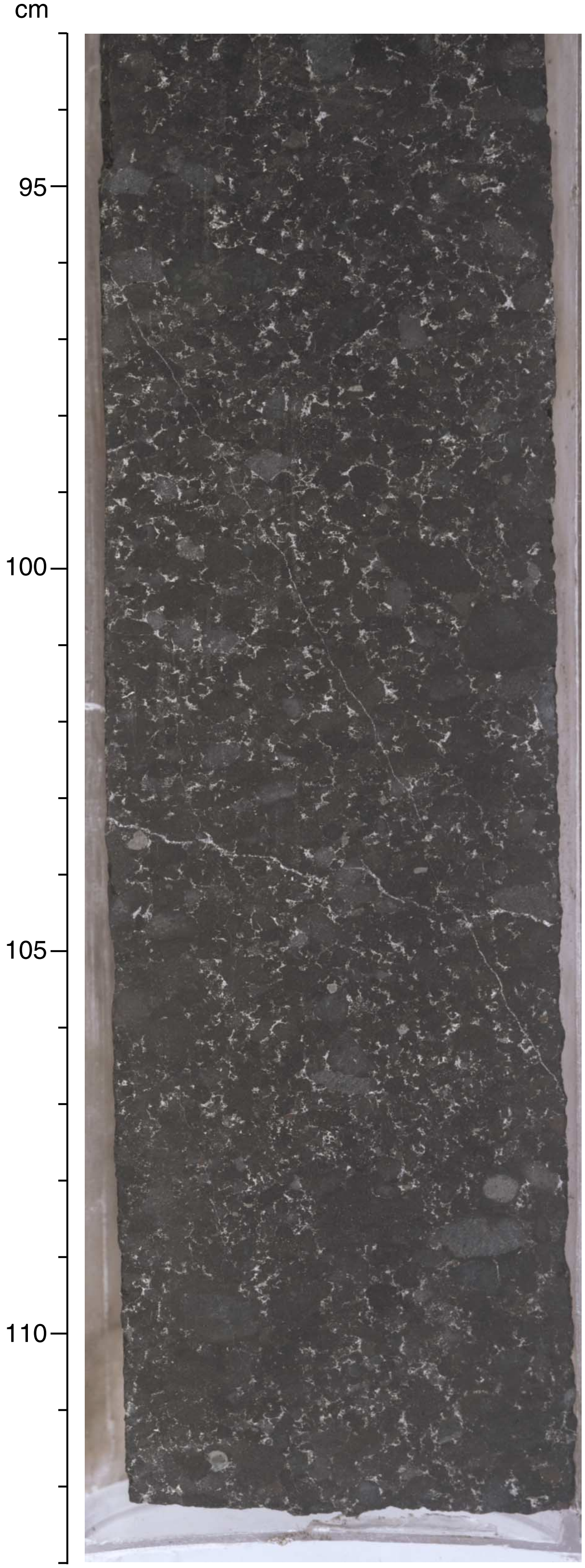

Figure F20. Downhole distribution of accretionary and armored lapilli, red lithic clasts, wood, and lithic clasts as a proportion of all ash- to lapilli-size clasts. Dashed lines = subunit boundaries.

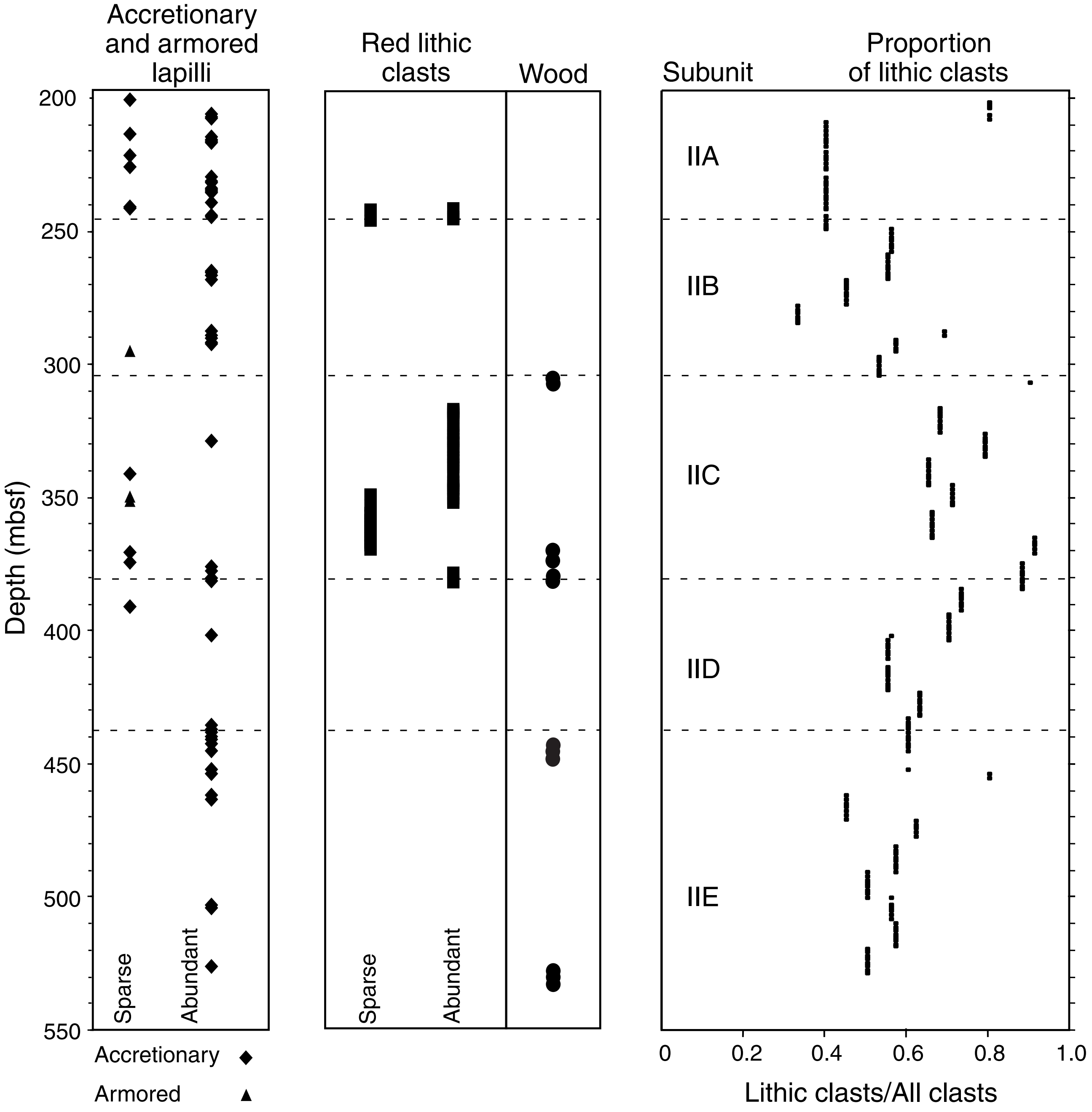

Figure F21. Inclined layering defined by alternations in grain size in typical vitric lithic tuff of Subunit IID (interval 192-1184A-31R-1, 0–45 cm).

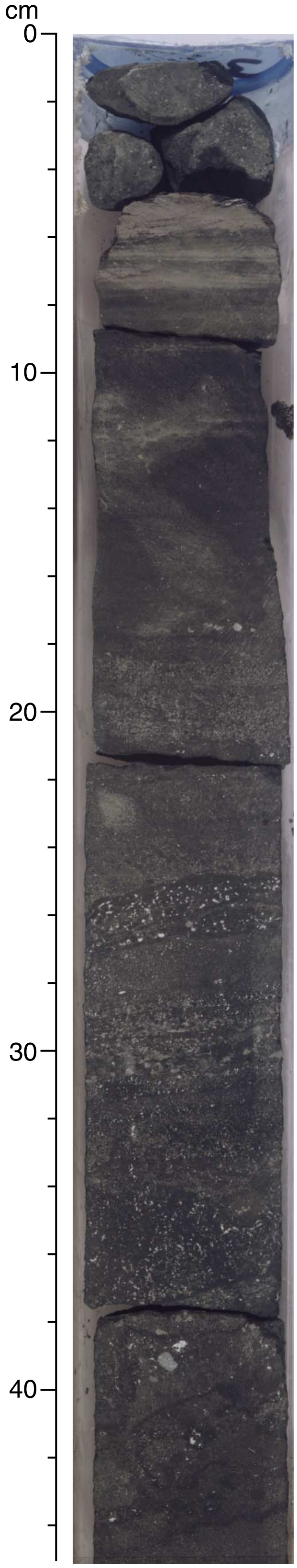

Figure F22. Wood and apparent organic carbon–rich layers in Subunit IIE (interval 192-1184A-45R-7, 48–65 cm).

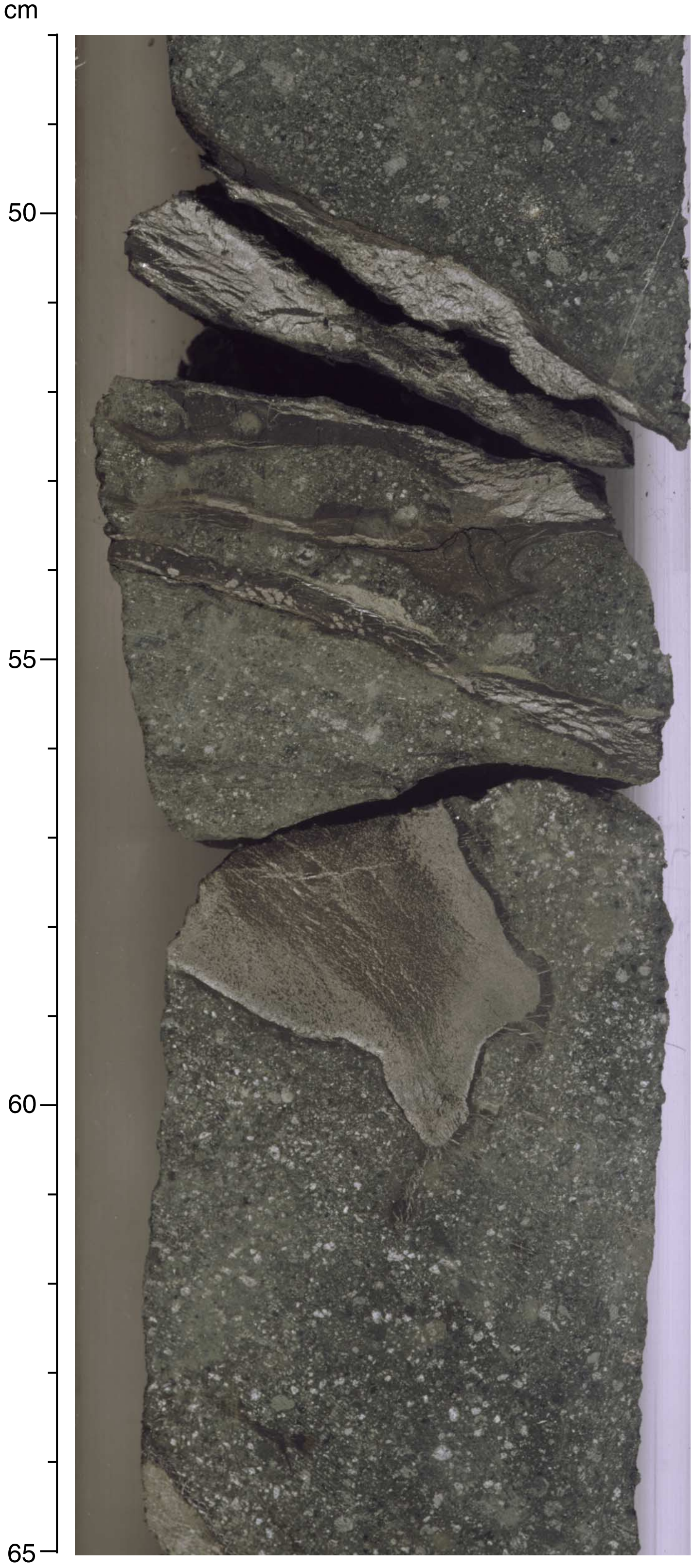

Figure F23. Deformed bedding defined by grain size in the lower portions of Subunit IIE (interval 192-1184A-45R-6, 107–130 cm).

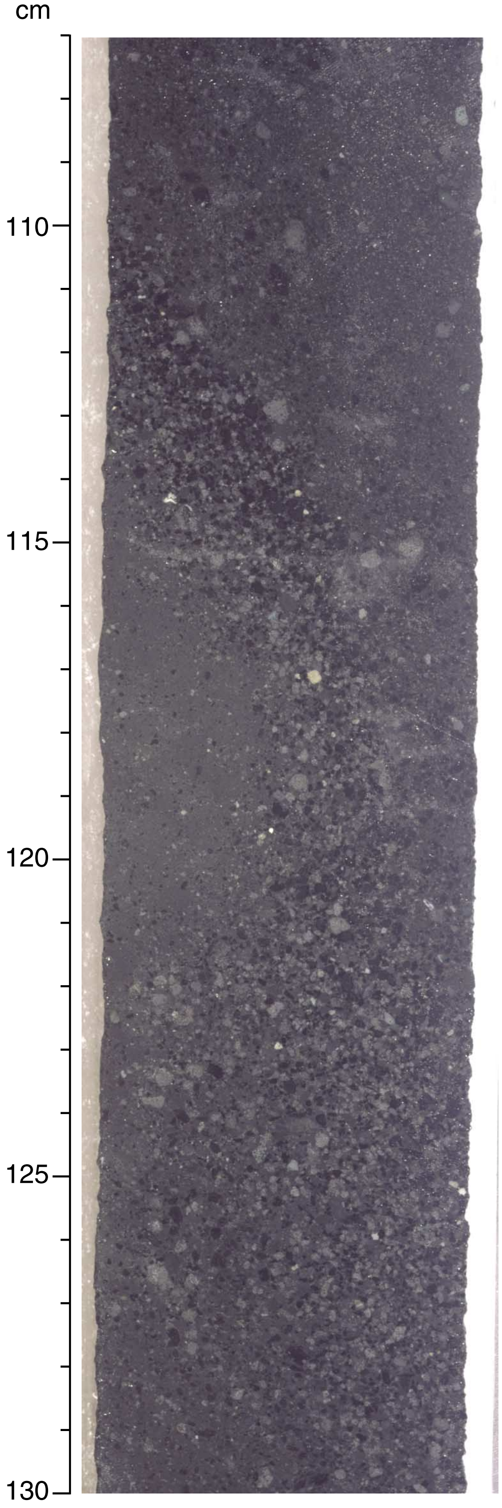

Figure F24. Wood in lower portion of Subunit IIE showing *Teredo*-like mollusk borings (interval 192-1184A-45R-6, 96–104 cm).

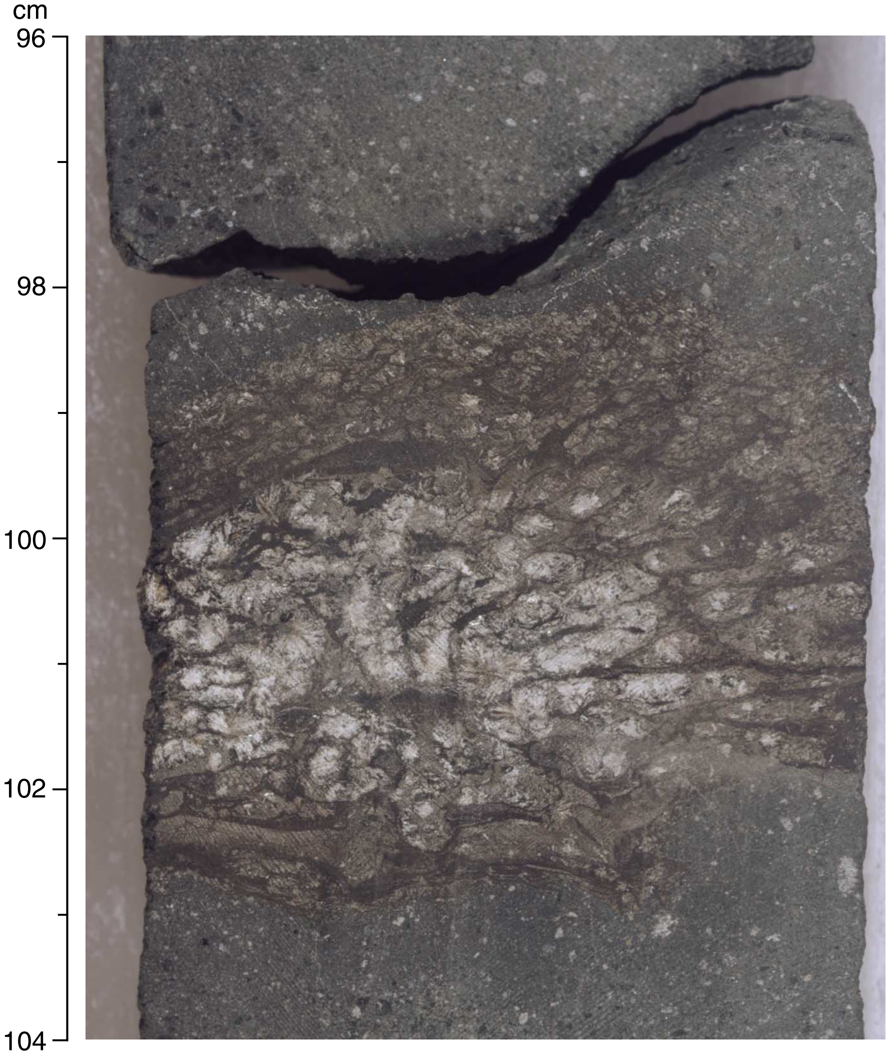

Figure F25. Orientation of the inclined layers measured from Unit II, Hole 1184A. Inclined layers are most abundant in Subunit IID and are rare in Subunit IIC. Dips are steepest in Subunit IID. The dominant dip directions are north to northwest. N = paleomagnetic north.

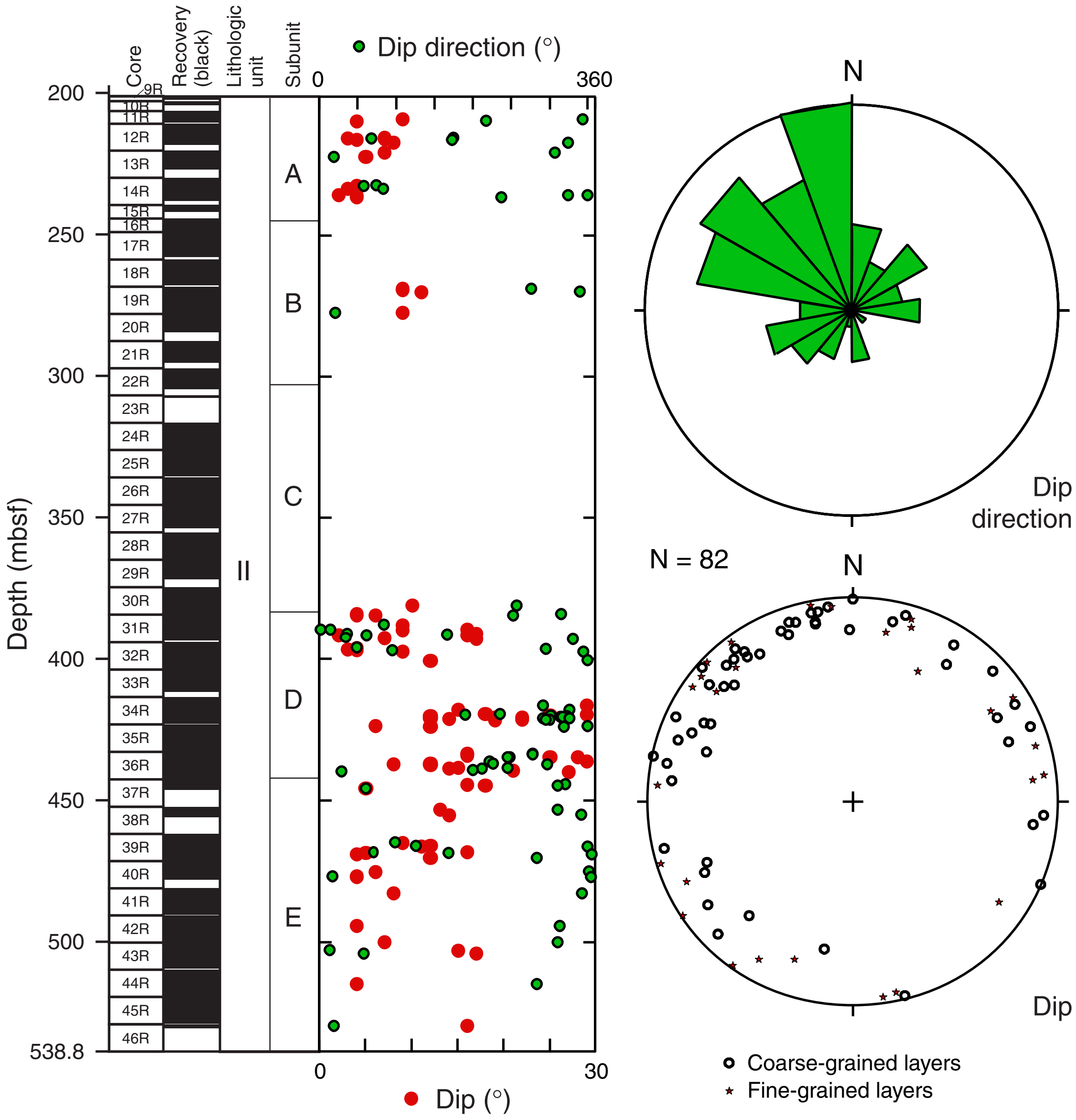

Figure F26. Schematic interpretation of the eruptive setting of the volcaniclastic rocks at Site 1184. These reworked pyroclastic deposits probably formed on top of a large seamount as it grew to within ~200 m of the sea surface. The presence of basalt at depth is conjectural. Letters A through F identify features for which we have evidence in the volcaniclastic rocks. A: The presence of blocky, nonvesicular glass shards suggests fragmentation of rapidly quenched magma in hydromagmatic eruptions under shallow water; abundant tachylite clasts in parts of the succession suggest that this process occurred in an environment that was at times subaerial. B: Accretionary and armored lapilli form in the atmosphere, in steam-rich columns of volcanic ash. C: The absence of blocks, bombs, or lapilli >20 mm suggests that the primary pyroclastic deposits formed several kilometers from the eruption center(s). D: Wood fragments found at the bases of four of the five subunits indicate proximity to land. E: Deposition or redeposition of the volcaniclastic material in a marine setting is indicated by the presence of nannofossils throughout the unit. F: Redeposition by turbidity currents is suggested by the presence of rip-up clasts and broken accretionary lapilli and by the absence of the layering that would be expected from material settling through water.

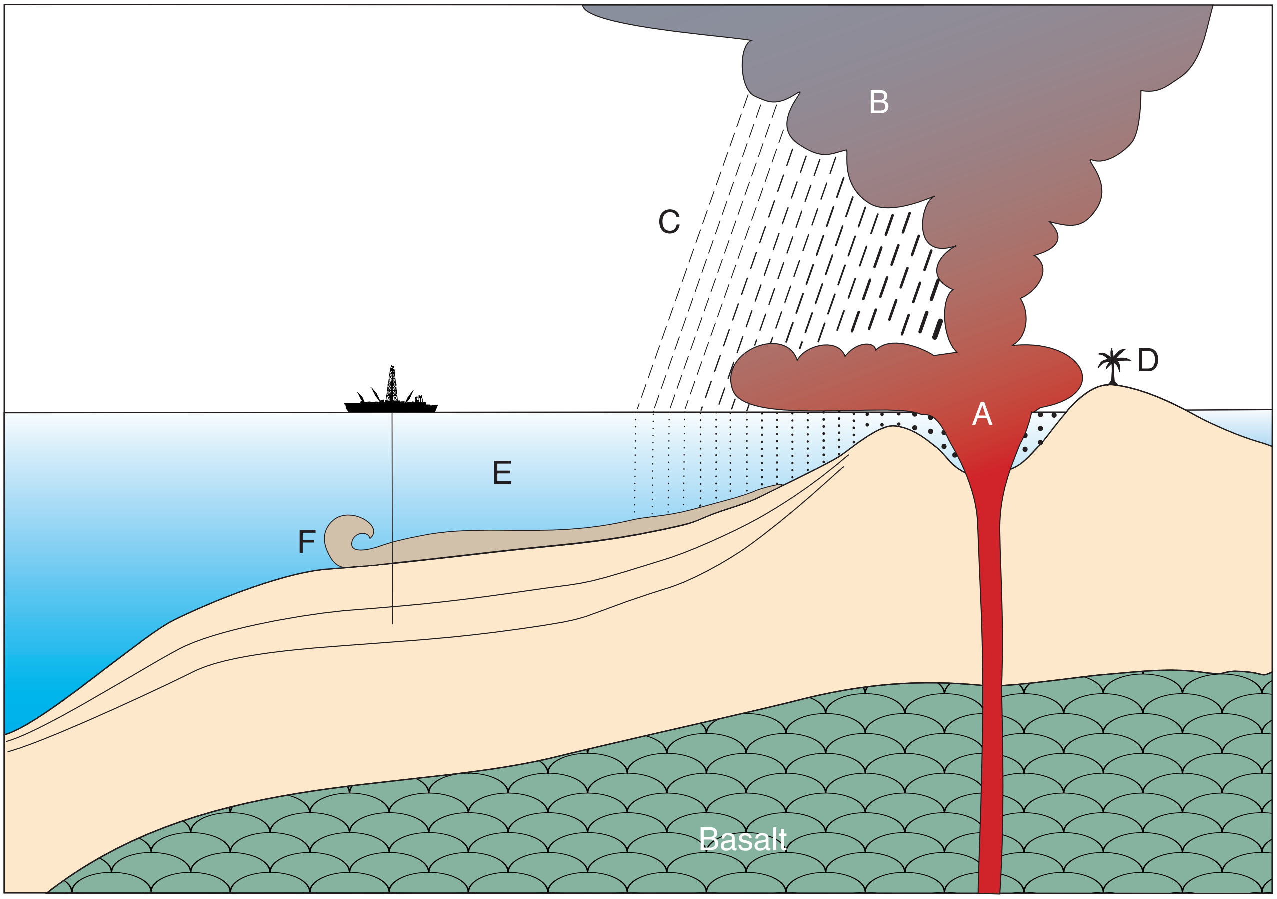

Figure F27. Calcareous microfossil biozonations with secondary events and the assigned zonation of the lower Miocene sediments recovered from Hole 1184A. Oligo. = Oligocene.

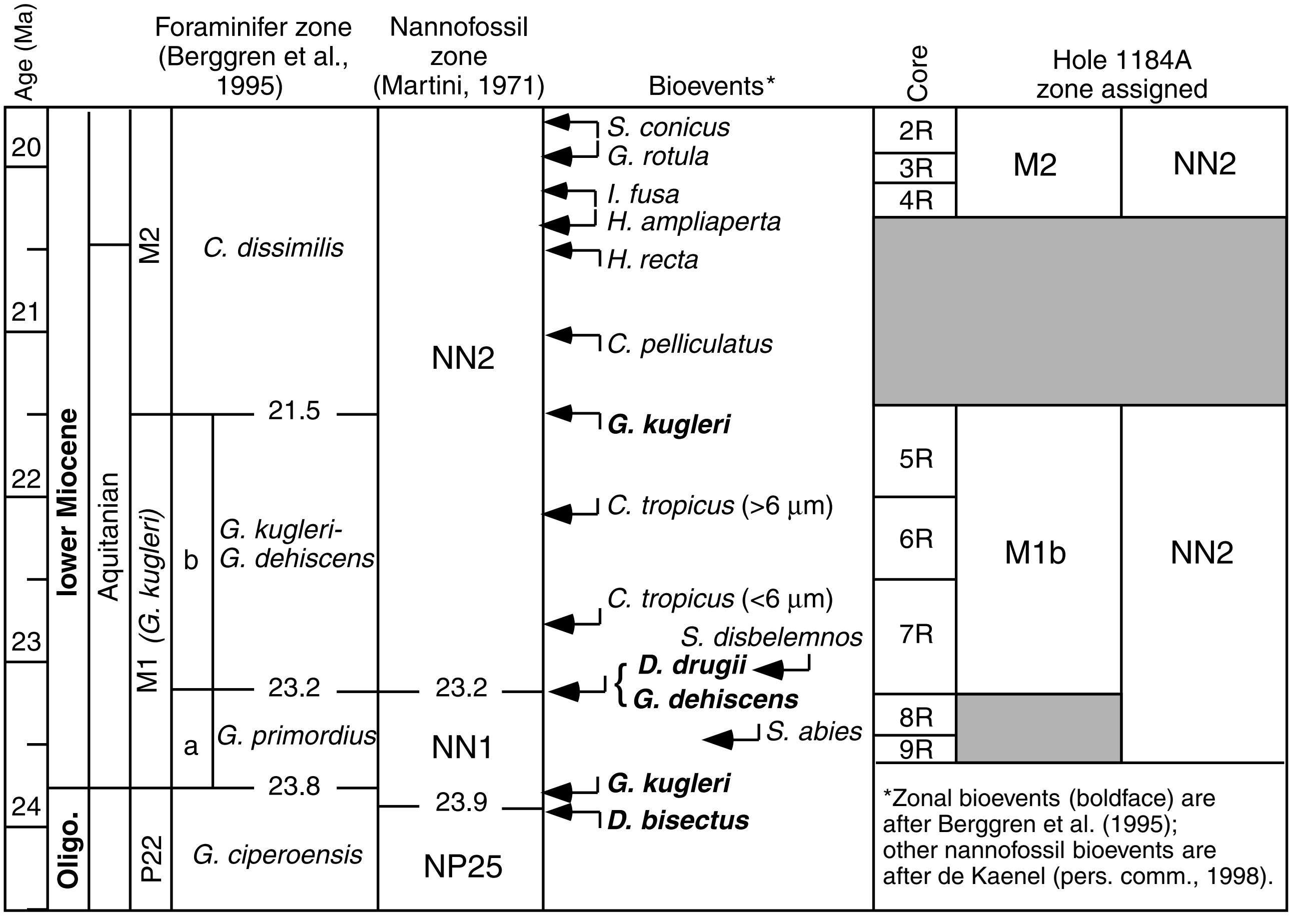

*Zonal bioevents (boldface) are after Berggren et al. (1995); other nannofossil bioevents are after de Kaenel (pers. comm., 1998).

Figure F28. Age vs. depth plot for lower Miocene calcareous oozes at Site 1184.

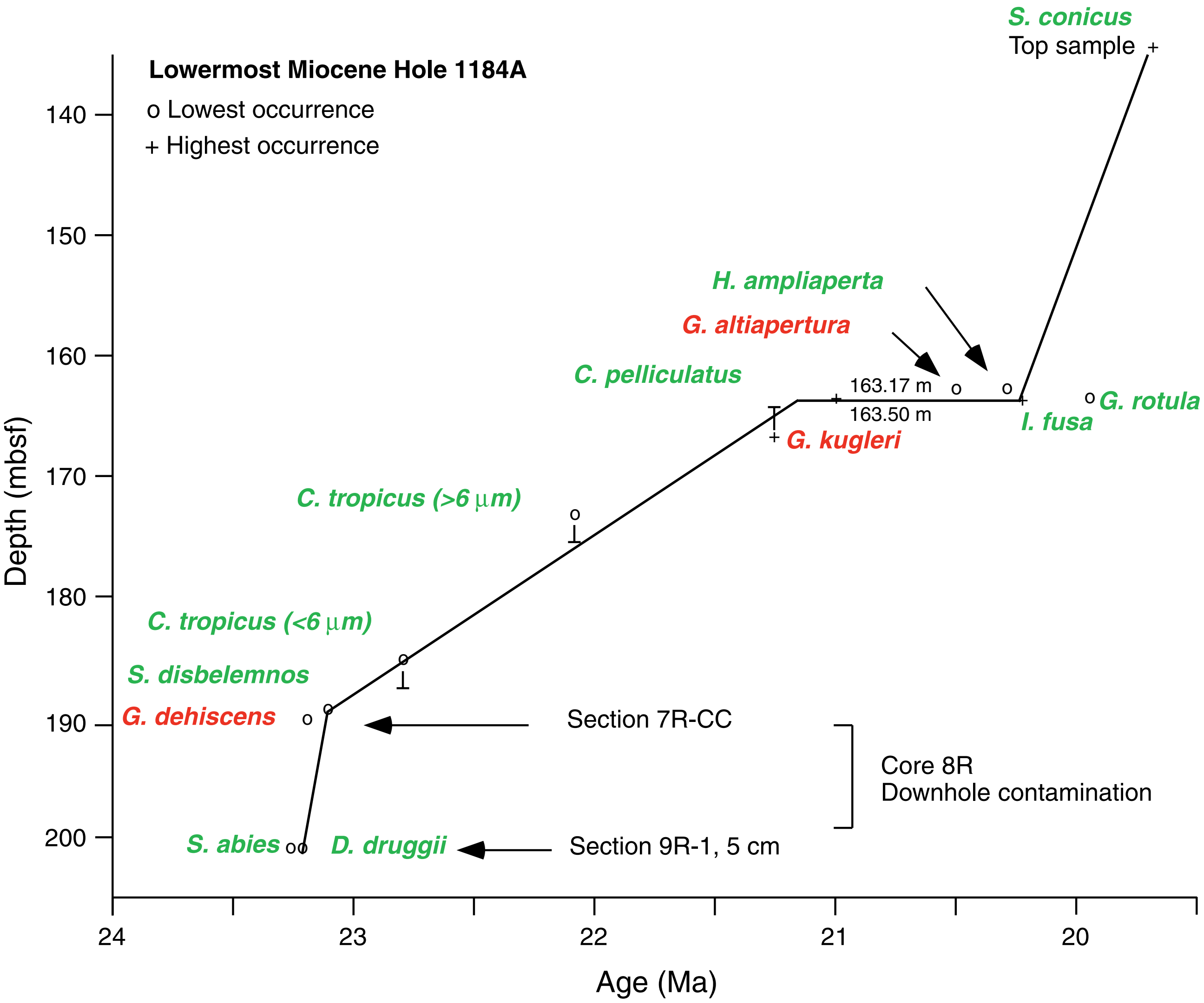

Figure F29. The variety of lithic and vitric clast types in Sample 192-1184A-31R-7, 40–43 cm, Subunit IID. In decreasing order of abundance, the clast types are nonvesicular basalt, vitric shards, sparsely vesicular basalt, plagioclase-rich basalt, and tachylite. Glass is completely altered to smectite, and the cement is composed mainly of zeolites (field of view = 5.5 mm; plane-polarized light; photomicrograph ID# 1184A_076).

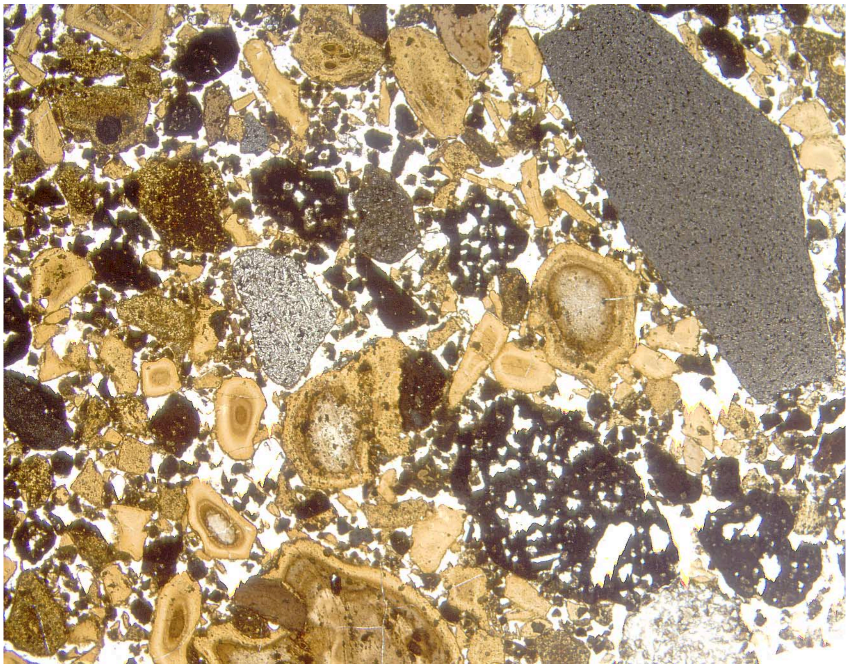

Figure F30. Interval 192-1184A-21R-6, 68–80 cm, showing lapilli tuff with basaltic clasts, altered black glass fragments, and accretionary and armored lapilli.

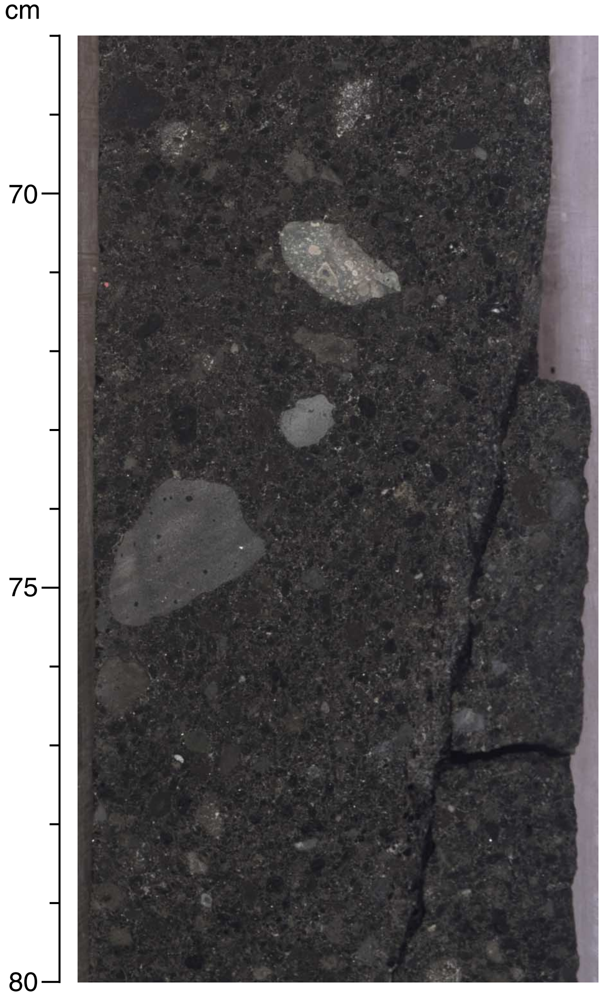

Figure F31. Alteration of titanomagnetite to maghemite in Sample 192-1184A-40R-3, 37–41 cm (field of view = 0.28 mm; reflected light; photomicrograph ID# 1184A_079c).

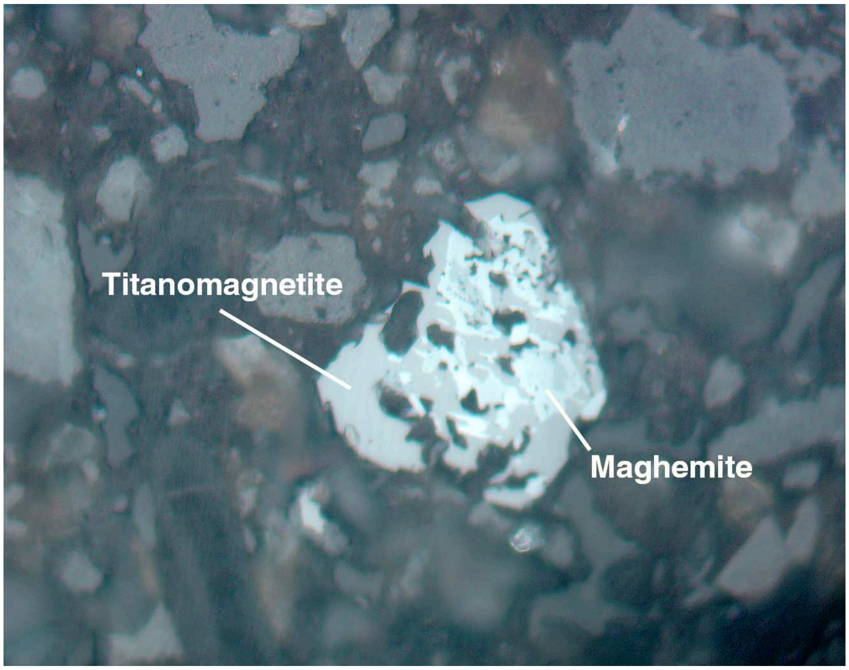

Figure F32. Glass inclusions in a discrete plagioclase crystal in **Sample 192-1184A-31R-7, 40–43 cm** (field of view = 1.4 mm; plane-polarized light; photomicrograph ID# 1184A_078).

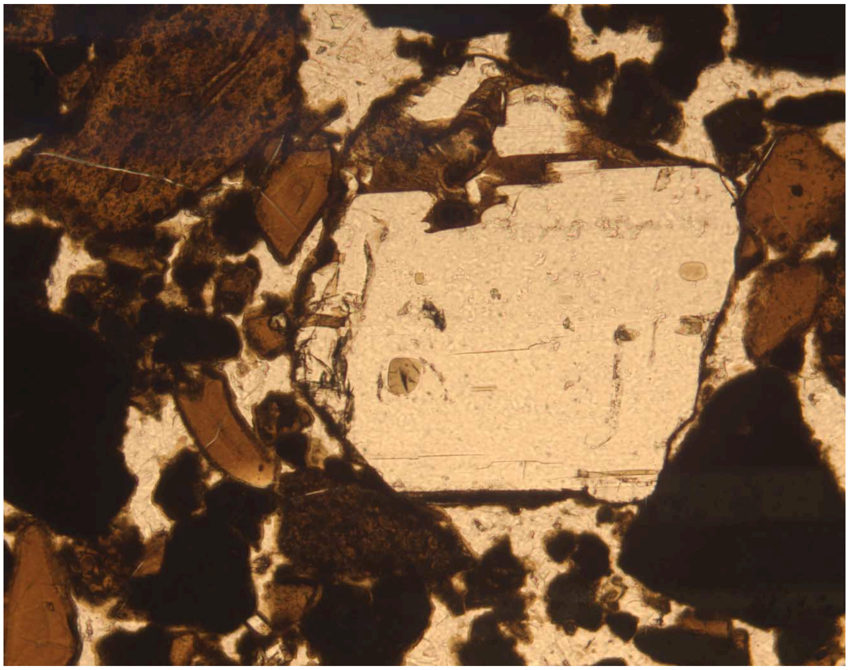

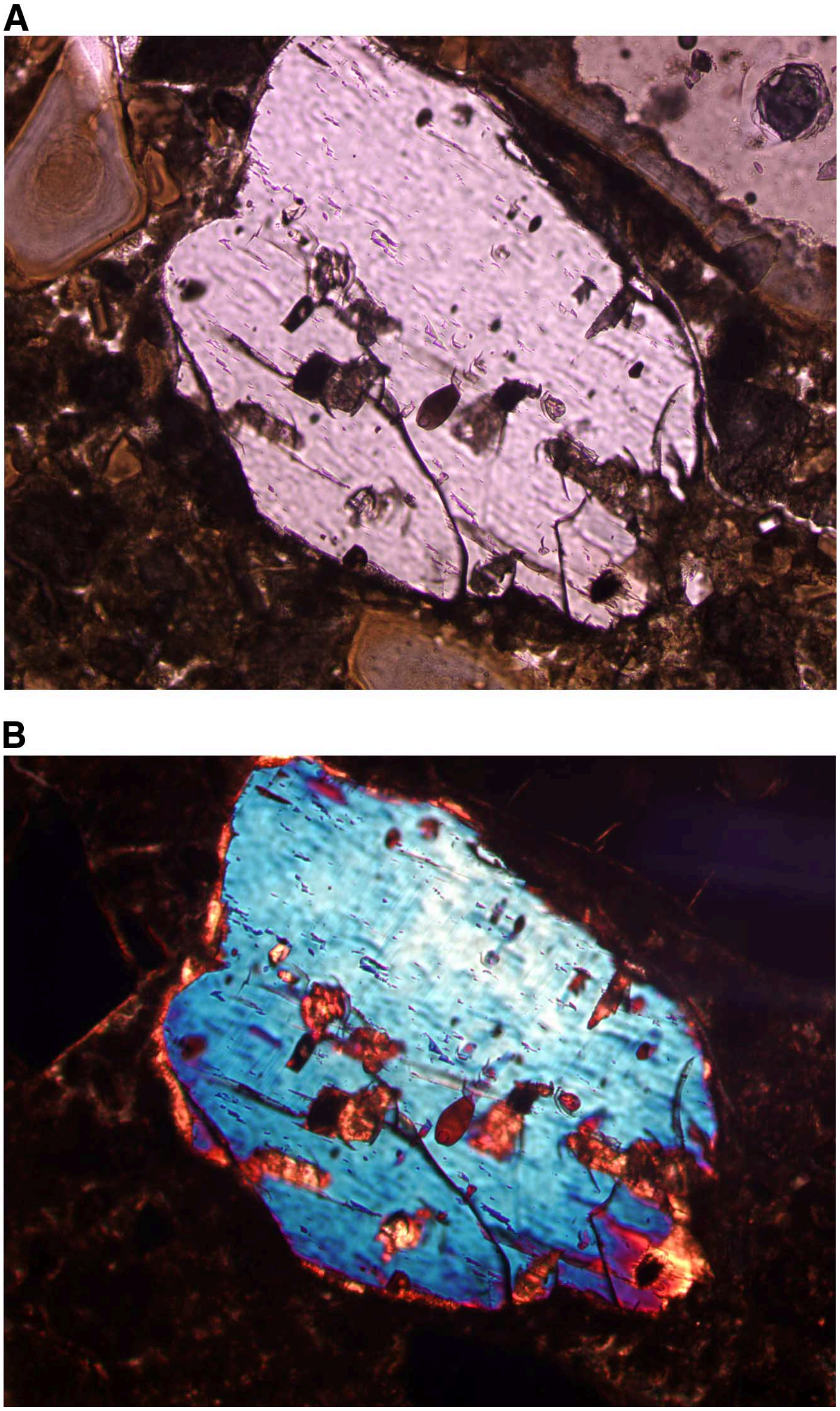

Figure F33. Glass inclusions (some devitrified) in a discrete clinopyroxene crystal in Sample 192-1184A-42R-1, 147–150 cm (field of view = 0.7 mm; photomicrograph ID# 1184A_083). **A.** Plane-polarized light. **B.** Crossed polars.

Figure F34. Interval 192-1184A-24R-8, 35–40 cm (working half of core), showing lapilli tuff with a large rip-up clast of red-brown tuff. The rip-up clast is bedded and contains fragments of accretionary lapilli.

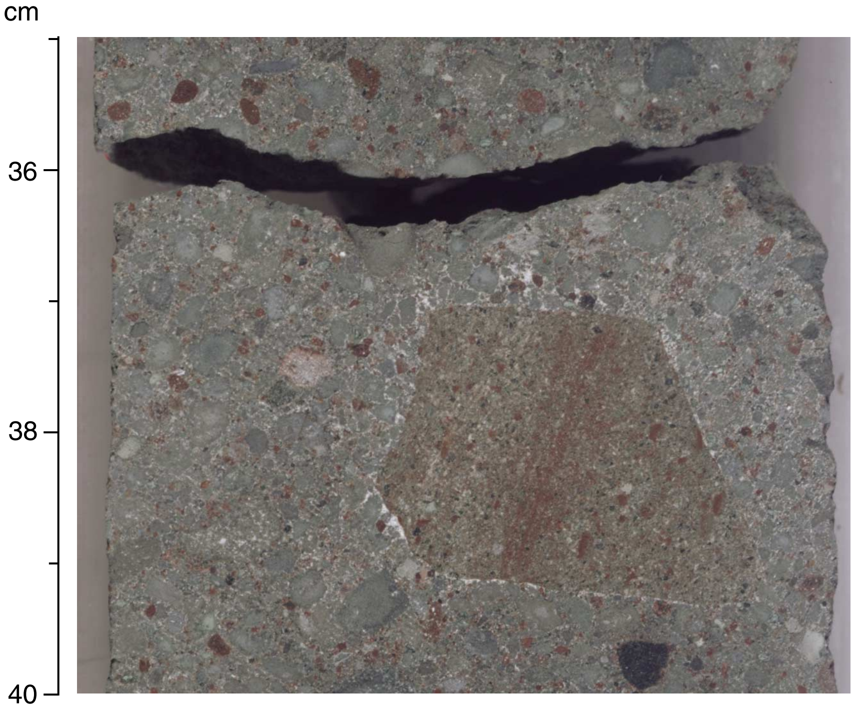

Figure F35. Fragments of altered aphyric basalt within a highly vesicular basalt clast in Sample 192-1184A-16R-CC, 7–10 cm (field of view = 2.8 mm; plane-polarized light; photomicrograph ID# 1184A_143).

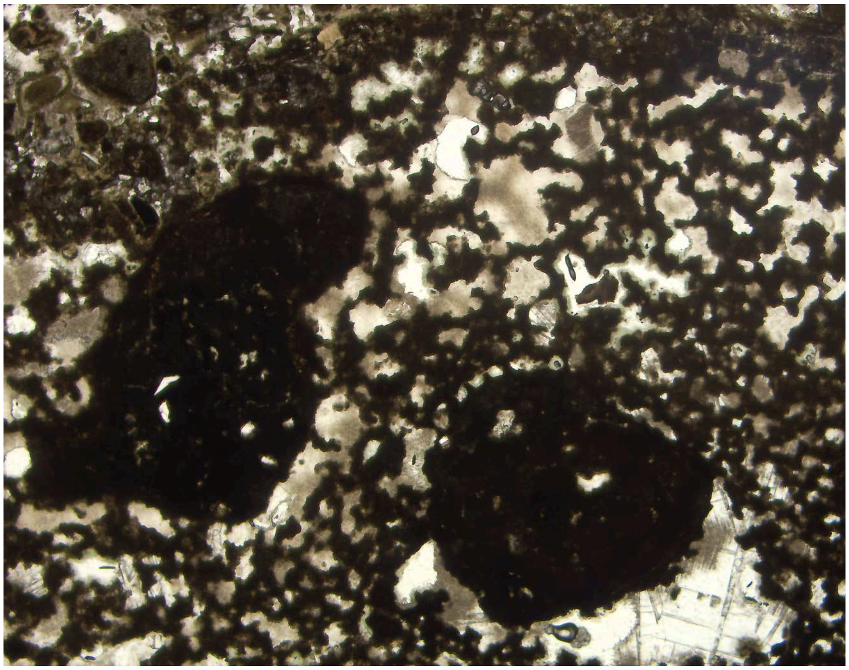

Figure F36. Subtrachytic texture in a basalt clast in Sample 192-1184A-20R-5, 41–44 cm (field of view = 1.4 mm; plane-polarized light; photomicrograph ID# 1184A_058).

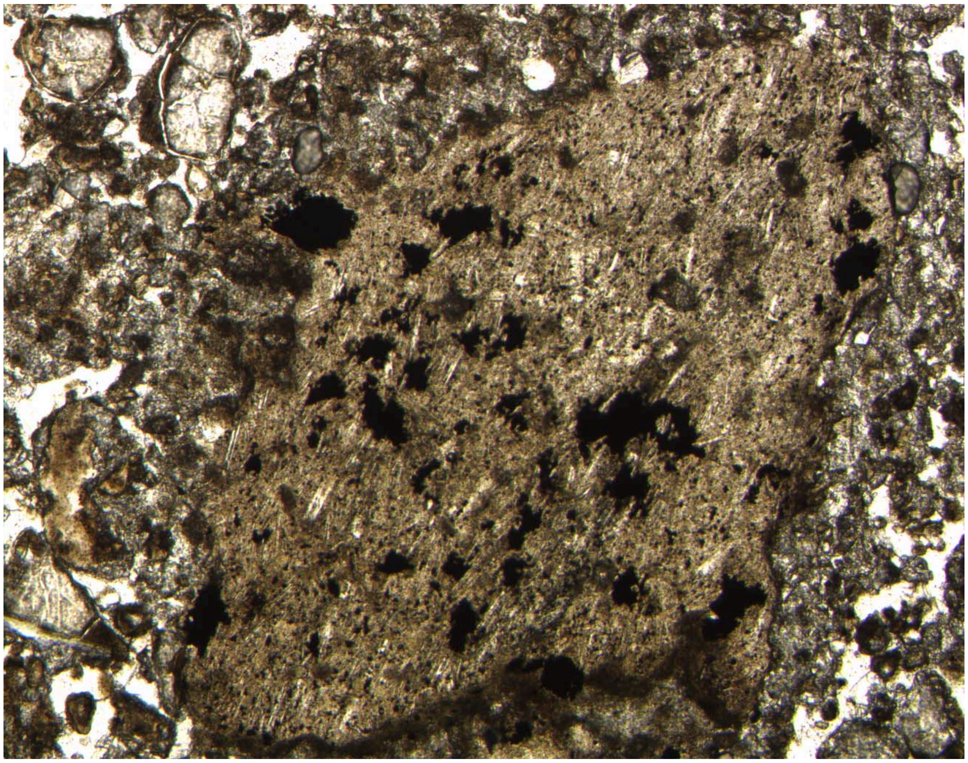

Figure F37. Rounded basalt clast (highlighted) with plagioclase, clinopyroxene, and titanomagnetite in Sample 192-1184A-20R-5, 41–44 cm (field of view = 1.4 mm; plane-polarized light; photomicrograph ID# 1184A_059).

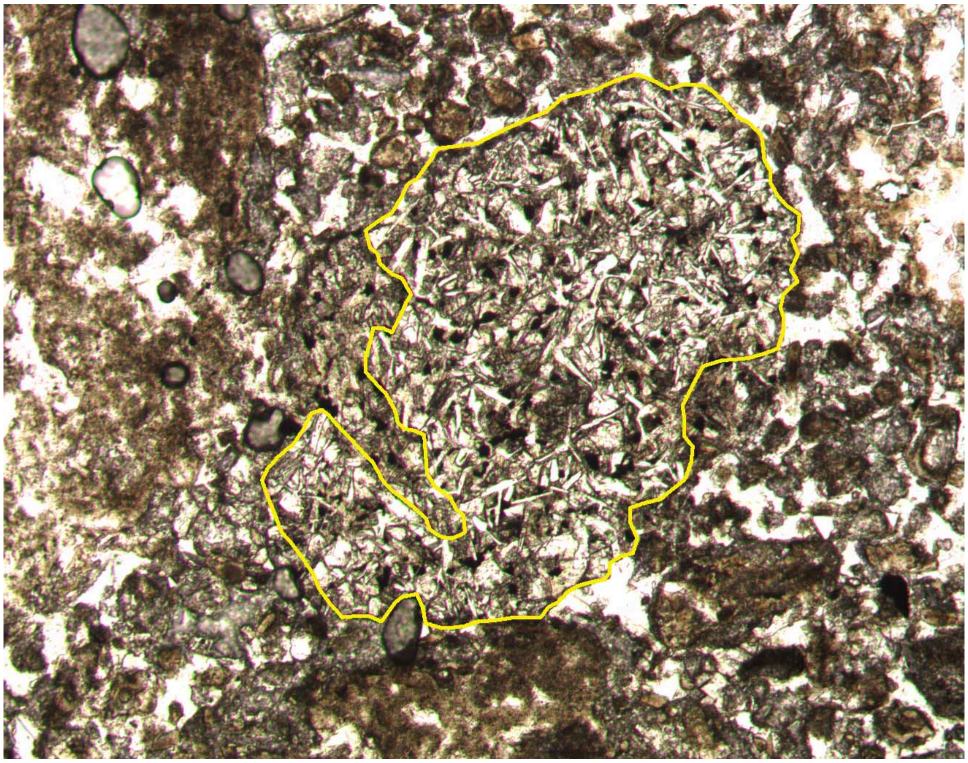

Figure F38. Phenocrysts of plagioclase (plag) and clinopyroxene (cpx) in a titanomagnetite-rich basalt clast in Sample 192-1184A-41R-3, 29–33 cm (field of view = 2.8 mm; plane-polarized light; photomicrograph ID# 1184A_081).

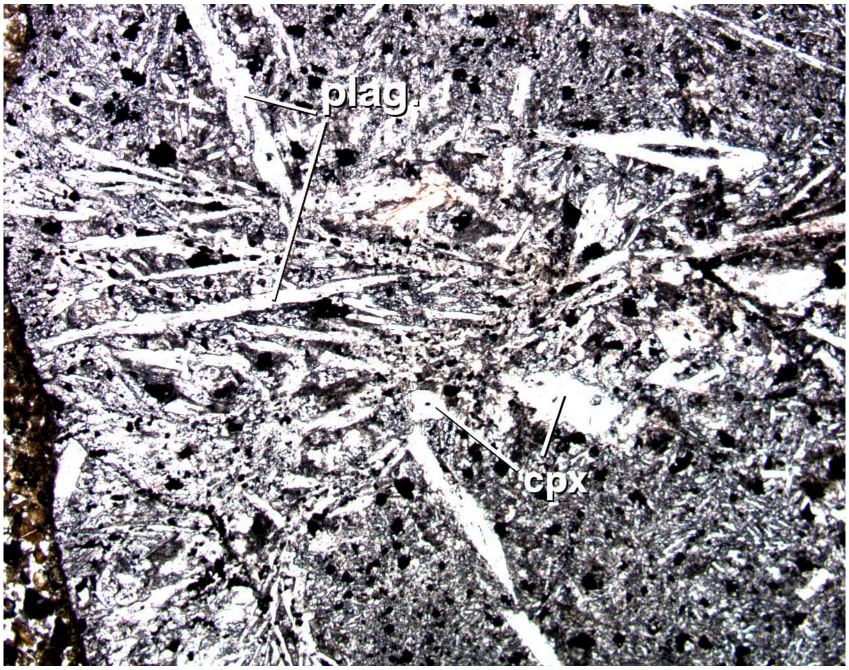

Figure F39. Titanomagnetite-rich basalt clast in Sample 192-1184A-31R-7, 40–43 cm (field of view = 1.4 mm; plane-polarized light; photomicrograph ID# 1184A_071).

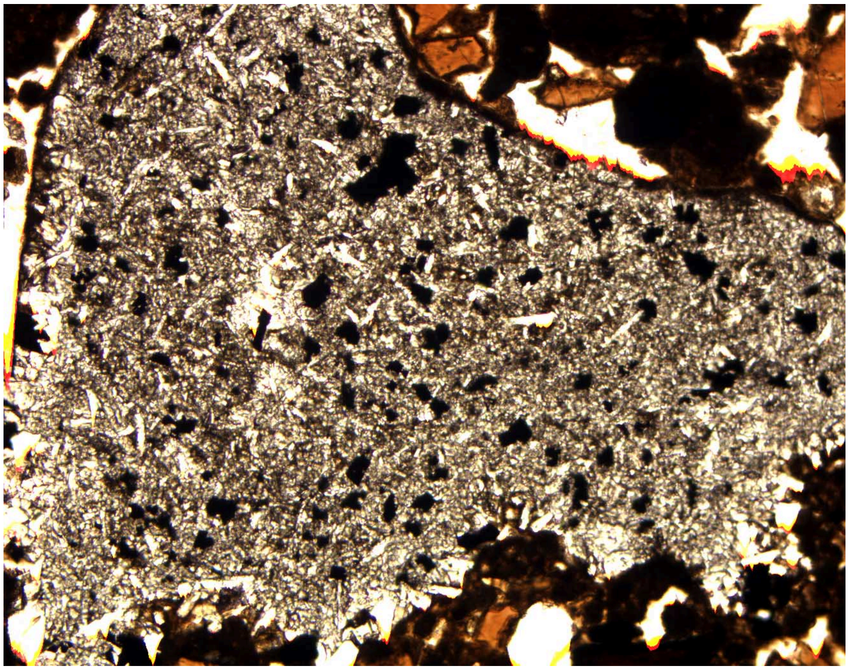

Figure F40. Diabase clast showing intergranular to subophitic plagioclase and clinopyroxene in Sample 192-1184A-20R-3, 34–37 cm (field of view = 2.8 mm; crossed polars; photomicrograph ID# 1184A_070).

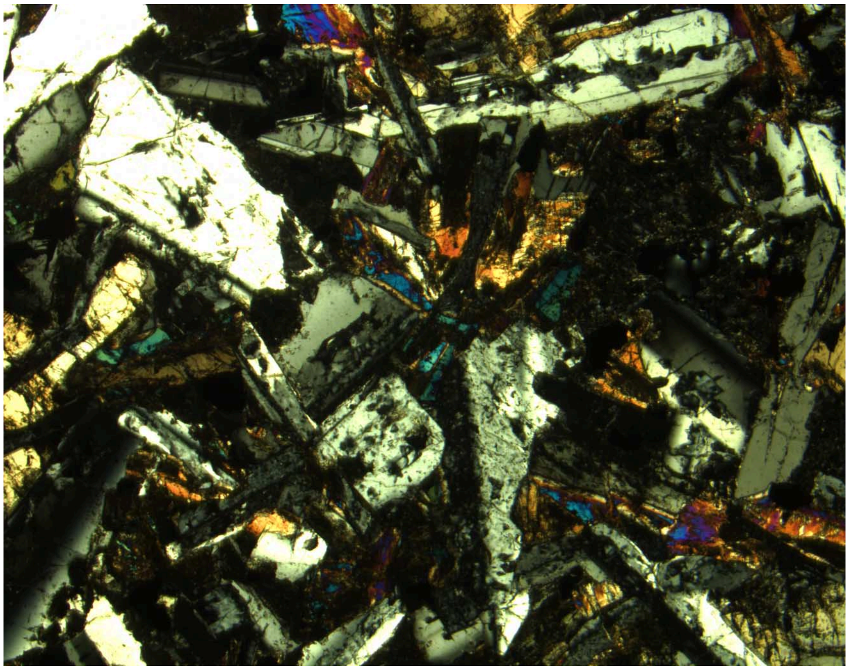

Figure F41. Skeletal titanomagnetite in a diabase clast in Sample 192-1184A-20R-3, 34–37 cm (field of view = 1.4 mm; reflected light; photomicrograph ID# 1184A_069).

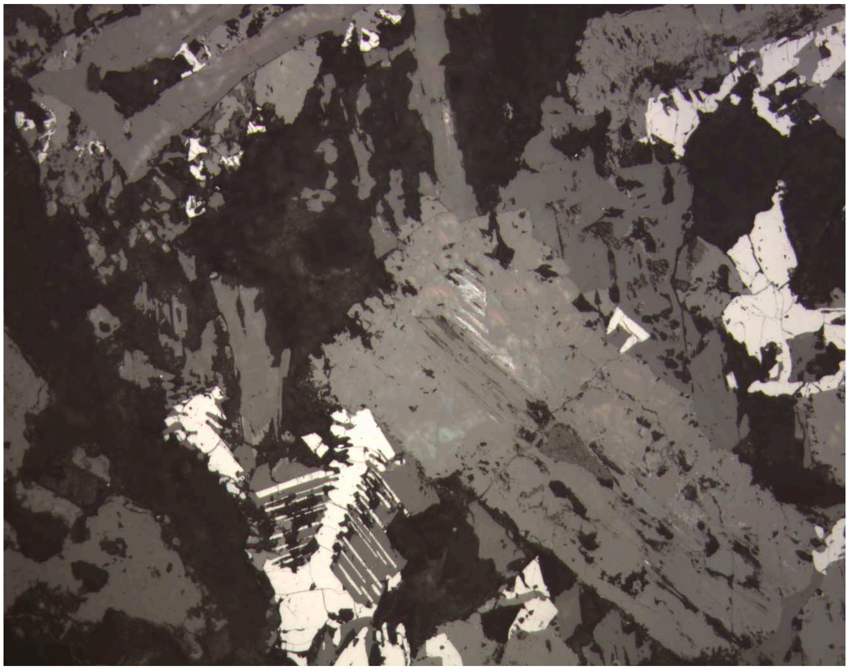

Figure F42. Interval 192-1184A-31R-5, 48–68 cm, showing tuff with concentrated bands of accretionary lapilli.

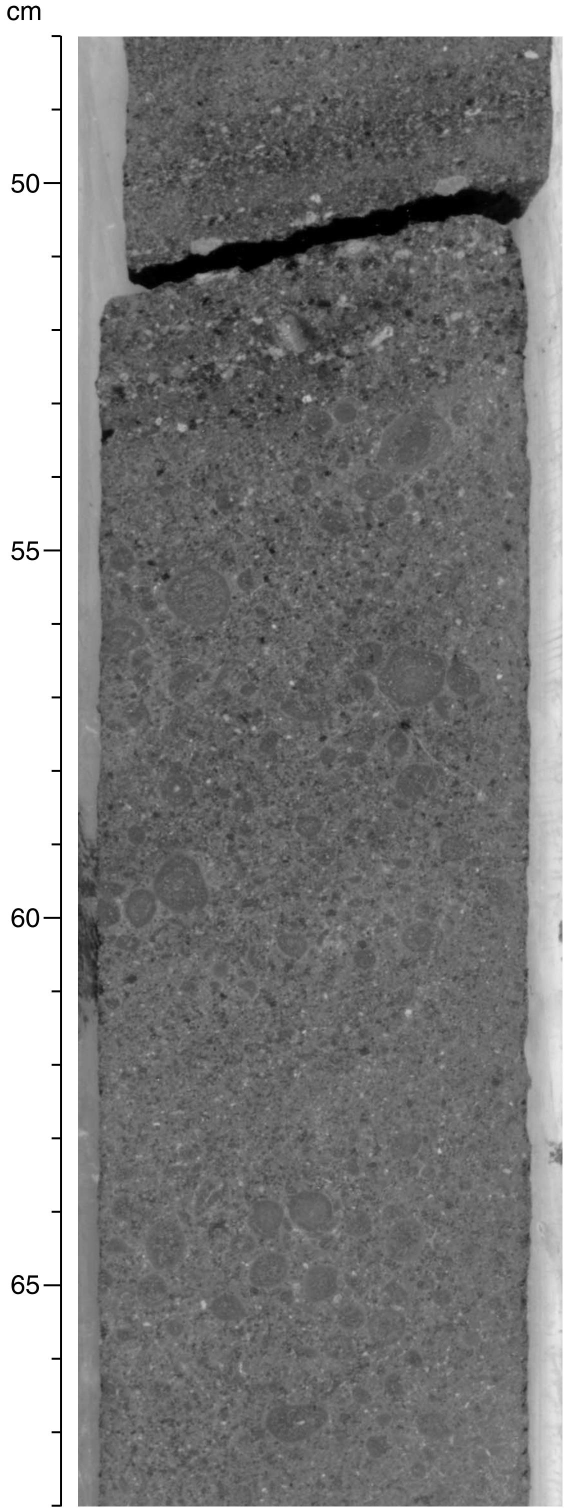

Figure F43. Interval 192-1184A-21R-4, 20–35 cm, showing accretionary lapilli in lapilli tuff.

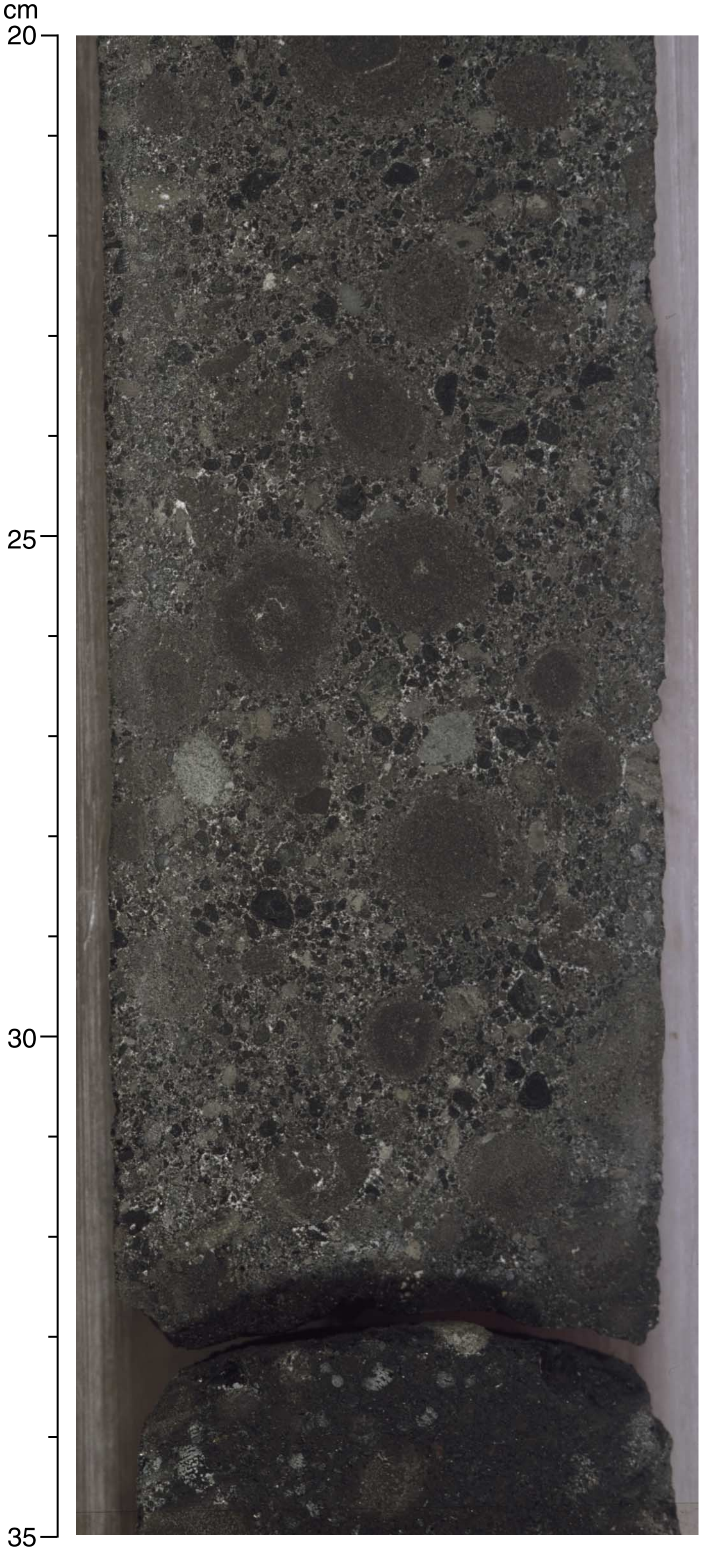

Figure F44. Interval 192-1184A-14R-1, 58–66 cm, showing tuff with whole accretionary and armored lapilli and a bed of fragmented accretionary lapilli.

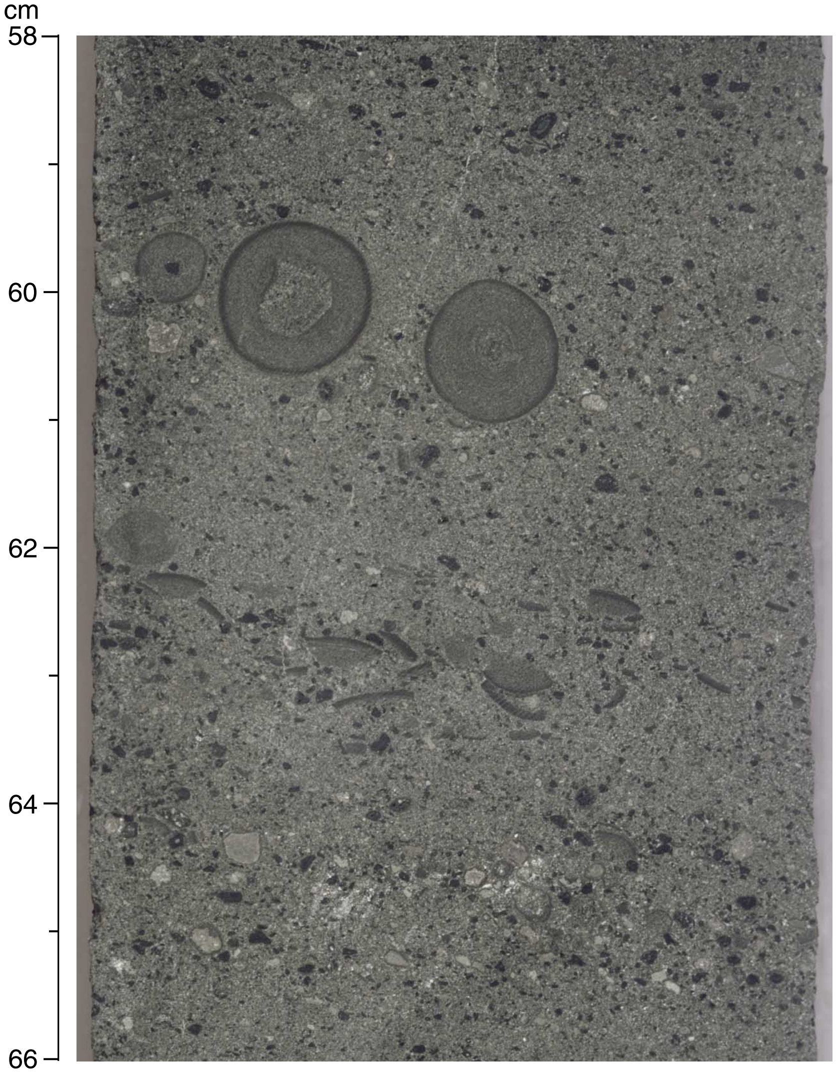

Figure F45. Interval 192-1184A-12R-4, 125–133 cm, showing tuff in which accretionary lapilli fragments have a preferred convex-upward orientation.

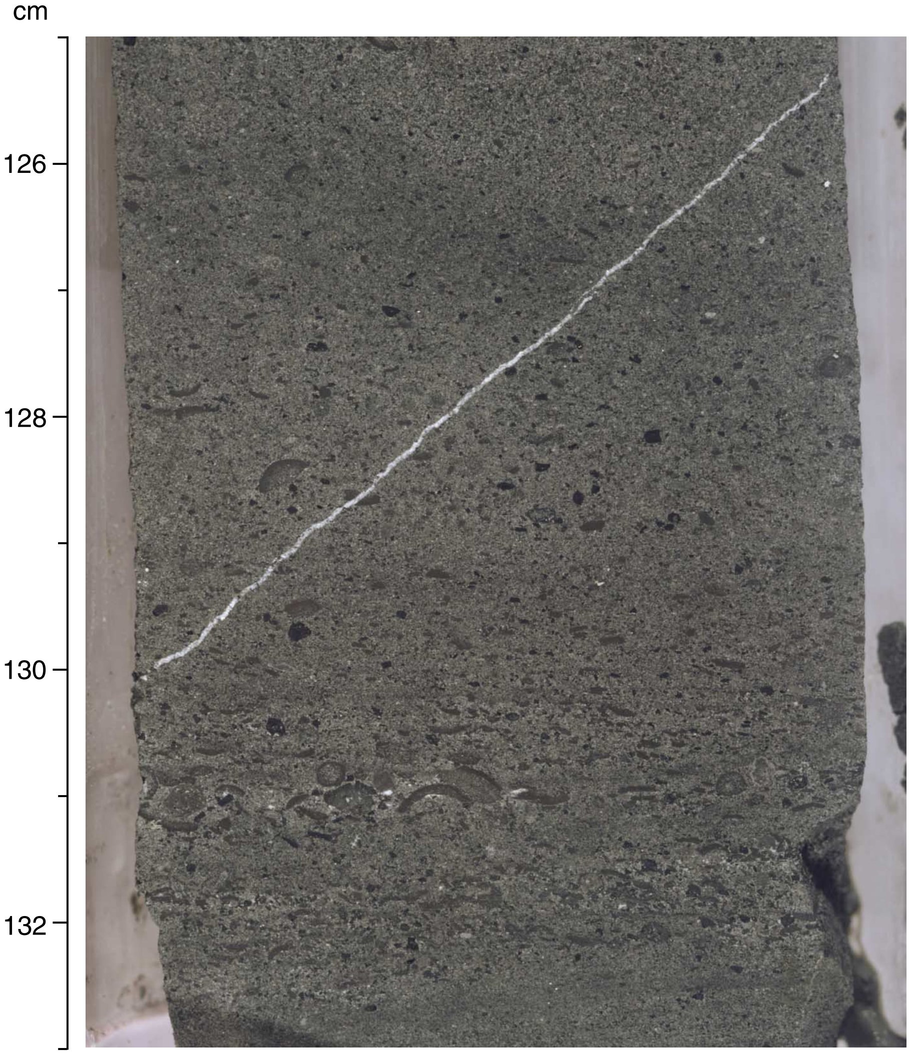

Figure F46. Armored lapillus in Sample 192-1184A-45R-6, 82–85 cm. A fine-grained basaltic fragment is armored by concentric layers of ash in the finer ash matrix of a lithic vitric lapilli tuff. The concentric layers of ash consist of fine glass and crystallites (field of view = 5.5 mm; plane-polarized light; photomicrograph ID# 1184A_094).

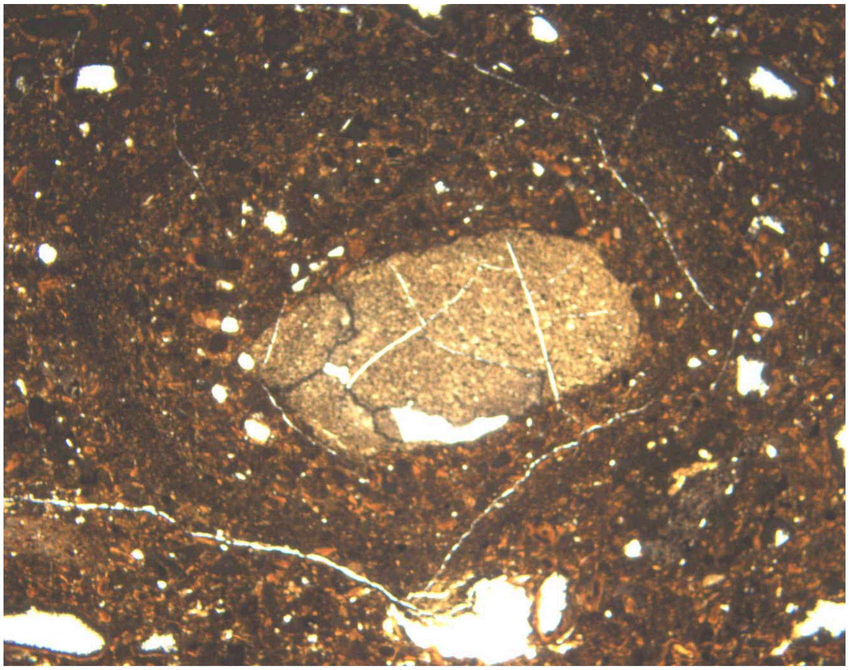

Figure F47. Coarse ash-size altered glass shard armored by very fine grained ash in Sample 192-1184A-40R-3, 37–41 cm (field of view = 1.4 mm; plane-polarized light; photomicrograph ID# 1184A_090).

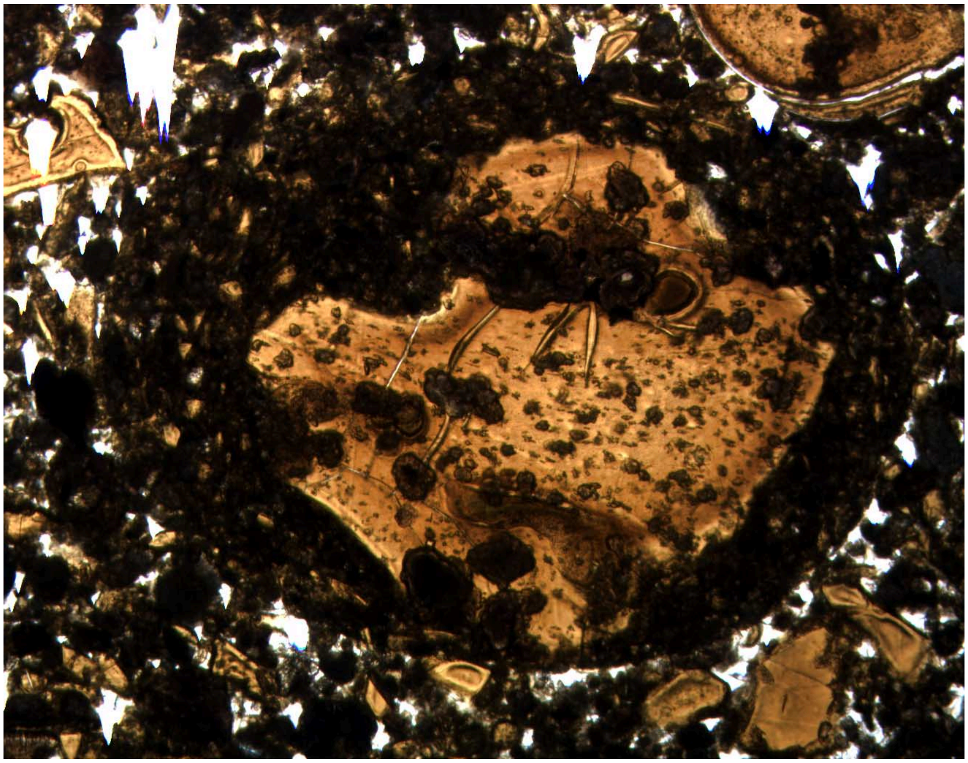

Figure F48. Unaltered glass in the interiors of vitric clasts in Sample 192-1184A-42R-1, 147–150 cm of Subunit IIE. Only a narrow rim of smectite alteration is present at the margins of these clasts (field of view = 2.8 mm; plane-polarized light; photomicrograph ID# 1184A_082).

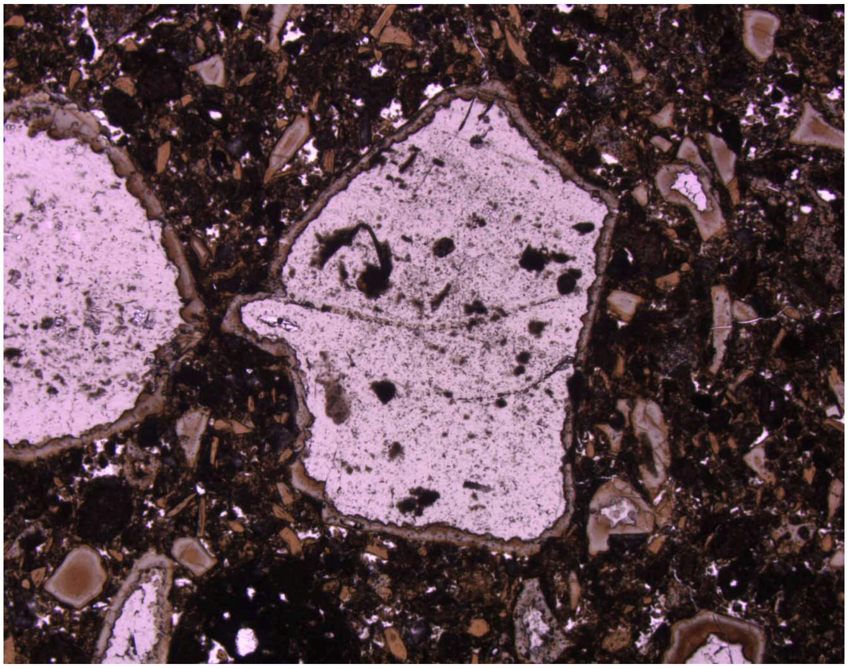

Figure F49. Lithic vitric tuff showing concentric bands of alteration in vitric clasts in Sample 192-1184A-11R-3, 123–125 cm. The glass is palagonitized and/or altered to smectite (field of view = 2.8 mm; plane-polarized light; photomicrograph ID# 1184A_039).

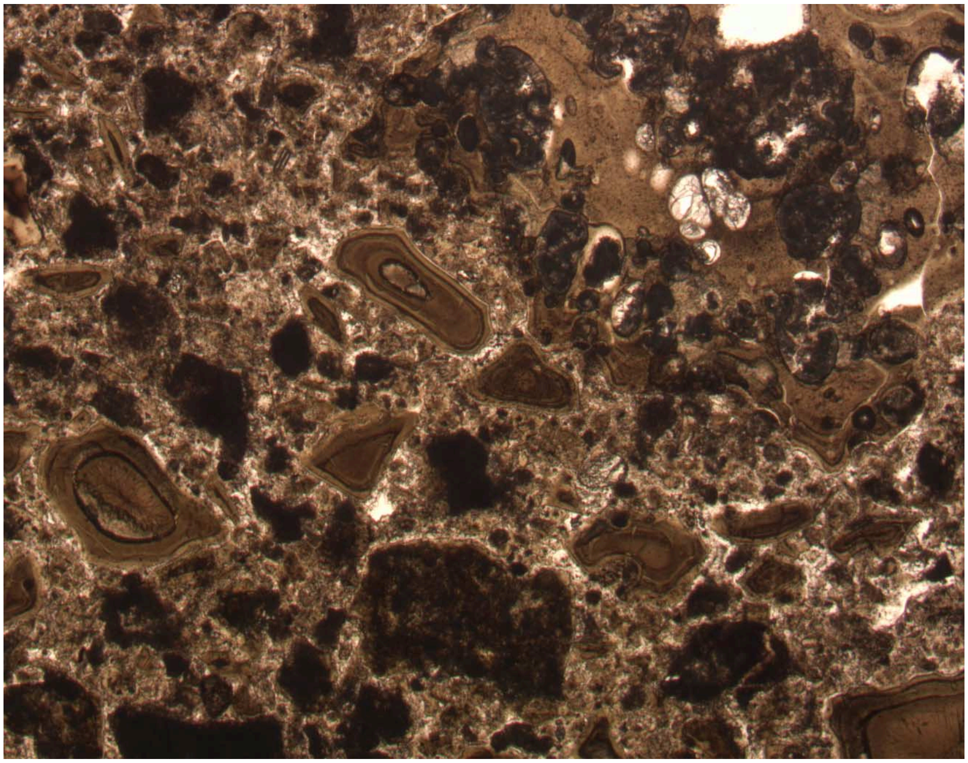

Figure F50. Flow banding in an unaltered glass clast in Sample 192-1184A-42R-1, 147–150 cm. The glass also contains plagioclase and clinopyroxene microlites (field of view = 1.4 mm; plane-polarized light; photomicrograph ID# 1184A_080).

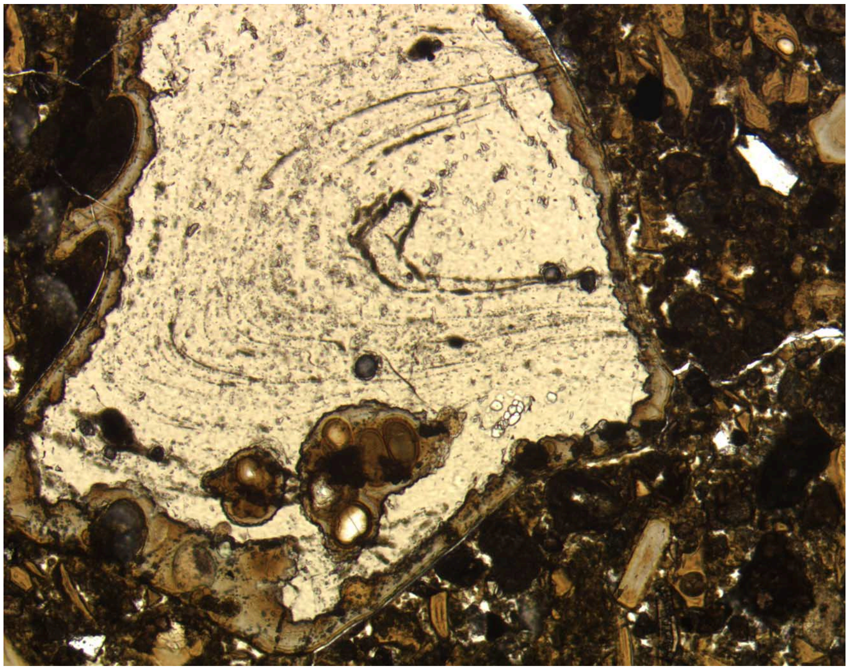

Figure F51. Photomicrograph showing a clast of plagioclase-clinopyroxene-phyric glass in Sample 192-1184A-31R-7, 40–43 cm. The glass is completely altered, but the phenocrysts remain relatively unaltered (field of view = 0.7 mm; plane-polarized light; photomicrograph ID# 1184A_073).

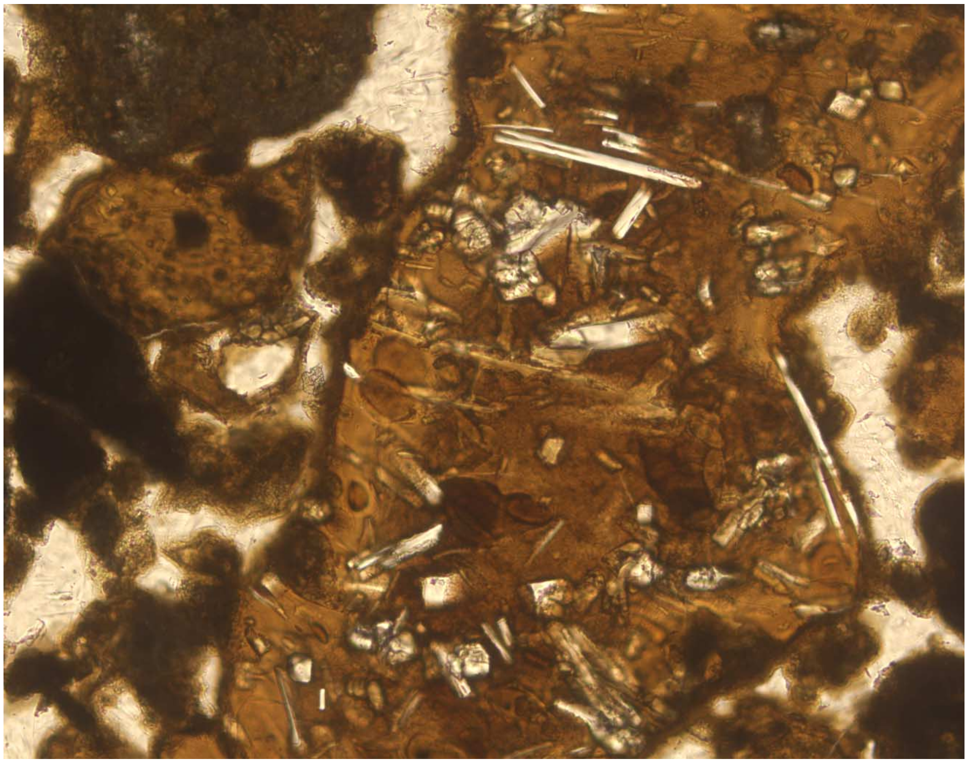

Figure F52. Finely disseminated titanomagnetite in a tachylitic lapillistone in Sample 192-1184A-22R-CC, 9–13 cm (field of view = 0.7 mm; reflected light; photomicrograph ID# 1184A_072).

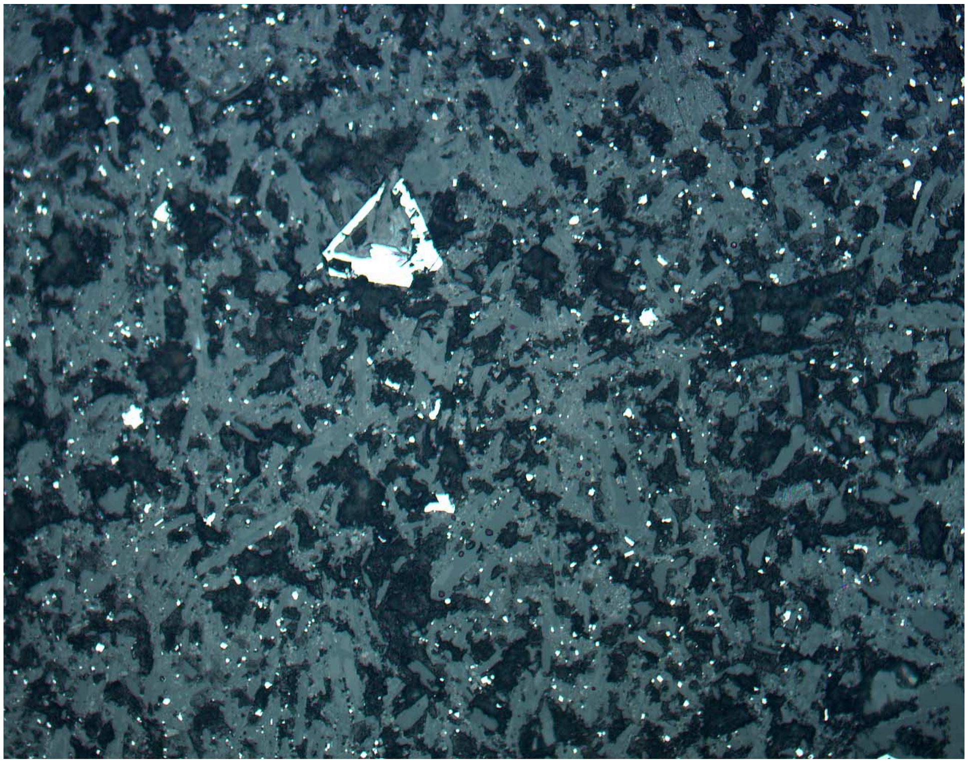

Figure F53. Tachylite with plagioclase microlites defining a subtrachytic texture between and around the clasts in Sample 192-1184A-22R-CC, 9–13 cm (field of view = 2.8 mm; plane-polarized light; photomicrograph ID# 1184A_074).

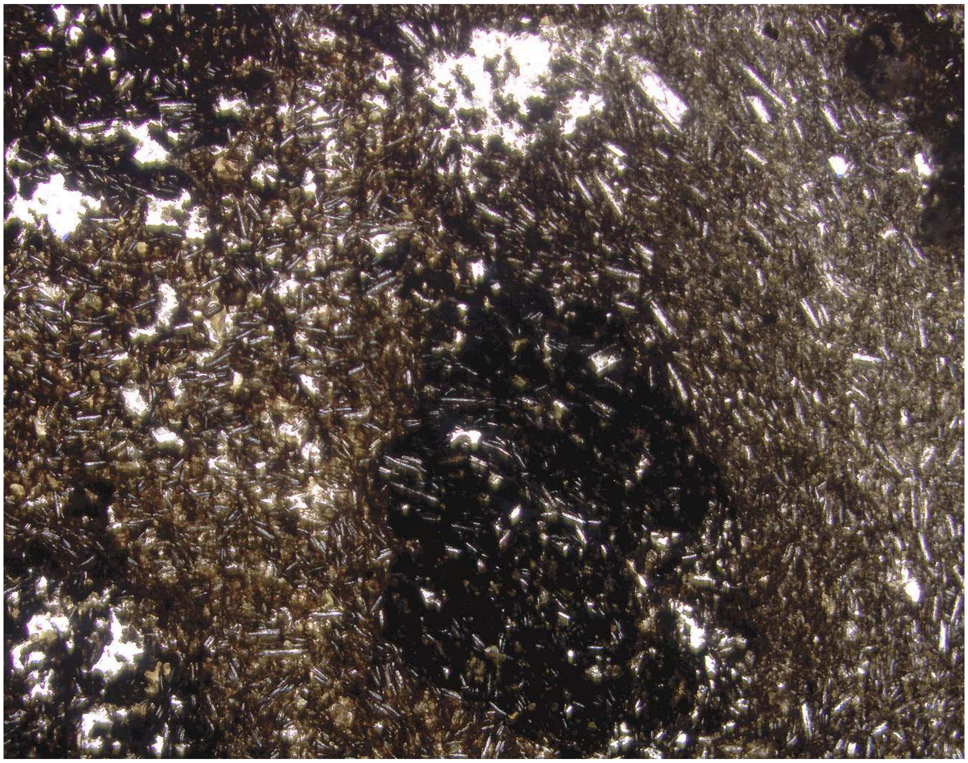

Figure F54. Plagioclase microlites defining a trachytic texture in tachylite clasts in Sample 192-1184A-22R-CC, 9–13 cm (field of view = 2.8 mm; plane-polarized light; photomicrograph ID# 1184A_077).

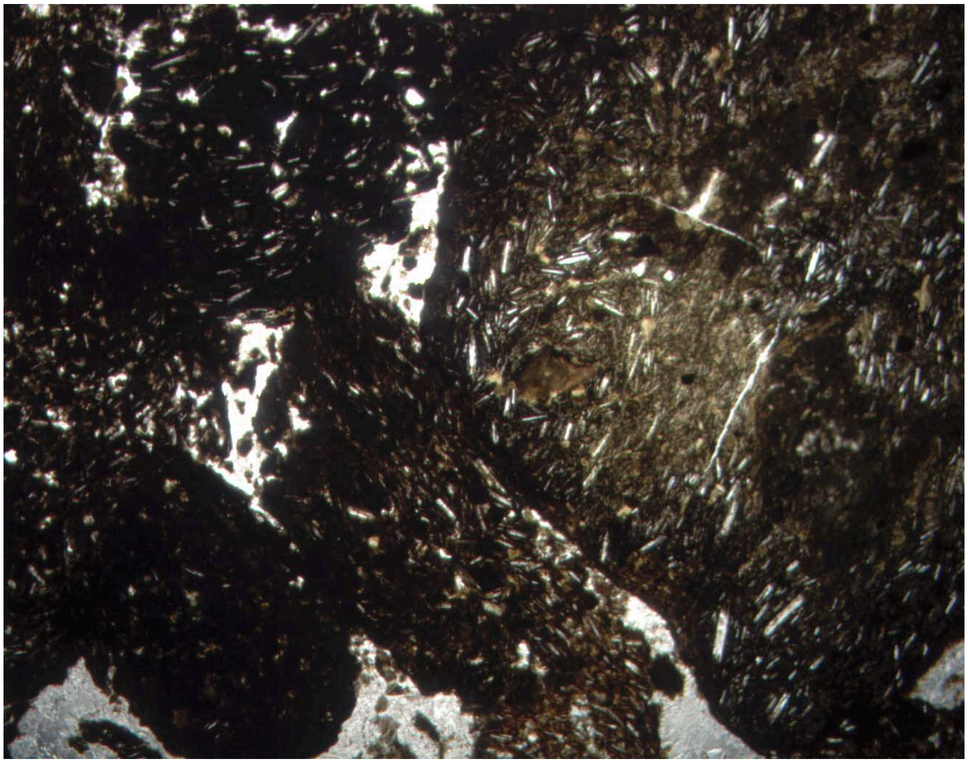

Figure F55. Total alkalies vs. silica diagram (after Le Bas et al., 1986) illustrating the tholeiitic and (apparently) alkalic compositions of samples of fine-grained lithic and vitric tuff from Site 1184. The high-alkali samples are from above Core 192-1184A-39R, whereas the low-alkali samples are from below this interval, where unaltered glass is generally present. The dashed line separates Hawaiian tholeiitic and alkalic lavas (Macdonald and Katsura, 1964).

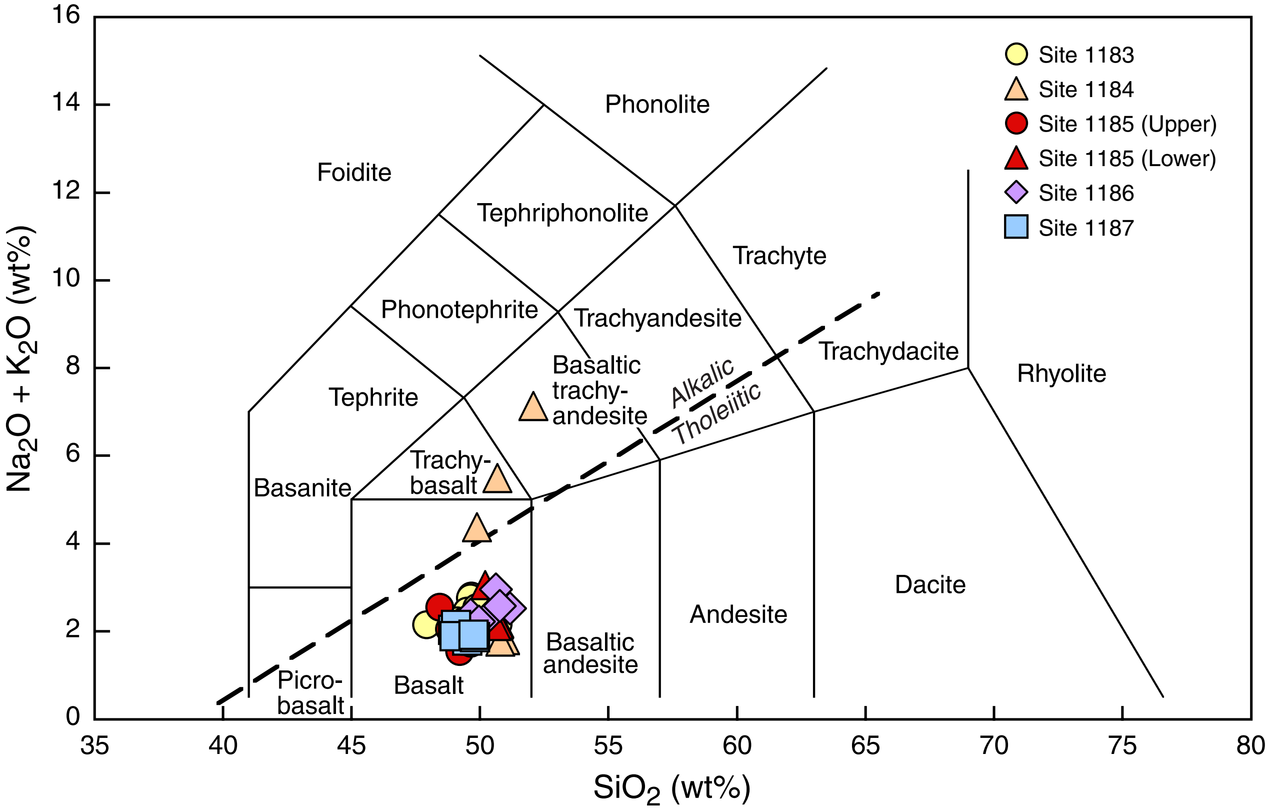

Figure F56. Zr vs. TiO_2, showing that five Site 1184 samples have compositions similar to the basalt of Units C–G at Site 807 (Mahoney et al., 1993), to the basalt flows of the Kwaimbaita Formation on Malaita (Tejada et al., in press), and to basalt units at Sites 1183, 1185 (lower group), and 1186. One sample is similar in composition to the basalt of Site 803, Unit A at Site 807, and the Singgalo Formation on Malaita.

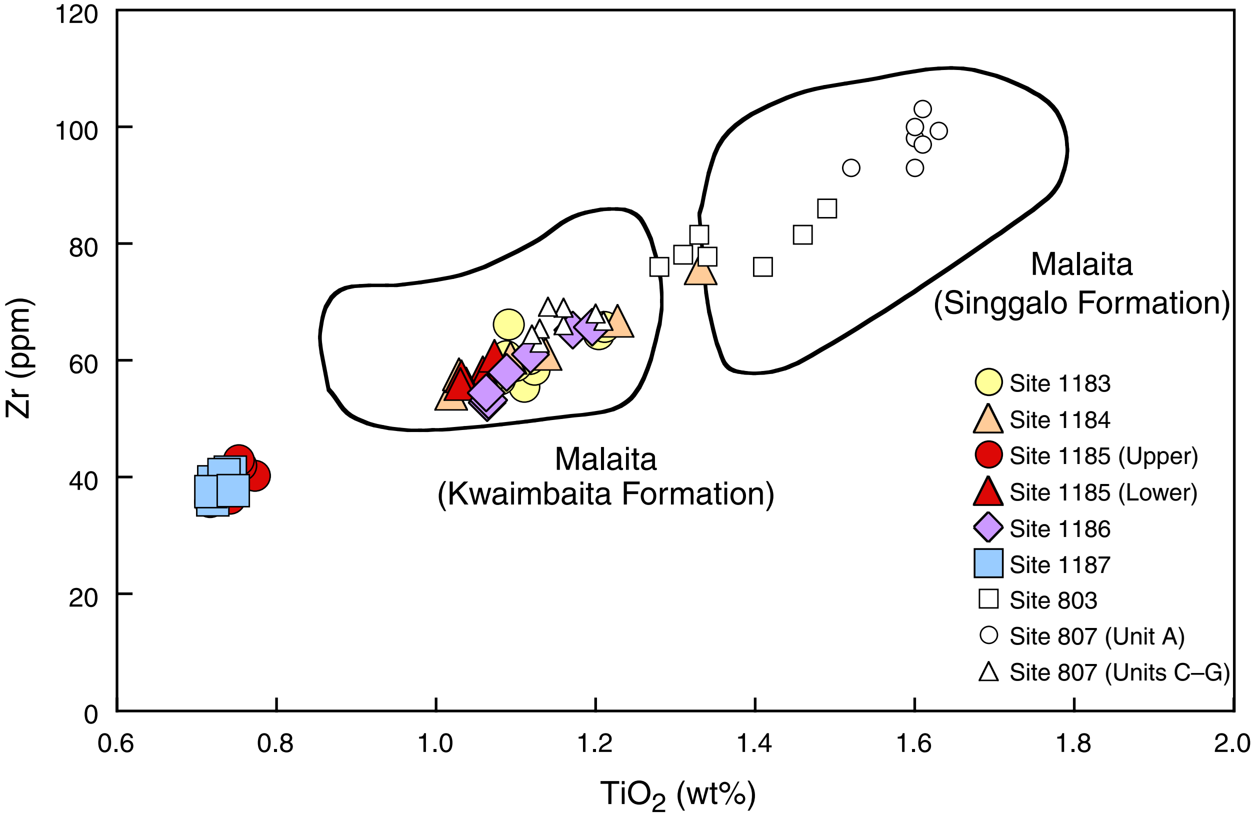

Figure F57. TiO_2 vs. Mg#, showing the similarity between the major element compositions of four of the Site 1184 samples, the basalt of Units C–G at Site 807 (Mahoney et al., 1993), and the basalt flows of the Kwaimbaita Formation on Malaita (Tejada et al., in press). Two samples are similar to the basalt from Site 803, Unit A at Site 807, and/or the Singgalo Formation on Malaita. Mg# is calculated assuming that 12% of the iron is Fe^{3+}, which is equivalent to $Fe_2O_3/(Fe_2O_3+FeO) = 0.13$, or $(Fe_2O_3/FeO = 0.15)$.

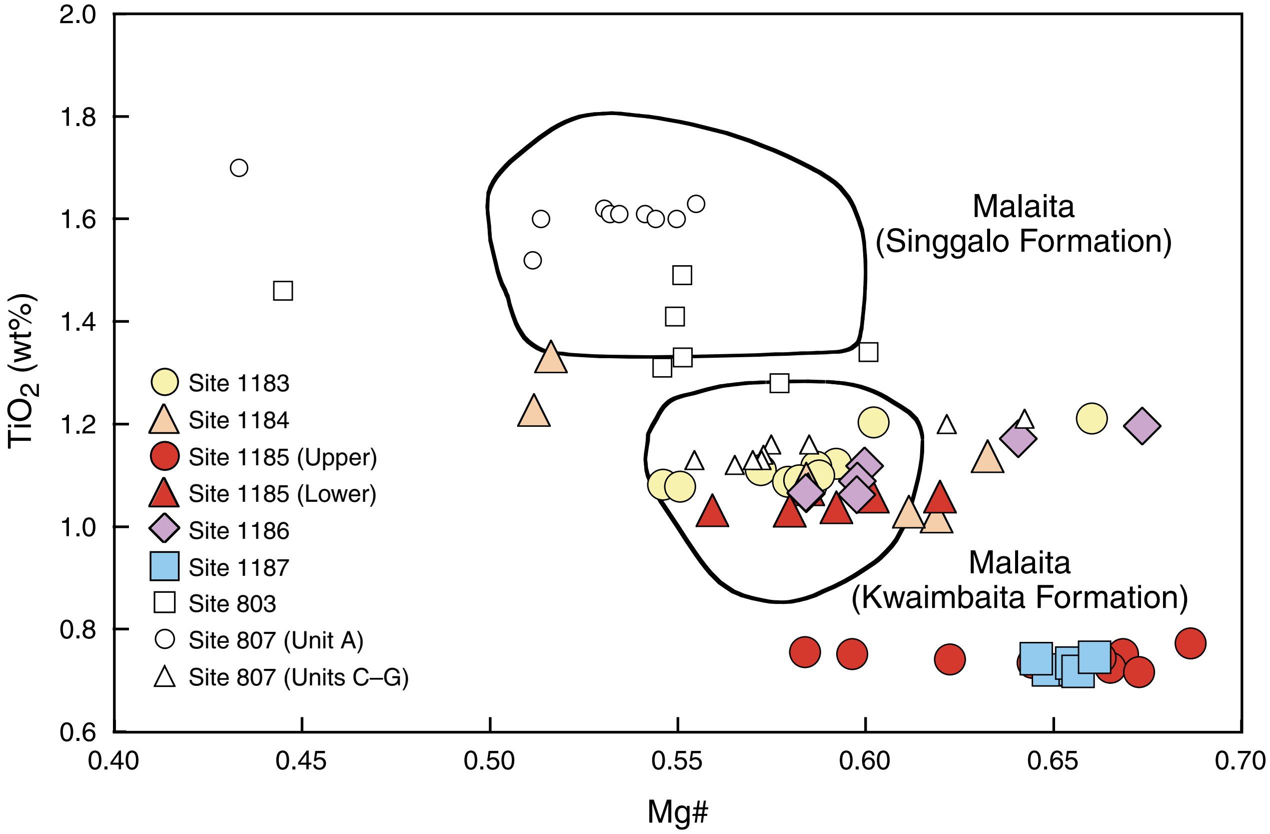

Figure F58. Cr vs. TiO_2, showing the elevated Cr abundances of the samples from the lower part of the cored section at Hole 1184A (three samples with ~300 ppm Cr) compared to those from the upper part. Data for basalt units from Sites 803, 807 (Mahoney et al., 1993), 1183, 1185, 1186, and 1187, and data fields for the Kwaimbaita and Singgalo Formations on Malaita (Tejada et al., in press) are also shown.

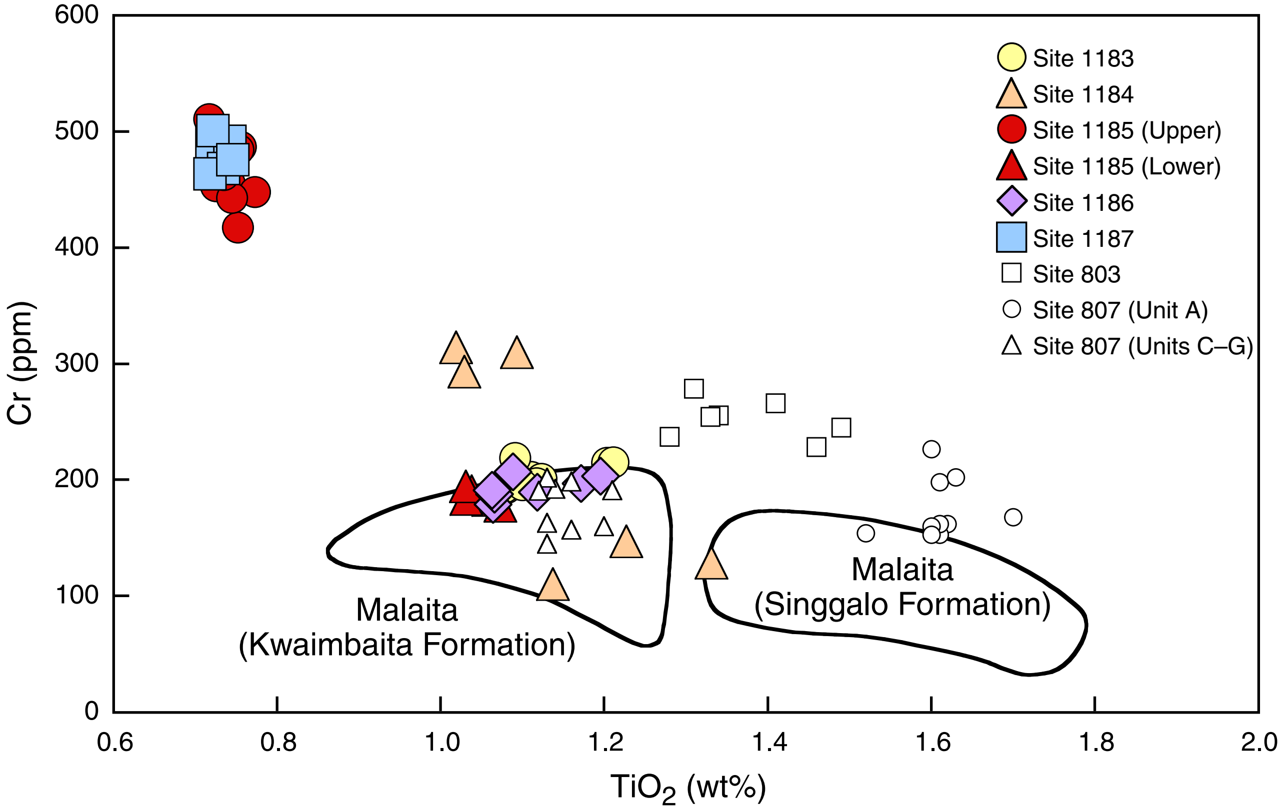

Figure F59. Glass fragments replaced by concentrically zoned smectite in Sample 192-1184A-11R-3, 123–125 cm (field of view = 2.8 mm; crossed polars; photomicrograph ID# 1184A_065).

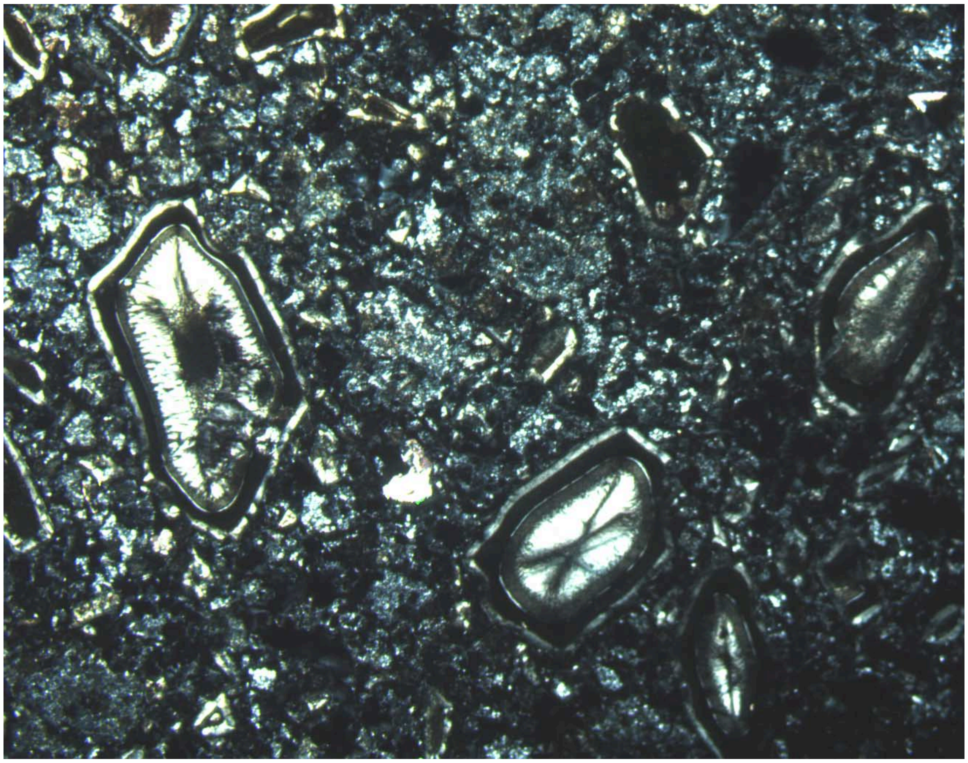

Figure F60. Altered glass fragment replaced by intricately zoned smectite at the rim and zeolite in the center in Sample 192-1184A-42R-1, 147–150 cm (field of view = 2.8 mm; photomicrograph ID#s 1184A_091 and 1184A_092). **A.** Plane-polarized light. **B.** Crossed polars.

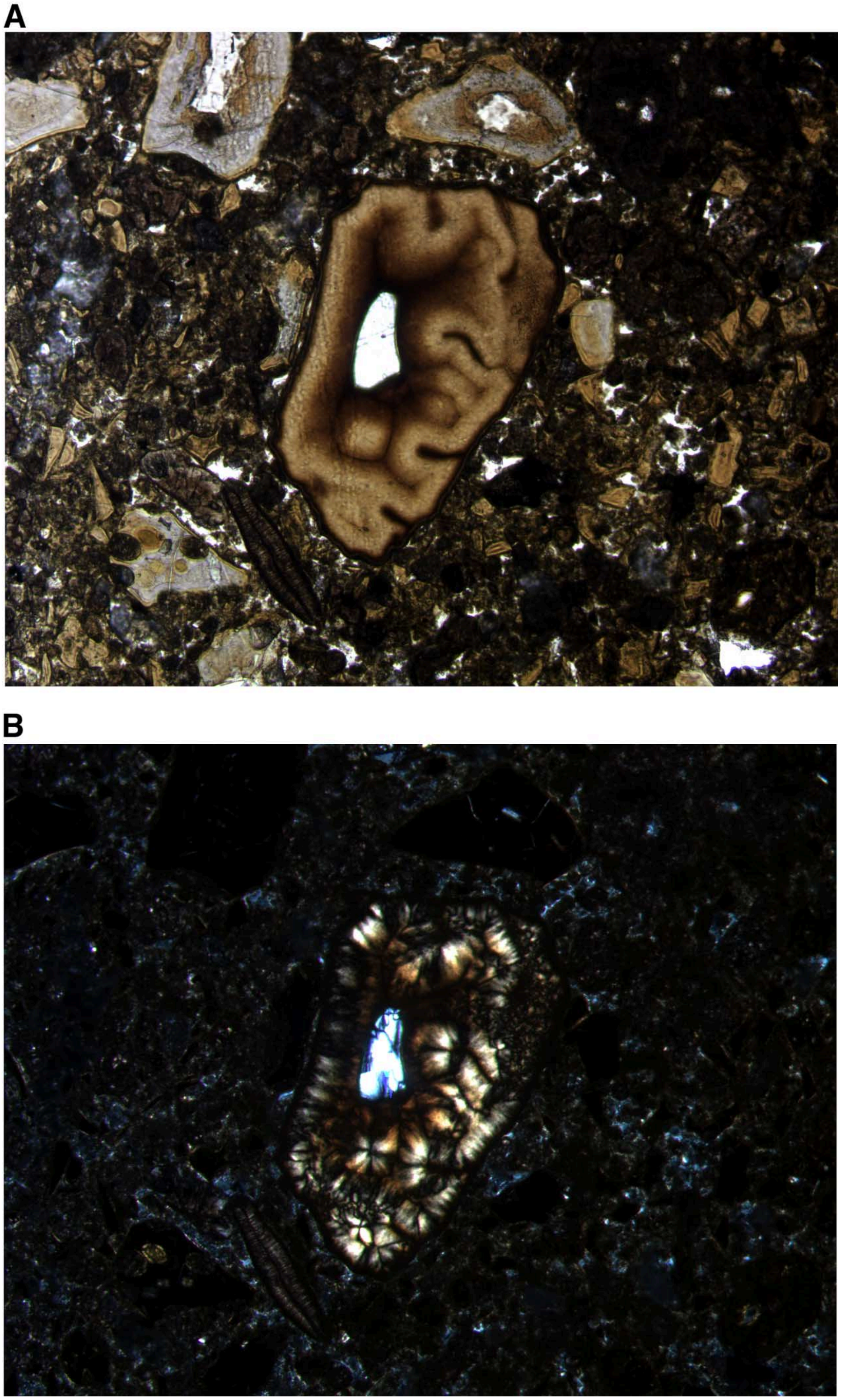

Figure F61. Altered glass fragment replaced by brown smectite at the rim and zeolite in the center in Sample 192-1184A-16R-CC, 7–10 cm (field of view = 2.8 mm; photomicrograph ID#s 1184A_062 and 1184A_061). **A.** Plane-polarized light. **B.** Crossed polars.

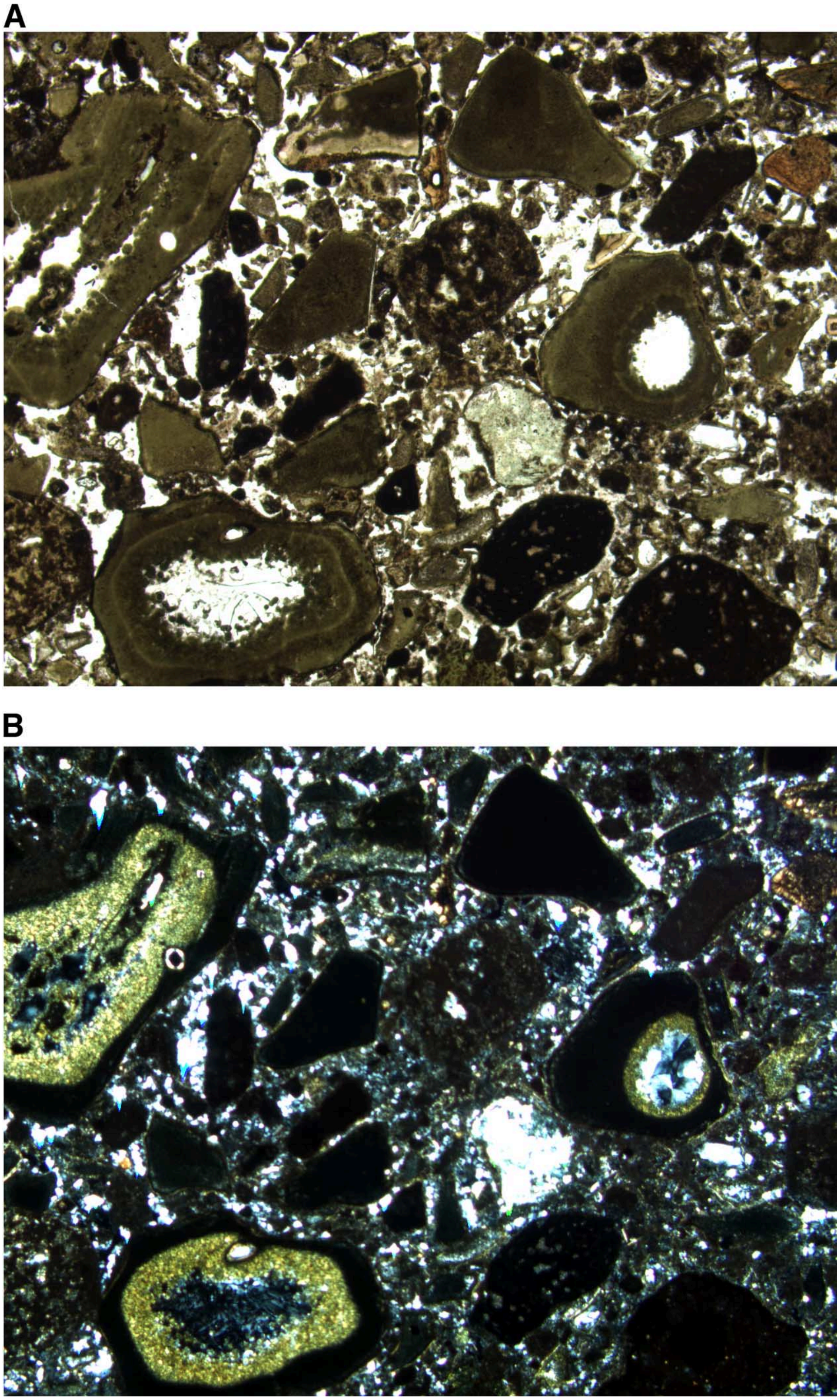

Figure F62. Complexly zoned, altered glass fragment rimmed by brown smectite with zeolite in the center in Sample 192-1184A-16R-CC, 7–10 cm. Smectite at the interface with zeolite shows a bulbous habit (field of view = 1.4 mm; plane-polarized light; photomicrograph ID# 1184A_093).

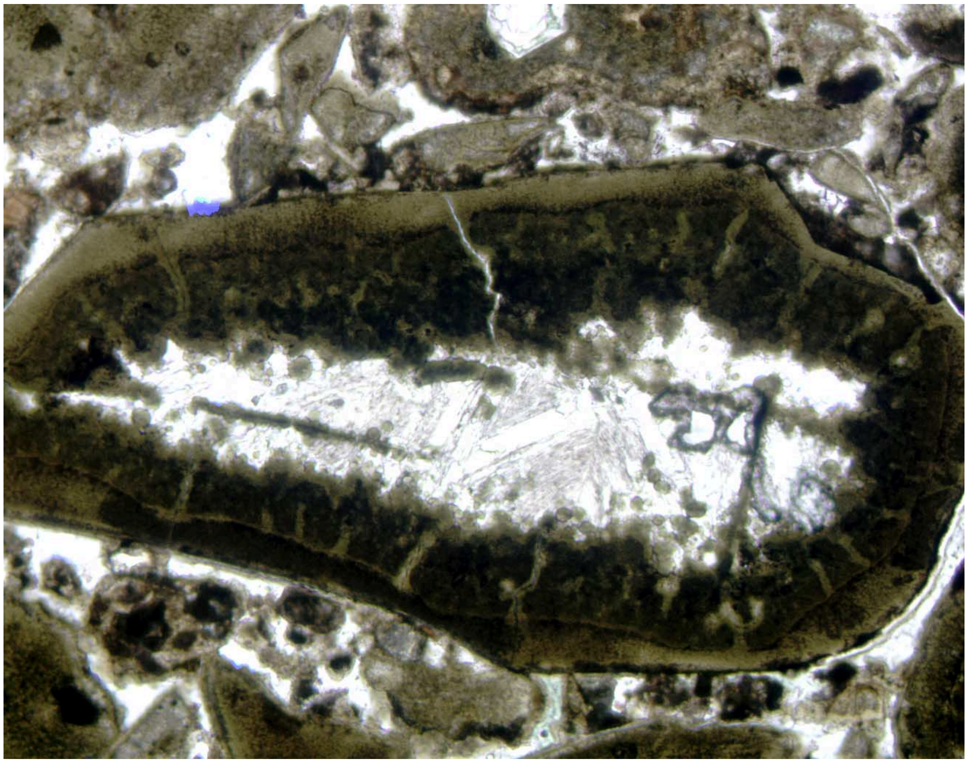

Figure F63. Altered glass shard replaced by brown smectite with an inner rim of celadonite in Sample 192-1184A-16R-CC, 7–10 cm (field of view = 2.8 mm; plane-polarized light; photomicrograph ID# 1184A_060).

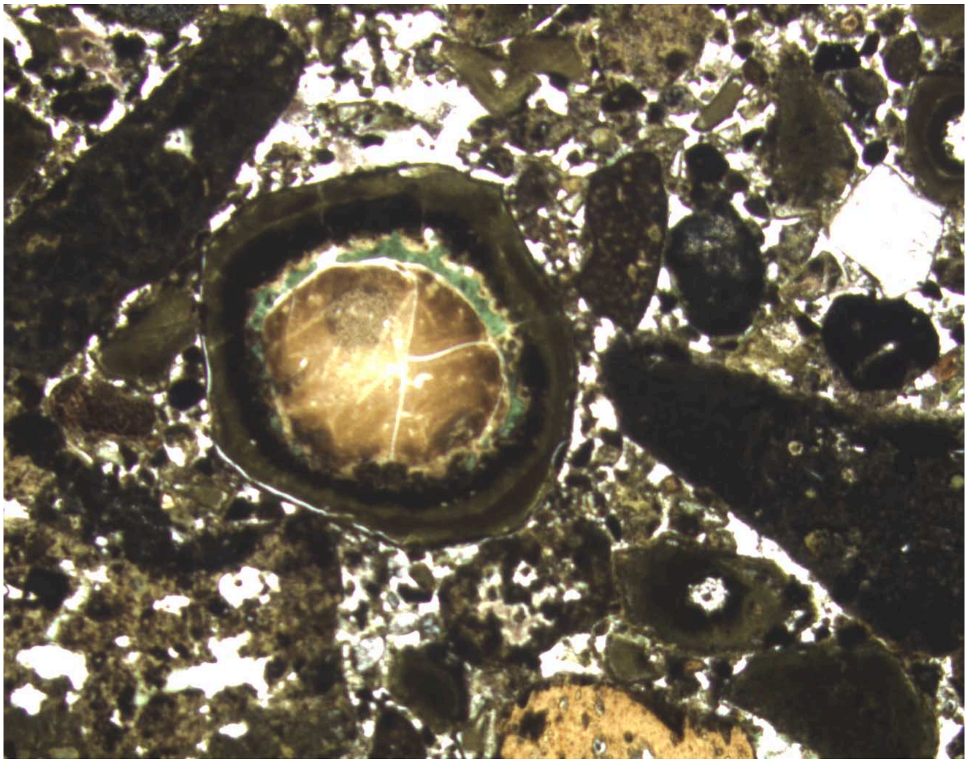

Figure F64. Altered glass fragments replaced by brownish smectite at the rims and greenish celadonite in the centers in Sample 192-1184A-21R-2, 92–94 cm (field of view = 2.8 mm; plane-polarized light; photomicrograph ID# 1184A_147).

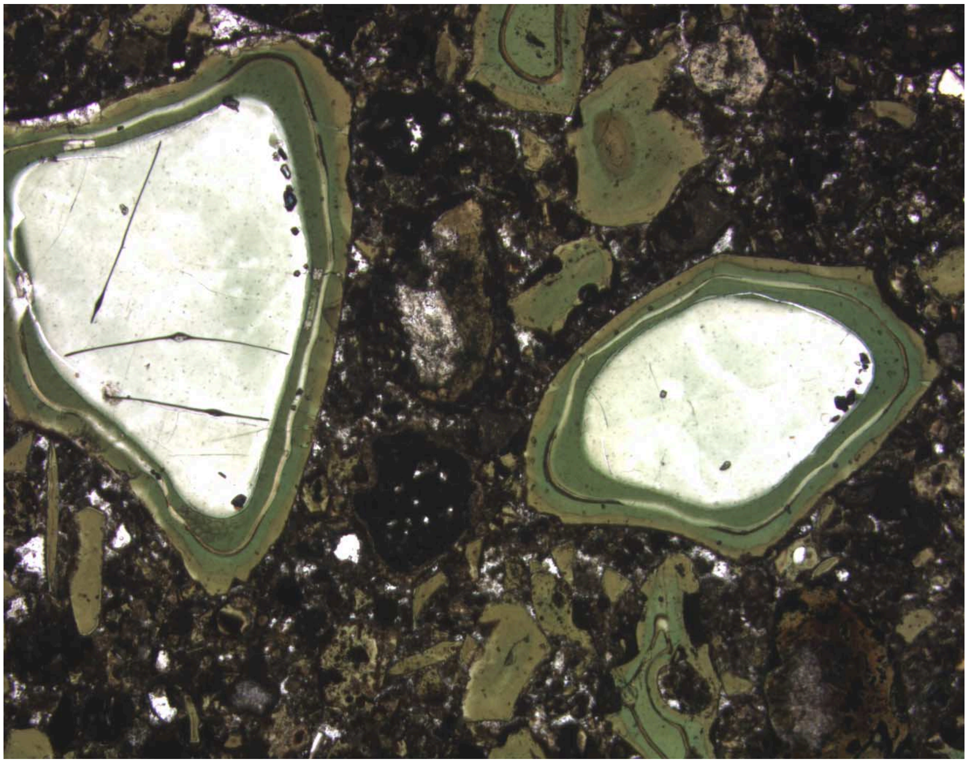

Figure F65. A portion of a highly vesicular altered glass fragment almost completely replaced by greenish celadonite in Sample **192-1184A-21R-2, 92–94 cm.** Minor brownish smectite and colorless zeolite also replace the glass and fill the vesicles (field of view = 2.8 mm; plane-polarized light; photomicrograph ID# 1184A_148).

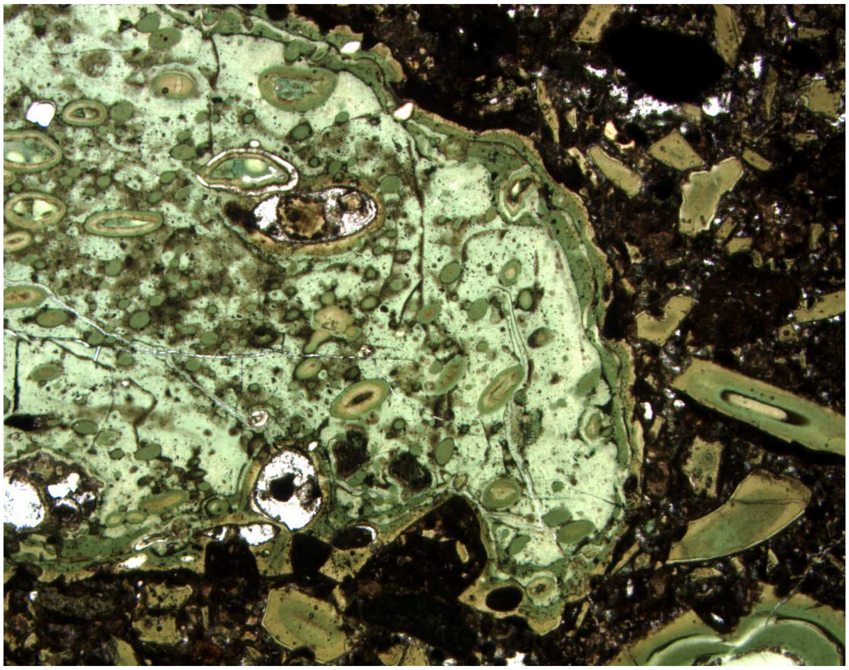

Figure F66. Liesegang rings developed in celadonite spheres, along with fine-grained celadonite filling a vesicle in a glass fragment in Sample 192-1184A-21R-2, 92–94 cm (field of view = 0.28 mm; plane-polarized light; photomicrograph ID# 1184A_146).

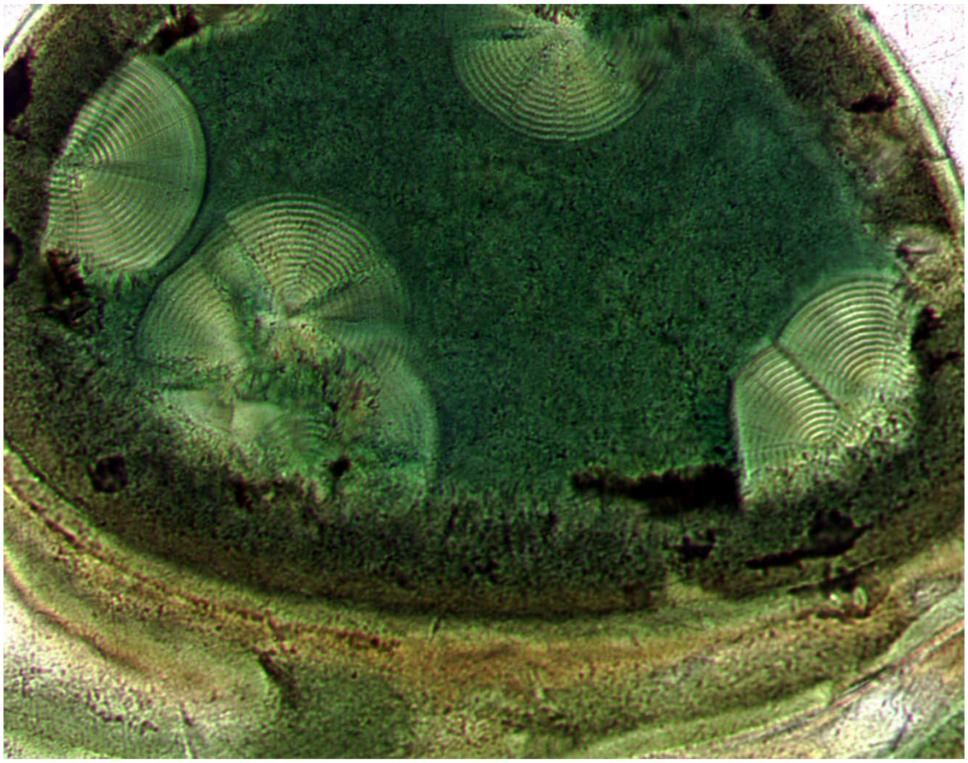

Figure F67. Altered glass fragment rimmed by two generations of smectite in Sample 192-1184A-42R-1, 147–150 cm. The outer rim of smectite mimics the outline of the glass clast and formed by replacement of the outer margin. The inner rim displays fibro-radial habit and formed later as the glass continued to be altered inward (field of view = 1.4 mm; photomicrograph ID#s 1184A_087 and 1184A_086). **A.** Plane-polarized light. **B.** Crossed polars; outer smectite rim has orange-brown polarization colors.

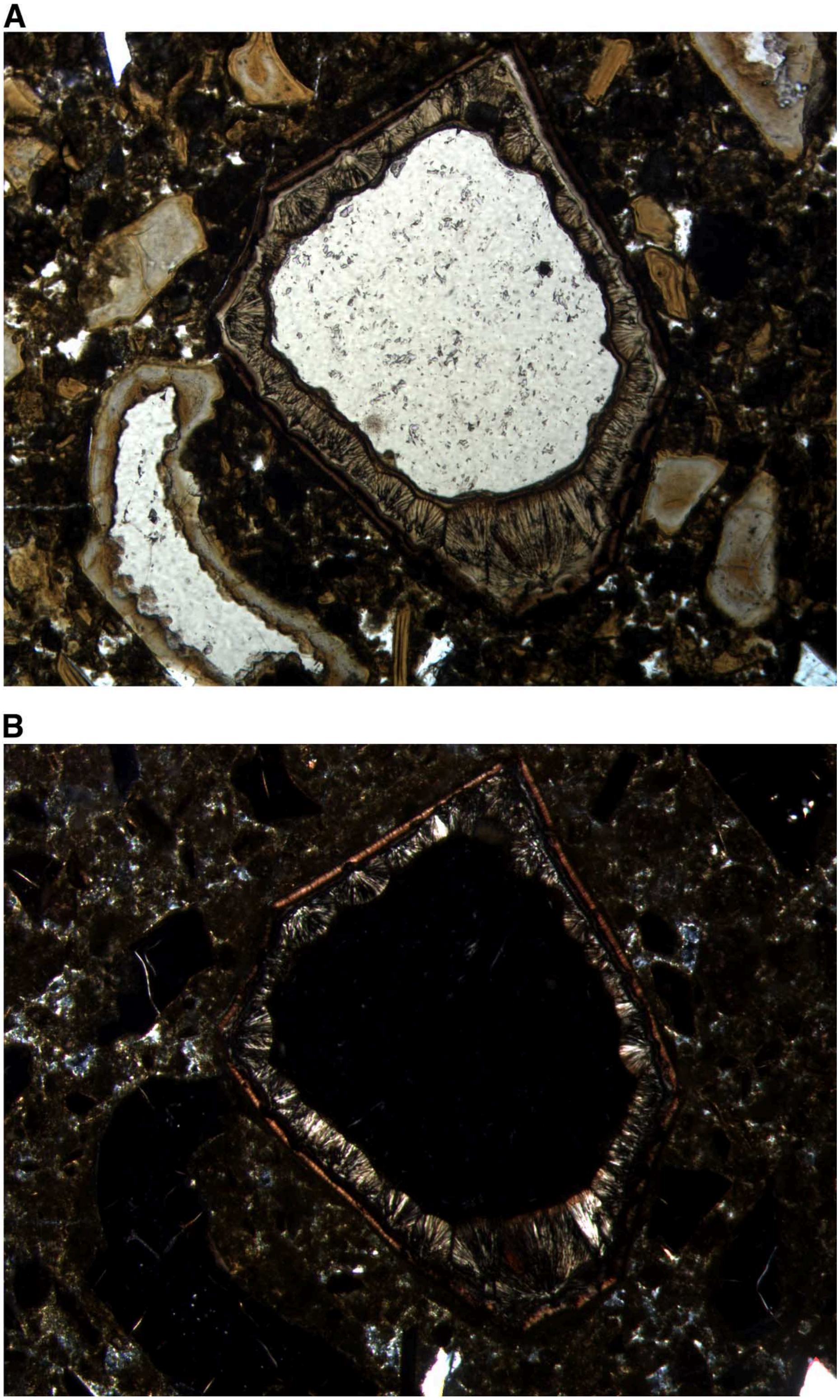

Figure F68. A. Partially altered glass fragment rimmed by brown smectite with larger vesicle (left) filled by brown smectite and smaller empty vesicle (right) in Sample 192-1184A-45R-6, 82–85 cm. The interfaces between smectite and fresh glass are characterized by "hairy" brown channels filled with smectite that possibly formed by microbially mediated alteration of the glass (field of view = 1.4 mm; plane-polarized light; photomicrograph ID# 1184A_152). **B.** High magnification photomicrograph of glass fragment shown in (A) (upper center portion) showing two distinct types of possible microbially mediated alteration features. String-of-pearls channels (center left) are characterized by spherical cavities joined by thin channels, whereas smooth-walled, gently curved channels (right) appear to be generally free of clay minerals and are possibly still open (Sample 192-1184A-45R-6, 82–85 cm; field of view = 0.28 mm; plane-polarized light; photomicrograph ID# 1184A_154).

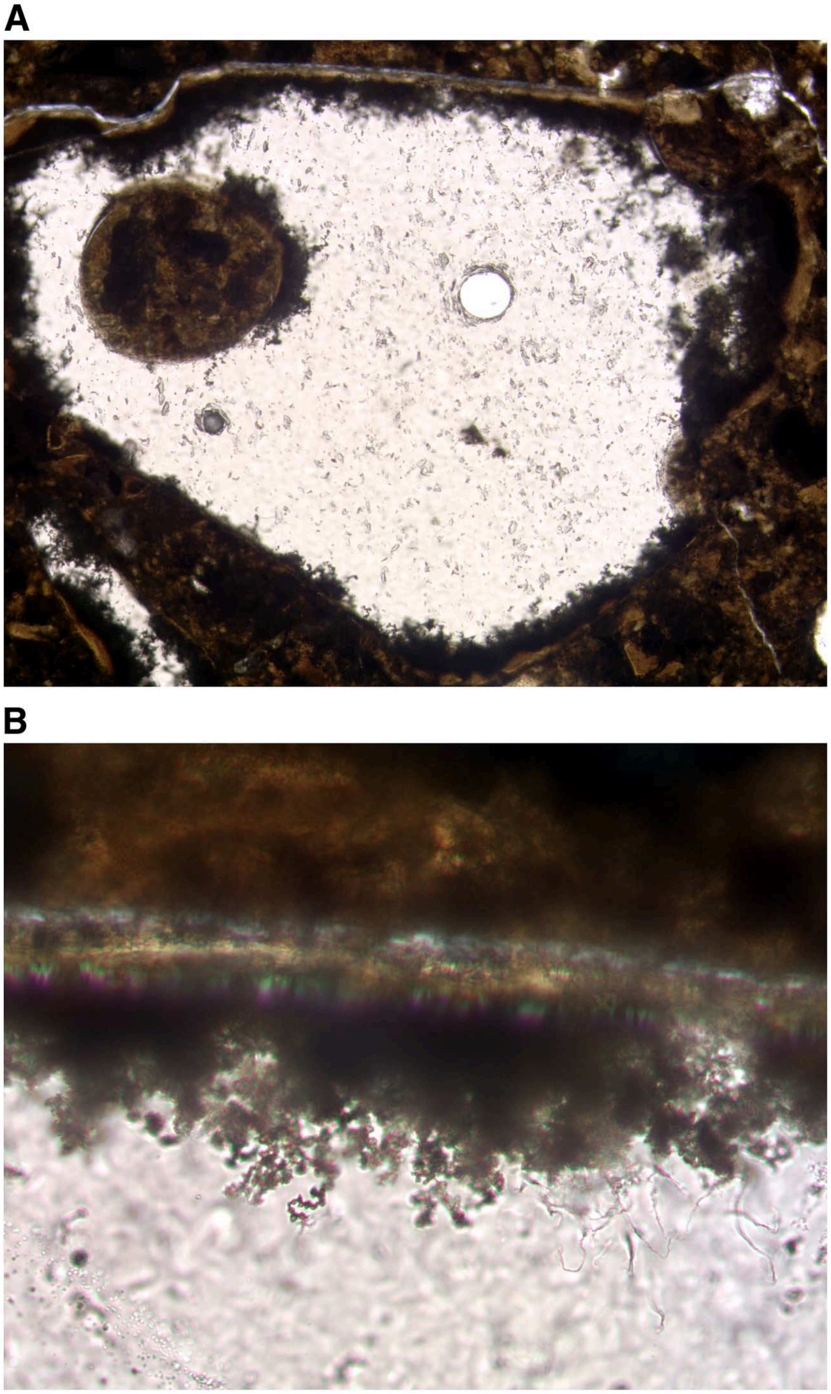

Figure F69. A. Highly vesicular glass fragment in which vesicles are completely filled with brown smectite in Sample 192-1184A-45R-6, 82–85 cm. The glass fragment (lower left) shows "fibril-like" features protruding into the fresh glass from the altered margin, possibly related to microbially mediated alteration (field of view = 2.8 mm; plane-polarized light; photomicrograph ID# 1184A_150). **B.** Close-up of Sample 192-1184A-45R-6, 82–85 cm, showing the highly vesicular glass fragment shown in (A) (field of view = 1.4 mm; plane-polarized light; photomicrograph ID# 1184A_151).

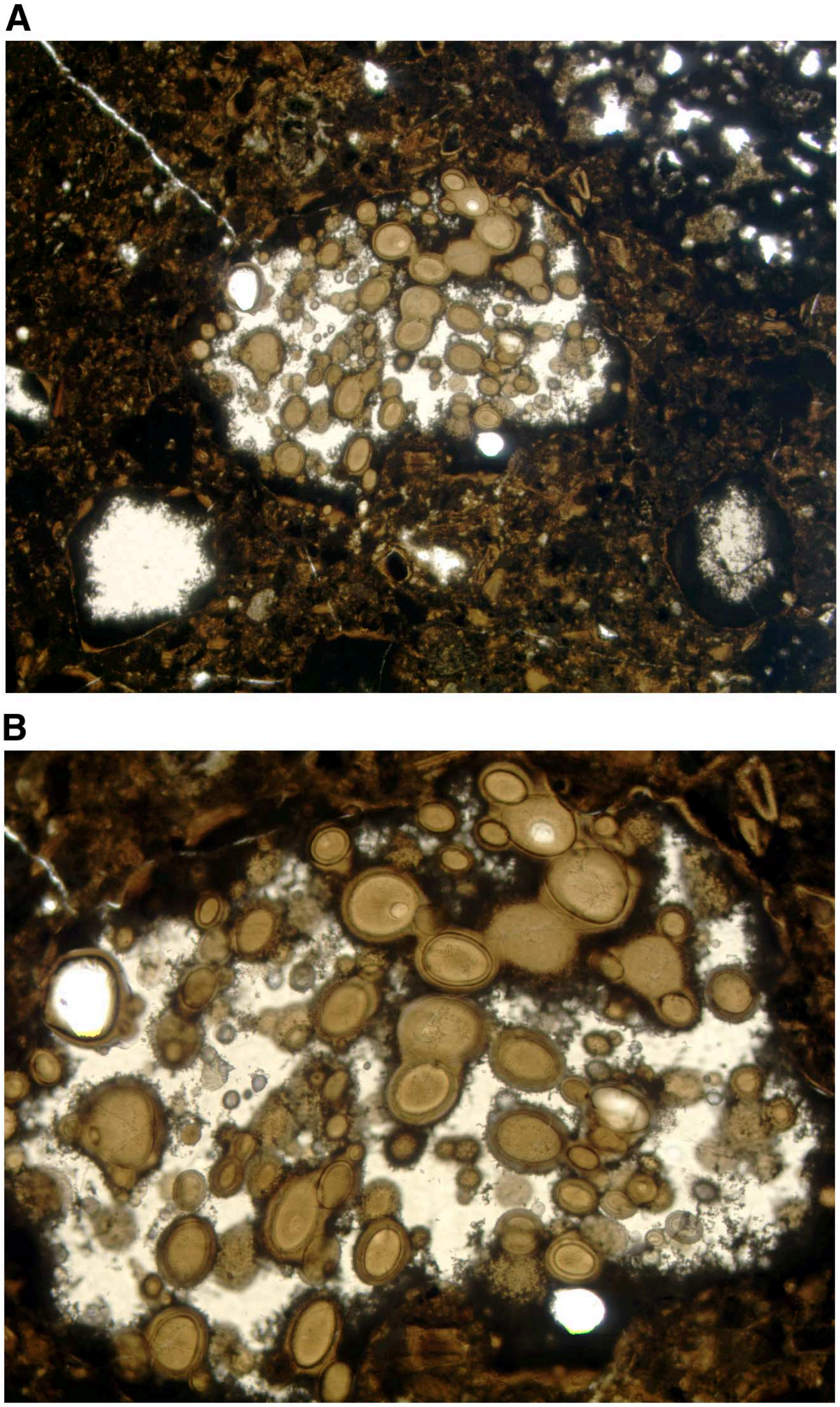

Figure F70. Altered glassy to tachylitic shards cemented by analcime + zeolite + calcite with rare greenish celadonite in the center of the field of view in Sample 192-1184A-16R-CC, 7–10 cm (field of view = 1.4 mm; plane-polarized light; photomicrograph ID# 1184A_64).

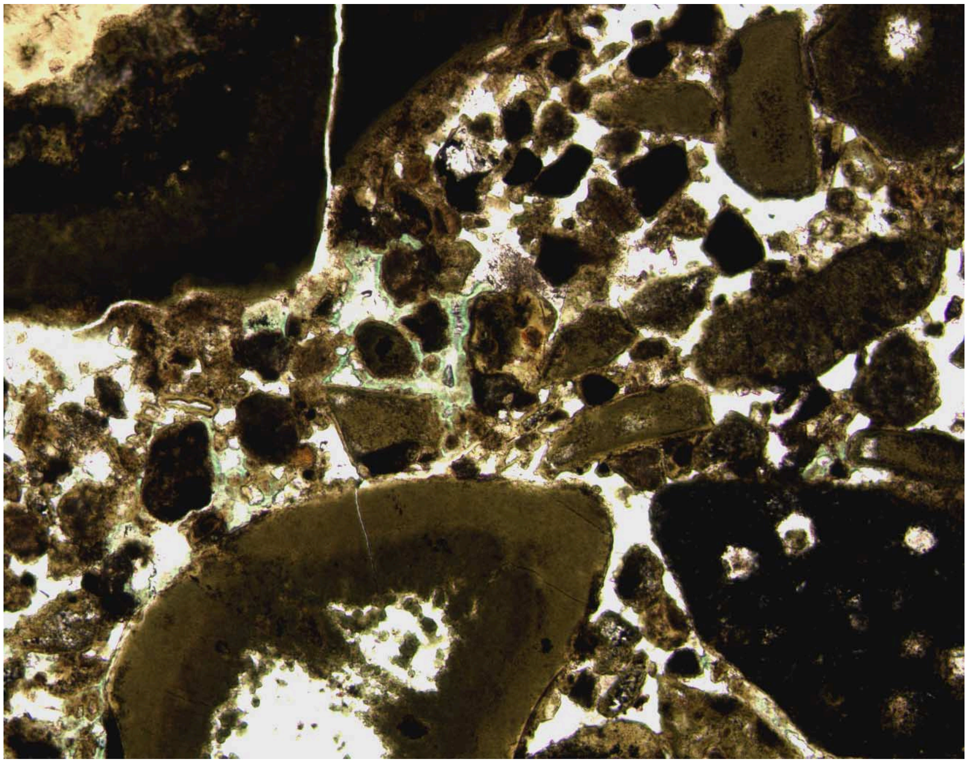

Figure F71. Examples of high-quality Zijderveld diagrams for volcaniclastic rocks. **A.** Thermal cleaning on discrete Sample 192-1184A-31R-4, 135–137 cm. **B.** AF cleaning on archive-half of Section 192-1184A-31R-5 at 110 cm. **C.** Magnetic remanence and susceptibility (measured at room temperature) as a function of heating temperature for Sample 192-1184A-31R-4, 135–137 cm. The drop in magnetic remanence and small increase in susceptibility at ~300°C are consistent with the destruction of maghemite.

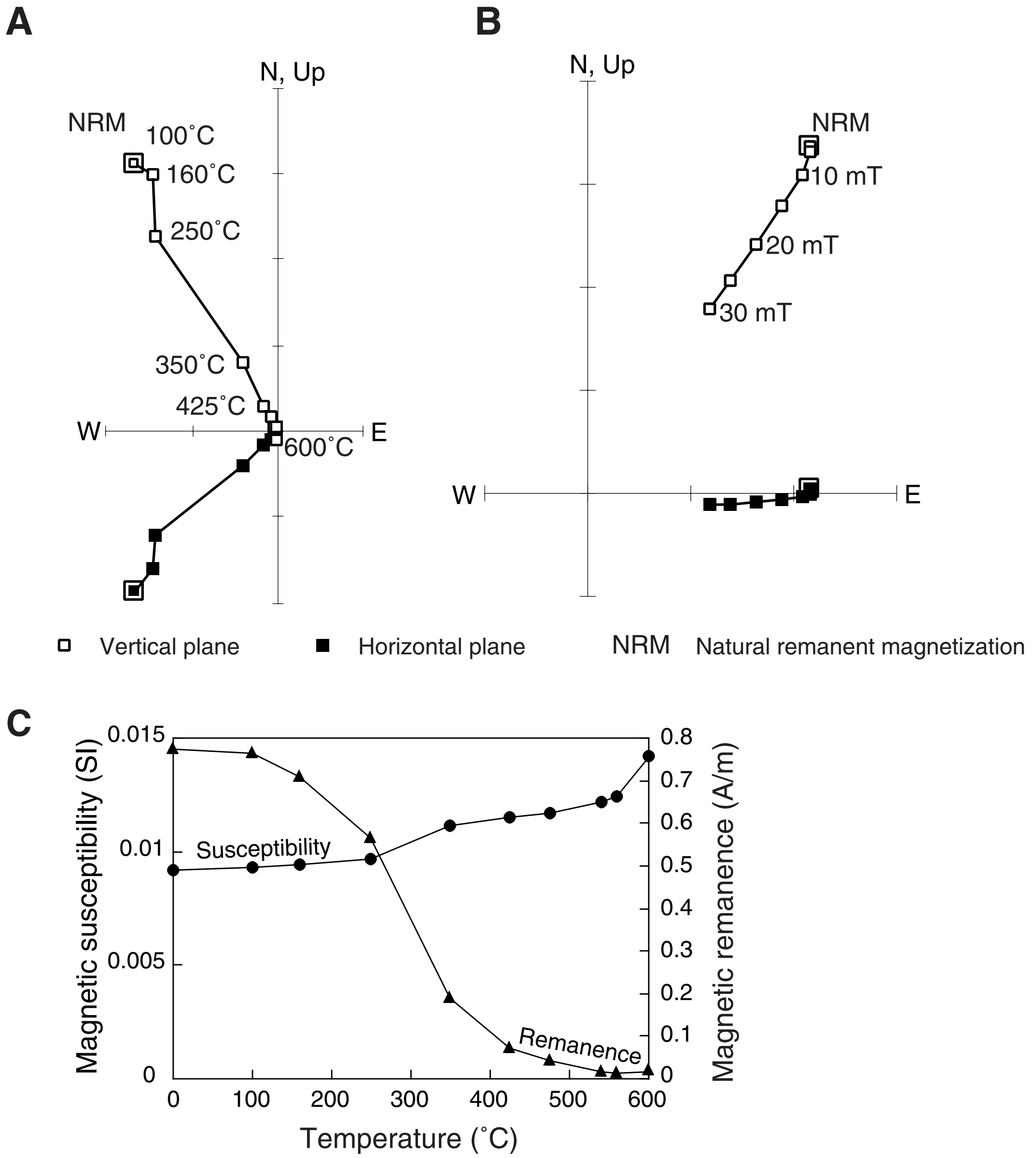

Figure F72. Downhole variation in natural remanent magnetization (NRM) intensity, magnetic susceptibility, Koenigsberger ratio (Q-ratio), and percentage of NRM removed by 20-mT alternating-field demagnetization for the volcaniclastic subunits in Hole 1184A. See **"Rock-Magnetic Properties,"** p. 20, for discussion. See legend in Figure **F10**, p. 38.

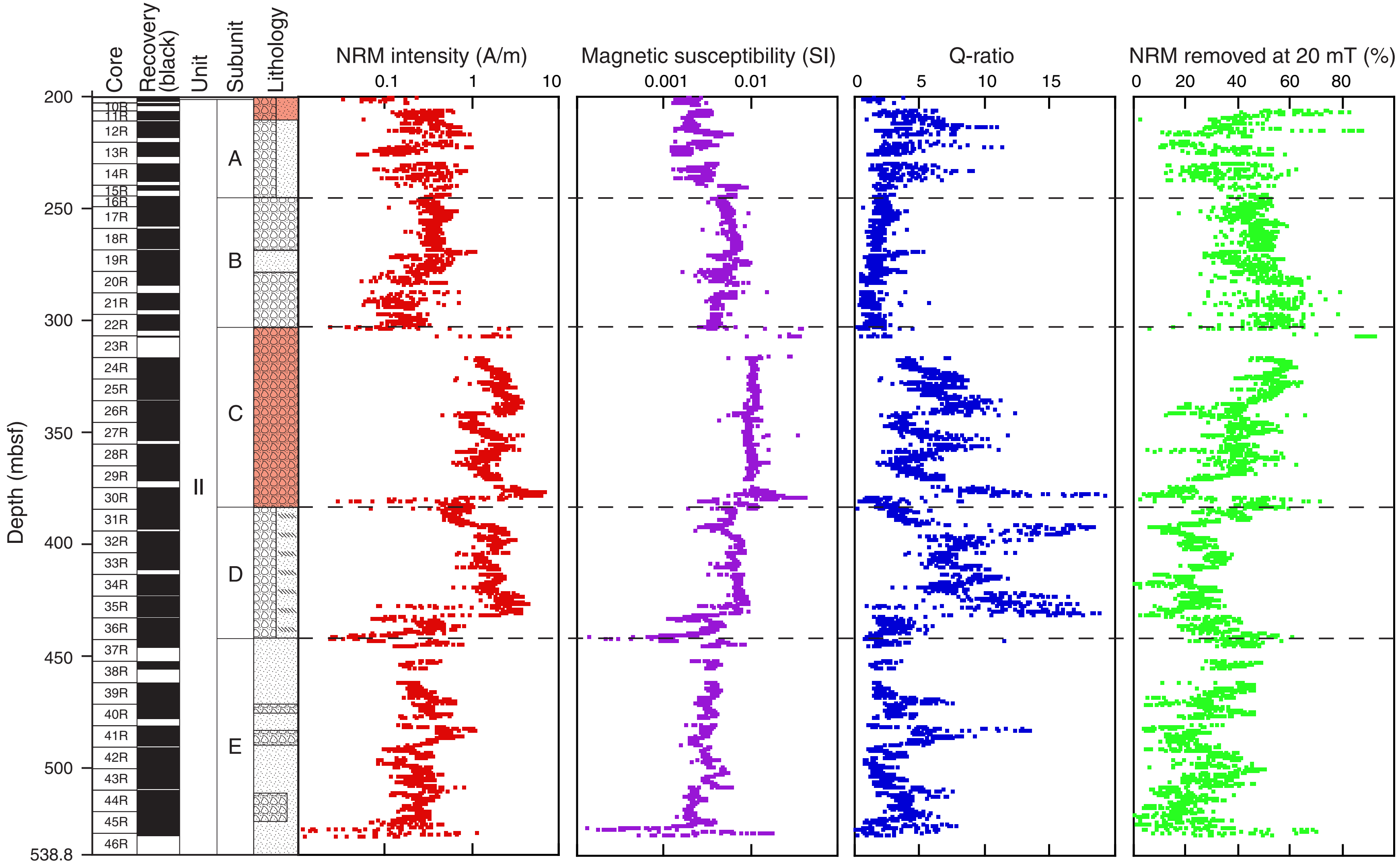

Figure F73. Variation with depth of (**A**) natural remanent magnetization (NRM) intensity and (**B**) percentage of NRM intensity removed by 20 mT alternating-field demagnetization within Subunit IIC of Hole 1184A. Dashed lines = the pattern of gradual NRM increase and coercivity decrease within layers discussed in text.

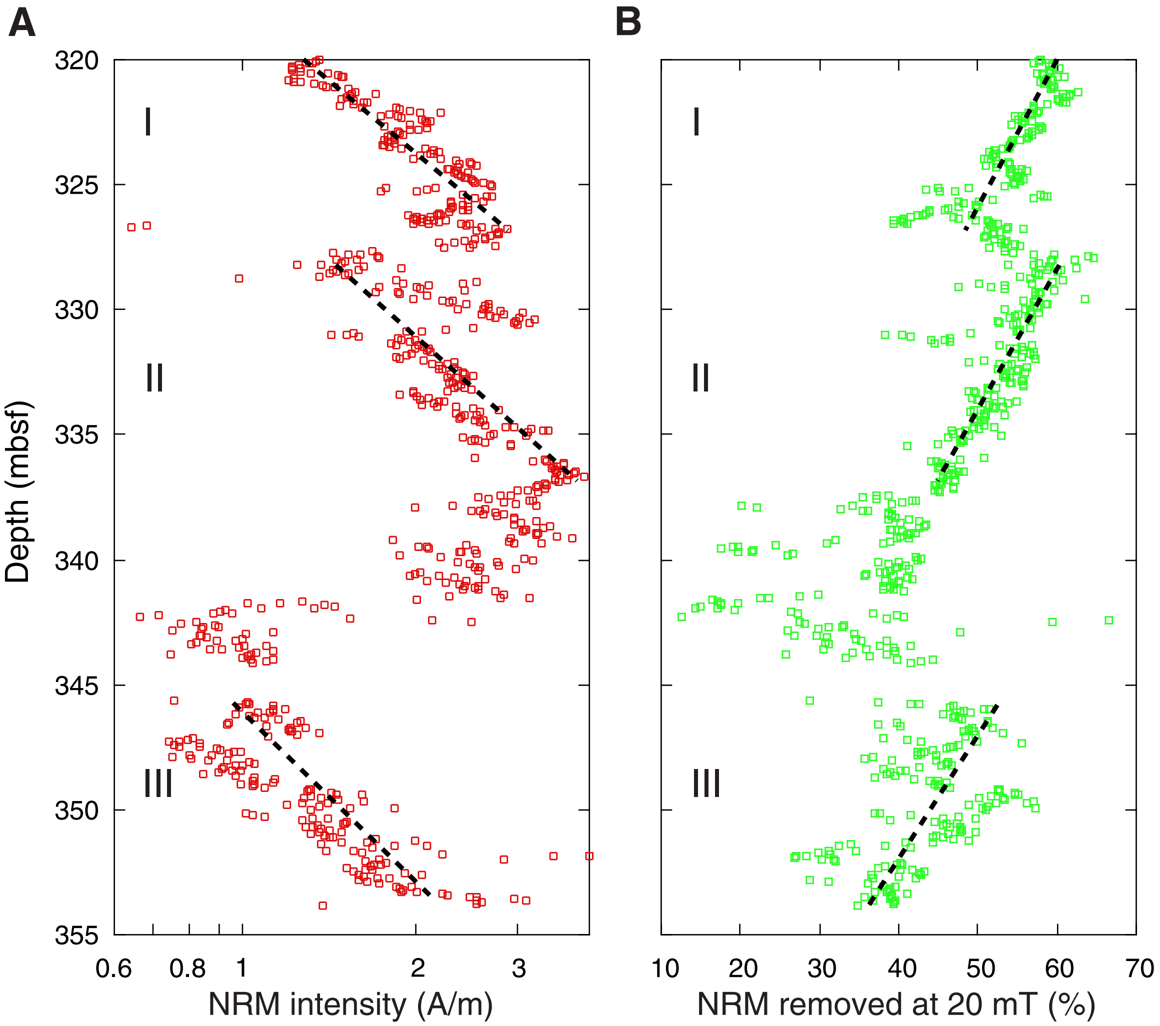

Figure F74. Mean paleomagnetic inclinations of the characteristic remanent magnetization (ChRM) for 5-m intervals within Unit II of Hole 1184A. Inc. = mean inclination. See legend in Figure F10, p. 38.

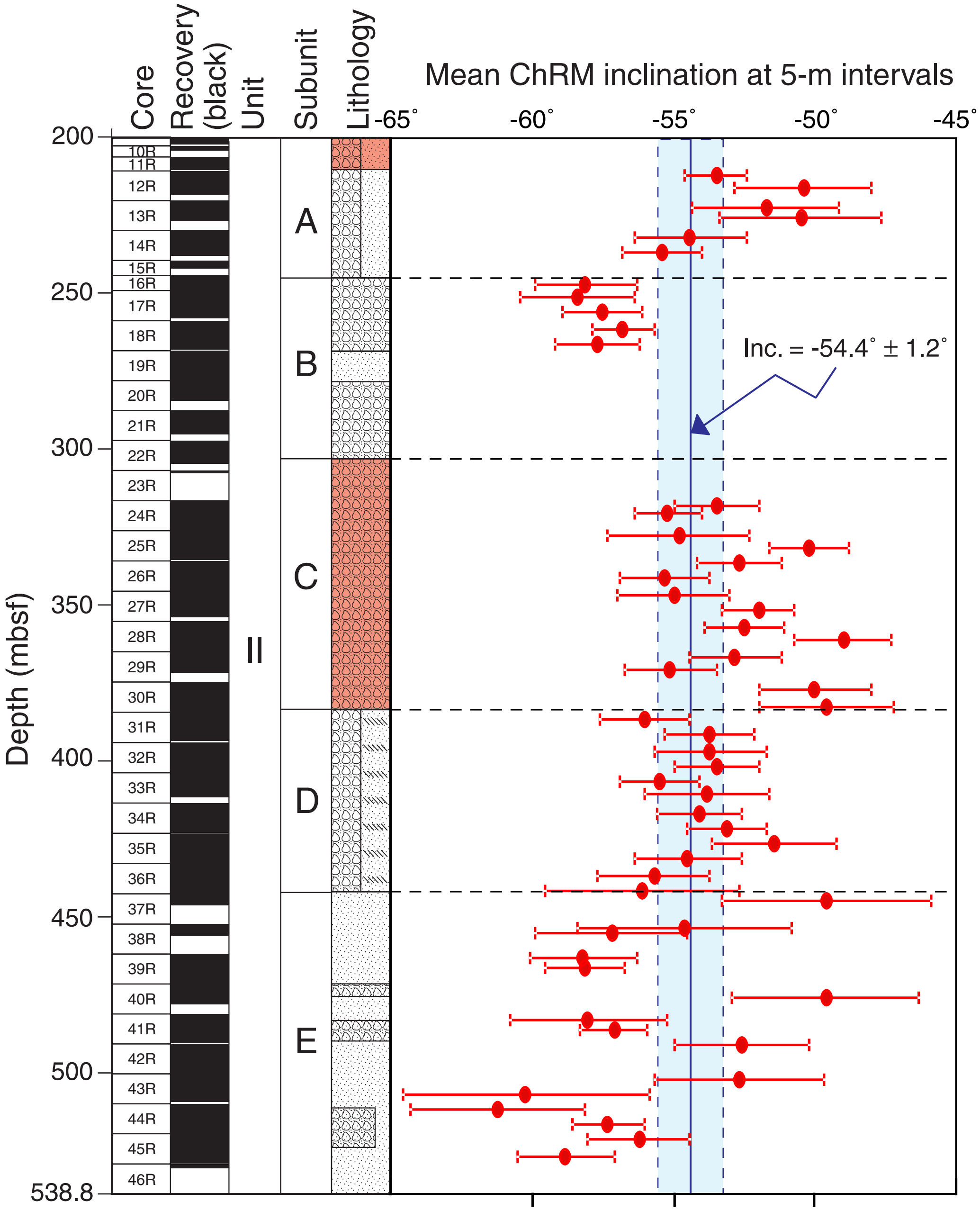

Figure F75. Dip angle and down-dip directions of inclined layers in (**A**) core coordinates and (**B**) paleomagnetic coordinates. Solid circles = layers interpreted to be cross-laminated deposits; triangles = inclined bed contacts.

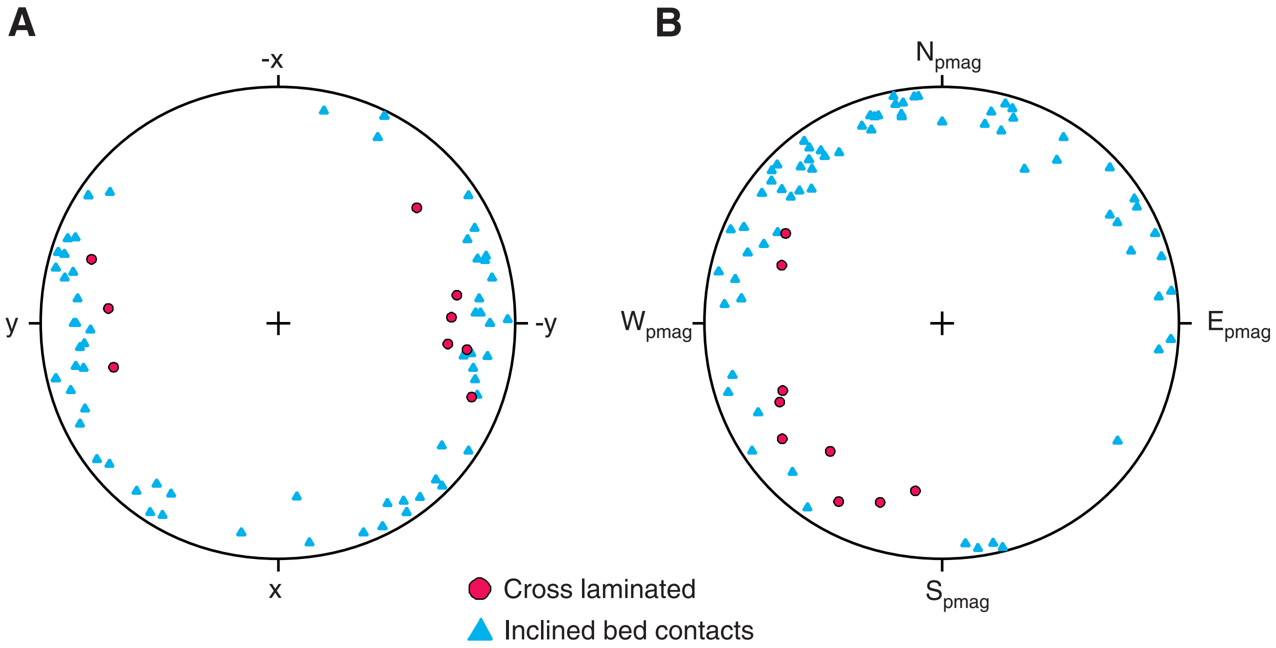

Figure F76. Index properties and thermal conductivity vs. depth at Hole 1184A. Horizontal solid line separates the lithologic units; dashed lines = boundaries of subunits.

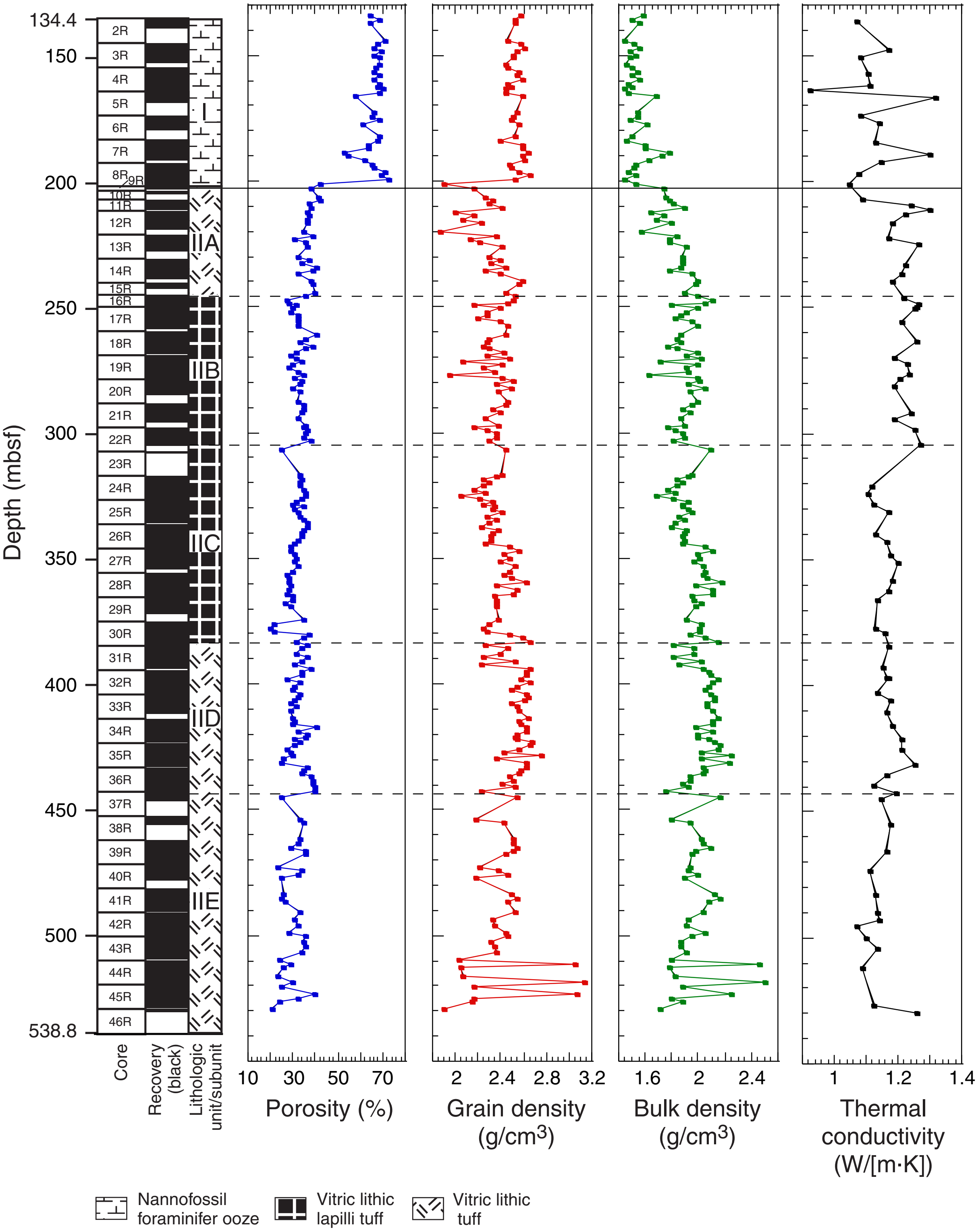

Figure F77. Magnetic susceptibility profiles obtained from (**A**) whole-core multisensor track (MST) measurements on the Bartington meter at 4-cm intervals and (**B**) split-core-section archive multisensor track (AMST) measurements on the point-susceptibility meter at 2-cm intervals.

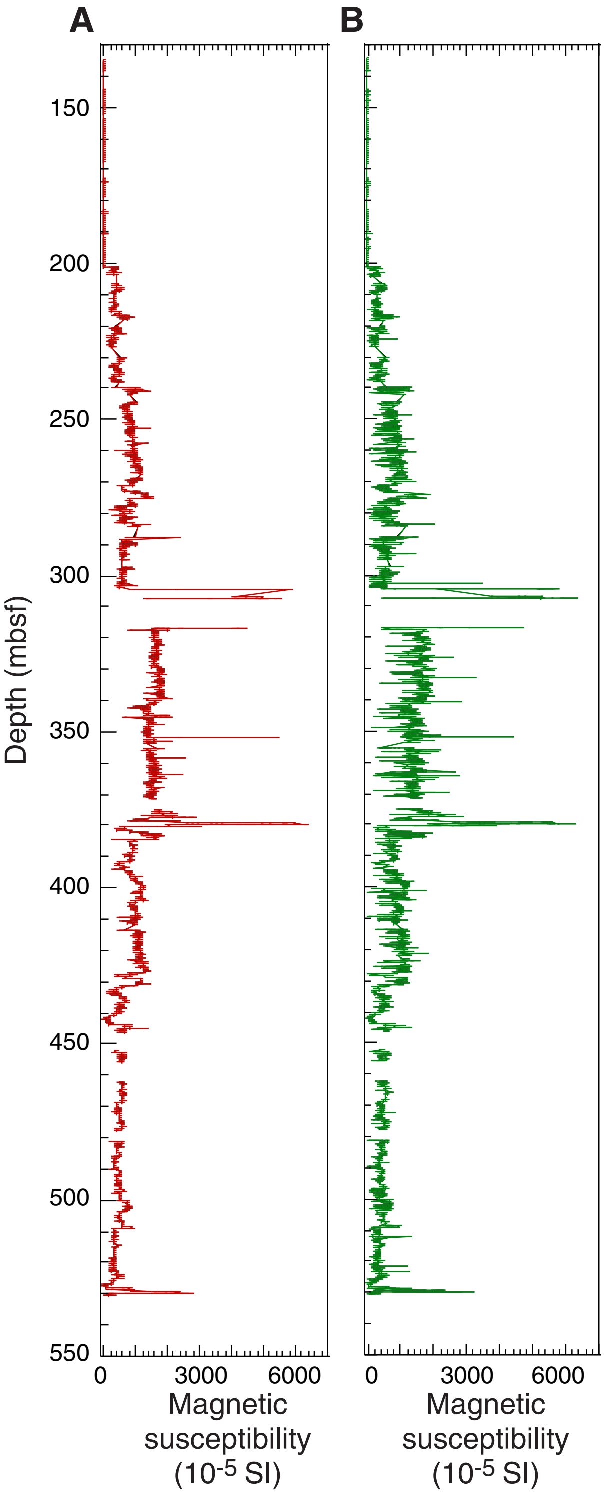

Figure F78. *P*-wave velocity and whole-core measurements vs. depth for Hole 1184A.

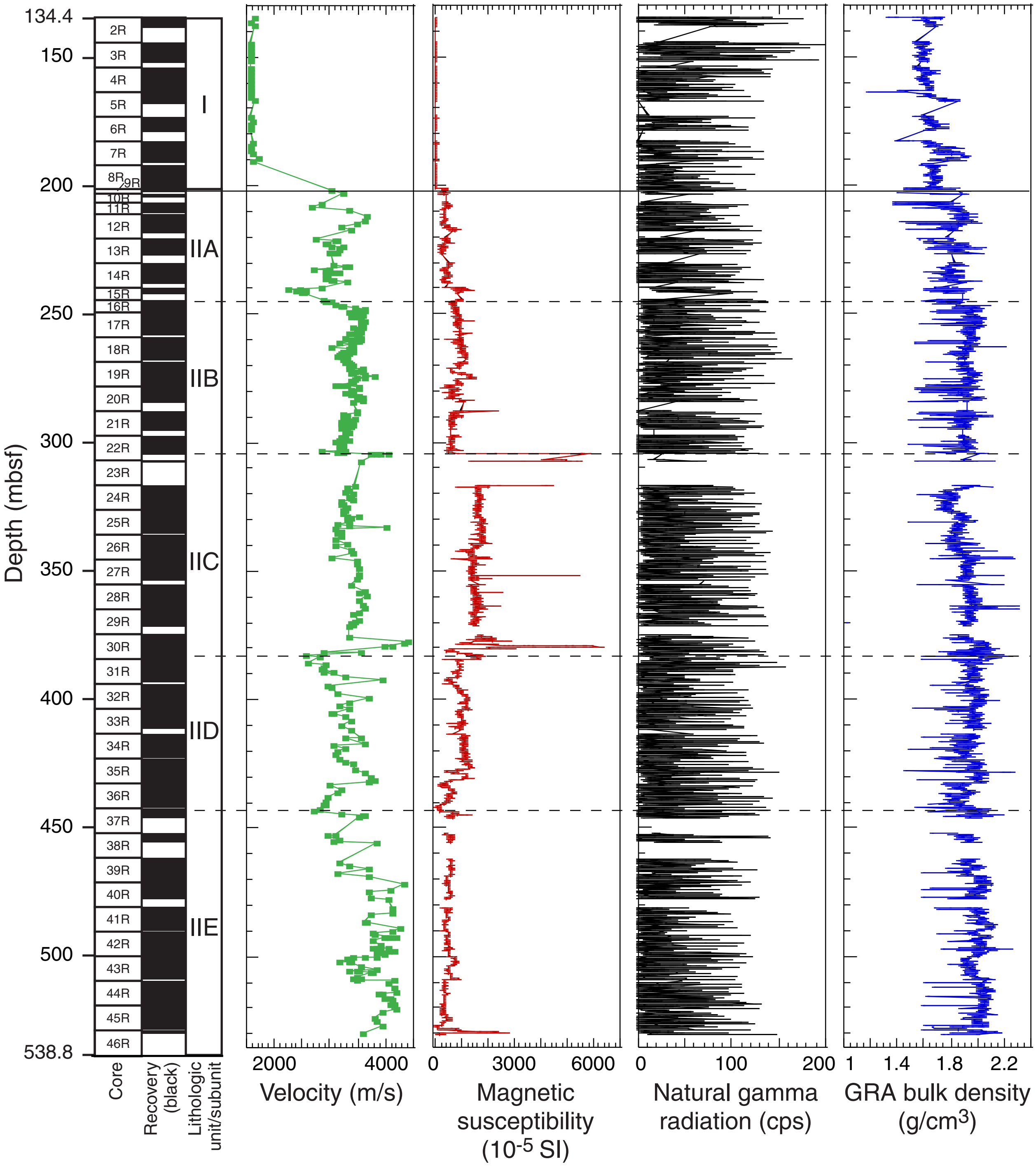

Table T1. Coring summary, Hole 1184A.

Core	Date (Oct 2000)	Time (local)	Depth (mbsf)		Length (m)		Recovery (%)
			Top	Bottom	Cored	Recovered	
192-1184A-							
1W	1	2350	0.0	134.4	0.0	NA	NA
2R	2	0045	134.4	144.0	9.6	3.90	40.6
3R	2	0125	144.0	153.7	9.7	7.96	82.1
4R	2	0200	153.7	163.3	9.6	9.52	99.2
5R	2	0235	163.3	172.9	9.6	4.55	47.4
6R	2	0340	172.9	182.5	9.6	5.93	61.8
7R	2	0410	182.5	191.8	9.3	8.38	90.1
8R	2	0440	191.8	201.1	9.3	9.59	103.1
9R	2	0635	201.1	202.9	1.8	1.24	68.9
10R	2	1055	202.9	206.4	3.5	1.43	40.9
11R	2	1310	206.4	210.9	4.5	4.11	91.3
12R	2	1700	210.9	220.4	9.5	7.52	79.2
13R	2	2040	220.4	230.0	9.6	6.61	68.9
14R	2	2340	230.0	239.6	9.6	8.13	84.7
15R	3	0355	239.6	244.4	4.8	2.49	51.9
16R	3	0655	244.4	249.2	4.8	4.98	103.8
17R	3	1255	249.2	258.9	9.7	8.86	91.3
18R	3	1725	258.9	268.5	9.6	9.13	95.1
19R	3	2240	268.5	278.1	9.6	9.56	99.6
20R	4	0340	278.1	287.7	9.6	6.41	66.8
21R	4	0825	287.7	297.3	9.6	7.57	78.9
22R	4	1335	297.3	306.9	9.6	7.35	76.6
23R	4	1830	306.9	316.6	9.7	0.84	8.7
24R	4	2225	316.6	326.2	9.6	10.18	106.0
25R	5	2115	326.2	335.9	9.7	9.30	95.9
26R	5	2359	335.9	345.6	9.7	10.12	104.3
27R	6	0335	345.6	355.3	9.7	8.28	85.4
28R	6	0715	355.3	365.0	9.7	9.94	102.5
29R	6	1035	365.0	374.7	9.7	6.80	70.1
30R	6	1440	374.7	384.4	9.7	9.98	102.9
31R	6	1725	384.4	394.1	9.7	9.18	94.6
32R	6	2015	394.1	403.8	9.7	10.06	103.7
33R	6	2310	403.8	413.5	9.7	7.86	81.0
34R	7	0215	413.5	423.2	9.7	9.44	97.3
35R	7	0505	423.2	432.9	9.7	9.52	98.1
36R	7	0745	432.9	442.6	9.7	9.60	99.0
37R	7	1140	442.6	452.3	9.7	3.73	38.5
38R	7	1505	452.3	461.9	9.6	3.69	38.4
39R	7	1855	461.9	471.5	9.6	9.82	102.3
40R	7	2240	471.5	481.1	9.6	6.50	67.7
41R	8	0250	481.1	490.7	9.6	9.35	97.4
42R	8	0725	490.7	500.3	9.6	9.99	104.1
43R	8	1105	500.3	509.9	9.6	9.09	94.7
44R	8	1500	509.9	519.5	9.6	9.54	99.4
45R	8	1900	519.5	529.2	9.7	9.43	97.2
46R	8	2140	529.2	538.8	9.6	1.30	13.5
				Cored:	404.4	328.76	81.3
				Drilled:	134.4		
				Total:	538.8		

Note: NA = not analyzed. This table is also available in **ASCII format.**

Table T2. Expanded coring summary, Site 1184. (See table notes. Continued on next seven pages.)

Core	Date (Oct 2000)	Time (local)	Core depth (mbsf)		Length (m)		Recovery (%)	Section	Length (m)		Section depth (mbsf)		Catwalk samples	Comment
			Top	Bottom	Cored	Recovered			Liner	Curated	Top	Bottom		
192-1184A-														
2R	2	0045	134.4	144.0	9.6	3.90	40.6							
								1	1.50	1.50	134.40	135.90		
								2	1.50	1.50	135.90	137.40		
								3	0.85	0.85	137.4	138.25		
								CC(NS)	0.05	0.05	138.25	138.30	PAL	All to PAL
								Totals:	3.90	3.90				
3R	2	0125	144.0	153.7	9.7	7.96	82.1							
								1	1.50	1.50	144.00	145.50		
								2	1.50	1.50	145.50	147.00		
								3	1.50	1.50	147.00	148.50		
								4	1.50	1.50	148.50	150.00		
								5	1.00	1.00	150.00	151.00		
								6	0.77	0.77	151.00	151.77		
								CC(w/6)	0.19	0.19	151.77	151.96	PAL	
								Totals:	7.96	7.96				
4R	2	0200	153.7	163.3	9.6	9.52	99.2							
								1	1.50	1.50	153.70	155.20		
								2	1.50	1.50	155.20	156.70		
								3	1.50	1.50	156.70	158.20		
								4	1.50	1.50	158.20	159.70		
								5	1.50	1.50	159.70	161.20		
								6	1.20	1.20	161.20	162.40		
								7	0.77	0.77	162.4	163.17		
								CC(NS)	0.05	0.05	163.17	163.22	PAL	All to PAL
								Totals:	9.52	9.52				
5R	2	0235	163.3	172.9	9.6	4.55	47.4							
								1	1.50	1.50	163.30	164.80		
								2	1.50	1.50	164.80	166.30		
								3	1.45	1.45	166.30	167.75		
								CC(w/CC)	0.10	0.10	167.75	167.85	PAL	All to PAL
								Totals:	4.55	4.55				
6R	2	0340	172.9	182.5	9.6	5.93	61.8							
								1	1.50	1.50	172.90	174.40		
								2	1.50	1.50	174.40	175.90		
								3	1.50	1.50	175.90	177.40		
								4	1.38	1.38	177.4	178.78		
								CC(NS)	0.05	0.05	178.78	178.83	PAL	All to PAL
								Totals:	5.93	5.93				
7R	2	0410	182.5	191.8	9.3	8.38	90.1							
								1	1.50	1.50	182.50	184.00		
								2	1.50	1.50	184.00	185.50		
								3	1.50	1.50	185.50	187.00		
								4	1.50	1.50	187.00	188.50		
								5	1.50	1.50	188.50	190.00		
								6	0.78	0.78	190.00	190.78		
								CC(NS)	0.10	0.10	190.78	190.88	PAL	All to PAL
								Totals:	8.38	8.38				

Table T2 (continued).

Core	Date (Oct 2000)	Time (local)	Core depth (mbsf)		Length (m)		Recovery (%)	Section	Length (m)		Section depth (mbsf)		Catwalk samples	Comment
			Top	Bottom	Cored	Recovered			Liner	Curated	Top	Bottom		
8R	2	0440	191.8	201.1	9.3	9.59	103.1							
								1	1.50	1.50	191.80	193.30		
								2	1.50	1.50	193.30	194.80		
								3	1.50	1.50	194.80	196.30		
								4	1.50	1.50	196.30	197.80		
								5	1.50	1.50	197.80	199.30		
								6	1.00	1.00	199.30	200.30		
								7	0.99	0.99	200.30	201.29		
								CC(NS)	0.10	0.10	201.29	201.39	PAL	All to PAL
								Totals:	9.59	9.59				
9R	2	0635	201.1	202.9	1.8	1.24	68.9							
								1	1.24	1.24	201.10	202.34	PAL, PAL	
								Totals:	1.24	1.24				
10R	2	1055	202.9	206.4	3.5	1.43	40.9							
								1	1.04	1.04	202.90	203.94		
								CC(w/1)	0.39	0.39	203.94	204.33	PAL, PAL	
								Totals:	1.43	1.43				
11R	2	1310	206.4	210.9	4.5	4.11	91.3							
								1	1.50	1.50	206.40	207.90	PAL	
								2	1.16	1.16	207.90	209.06	BANC	
								3	1.45	1.45	209.06	210.51		
								Totals:	4.11	4.11				
12R	2	1700	210.9	220.4	9.5	7.52	79.2							
								1	1.50	1.50	210.90	212.40		
								2	1.37	1.37	212.40	213.77	BANC	
								3	1.50	1.47	213.77	215.24		
								4	1.32	1.32	215.24	216.56		
								5	1.50	1.50	216.56	218.06		
								CC(w/CC)	0.33	0.33	218.06	218.39		
								Totals:	7.52	7.49				
13R	2	2040	220.4	230.0	9.6	6.61	68.9							
								1	1.44	1.44	220.40	221.84		
								2	1.23	1.23	221.84	223.07		
								3	1.51	1.51	223.07	224.58	BANC	
								4	1.47	1.47	224.58	226.05		
								5	0.65	0.65	226.05	226.70		
								CC(w/5)	0.31	0.31	226.70	227.01		
								Totals:	6.61	6.61				
14R	2	2340	230.0	239.6	9.6	8.13	84.7							
								1	1.43	1.43	230.00	231.43		
								2	1.41	1.41	231.43	232.84		
								3	1.33	1.33	232.84	234.17		
								4	1.36	1.36	234.17	235.53		
								5	1.41	1.41	235.53	236.94		
								6	1.00	1.00	236.94	237.94		
								CC(w/6)	0.19	0.19	237.94	238.13		
								Totals:	8.13	8.13				
15R	3	0355	239.6	244.4	4.8	2.49	51.9							
								1	1.48	1.48	239.60	241.08		

Table T2 (continued).

Core	Date (Oct 2000)	Time (local)	Core depth (mbsf)		Length (m)		Recovery (%)	Section	Length (m)		Section depth (mbsf)		Catwalk samples	Comment
			Top	Bottom	Cored	Recovered			Liner	Curated	Top	Bottom		
								2	0.86	0.86	241.08	241.94		
								CC(w/2)	0.15	0.15	241.94	242.09		
								Totals:	2.49	2.49				
16R	3	0655	244.4	249.2	4.8	4.98	103.8							
								1	1.50	1.50	244.40	245.90		
								2	1.48	1.48	245.90	247.38		
								3	1.11	1.11	247.38	248.49		
								4	0.58	0.58	248.49	249.07		
								CC(w/4)	0.31	0.31	249.07	249.38		
								Totals:	4.98	4.98				
17R	3	1255	249.2	258.9	9.7	8.86	91.3							
								1	1.39	1.39	249.20	250.59		
								2	1.51	1.51	250.59	252.10		
								3	1.43	1.43	252.10	253.53		
								4	1.25	1.25	253.53	254.78		
								5	1.30	1.30	254.78	256.08		
								6	1.48	1.48	256.08	257.56		
								7	0.50	0.50	257.56	258.06		
								Totals:	8.86	8.86				
18R	3	1725	258.9	268.5	9.6	9.13	95.1							
								1	1.04	1.04	258.90	259.94		
								2	1.36	1.36	259.94	261.30		
								3	1.52	1.52	261.3	262.82		
								4	1.38	1.38	262.82	264.2		
								5	1.50	1.50	264.20	265.70		
								6	0.99	0.99	265.70	266.69		
								7	1.13	1.13	266.69	267.82		
								CC(w/7)	0.21	0.21	267.82	268.03		
								Totals:	9.13	9.13				
19R	3	2240	268.5	278.1	9.6	9.56	99.6							
								1	0.81	0.81	268.50	269.31		
								2	1.29	1.29	269.31	270.60		
								3	1.06	1.06	270.60	271.66		
								4	1.41	1.41	271.66	273.07		
								5	1.26	1.26	273.07	274.33		
								6	1.51	1.51	274.33	275.84		
								7	1.51	1.51	275.84	277.35		
								8	0.71	0.71	277.35	278.06		
								Totals:	9.56	9.56				
20R	4	0340	278.1	287.7	9.6	6.41	66.8							
								1	1.50	1.50	278.10	279.60		
								2	1.31	1.31	279.60	280.91		
								3	1.48	1.48	280.91	282.39		
								4	1.09	1.09	282.39	283.48		
								5	0.76	0.76	283.48	284.24		
								CC(w/5)	0.27	0.27	284.24	284.51		
								Totals:	6.41	6.41				
21R	4	0825	287.7	297.3	9.6	7.57	78.9							
								1	1.44	1.44	287.70	289.14		

Table T2 (continued).

Core	Date (Oct 2000)	Time (local)	Core depth (mbsf)		Length (m)		Recovery (%)	Section	Length (m)		Section depth (mbsf)		Catwalk samples	Comment
			Top	Bottom	Cored	Recovered			Liner	Curated	Top	Bottom		
								2	1.51	1.51	289.14	290.65		
								3	1.20	1.20	290.65	291.85		
								4	0.83	0.83	291.85	292.68		
								5	1.50	1.50	292.68	294.18		
								6	0.93	0.93	294.18	295.11		
								CC(w/6)	0.16	0.16	295.11	295.27		
								Totals:	7.57	7.57				
22R	4	1335	297.3	306.9	9.6	7.35	76.6							
								1	0.80	0.80	297.30	298.10		
								2	1.02	1.02	298.10	299.12		
								3	1.45	1.45	299.12	300.57		
								4	1.34	1.34	300.57	301.91		
								5	1.37	1.37	301.91	303.28		
								6	1.13	1.13	303.28	304.41		
								CC(w/6)	0.24	0.24	304.41	304.65		
								Totals:	7.35	7.35				
23R	4	1830	306.9	316.6	9.7	0.84	8.7							
								1	0.84	0.84	306.90	307.74	PAL	
								Totals:	0.84	0.84				
24R	4	2225	316.6	326.2	9.6	10.18	106.0							
								1	0.75	0.75	316.60	317.35		
								2	1.34	1.34	317.35	318.69		
								3	1.08	1.08	318.69	319.77		
								4	1.47	1.47	319.77	321.24		
								5	1.40	1.40	321.24	322.64		
								6	1.26	1.26	322.64	323.90		
								7	1.45	1.45	323.90	325.35		
								8	1.43	1.43	325.35	326.78		
								Totals:	10.18	10.18				
25R	5	2115	326.2	335.9	9.7	9.30	95.9							
								1	1.43	1.43	326.20	327.63		
								2	1.15	1.15	327.63	328.78		
								3	0.73	0.73	328.78	329.51		
								4	1.18	1.18	329.51	330.69		
								5	1.26	1.26	330.69	331.95		
								6	1.50	1.50	331.95	333.45		
								7	1.12	1.12	333.45	334.57		
								8	0.93	0.93	334.57	335.50		
								Totals:	9.30	9.30				
26R	5	2359	335.9	345.6	9.7	10.12	104.3							
								1	1.47	1.47	335.90	337.37		
								2	1.20	1.20	337.37	338.57		
								3	1.31	1.31	338.57	339.88		
								4	1.49	1.49	339.88	341.37		
								5	1.50	1.50	341.37	342.87		
								6	1.44	1.44	342.87	344.31		
								7	1.05	1.05	344.31	345.36		
								CC(w/CC)	0.66	0.66	345.36	346.02		Disturbed
								Totals:	10.12	10.12				

Table T2 (continued).

Core	Date (Oct 2000)	Time (local)	Core depth (mbsf)		Length (m)		Recovery (%)	Section	Length (m)		Section depth (mbsf)		Catwalk samples	Comment
			Top	Bottom	Cored	Recovered			Liner	Curated	Top	Bottom		
27R	6	0335	345.6	355.3	9.7	8.28	85.4							
								1	1.51	1.51	345.60	347.11		
								2	1.51	1.51	347.11	348.62		
								3	1.46	1.46	348.62	350.08		
								4	1.50	1.50	350.08	351.58		
								5	1.44	1.44	351.58	353.02		
								6	0.86	0.86	353.02	353.88		
								Totals:	8.28	8.28				
28R	6	0715	355.3	365.0	9.7	9.94	102.5							
								1	1.50	1.50	355.30	356.80		
								2	1.29	1.29	356.80	358.09		
								3	1.47	1.47	358.09	359.56		
								4	1.50	1.50	359.56	361.06		
								5	1.50	1.50	361.06	362.56		
								6	1.50	1.50	362.56	364.06		
								7	0.95	0.95	364.06	365.01		
								CC(w/7)	0.23	0.23	365.01	365.24		
								Totals:	9.94	9.94				
29R	6	1035	365.0	374.7	9.7	6.80	70.1							
								1	1.50	1.50	365.00	366.50		
								2	1.38	1.38	366.50	367.88		
								3	1.50	1.50	367.88	369.38		
								4	1.50	1.50	369.38	370.88		
								5	0.92	0.92	370.88	371.80		
								Totals:	6.80	6.80				
30R	6	1440	374.7	384.4	9.7	9.98	102.9							
								1	1.50	1.50	374.70	376.20		
								2	1.50	1.50	376.20	377.70		
								3	1.50	1.50	377.70	379.00		
								4	1.19	1.19	379.20	380.39		
								5	1.26	1.26	380.39	381.65		
								6	1.41	1.41	381.65	383.06	PAL, PAL	
								7	1.34	1.34	383.06	384.40		
								CC(w/CC)	0.28	0.28	384.40	384.68		
								Totals:	9.98	9.98				
31R	6	1725	384.4	394.1	9.7	9.18	94.6							
								1	1.52	1.52	384.40	385.92		
								2	0.99	0.99	385.92	386.91		
								3	1.05	1.05	386.91	387.96		
								4	1.47	1.47	387.96	389.43		
								5	1.37	1.37	389.43	390.80		
								6	1.52	1.52	390.80	392.32		
								7	1.26	1.26	392.32	393.58		
								Totals:	9.18	9.18				
32R	6	2015	394.1	403.8	9.7	10.06	103.7							
								1	0.93	0.93	394.10	395.03		
								2	1.50	1.50	395.03	396.53		
								3	1.50	1.50	396.53	398.03		

Table T2 (continued).

Core	Date (Oct 2000)	Time (local)	Core depth (mbsf)		Length (m)		Recovery (%)	Section	Length (m)		Section depth (mbsf)		Catwalk samples	Comment
			Top	Bottom	Cored	Recovered			Liner	Curated	Top	Bottom		
								4	1.52	1.52	398.03	399.55		
								5	1.50	1.50	399.55	401.05		
								6	1.50	1.50	401.05	402.55		
								7	1.22	1.22	402.55	403.77		
								8	0.39	0.39	403.77	404.16		
								Totals:	10.06	10.06				
33R	6	2310	403.8	413.5	9.7	7.86	81.0							
								1	1.39	1.39	403.80	405.19		
								2	1.10	1.10	405.19	406.29		
								3	1.50	1.50	406.29	407.79		
								4	1.21	1.21	407.79	409.00		
								5	1.50	1.50	409.00	410.50		
								6	1.16	1.16	410.50	411.66		
								Totals:	7.86	7.86				
34R	7	0215	413.5	423.2	9.7	9.44	97.3							
								1	1.24	1.24	413.50	414.74		
								2	1.18	1.18	414.74	415.92		
								3	1.28	1.28	415.92	417.20		
								4	1.50	1.50	417.20	418.70		
								5	1.35	1.35	418.70	420.05		
								6	1.15	1.15	420.05	421.20		
								7	0.95	0.95	421.20	422.15		
								8	0.79	0.79	422.15	422.94		
								Totals:	9.44	9.44				
35R	7	0505	423.2	432.9	9.7	9.52	98.1							
								1	1.35	1.35	423.02	424.55		
								2	1.23	1.23	424.55	425.78		
								3	1.47	1.47	425.78	427.25		
								4	1.23	1.23	427.25	428.48		
								5	1.18	1.18	428.48	429.66		
								6	1.50	1.50	429.66	431.16		
								7	0.82	0.82	431.16	431.98		
								8	0.74	0.74	431.98	432.72		
								Totals:	9.52	9.52				
36R	7	0745	432.9	442.6	9.7	9.60	99.0							
								1	1.44	1.44	432.90	434.34		
								2	1.25	1.25	434.34	435.59		
								3	1.30	1.30	435.59	436.89		
								4	1.51	1.51	436.89	438.40		
								5	1.50	1.50	438.40	439.90		
								6	1.10	1.10	439.90	441.00		
								7	1.50	1.50	441.00	442.50		
								CC(NS)	0.00	0.00				
								Totals:	9.60	9.60				
37R	7	1140	442.6	452.3	9.7	3.73	38.5							
								1	1.02	1.02	442.60	443.62		
								2	1.50	1.50	443.62	445.12		
								3	1.21	1.21	445.12	446.33		
								Totals:	3.73	3.73				

Table T2 (continued).

Core	Date (Oct 2000)	Time (local)	Core depth (mbsf)		Length (m)		Recovery (%)	Section	Length (m)		Section depth (mbsf)		Catwalk samples	Comment
			Top	Bottom	Cored	Recovered			Liner	Curated	Top	Bottom		
38R	7	1505	452.3	461.9	9.6	3.69	38.4							
								1	1.52	1.52	452.30	453.82		
								2	1.48	1.48	453.82	455.30		
								3	0.69	0.69	455.30	455.99		
									3.69	3.69				
39R	7	1855	461.9	471.5	9.6	9.82	102.3							
								1	1.50	1.50	461.90	463.40		
								2	1.50	1.50	463.40	464.90		
								3	1.36	1.36	464.9	466.26		
								4	1.41	1.41	466.26	467.67		
								5	1.50	1.50	467.67	469.17		
								6	1.50	1.50	469.17	470.67		
								7	1.05	1.05	470.67	471.72	BANC	
								Totals:	9.82	9.82				
40R	7	2240	471.5	481.1	9.6	6.50	67.7							
								1	1.39	1.39	471.50	472.89		
								2	1.41	1.41	472.89	474.30		
								3	1.50	1.50	474.30	475.80		
								4	1.50	1.50	475.80	477.30		
								5	0.70	0.70	477.30	478.00	BANC	
								Totals:	6.50	6.50				
41R	8	0250	481.1	490.7	9.6	9.35	97.4							
								1	1.51	1.51	481.10	482.61		
								2	1.03	1.03	482.61	483.64		
								3	1.48	1.48	483.64	485.12		
								4	1.49	1.49	485.12	486.61		
								5	1.44	1.44	486.61	488.05		
								6	1.06	1.06	488.05	489.11		
								7	1.34	1.34	489.11	490.45	BANC	
								CC(NS)	0.00	0.00				
								Totals:	9.35	9.35				
42R	8	0725	490.7	500.3	9.6	9.99	104.1							
								1	1.50	1.50	490.70	492.20		
								2	1.50	1.50	492.20	493.70		
								3	1.50	1.50	493.70	495.20		
								4	1.04	1.04	495.2	496.24		
								5	1.17	1.17	496.24	497.41		
								6	1.50	1.50	497.41	498.91		
								7	1.51	1.51	498.91	500.42		
								CC(w/CC)	0.27	0.27	500.42	500.69	BANC	
								Totals:	9.99	9.99				
43R	8	1105	500.3	509.9	9.6	9.09	94.7							
								1	1.50	1.50	500.30	501.80		
								2	0.93	0.93	501.80	502.73		
								3	1.50	1.50	502.73	504.23	BANC	
								4	1.05	1.05	504.23	505.28		
								5	1.50	1.50	505.28	506.78		
								6	1.46	1.46	506.78	508.24		

Table T2 (continued).

Core	Date (Oct 2000)	Time (local)	Core depth (mbsf)		Length (m)		Recovery (%)	Section	Length (m)		Section depth (mbsf)		Catwalk samples	Comment
			Top	Bottom	Cored	Recovered			Liner	Curated	Top	Bottom		
								7	1.15	1.15	508.24	509.39		
								Totals:	9.09	9.09				
44R	8	1500	509.9	519.5	9.6	9.54	99.4							
								1	1.52	1.52	509.90	511.42		
								2	1.33	1.33	511.42	512.75	BANC	
								3	1.34	1.34	512.75	514.09		
								4	1.11	1.11	514.09	515.20		
								5	1.30	1.30	515.20	516.50		
								6	1.39	1.39	516.5	517.89		
								7	0.80	0.80	517.89	518.69		
								8	0.75	0.75	518.69	519.44		
								Totals:	9.54	9.54				
45R	8	1900	519.5	529.2	9.7	9.43	97.2							
								1	1.15	1.15	519.50	520.65	BANC	
								2	1.34	1.34	520.65	521.99		
								3	1.46	1.46	521.99	523.45		
								4	1.37	1.37	523.45	524.82		
								5	1.30	1.30	524.82	526.12		
								6	1.49	1.49	526.12	527.61		
								7	1.32	1.32	527.61	528.93		Other
								Totals:	9.43	9.43				
46R	8	2140	529.2	538.8	9.6	1.30	13.5							
								1	1.30	1.30	529.20	530.50		
								Totals:	1.30	1.30				
			Hole coring totals:		404.4	328.76	81.3							

Notes: CC = core catcher, NS = not stored. Sample codes: PAL = paleontology, BANC = microbiological study. This table is also available in **ASCII format.**

Table T3. Inorganic carbon and carbonate contents and X-ray diffraction analyses for samples from Unit I, Hole 1184A.

Core, section, interval (cm)	Depth (mbsf)	Lithology	Inorganic carbon (wt%)	$CaCO_3$ (wt%)	Mineral components (by XRD)
192-1184A-					
2R-1, 52	134.92	Carbonate ooze	11.57	96.4	Calcite
2R-3, 51	137.91	Carbonate ooze	11.29	94.1	—
3R-1, 35	144.35	Carbonate ooze	11.34	94.5	Calcite
4R-1, 42	154.12	Carbonate ooze	11.28	94.0	Calcite
5R-1, 38	163.68	Carbonate ooze	11.23	93.5	Calcite
6R-1, 29	173.19	Carbonate ooze	11.32	94.3	Calcite
7R-1, 39	182.89	Carbonate ooze	11.41	95.0	Calcite
8R-3, 89	195.69	Carbonate ooze	11.41	95.0	Calcite

Notes: XRD = X-ray diffraction. — = not analyzed.

Table T4. Key characteristics of lithologic facies recognized from Unit II, Hole 1184A.

Facies	Sedimentary structures	Grain size	Sorting	Thickness	Lithology	Interpretation	Core, section, interval (cm)
							192-1184A-
1	Massive with some subtle gradations in grain size; includes thin layers of very coarse sand to granules	Very fine sand to pebble	Very poor	20 cm to >10 m	Lithic vitric lapilli tuff	Muddy debris flow deposit	40R-1, 0-137
2	Massive, grain-size oscillations	Coarse sand to pebble	Very poor	2-30 m	Lithic vitric lapilli tuff to lapillistone	Stony debris flow deposit	28R-4, 0-150
3	Inclined granule lamination	Medium sand to granule	Poor	2-5 m	Lithic vitric lapilli tuff	Current-reworked deposit	36R-2, 0-60
4	Grading, parallel lamination, traction carpet	Fine to very coarse sand	Moderate	5-200 cm	Lithic vitric tuff	Turbidite	12R-4, 57-68
5	Massive, clast supported	Granule to pebble	Moderate	20 cm to 10 m	Tachylitic lapillistone	Quenched subaerial eruptive products	22R-6, 92-112
6	Chaotic bedding	Fine sand to pebble	Very poor	>3 m	Lithic vitric lapilli tuff	Slump deposit	45R-6, 100-150
7	Inverse grading, mud drape	Clay, very fine to coarse sand	Good	~20 cm	Lithic vitric tuff and mudstone	Fluvial deposit (?)	46R-1, 27-47
8	Massive	Silt to very fine sand	Good	5 cm	Lithic vitric tuff	Air-fall ash	27R-5, 30-35

Note: The last column gives an interval in which the lithology is well expressed.

Table T5. List of planktonic foraminifer and calcareous nannofossil highest and lowest occurrences in Unit I, Hole 1184A.

Event	Species	Core, section, interval (cm)	Depth (mbsf)	Age (Ma)
		192-1184A-		
HO	*S. conicus*	2R-1, 20	134.60	19.70
HO	*S. calyculus*	4R-1, 10	153.80	
HO	*S. cometa*	4R-1, 10	153.80	
LO	*D. altiformis globosa*	4R-1, 10	153.80	
HO	*G. fariasi*	4R-7, 10	162.50	
HO	*H. gertae*	4R-CC	163.17	
LO	*H. ampliaperta*	4R-CC	163.17	20.30
LO	*G. altiapertura*	4R-CC	163.17	20.50
HO	*I. fusa*	5R-1, 20	163.50	20.23
HO	*C. pelliculatus*	5R-1, 20	163.50	21.00
LO	*G. rotula*	5R-1, 20	163.50	19.95
LO	*G. primordius*	5R-1, 20	163.50	
LO	*J. bella*	5R-1, 20	163.50	
HO	*G. kugleri*	5R-3, 20	166.50	21.50
HO	*G. ciperoensis*	5R-3, 20	166.50	
HO	*S. disbelemnos*	5R-CC	167.75	
HO	*H. recta*	6R-1, 10	173.00	
LO	*C. tropicus* (>6 µm)	6R-1, 10	173.00	22.10
LO	*H. perplexus*	6R-1, 10	173.00	
LO	*S. cometa*	6R-3, 10	176.00	
LO	*S. disbelemnos* (short)	6R-3, 10	176.00	
LO	*C. leptoporus*	7R-3, 15	185.65	
LO	*C. tropicus* (<6 µm)	7R-3, 15	185.65	22.81
LO	*S. disbelemnos*	7R-3, 15	188.65	23.10
LO	*T. serratus*	7R-3, 15	188.65	23.20
LO	*G. dehiscens*	7R-CC	190.78	23.20
LO	*D. druggii*	9R-1, 5	201.15	23.20
LO	*S. abies*	9R-1, 5	201.15	23.25

Notes: Shaded area = planktonic foraminifers; unshaded area = calcareous nannofossils. HO = highest occurrence, LO = lowest occurrence. Ages are from Berggren et al. (1995) and E. de Kaenel (pers. comm., 1998). This table is also available in **ASCII format.**

Table T6. Summary table of thin section descriptions for the Unit II volcaniclastic rocks.

Subunit	No.	Rock types	Lithic clasts	Vitric clasts	Discrete crystal fragments	Matrix	Cement
IIA	2	Tuff	Basalt; vesicular and nonvesicular; aphyric > phyric	Blocky, nonvesicular glass shards, altered to smectite	Clinopyroxene > plagioclase; Ti magnetite > sulfide	Fine ash altered to zeolite and smectite with minor calcite	None
			5%-55%	30%-70%	1%	15%-25%	0%
IIB	7	Tuff and lapilli tuff	Basalt; fine-grained; vesicular > nonvesicular; aphyric > phyric	Blocky, vesicular and nonvesicular glass shards, altered to smectite	Clinopyroxene, plagioclase, Ti magnetite, sulfide	Fine ash altered to smectite and zeolite with minor calcite	Zeolite
			25%-70%	25%-50%	1%-5%	15%-20%	0%-10%
IIC	1	Lapillistone	None	Tachylite, nonvesicular > vesicular; sparsely phyric > aphyric; trachytic texture	Rare clinopyroxene	None	Zeolite and smectite
				95%	<<1%	0%	5%
IID	3	Tuff	Basalt, mostly nonvesicular, sparsely phyric to aphyric; fine-grained tuff; diabase	Blocky glass shards, mostly nonvesicular, altered to smectite; some tachylite	Clinopyroxene, plagioclase, Ti magnetite, sulfide	Fine ash altered to smectite	Zeolite
			10%-45%	35%-45%	1%-2%	15%-20%	5%-15%
IIE	6	Tuff	Basalt, nonvesicular and vesicular, aphyric > phyric	Blocky glass shards, mostly nonvesicular, most altered to smectite but some with unaltered interiors	Plagioclase > clinopyroxene, Ti magnetite > sulfide	Fine ash altered to smectite and zeolite	Zeolite
			25%-50%	25%-35%	<1%	20%-40%	0%-5%

Table T7. Whole-rock compositions of six fine-grained bulk samples, Hole 1184A.

	192-1184A-					
Core, section:	18R-6	31R-1	36R-7	40R-3	42R-1	45R-6
Interval (cm):	43-45	140-142	74-76	37-41	147-150	82-85
Subunit:	IIB	IID	IIE	IIE	IIE	IIE
Depth (mbsf):	266.13	385.81	441.74	474.67	492.17	526.94
Major element (wt%):						
SiO_2	52.09	50.68	49.89	50.38	50.98	50.79
TiO_2	1.14	1.23	1.33	1.02	1.03	1.09
Al_2O_3	13.84	13.71	13.57	14.34	14.33	14.59
Fe_2O_3T	13.03	13.51	14.61	11.60	11.96	12.41
MnO	0.20	0.23	0.25	0.19	0.20	0.25
MgO	9.96	6.29	6.93	8.37	8.37	7.75
CaO	2.24	7.80	8.05	11.76	11.42	10.74
Na_2O	5.06	4.95	4.27	2.06	1.79	1.66
K_2O	2.07	0.54	0.10	0.09	BD	0.10
P_2O_5	0.11	0.11	0.12	0.11	0.10	0.11
Total:	99.73	99.06	99.11	99.91	100.18	99.50
LOI	8.01	7.03	5.82	5.89	5.97	7.39
Mg#	0.63	0.51	0.52	0.62	0.61	0.58
CIPW norms:						
Q	0.0	0.0	0.0	0.2	2.5	3.9
Or	12.4	3.2	0.6	0.5	0.0	0.6
Ab	41.8	37.3	36.9	17.6	15.3	14.3
An	9.1	13.9	17.9	29.9	31.3	32.5
Ne	0.9†	3.0†	0.0	0.0	0.0	0.0
Di	1.2	20.6	18.3	23.1	20.6	17.1
Hy	0.0	0.0	3.1	24.2	25.9	26.9
Ol	29.8	16.8	17.6	0.0	0.0	0.0
Il	2.2	2.4	2.6	2.0	2.0	2.1
Mt	2.3	2.4	2.6	2.0	2.1	2.2
Ap	0.2	0.2	0.3	0.2	0.2	0.2
Trace element (ppm):						
Ni	82	81	79	106	118	114
Cr	110	147	129	314	293	310
V	334	343	379	303	315	330
Zr	61	67	76	54	58	60
Sc	49	50	51	48	46	51
Y	24	31	33	23	22	23
Sr	1142	108	104	97	95	87
Ba	36	16	29	19	18	22

Notes: Fe_2O_3T = total Fe expressed as Fe_2O_3. LOI = weight loss on ignition at 1100°C; all analyses were conducted on ignited samples. Mg# and CIPW norms were calculated assuming $Fe_2O_3/(Fe_2O_3 + FeO) = 0.13$ or $Fe_2O_3/FeO = 0.15$. † = the appearance of nepheline in the norm is due to alkali gain in these highly altered rocks. BD = below detection limit (0.01% is assumed for norm calculations). This table is also available in **ASCII format.**

Table T8. Downhole distribution of minerals identified by X-ray diffraction in bulk-rock and vein samples, Hole 1184A.

			Minerals																
			Primary			Secondary													
														Zeolites					
Core, section, interval (cm)	Depth (mbsf)	Analysis type	Plagioclase	Clinopyroxene	Magnetite	Analcime	Smectite	Quartz	Calcite	Celadonite	Fluorapatite	Hematite	Apophylite	Gmelinite	Chabazite	Levyne	Natrolite	Clinoptilolite	Mordenite
192-1184A-																			
9R-1, 3-4	201.13	Bulk				x			x		X								
9R-1, 46-47	201.56	Bulk				X	x		x										
9R-1, 106-107	202.16	Bulk				X	x	(x)	x										
10R-1, 1-3	202.91	Bulk				X	x												
11R-1, 135-136	207.75	Bulk				X	x	(x)	x		(x)			x		x			
11R-3, 0-1	209.06	Bulk				X	X	(x)	x					x		x			
15R-1, 101-102	240.61	Bulk				X	X												
16R-1, 58-60	244.98	Bulk				X	X												
17R-2, 112-114	251.71	Bulk				X	X			(x)									
19R-1, 67-69	269.17	Bulk	x			X	X												
19R-8, 30-30	277.65	Bulk	x			X	X			x									
20R-1, 34-35	278.44	Vein				x	x		X										
20R-2, 29-34	279.89	Vein				X	x		x								x		
21R-1, 111-111	288.81	Vein							X										
21R-2, 25-26	289.39	Vein				x			X										
23R-1, 69-70	307.59	Bulk	x			X	x											X	
26R-5, 32-37	341.69	Bulk				x	X								X				
28R-4, 1-3	359.57	Bulk			x	X	x			x						x			
29R-3, 147-149	369.35	Bulk			x	X	x	(x)								x			
30R-6, 34-39	381.99	Vein				X													
30R-6, 55-57	382.20	Bulk	x			x	x					x							
32R-6, 38-39	401.43	Bulk	x			x	x								X				
33R-1, 138-139	405.18	Bulk	x			x	x								X				
33R-5, 19-27	409.19	Vein				X			x						X				
33R-6, 115-116	411.65	Vein				X			x				x			x			
35R-4, 84-104	428.09	Vein							X				x						
36R-7, 136-138	442.36	Vein							X										
36R-7, 136.5-138.5	442.36	Vein							x				x						
40R-5, 49-51	477.79	Bulk	x	x			x		x										
42R-6, 0-2	497.41	Bulk	x	x			x		x										
46R-1, 124-125	530.44	Vein				X		(x)	x										x

Notes: Bulk = bulk rock. X = major component, x = minor component, (x) = trace.

Table T9. Index properties data, Hole 1184A. (See table note. Continued on next three pages.)

Core, section, interval (cm)	Depth (mbsf)	Water content (%)		Density (g/cm^3)			Porosity (%)	Void ratio
		Bulk	Dry	Bulk	Dry	Grain		
192-1184A-								
2R-1, 59-61	134.99	41.588	71.197	1.581	0.924	2.580	64.210	1.794
2R-2, 60-62	136.50	46.766	87.849	1.499	0.798	2.533	68.481	2.173
2R-3, 59-61	137.99	42.588	74.178	1.555	0.893	2.526	64.666	1.830
3R-1, 59-61	144.59	50.436	101.759	1.440	0.714	2.452	70.905	2.437
3R-2, 59-61	146.09	45.849	84.670	1.519	0.823	2.572	68.020	2.127
3R-3, 59-61	147.59	43.484	76.940	1.559	0.881	2.606	66.192	1.958
3R-4, 59-61	149.09	47.677	91.120	1.489	0.779	2.541	69.333	2.261
3R-5, 59-61	150.59	44.691	80.802	1.521	0.842	2.505	66.402	1.976
3R-6, 59-61	151.59	47.372	90.014	1.488	0.783	2.516	68.860	2.211
4R-1, 59-61	154.29	48.180	92.977	1.464	0.759	2.437	68.877	2.213
4R-2, 59-61	155.79	45.627	83.914	1.499	0.815	2.453	66.783	2.011
4R-3, 59-61	157.29	44.017	78.626	1.541	0.863	2.556	66.248	1.963
4R-4, 59-61	158.79	46.627	87.361	1.502	0.802	2.537	68.399	2.164
4R-5, 59-61	160.29	43.258	76.236	1.559	0.885	2.592	65.869	1.930
4R-6, 59-61	161.79	47.428	90.217	1.476	0.776	2.455	68.382	2.163
4R-7, 59-61	162.99	46.412	86.610	1.497	0.802	2.494	67.842	2.110
5R-1, 59-61	163.89	49.551	98.220	1.449	0.731	2.444	70.095	2.344
5R-2, 59-61	165.39	47.768	91.452	1.470	0.768	2.445	68.586	2.183
5R-3, 59-61	166.89	35.476	54.982	1.680	1.084	2.594	58.210	1.393
6R-1, 61-63	173.51	43.732	77.722	1.543	0.868	2.546	65.903	1.933
6R-2, 59-61	174.99	43.371	76.587	1.540	0.872	2.506	65.205	1.874
6R-3, 59-61	176.49	46.959	88.533	1.490	0.790	2.496	68.334	2.158
6R-4, 59-61	177.99	38.814	63.436	1.616	0.989	2.553	61.266	1.582
7R-1, 59-61	183.09	46.803	87.980	1.497	0.796	2.522	68.419	2.166
7R-2, 59-61	184.59	47.591	90.807	1.462	0.766	2.391	67.951	2.120
7R-3, 59-61	186.09	40.535	68.166	1.598	0.950	2.586	63.255	1.721
7R-4, 59-61	187.59	40.822	68.981	1.594	0.943	2.588	63.546	1.743
7R-5, 59-61	189.09	30.430	43.739	1.784	1.241	2.642	53.021	1.129
7R-6, 59-61	190.59	32.417	47.965	1.732	1.171	2.592	54.840	1.214
8R-1, 92-94	192.72	39.152	64.344	1.626	0.989	2.615	62.170	1.643
8R-2, 90-92	194.20	43.646	77.451	1.530	0.862	2.478	65.207	1.874
8R-3, 50-52	195.30	44.723	80.907	1.518	0.839	2.488	66.280	1.966
8R-4, 48-50	196.78	49.833	99.333	1.465	0.735	2.561	71.297	2.484
8R-5, 48-50	198.28	46.897	88.312	1.521	0.808	2.664	69.676	2.298
8R-6, 90-92	200.20	51.411	105.809	1.440	0.700	2.529	72.322	2.613
9R-1, 79-81	201.89	28.080	39.043	1.528	1.099	1.892	41.907	0.721
10R-1, 36-38	203.26	22.239	28.600	1.738	1.352	2.171	37.749	0.606
11R-1, 75-77	207.15	24.001	31.580	1.753	1.332	2.261	41.086	0.697
11R-2, 70-72	208.60	24.409	32.291	1.777	1.344	2.331	42.366	0.735
11R-3, 17-19	209.23	21.122	26.777	1.817	1.433	2.292	37.473	0.599
12R-1, 47-48	211.37	20.377	25.592	1.893	1.507	2.418	37.672	0.604
12R-2, 130-132	213.70	22.673	29.321	1.642	1.270	1.995	36.358	0.571
12R-3, 84-86	214.61	22.128	28.416	1.737	1.352	2.164	37.525	0.601
12R-4, 88-89	216.12	22.273	28.656	1.685	1.309	2.067	36.641	0.578
12R-5, 73-75	217.29	20.823	26.299	1.792	1.419	2.232	36.433	0.573
13R-1, 79-81	221.19	22.462	28.969	1.576	1.222	1.868	34.580	0.529
13R-2, 87-89	222.71	21.695	27.706	1.843	1.443	2.367	39.038	0.640
13R-3, 97-99	224.04	17.523	21.246	1.787	1.474	2.122	30.573	0.440
13R-4, 125-127	225.83	20.587	25.925	1.784	1.417	2.209	35.871	0.559
13R-5, 9-11	226.14	19.674	24.493	1.902	1.528	2.408	36.547	0.576
14R-1, 130-132	231.30	17.345	20.985	1.887	1.560	2.292	31.961	0.470
14R-2, 133-135	232.76	20.049	25.076	1.887	1.508	2.392	36.937	0.586
14R-3, 96-98	233.80	18.437	22.604	1.878	1.532	2.314	33.812	0.511
14R-4, 46-48	234.63	22.313	28.722	1.866	1.449	2.442	40.651	0.685
14R-5, 116-118	236.69	22.195	28.527	1.784	1.388	2.262	38.659	0.630
14R-6, 20-22	237.14	16.858	20.277	1.949	1.620	2.386	32.086	0.472
15R-1, 98-100	240.58	19.456	24.155	1.996	1.608	2.591	37.932	0.611
15R-2, 41-43	241.49	19.985	24.977	1.973	1.578	2.566	38.499	0.626
16R-1, 58-60	244.98	21.404	27.233	1.888	1.484	2.451	39.457	0.652
16R-2, 90-92	246.80	18.274	22.360	1.989	1.626	2.521	35.503	0.550
16R-3, 65-67	248.03	13.397	15.470	2.103	1.821	2.512	27.513	0.380
16R-4, 42-44	248.91	14.144	16.474	2.057	1.766	2.467	28.408	0.397
17R-1, 24-26	249.44	18.054	22.032	1.802	1.477	2.164	31.770	0.466
17R-2, 25-27	250.84	15.356	18.142	1.989	1.684	2.400	29.831	0.425
17R-3, 4-6	252.14	15.486	18.324	1.911	1.615	2.272	28.904	0.407
17R-4, 98-100	254.51	17.882	21.776	1.872	1.537	2.283	32.682	0.485

Table T9 (continued).

Core, section, interval (cm)	Depth (mbsf)	Water content (%)		Density (g/cm^3)			Porosity (%)	Void ratio
		Bulk	Dry	Bulk	Dry	Grain		
17R-5, 79-81	255.57	18.292	22.387	1.820	1.487	2.204	32.514	0.482
17R-6, 107-109	257.15	16.875	20.301	1.955	1.625	2.397	32.214	0.475
17R-7, 46-48	258.02	16.450	19.689	2.000	1.671	2.463	32.136	0.474
18R-3, 44-46	261.74	22.123	28.407	1.870	1.456	2.443	40.392	0.678
18R-4, 89-90	263.71	19.936	24.899	1.837	1.471	2.290	35.765	0.557
18R-5, 86-88	265.06	18.233	22.299	1.861	1.522	2.276	33.142	0.496
18R-6, 23-25	265.93	22.651	29.285	1.767	1.367	2.244	39.088	0.642
18R-7, 1-3	266.70	19.732	24.583	1.842	1.479	2.293	35.502	0.550
19R-1, 67-69	269.17	16.100	19.189	1.992	1.671	2.433	31.312	0.456
19R-2, 87-89	270.18	15.731	18.667	1.906	1.606	2.272	29.285	0.414
19R-3, 61-63	271.21	15.684	18.601	2.027	1.709	2.478	31.041	0.450
19R-4, 50-52	272.16	20.264	25.414	1.711	1.364	2.062	33.856	0.512
19R-5, 14-16	273.21	15.380	18.175	1.996	1.689	2.412	29.977	0.428
19R-6, 49-51	274.82	15.053	17.720	1.905	1.619	2.248	28.010	0.389
19R-7, 18-20	276.02	17.400	21.066	1.916	1.583	2.346	32.556	0.483
19R-8, 17-19	277.52	22.004	28.212	1.629	1.271	1.955	35.012	0.539
20R-1, 66-68	278.76	15.596	18.478	1.992	1.681	2.413	30.338	0.435
20R-2, 81-83	280.41	17.045	20.547	2.014	1.671	2.514	33.527	0.504
20R-3, 120-122	282.11	17.446	21.134	1.919	1.584	2.353	32.691	0.486
20R-4, 74-76	283.13	14.968	17.603	2.054	1.746	2.496	30.022	0.429
20R-5, 68-70	284.16	17.409	21.078	1.931	1.595	2.375	32.836	0.489
21R-1, 71-73	288.41	16.738	20.102	1.991	1.657	2.457	32.537	0.482
21R-2, 145-147	290.59	18.094	22.091	1.954	1.600	2.444	34.521	0.527
21R-3, 36-37	291.01	19.146	23.680	1.875	1.516	2.333	35.049	0.540
21R-4, 37-38	292.22	17.851	21.730	1.934	1.589	2.397	33.712	0.509
21R-6, 21-23	294.39	17.660	21.448	1.860	1.531	2.255	32.076	0.472
22R-1, 68-70	297.98	19.065	23.556	1.895	1.534	2.371	35.290	0.545
22R-2, 3-4	298.13	20.096	25.150	1.771	1.415	2.170	34.762	0.533
22R-3, 125-126	300.37	20.615	25.968	1.821	1.446	2.283	36.664	0.579
22R-4, 39-41	300.96	19.348	23.990	1.882	1.518	2.355	35.559	0.552
22R-5, 116-117	303.07	19.019	23.486	1.889	1.529	2.356	35.079	0.540
22R-6, 12-14	303.40	21.342	27.133	1.812	1.425	2.290	37.765	0.607
23R-1, 69-71	307.59	12.017	13.658	2.092	1.841	2.440	24.555	0.325
24R-1, 50-52	317.10	17.150	20.701	1.953	1.618	2.405	32.714	0.486
24R-2, 110-112	318.45	17.460	21.153	1.921	1.586	2.359	32.762	0.487
24R-3, 73-75	319.42	18.700	23.000	1.835	1.492	2.244	33.510	0.504
24R-4, 106-108	320.83	17.922	21.835	1.877	1.541	2.294	32.851	0.489
24R-5, 117-119	322.41	18.575	22.812	1.838	1.497	2.245	33.343	0.500
24R-6, 108-110	323.72	20.025	25.039	1.768	1.414	2.162	34.580	0.529
24R-7, 108-110	324.98	19.930	24.891	1.823	1.459	2.262	35.475	0.550
24R-8, 116-118	326.51	21.644	27.623	1.685	1.320	2.051	35.619	0.553
25R-1, 11-13	326.31	19.396	24.063	1.808	1.457	2.217	34.249	0.521
25R-2, 21-23	327.84	16.891	20.325	1.917	1.593	2.329	31.617	0.462
25R-3, 13-15	328.91	16.032	19.093	1.882	1.580	2.240	29.463	0.418
25R-4, 13-15	329.64	19.127	23.650	1.882	1.522	2.347	35.153	0.542
25R-5, 21-23	330.90	16.322	19.505	1.929	1.614	2.330	30.741	0.444
25R-6, 21-23	332.16	17.076	20.592	1.953	1.620	2.402	32.569	0.483
25R-7, 17-19	333.62	18.449	22.623	1.858	1.515	2.277	33.469	0.503
25R-8, 12-14	334.69	19.016	23.480	1.888	1.529	2.354	35.052	0.540
26R-1, 27-29	336.17	20.287	25.450	1.831	1.459	2.290	36.270	0.569
26R-2, 27-29	337.64	20.780	26.232	1.795	1.422	2.236	36.421	0.573
26R-3, 98-100	339.55	18.421	22.581	1.911	1.559	2.375	34.372	0.524
26R-4, 24-26	340.12	18.355	22.482	1.889	1.542	2.332	33.862	0.512
26R-5, 67-69	342.04	18.444	22.615	1.875	1.529	2.309	33.771	0.510
26R-6, 33-35	343.20	17.568	21.312	1.893	1.560	2.311	32.474	0.481
26R-7, 23-25	344.54	16.600	19.904	1.881	1.569	2.257	30.494	0.439
27R-1, 21-23	345.81	14.632	17.140	2.051	1.751	2.477	29.312	0.415
27R-2, 22-24	347.33	14.121	16.442	2.108	1.810	2.552	29.065	0.410
27R-3, 37-39	348.99	15.924	18.939	1.989	1.672	2.421	30.926	0.448
27R-4, 95-97	351.03	16.014	19.067	2.014	1.691	2.468	31.489	0.460
27R-5, 17-19	351.75	15.881	18.879	1.971	1.658	2.388	30.571	0.440
27R-6, 18-20	353.20	16.126	19.226	2.042	1.713	2.524	32.153	0.474
28R-1, 37-39	355.67	14.903	17.514	2.043	1.738	2.474	29.733	0.423
28R-2, 113-115	357.93	13.876	16.112	2.035	1.753	2.420	27.581	0.381
28R-3, 33-35	358.42	14.114	16.433	2.069	1.777	2.485	28.512	0.399
28R-4, 17-19	359.73	13.086	15.056	2.180	1.894	2.626	27.855	0.386
28R-5, 18-20	361.24	14.818	17.396	1.982	1.688	2.367	28.682	0.402
28R-6, 38-40	362.94	13.640	15.794	2.111	1.823	2.537	28.124	0.391
28R-7, 18-20	364.24	13.502	15.610	2.101	1.817	2.514	27.705	0.383

Table T9 (continued).

Core, section, interval (cm)	Depth (mbsf)	Water content (%)		Density (g/cm^3)			Porosity (%)	Void ratio
		Bulk	Dry	Bulk	Dry	Grain		
29R-1, 134-136	366.34	15.728	18.663	1.950	1.643	2.346	29.949	0.428
29R-2, 2-4	366.52	15.520	18.371	1.965	1.660	2.365	29.786	0.424
29R-3, 147-149	369.35	13.338	15.391	2.015	1.746	2.368	26.246	0.356
29R-4, 2-4	369.40	15.168	17.880	1.974	1.674	2.366	29.236	0.413
30R-1, 71-73	375.41	18.552	22.778	1.906	1.552	2.371	34.526	0.527
30R-2, 126-128	377.46	10.750	12.044	2.021	1.804	2.289	21.214	0.269
30R-3, 17-19	377.87	10.061	11.186	2.010	1.807	2.252	19.745	0.246
30R-4, 1-3	379.21	11.194	12.605	2.001	1.777	2.274	21.871	0.280
30R-5, 88-90	381.27	19.458	24.158	1.944	1.566	2.484	36.947	0.586
30R-6, 114-116	382.79	17.148	20.697	2.052	1.700	2.590	34.362	0.523
30R-7, 36-38	383.42	14.836	17.420	2.151	1.832	2.661	31.163	0.453
31R-1, 141-143	385.81	20.376	25.590	1.817	1.447	2.266	36.152	0.566
31R-2, 96-98	386.88	17.794	21.645	1.972	1.621	2.465	34.259	0.521
31R-4, 135-137	389.31	16.532	19.806	1.959	1.635	2.392	31.630	0.463
31R-5, 11-13	389.54	20.522	25.821	1.808	1.437	2.253	36.225	0.568
31R-6, 26-28	391.06	16.986	20.461	2.025	1.681	2.532	33.597	0.506
31R-7, 16-18	392.48	16.896	20.332	1.859	1.545	2.228	30.674	0.442
32R-1, 71-73	394.81	18.912	23.323	2.038	1.652	2.649	37.632	0.603
32R-2, 8-10	395.11	16.642	19.964	2.083	1.736	2.625	33.848	0.512
32R-3, 88-90	397.41	16.490	19.747	2.090	1.745	2.631	33.655	0.507
32R-4, 136-138	399.39	13.001	14.943	2.147	1.868	2.568	27.258	0.375
32R-5, 130-132	400.85	16.241	19.390	2.106	1.764	2.650	33.409	0.502
32R-6, 129-131	402.34	15.164	17.875	2.077	1.762	2.545	30.759	0.444
32R-7, 69-71	403.24	15.080	17.757	2.051	1.742	2.496	30.205	0.433
33R-1, 118-120	404.98	16.001	19.049	2.099	1.763	2.623	32.794	0.488
33R-2, 25-27	405.44	15.576	18.450	2.123	1.793	2.648	32.299	0.477
33R-3, 22-24	406.51	14.711	17.248	2.127	1.814	2.613	30.560	0.440
33R-4, 11-13	407.90	14.607	17.106	2.060	1.759	2.491	29.384	0.416
33R-5, 113-115	410.13	15.473	18.305	2.066	1.746	2.538	31.213	0.454
33R-6, 106-108	411.56	14.266	16.640	2.103	1.803	2.551	29.305	0.415
34R-1, 109-111	414.59	14.301	16.688	2.154	1.846	2.639	30.076	0.430
34R-2, 25-27	414.99	14.742	17.291	2.100	1.790	2.566	30.229	0.433
34R-3, 122-124	417.14	14.441	16.879	2.110	1.805	2.570	29.759	0.424
34R-4, 59-61	417.79	20.950	26.502	1.977	1.563	2.624	40.449	0.679
34R-5, 28-30	418.98	15.745	18.687	2.109	1.777	2.629	32.424	0.480
34R-6, 12-14	420.17	18.520	22.729	1.995	1.626	2.544	36.088	0.565
34R-7, 7-9	421.27	18.068	22.052	1.998	1.637	2.529	35.260	0.545
34R-8, 63-65	422.78	15.201	17.926	2.075	1.760	2.543	30.807	0.445
35R-1, 96-98	424.16	16.130	19.232	2.120	1.778	2.670	33.400	0.501
35R-2, 17-19	424.72	14.433	16.868	2.159	1.847	2.655	30.426	0.437
35R-3, 108-110	426.86	12.964	14.895	2.145	1.867	2.562	27.152	0.373
35R-4, 13-15	427.38	14.778	17.340	2.018	1.720	2.426	29.123	0.411
35R-5, 20-22	428.68	13.535	15.654	2.244	1.940	2.758	29.658	0.422
35R-6, 63-65	430.29	13.129	15.113	2.017	1.752	2.363	25.854	0.349
35R-7, 30-32	431.46	11.475	12.962	2.228	1.972	2.628	24.964	0.333
36R-1, 50-52	433.40	18.471	22.656	2.037	1.661	2.626	36.752	0.581
36R-2, 56-58	434.90	17.247	20.841	2.045	1.692	2.582	34.446	0.525
36R-3, 26-28	435.85	16.978	20.449	2.037	1.691	2.553	33.765	0.510
36R-4, 80-82	437.69	19.924	24.881	1.934	1.549	2.484	37.638	0.604
36R-5, 119-121	439.59	20.521	25.819	1.931	1.535	2.504	38.700	0.631
36R-6, 96-98	440.86	21.004	26.589	1.875	1.481	2.406	38.454	0.625
36R-7, 10-12	441.10	21.157	26.834	1.930	1.522	2.531	39.880	0.663
37R-1, 3-5	442.63	23.031	29.922	1.754	1.350	2.230	39.454	0.652
37R-3, 2-4	445.14	11.742	13.304	2.163	1.909	2.539	24.806	0.330
38R-2, 84-86	454.66	19.080	23.578	1.796	1.453	2.184	33.458	0.503
38R-3, 4-6	455.34	18.288	22.381	1.943	1.588	2.432	34.705	0.532
39R-1, 148-150	463.38	16.621	19.934	2.026	1.689	2.517	32.888	0.490
39R-2, 103-105	464.43	16.315	19.496	2.031	1.699	2.512	32.354	0.478
39R-3, 65-67	465.55	14.334	16.732	2.095	1.795	2.540	29.330	0.415
39R-4, 110-112	467.36	18.470	22.654	1.981	1.615	2.514	35.739	0.556
39R-5, 85-87	471.89	18.654	22.931	1.945	1.582	2.450	35.431	0.549
40R-2, 126-128	474.15	12.322	14.054	1.939	1.700	2.218	23.338	0.304
40R-3, 55-57	474.85	18.192	22.237	1.917	1.568	2.379	34.061	0.517
40R-4, 118-120	476.98	16.598	19.902	1.996	1.664	2.460	32.348	0.478
40R-5, 49-51	477.79	13.339	15.392	1.898	1.645	2.185	24.724	0.328
41R-3, 9-11	483.73	12.341	14.079	2.116	1.855	2.489	25.497	0.342
41R-4, 134-136	486.46	11.916	13.528	2.163	1.905	2.547	25.174	0.336
41R-5, 11-13	486.72	13.112	15.091	2.077	1.805	2.459	26.598	0.362
42R-1, 60-62	491.30	16.720	20.076	2.029	1.690	2.527	33.127	0.495

Table T9 (continued).

Core, section, interval (cm)	Depth (mbsf)	Water content (%)		Density (g/cm^3)			Porosity (%)	Void ratio
		Bulk	Dry	Bulk	Dry	Grain		
42R-3, 15-17	493.85	16.462	19.706	1.928	1.611	2.334	30.995	0.449
42R-5, 13-15	496.37	17.344	20.984	1.915	1.582	2.342	32.428	0.480
42R-7, 6-8	498.97	13.911	16.159	2.047	1.762	2.440	27.803	0.385
43R-1, 144-146	501.74	18.407	22.560	1.958	1.597	2.465	35.191	0.543
43R-3, 119-121	503.92	18.900	23.305	1.871	1.517	2.317	34.527	0.527
43R-4, 85-87	505.08	19.486	24.203	1.873	1.508	2.344	35.651	0.554
43R-6, 125-127	508.03	18.387	22.530	1.904	1.554	2.361	34.187	0.519
44R-1, 24-26	510.14	13.577	15.710	1.792	1.549	2.031	23.760	0.312
44R-2, 55-57	511.97	12.148	13.827	2.457	2.159	3.047	29.149	0.411
44R-3, 99-101	513.74	14.599	17.094	1.785	1.524	2.044	25.442	0.341
44R-6, 56-58	517.06	12.993	14.934	1.827	1.589	2.069	23.180	0.302
44R-8, 61-63	519.30	12.236	13.942	2.504	2.197	3.135	29.917	0.427
45R-2, 83-85	521.48	13.636	15.789	1.880	1.624	2.166	25.038	0.334
45R-4, 65-67	524.10	18.174	22.211	2.251	1.842	3.067	39.946	0.665
45R-5, 12-14	524.94	18.309	22.412	1.793	1.465	2.156	32.063	0.472
45R-6, 58-60	526.70	12.995	14.936	1.884	1.639	2.154	23.904	0.314
46R-1, 104-106	530.24	12.465	14.241	1.716	1.502	1.899	20.892	0.264

Note: This table is also available in **ASCII format.**

Table T10. *P*-wave velocity measured using the contact probe system. (See table notes. Continued on next four pages.)

Core, section, interval (cm)	Depth (mbsf)	Direction	Velocity (m/s)	Anisotropy
192-1184A-				
2R-1, 52-54	134.93	_x	1628.2	
2R-2, 62-64	136.53	_x	1576.3	
2R-3, 52-54	137.93	_x	1626.1	
3R-1, 61-63	144.62	_x	1562.7	
3R-2, 62-64	146.13	_x	1581.6	
3R-3, 60-62	147.61	_x	1582.9	
3R-4, 59-61	149.10	_x	1582.8	
3R-5, 62-64	150.63	_x	1581.5	
3R-6, 62-64	151.63	_x	1567.8	
4R-1, 62-64	154.33	_x	1578.9	
4R-2, 62-64	155.83	_x	1576.8	
4R-3, 62-64	157.33	_x	1572.3	
4R-4, 62-64	158.83	_x	1566.6	
4R-5, 62-64	160.34	_x	1572.9	
4R-6, 63-65	161.82	_x	1564.7	
4R-7, 61-63	163.02	_x	1574.3	
5R-1, 61-63	163.77	_x	1577.3	
5R-2, 46-48	165.44	_x	1563.2	
5R-3, 63-65	166.95	_x	1653.2	
6R-1, 64-66	173.55	_x	1589.0	
6R-2, 64-66	175.05	_x	1593.5	
6R-3, 63-65	176.54	_x	1570.6	
6R-4, 64-66	178.05	_x	1564.9	
7R-1, 62-64	183.13	_x	1591.8	
7R-2, 62-64	184.63	_x	1573.0	
7R-3, 62-64	186.13	_x	1585.0	
7R-4, 62-64	187.64	_x	1595.7	
7R-5, 65-67	189.16	_x	1720.9	
7R-6, 62-64	190.63	_x	1613.5	
9R-1, 78-80	201.89	Cx	3031.0	0.056
9R-1, 78-80	201.89	Cy	3025.6	
9R-1, 78-80	201.89	Cz	2864.9	
10R-1, 35-37	203.26	Cx	3214.5	0.028
10R-1, 35-37	203.26	Cy	3298.0	
10R-1, 35-37	203.26	Cz	3205.9	
11R-1, 74-76	207.15	Cx	2833.6	0.025
11R-1, 74-76	207.15	Cy	2830.8	
11R-1, 74-76	207.15	Cz	2764.3	
11R-2, 69-71	208.60	Cx	2666.9	0.031
11R-2, 69-71	208.60	Cy	2607.9	
11R-2, 69-71	208.60	Cz	2585.4	
11R-3, 21-23	209.28	Mx	3324.2	
12R-1, 113-115	212.04	Mx	3654.5	
12R-2, 129-131	213.70	Mx	3629.1	
12R-3, 83-85	214.61	Mx	3463.3	
12R-4, 88-90	216.13	Mx	3189.6	
12R-5, 72-74	217.29	Mx	3354.6	
13R-1, 22-24	220.63	_x	2739.3	
13R-1, 77-79	221.18	_x	3132.7	
13R-1, 80-82	221.21	Mx	3080.6	
13R-2, 87-89	222.72	Cx	2923.3	0.011
13R-2, 87-89	222.72	Cz	2913.0	
13R-2, 87-89	222.72	Cy	2891.1	
13R-2, 89-91	222.74	_x	2936.7	
13R-3, 62-64	223.70	_x	3028.4	
13R-3, 97-99	224.05	Mx	3233.0	
13R-3, 123-125	224.31	_x	3155.2	
13R-4, 29-31	224.88	_x	3150.3	
13R-4, 125-127	225.84	Cx	3095.2	0.016
13R-4, 125-127	225.84	Cz	3045.3	
13R-4, 125-127	225.84	Cy	3077.3	
13R-4, 129-131	225.88	_x	3123.2	
13R-5, 9-11	226.15	Mx	2981.0	
13R-5, 29-31	226.35	_x	3001.7	
14R-1, 66-68	230.67	_x	3052.8	
14R-1, 130-132	231.31	Mx	3269.3	
14R-1, 134-136	231.35	_x	3338.3	
14R-2, 95-97	232.39	_x	2706.6	
14R-2, 133-135	232.77	Cx	2976.0	0.005
14R-2, 133-135	232.77	Cz	2970.1	
14R-2, 133-135	232.77	Cy	2986.0	
14R-3, 11-13	232.96	_x	2924.6	
14R-3, 96-98	233.81	Mx	3159.0	
14R-3, 106-108	233.91	_x	3046.0	
14R-4, 35-37	234.53	_x	2927.7	
14R-4, 46-48	234.64	Cx	2952.8	0.010
14R-4, 46-48	234.64	Cz	2941.7	
14R-4, 46-48	234.64	Cy	2970.7	
14R-4, 80-82	234.98	_x	2932.6	
14R-5, 49-51	236.03	_x	2926.2	
14R-5, 109-111	236.63	_x	3055.2	
14R-5, 117-119	236.71	Mx	3002.2	
14R-6, 19-21	237.14	_x	3287.5	
14R-6, 20-22	237.15	Cx	3296.8	0.019
14R-6, 20-22	237.15	Cz	3285.2	
14R-6, 20-22	237.15	Cy	3234.9	
14R-6, 69-71	237.64	_x	3287.2	
15R-1, 11-13	239.72	_x	2850.6	
15R-1, 79-81	240.40	_x	2240.0	
15R-1, 98-100	240.59	Cx	2446.3	0.048
15R-1, 98-100	240.59	Cz	2330.4	
15R-1, 98-100	240.59	Cy	2446.1	
15R-1, 106-108	240.67	_x	2373.8	
15R-1, 133-135	240.94	_x	2555.4	
15R-2, 41-43	241.50	Cz	2477.8	0.030
15R-2, 41-43	241.50	Cx	2530.4	
15R-2, 41-43	241.50	Cy	2553.9	
15R-2, 51-53	241.60	_x	2497.6	
16R-1, 29-31	244.70	_x	2883.1	
16R-1, 58-60	244.99	Cx	2903.0	0.012
16R-1, 58-60	244.99	Cz	2866.9	
16R-1, 58-60	244.99	Cy	2895.3	
16R-1, 99-101	245.40	_x	3011.8	
16R-2, 11-13	246.02	_x	3096.2	
16R-2, 90-92	246.81	Cx	3213.2	0.026
16R-2, 90-92	246.81	Cz	3131.7	
16R-2, 90-92	246.81	Cy	3152.2	
16R-2, 119-121	247.10	_x	3225.4	
16R-3, 19-21	247.58	_x	3438.7	
16R-3, 65-67	248.04	Cx	3612.1	0.006
16R-3, 65-67	248.04	Cz	3592.1	
16R-3, 65-67	248.04	Cy	3594.5	
16R-3, 99-101	248.38	_x	3561.2	
16R-4, 19-21	248.69	_x	3549.4	
16R-4, 42-44	248.92	Cy	3569.9	0.025
16R-4, 42-44	248.92	Cx	3606.9	
16R-4, 42-44	248.92	Cz	3517.0	
17R-1, 24-26	249.45	Mx	3455.1	
17R-1, 31-33	249.52	_x	3346.7	
17R-1, 69-71	249.90	_x	3498.8	
17R-1, 129-131	250.50	_x	3590.6	
17R-2, 24-26	250.84	Cx	3376.7	0.065
17R-2, 24-26	250.84	Cy	3605.7	
17R-2, 24-26	250.84	Cz	3588.7	
17R-2, 49-51	251.09	_x	3495.5	
17R-2, 71-73	251.31	_x	3525.3	
17R-3, 3-5	252.14	Cx	3544.8	0.056
17R-3, 3-5	252.14	Cy	3704.1	
17R-3, 3-5	252.14	Cz	3749.0	
17R-3, 79-81	252.90	_x	3612.4	
17R-3, 134-136	253.45	_x	3599.9	
17R-4, 9-11	253.63	_x	3540.1	
17R-4, 74-76	254.28	_x	3550.0	
17R-4, 99-101	254.53	Mx	3573.0	
17R-5, 9-11	254.88	_x	3549.6	

Table T10 (continued).

Core, section, interval (cm)	Depth (mbsf)	Direction	Velocity (m/s)	Anisotropy
17R-5, 29-31	255.08	_x	3593.5	
17R-5, 59-61	255.38	_x	3405.5	
17R-5, 78-80	255.57	Cx	3549.8	0.024
17R-5, 78-80	255.57	Cy	3634.5	
17R-5, 78-80	255.57	Cz	3611.2	
17R-5, 99-101	255.78	_x	3497.0	
17R-5, 127-129	256.06	_x	3538.9	
17R-6, 9-11	256.18	_x	3477.6	
17R-6, 19-21	256.28	_x	3521.6	
17R-6, 29-31	256.38	_x	3470.6	
17R-6, 39-41	256.48	_x	3538.4	
17R-6, 49-51	256.58	_x	3498.4	
17R-6, 59-61	256.68	_x	3563.5	
17R-6, 69-71	256.78	_x	3463.4	
17R-6, 106-108	257.15	Mx	3523.1	
17R-6, 119-121	257.28	_x	3484.0	
17R-6, 139-141	257.48	_x	3431.7	
17R-7, 9-11	257.66	_x	3530.8	
17R-7, 19-21	257.76	_x	3350.6	
17R-7, 34-36	257.91	_x	3501.9	
17R-7, 45-47	258.02	Cy	3534.0	0.011
17R-7, 45-47	258.02	Cz	3553.1	
17R-7, 45-47	258.02	Cx	3512.8	
18R-1, 9-11	259.00	_x	3489.2	
18R-1, 29-31	259.20	_x	3550.4	
18R-1, 59-61	259.50	_x	3269.0	
18R-1, 85-87	259.76	Mx	3355.4	
18R-1, 119-121	260.00	_x	3480.5	
18R-2, 9-11	260.04	_x	3551.4	
18R-2, 29-31	260.24	_x	3480.5	
18R-2, 59-61	260.54	_x	3482.4	
18R-2, 79-81	260.74	_x	3508.4	
18R-2, 96-98	260.91	Cx	3146.7	0.094
18R-2, 96-98	260.91	Cy	3462.3	
18R-2, 96-98	260.91	Cz	3455.5	
18R-3, 44-46	261.75	Mx	3413.5	
18R-3, 59-61	261.90	_x	3385.7	
18R-4, 29-31	263.12	_x	3025.2	
18R-4, 59-61	263.42	_x	3390.9	
18R-4, 88-90	263.71	Cx	3329.6	0.028
18R-4, 88-90	263.71	Cy	3424.6	
18R-4, 88-90	263.71	Cz	3391.1	
18R-4, 119-121	264.02	_x	3374.5	
18R-5, 9-11	264.30	_x	3417.3	
18R-5, 29-31	264.50	_x	3394.8	
18R-5, 49-51	264.70	_x	3236.4	
18R-5, 85-87	265.06	Cx	3328.9	0.018
18R-5, 85-87	265.06	Cy	3387.8	
18R-5, 85-87	265.06	Cz	3338.6	
18R-5, 99-101	265.20	_x	3283.5	
18R-5, 119-121	265.40	_x	3200.6	
18R-5, 134-136	265.55	_x	3266.7	
18R-6, 23-25	265.94	Mx	3161.6	
18R-6, 49-51	266.20	_x	3124.2	
18R-6, 64-66	266.35	_x	3201.5	
18R-6, 79-81	266.50	_x	3185.2	
18R-7, 9-11	266.79	_x	3219.4	
18R-7, 19-21	266.89	_x	3311.7	
18R-7, 39-41	267.09	_x	3277.8	
18R-7, 49-51	267.19	_x	3279.0	
18R-7, 69-71	267.39	_x	3215.7	
18R-7, 89-91	267.59	_x	3223.1	
18R-7, 109-111	267.79	_x	3260.3	
19R-1, 19-21	268.70	_x	3264.0	
19R-1, 57-59	269.08	_x	3328.8	
19R-1, 67-69	269.18	Cx	3359.4	0.036
19R-1, 67-69	269.18	Cz	3240.8	
19R-1, 67-69	269.18	Cy	3307.1	
19R-2, 79-81	270.11	_x	3352.0	
19R-2, 87-89	270.19	Mx	3390.0	
19R-3, 19-21	270.80	_x	3365.9	
19R-3, 61-63	271.22	Cx	3320.0	0.029
19R-3, 61-63	271.22	Cz	3418.6	
19R-3, 61-63	271.22	Cy	3386.9	
19R-3, 79-81	271.40	_x	3572.1	
19R-4, 19-21	271.86	_x	3554.5	
19R-4, 50-52	272.17	Mx	3426.2	
19R-4, 89-91	272.56	_x	3580.5	
19R-5, 14-16	273.22	Cx	3395.9	0.016
19R-5, 14-16	273.22	Cz	3447.8	
19R-5, 14-16	273.22	Cy	3451.3	
19R-5, 17-19	273.25	_x	3370.5	
19R-5, 69-71	273.77	_x	3632.8	
19R-5, 99-101	274.07	_x	3795.2	
19R-6, 49-51	274.83	_x	3606.6	
19R-6, 49-51	274.83	Mx	3495.3	
19R-6, 114-116	275.48	_x	3453.6	
19R-7, 16-18	276.01	_x	3388.3	
19R-7, 18-20	276.03	Cx	3372.3	0.027
19R-7, 18-20	276.03	Cz	3447.0	
19R-7, 18-20	276.03	Cy	3355.5	
19R-7, 92-94	276.77	_x	3420.2	
19R-8, 9-11	277.45	_x	3139.1	
19R-8, 17-19	277.53	Mx	3199.8	
19R-8, 29-31	277.65	_x	3086.1	
19R-8, 49-51	277.85	_x	3293.3	
20R-1, 49-51	278.60	_x	3502.8	
20R-1, 66-68	278.77	Mx	3530.4	
20R-1, 119-121	279.30	_x	3383.2	
20R-2, 67-69	280.28	_x	3424.0	
20R-2, 81-83	280.42	Cx	3265.2	0.035
20R-2, 81-83	280.42	Cz	3381.1	
20R-2, 81-83	280.42	Cy	3366.5	
20R-3, 17-19	281.09	_x	3418.9	
20R-3, 64-66	281.56	_x	3375.8	
20R-3, 120-122	282.12	Mx	3512.4	
20R-4, 29-31	282.69	_x	3585.2	
20R-4, 73-75	283.13	Cx	3460.6	0.009
20R-4, 73-75	283.13	Cz	3485.9	
20R-4, 73-75	283.13	Cy	3492.3	
20R-5, 7-9	283.56	_x	3583.3	
20R-5, 68-70	284.17	Mx	3397.7	
21R-1, 9-11	287.80	_x	3491.1	
21R-1, 70-72	288.41	Cx	3487.5	0.006
21R-1, 70-72	288.41	Cy	3491.6	
21R-1, 70-72	288.41	Cz	3472.4	
21R-1, 132-134	289.03	_x	3240.9	
21R-2, 59-61	289.74	_x	3300.5	
21R-2, 144-146	290.59	Cx	3237.8	0.012
21R-2, 144-146	290.59	Cy	3259.8	
21R-2, 144-146	290.59	Cz	3277.0	
21R-3, 35-37	291.01	Mx	3446.4	
21R-3, 79-81	291.45	_x	3268.5	
21R-3, 109-111	291.75	_x	3186.6	
21R-4, 9-11	291.95	_x	3197.1	
21R-4, 19-21	292.05	_x	3209.8	
21R-4, 29-31	292.15	_x	3355.1	
21R-4, 36-38	292.22	Cx	3393.4	0.011
21R-4, 36-38	292.22	Cy	3398.1	
21R-4, 36-38	292.22	Cz	3360.1	
21R-4, 59-61	292.45	_x	3355.7	
21R-4, 69-71	292.55	_x	3193.9	
21R-4, 79-81	292.65	_x	3286.3	
21R-5, 9-11	292.78	_x	3197.9	
21R-5, 19-21	292.88	_x	3343.9	
21R-5, 29-31	292.98	_x	3267.2	
21R-5, 37-39	293.06	Mx	3277.9	
21R-5, 39-41	293.08	_x	3285.7	
21R-5, 49-51	293.18	_x	3416.0	
21R-5, 59-61	293.28	_x	3369.1	

Table T10 (continued).

Core, section, interval (cm)	Depth (mbsf)	Direction	Velocity (m/s)	Anisotropy
21R-5, 99-101	293.68	_x	3370.4	
21R-5, 119-121	293.88	_x	3358.4	
21R-5, 139-141	294.08	_x	3293.2	
21R-6, 9-11	294.28	_x	3180.1	
21R-6, 20-22	294.39	Mx	3289.0	
21R-7, 39-41	296.08	_x	3340.7	
21R-7, 49-51	296.18	_x	3279.4	
21R-7, 59-61	296.28	_x	3346.5	
22R-1, 9-11	297.40	_x	3258.6	
22R-1, 67-69	297.98	Cx	3202.2	0.010
22R-1, 67-69	297.98	Cy	3233.4	
22R-1, 67-69	297.98	Cz	3226.7	
22R-2, 2-4	298.13	Mx	3225.7	
22R-2, 49-51	298.60	_x	3205.4	
22R-2, 99-101	299.10	_x	3325.7	
22R-3, 9-11	299.22	_x	3246.9	
22R-3, 19-21	299.32	_x	3162.1	
22R-3, 37-39	299.50	_x	3092.4	
22R-3, 99-101	300.12	_x	3184.5	
22R-3, 124-126	300.37	Mx	3241.9	
22R-4, 9-11	300.67	_x	3194.7	
22R-4, 19-21	300.77	_x	3147.2	
22R-4, 38-40	300.96	Cx	3215.4	0.018
22R-4, 38-40	300.96	Cy	3273.3	
22R-4, 38-40	300.96	Cz	3247.7	
22R-4, 129-131	301.87	_x	3219.3	
22R-5, 9-11	302.01	_x	3219.0	
22R-5, 69-71	302.61	_x	3150.5	
22R-5, 117-119	303.09	Mx	3263.3	
22R-6, 11-13	303.40	Cx	2840.3	0.133
22R-6, 11-13	303.40	Cy	3234.9	
22R-6, 11-13	303.40	Cz	3252.4	
22R-6, 69-71	303.98	_x	3131.6	
22R-6, 74-76	304.03	_x	3239.6	
22R-6, 99-101	304.28	_x	3741.6	
22R-6, 104-106	304.33	_x	3888.0	
22R-6, 109-111	304.38	_x	4058.6	
22R-CC, 1-3	304.43	_x	3838.0	
23R-1, 69-71	307.60	Mx	3531.1	
24R-1, 29-31	316.90	_x	3455.0	
24R-2, 29-31	317.65	_x	3304.4	
24R-2, 110-112	318.46	Mx	3346.7	
24R-3, 29-31	318.99	_x	3263.1	
24R-3, 73-75	319.43	Cx	3282.6	0.008
24R-3, 73-75	319.43	Cz	3292.6	
24R-3, 73-75	319.43	Cy	3308.6	
24R-4, 29-31	320.07	_x	3418.6	
24R-4, 106-108	320.84	Mx	3327.3	
24R-5, 29-31	321.54	_x	3365.4	
24R-5, 117-119	322.42	Cx	3419.5	0.032
24R-5, 117-119	322.42	Cz	3315.2	
24R-5, 117-119	322.42	Cy	3312.8	
24R-6, 29-31	322.94	_x	3183.9	
24R-6, 108-110	323.73	Mx	3207.5	
24R-7, 29-31	324.20	_x	3232.0	
24R-7, 108-110	324.99	Cx	3285.4	0.025
24R-7, 108-110	324.99	Cz	3205.3	
24R-7, 108-110	324.99	Cy	3217.5	
24R-8, 29-31	325.65	_x	3252.8	
25R-1, 11-13	326.32	Mx	3239.2	
24R-8, 115-117	326.51	Mx	3249.3	
25R-1, 119-121	327.40	_x	3215.9	
25R-2, 21-23	327.85	Cx	3238.7	0.007
25R-2, 21-23	327.85	Cz	3227.2	
25R-2, 21-23	327.85	Cy	3215.2	
25R-2, 119-121	328.83	_x	3311.5	
25R-3, 13-15	328.92	Mx	3516.5	
25R-3, 59-61	329.38	_x	3367.3	
25R-4, 13-15	329.65	Cx	3290.8	0.003
25R-4, 13-15	329.65	Cz	3290.6	
25R-4, 13-15	329.65	Cy	3280.0	
25R-4, 99-101	330.51	_x	3335.8	
25R-5, 21-23	330.91	Mx	3335.8	
25R-5, 89-91	331.59	_x	3111.6	
25R-6, 21-23	332.17	Cx	3331.8	0.030
25R-6, 21-23	332.17	Cz	3292.5	
25R-6, 21-23	332.17	Cy	3234.4	
25R-6, 119-121	333.15	_x	4012.9	
25R-7, 17-19	333.63	Mx	3088.7	
25R-7, 99-101	334.45	_x	3113.1	
25R-8, 12-14	334.70	Cx	3183.3	0.025
25R-8, 12-14	334.70	Cz	3265.0	
25R-8, 12-14	334.70	Cy	3219.8	
25R-8, 69-71	335.27	_x	3110.9	
26R-1, 27-29	336.18	Cx	3181.0	0.021
26R-1, 27-29	336.18	Cz	3126.5	
26R-1, 27-29	336.18	Cy	3114.0	
26R-2, 27-29	337.65	Mx	3076.4	
26R-3, 98-100	339.56	Cx	3302.6	0.007
26R-3, 98-100	339.56	Cz	3324.6	
26R-3, 98-100	339.56	Cy	3319.0	
26R-4, 24-26	340.13	Mx	3106.7	
26R-5, 67-69	342.05	Cx	3364.8	0.016
26R-5, 67-69	342.05	Cz	3375.6	
26R-5, 67-69	342.05	Cy	3322.5	
26R-6, 33-35	343.21	Mx	3405.4	
26R-7, 23-25	344.55	Cx	3017.2	0.012
26R-7, 23-25	344.55	Cz	3053.3	
26R-7, 23-25	344.55	Cy	3021.1	
27R-1, 21-23	345.82	Mx	3493.4	
27R-2, 22-24	347.34	Cx	3495.5	0.014
27R-2, 22-24	347.34	Cz	3446.7	
27R-2, 22-24	347.34	Cy	3492.5	
27R-3, 37-39	349.00	Mx	3517.0	
27R-4, 95-97	351.04	Cx	3526.6	0.039
27R-4, 95-97	351.04	Cz	3395.3	
27R-4, 95-97	351.04	Cy	3392.9	
27R-5, 17-19	351.76	Mx	3512.1	
27R-6, 18-20	353.21	Cx	3480.0	0.022
27R-6, 18-20	353.21	Cz	3440.0	
27R-6, 18-20	353.21	Cy	3403.6	
28R-1, 37-39	355.68	Mx	3388.1	
28R-2, 113-115	357.94	Cx	3612.5	0.027
28R-2, 113-115	357.94	Cz	3591.0	
28R-2, 113-115	357.94	Cy	3515.8	
28R-3, 33-35	358.43	Mx	3502.8	
28R-4, 17-19	359.74	Cx	3665.2	0.002
28R-4, 17-19	359.74	Cz	3663.9	
28R-4, 17-19	359.74	Cy	3658.5	
28R-5, 18-20	361.25	Mx	3499.1	
28R-6, 38-40	362.95	Cx	3575.5	0.029
28R-6, 38-40	362.95	Cz	3485.1	
28R-6, 38-40	362.95	Cy	3473.3	
28R-7, 18-20	364.25	Mx	3616.7	
29R-1, 133-135	366.34	Mx	3496.7	
29R-2, 1-3	366.52	Cx	3406.6	0.012
29R-2, 1-3	366.52	Cy	3410.8	
29R-2, 1-3	366.52	Cz	3368.4	
29R-3, 146-148	369.35	Cx	3509.7	0.035
29R-3, 146-148	369.35	Cy	3389.0	
29R-3, 146-148	369.35	Cz	3502.7	
29R-4, 1-3	369.40	Cx	3438.6	0.020
29R-4, 1-3	369.40	Cy	3506.7	
29R-4, 1-3	369.40	Cz	3484.6	
29R-4, 89-91	370.28	_x	3403.9	
29R-4, 109-111	370.48	_x	3379.8	
29R-4, 139-141	370.78	_x	3400.2	
29R-5, 39-41	371.28	_x	3354.5	
29R-5, 65-67	371.54	Mx	3332.1	
30R-1, 70-72	375.41	Cx	3321.9	0.049

Table T10 (continued).

Core, section, interval (cm)	Depth (mbsf)	Direction	Velocity (m/s)	Anisotropy
30R-1, 70-72	375.41	Cy	3241.4	
30R-1, 70-72	375.41	Cz	3164.5	
30R-2, 125-127	377.46	Cx	4407.8	0.034
30R-2, 125-127	377.46	Cy	4261.7	
30R-2, 125-127	377.46	Cz	4289.6	
30R-3, 16-18	377.87	Mx	4316.7	
30R-3, 139-141	379.10	_x	3975.0	
30R-4, 0-2	379.21	Cy	4218.8	
30R-4, 0-2	379.21	Cz	4019.6	
30R-4, 17-19	379.38	_x	4110.0	
30R-5, 87-89	381.27	Cx	2866.5	0.065
30R-5, 87-89	381.27	Cy	2890.7	
30R-5, 87-89	381.27	Cz	2708.3	
30R-5, 109-111	381.49	_x	3542.5	
30R-6, 113-115	382.79	Cx	2576.1	0.046
30R-6, 113-115	382.79	Cy	2588.1	
30R-6, 113-115	382.79	Cz	2470.7	
30R-7, 35-37	383.42	Cx	2793.9	0.053
30R-7, 35-37	383.42	Cy	2806.1	
30R-7, 35-37	383.42	Cz	2660.6	
31R-1, 140-142	385.81	Cz	2591.5	0.004
31R-1, 140-142	385.81	Cy	2580.2	
31R-1, 140-142	385.81	Cx	2580.9	
31R-2, 29-31	386.22	_x	2908.0	
31R-3, 39-41	387.31	_x	2868.0	
31R-3, 89-91	387.81	_x	2841.4	
31R-4, 134-136	389.31	Cx	3062.3	0.018
31R-4, 134-136	389.31	Cy	3081.9	
31R-4, 134-136	389.31	Cz	3026.8	
31R-5, 10-12	389.54	Cx	2862.6	0.050
31R-5, 10-12	389.54	Cy	2920.1	
31R-5, 10-12	389.54	Cz	2777.7	
31R-6, 25-27	391.06	Cx	3266.1	0.046
31R-6, 25-27	391.06	Cy	3339.2	
31R-6, 25-27	391.06	Cz	3187.6	
31R-7, 15-17	392.48	Cx	3922.8	0.022
31R-7, 15-17	392.48	Cy	3999.5	
31R-7, 15-17	392.48	Cz	3914.0	
32R-1, 71-73	394.82	Cx	2958.2	0.026
32R-1, 71-73	394.82	Cz	2881.7	
32R-1, 71-73	394.82	Cy	2923.7	
32R-2, 8-10	395.12	Cx	3032.2	0.002
32R-2, 8-10	395.12	Cz	3034.6	
32R-2, 8-10	395.12	Cy	3038.3	
32R-3, 88-90	397.42	Cx	3138.9	0.035
32R-3, 88-90	397.42	Cz	3029.5	
32R-3, 88-90	397.42	Cy	3088.3	
32R-4, 136-138	399.40	Mx	3687.2	
32R-5, 130-132	400.86	Cx	3343.0	0.009
32R-5, 130-132	400.86	Cz	3313.2	
32R-5, 130-132	400.86	Cy	3377.0	
32R-6, 129-131	402.35	Mx	3149.1	
32R-7, 69-71	403.25	Cx	3349.8	0.045
32R-7, 69-71	403.25	Cz	3203.8	
32R-7, 69-71	403.25	Cy	3229.5	
33R-1, 118-120	404.99	Cz	3007.7	0.017
33R-1, 118-120	404.99	Cy	3058.6	
33R-1, 118-120	404.99	Cx	3050.0	
33R-2, 25-27	405.45	Cx	3019.9	0.029
33R-2, 25-27	405.45	Cz	3109.0	
33R-2, 25-27	405.45	Cy	3031.1	
33R-3, 22-24	406.52	Cx	3276.2	0.017
33R-3, 22-24	406.52	Cz	3332.3	
33R-3, 22-24	406.52	Cy	3294.8	
33R-4, 19-21	407.99	_x	3386.6	
33R-5, 113-115	410.14	Cx	3192.8	0.023
33R-5, 113-115	410.14	Cz	3189.9	
33R-5, 113-115	410.14	Cy	3263.6	
33R-6, 106-108	411.57	Mx	3356.3	
34R-1, 109-111	414.60	Cx	3559.2	0.021
34R-1, 109-111	414.60	Cz	3505.8	
34R-1, 109-111	414.60	Cy	3582.0	
34R-2, 25-27	415.00	Cx	3279.3	0.007
34R-2, 25-27	415.00	Cz	3278.0	
34R-2, 25-27	415.00	Cy	3301.2	
34R-3, 122-124	417.15	Cx	3636.4	0.041
34R-3, 122-124	417.15	Cz	3489.7	
34R-3, 122-124	417.15	Cy	3512.8	
34R-4, 59-61	417.80	Mx	3042.4	
34R-5, 28-30	418.99	Cx	3270.2	0.008
34R-5, 28-30	418.99	Cz	3267.2	
34R-5, 28-30	418.99	Cy	3292.8	
34R-6, 12-14	420.18	Mx	3127.6	
34R-7, 7-9	421.28	Cx	3073.6	0.013
34R-7, 7-9	421.28	Cz	3078.6	
34R-7, 7-9	421.28	Cy	3112.5	
34R-8, 63-65	422.79	Cx	3172.7	0.010
34R-8, 63-65	422.79	Cz	3143.3	
34R-8, 63-65	422.79	Cy	3174.5	
35R-1, 96-98	424.17	Mx	3263.0	
35R-2, 17-19	424.73	Cx	3392.2	0.029
35R-2, 17-19	424.73	Cz	3295.6	
35R-2, 17-19	424.73	Cy	3338.0	
35R-4, 12-14	427.38	Cx	3459.7	0.026
35R-4, 12-14	427.38	Cz	3539.5	
35R-4, 12-14	427.38	Cy	3552.7	
35R-5, 20-22	428.69	Cx	3635.4	0.017
35R-5, 20-22	428.69	Cz	3580.5	
35R-5, 20-22	428.69	Cy	3573.0	
35R-6, 64-66	430.31	Cx	3735.3	0.035
35R-6, 64-66	430.31	Cz	3639.2	
35R-6, 64-66	430.31	Cy	3607.3	
35R-7, 30-32	431.47	Cz	3685.8	0.046
35R-7, 30-32	431.47	Cy	3618.6	
35R-7, 30-32	431.47	Cx	3789.2	
35R-8, 11-13	432.10	Cx	3698.4	0.003
35R-8, 11-13	432.10	Cz	3700.7	
35R-8, 11-13	432.10	Cy	3690.4	
36R-1, 50-52	433.41	Cx	2969.3	0.041
36R-1, 50-52	433.41	Cz	2849.3	
36R-1, 50-52	433.41	Cy	2895.7	
36R-2, 56-58	434.91	Cx	3180.4	0.037
36R-2, 56-58	434.91	Cz	3129.2	
36R-2, 56-58	434.91	Cy	3246.1	
36R-3, 26-28	435.86	Cx	3119.0	0.035
36R-3, 26-28	435.86	Cz	3021.3	
36R-3, 26-28	435.86	Cy	3128.5	
36R-4, 80-82	437.70	Cx	2938.2	0.033
36R-4, 80-82	437.70	Cz	2900.5	
36R-4, 80-82	437.70	Cy	2998.1	
36R-5, 119-121	439.60	Cx	2918.3	0.051
36R-5, 119-121	439.60	Cz	2804.6	
36R-5, 119-121	439.60	Cy	2953.1	
36R-6, 96-98	440.87	Mx	2906.8	
36R-7, 10-12	441.11	Cx	2866.4	0.034
36R-7, 10-12	441.11	Cz	2794.6	
36R-7, 10-12	441.11	Cy	2891.8	
37R-1, 2-4	442.63	Cx	2823.8	0.045
37R-1, 2-4	442.63	Cy	2953.1	
37R-1, 2-4	442.63	Cz	2901.7	
37R-1, 85-87	443.46	_x	2714.1	
37R-2, 99-101	444.62	Mx	3210.7	
37R-2, 135-137	444.98	_x	3631.0	
37R-3, 1-3	445.14	Cx	3598.9	0.061
37R-3, 1-3	445.14	Cy	3634.3	
37R-3, 1-3	445.14	Cz	3418.8	
37R-3, 62-64	445.75	_x	3500.0	
38R-1, 29-31	452.60	_x	3106.9	
38R-1, 59-61	452.90	_x	2960.9	
38R-2, 83-85	454.66	Mx	3144.7	

Table T10 (continued).

Core, section, interval (cm)	Depth (mbsf)	Direction	Velocity (m/s)	Anisotropy
38R-3, 3-5	455.34	Cx	3061.1	0.022
38R-3, 3-5	455.34	Cy	3102.4	
38R-3, 3-5	455.34	Cz	3035.0	
38R-3, 39-41	455.70	_x	3829.7	
38R-3, 59-61	455.90	_x	3839.4	
39R-1, 147-149	463.38	Cx	3173.9	0.079
39R-1, 147-149	463.38	Cy	3237.4	
39R-1, 147-149	463.38	Cz	2989.1	
39R-2, 102-104	464.43	Cx	3346.8	0.091
39R-2, 102-104	464.43	Cy	3271.1	
39R-2, 102-104	464.43	Cz	3052.7	
39R-3, 64-66	465.55	Cx	3697.2	0.022
39R-3, 64-66	465.55	Cy	3777.5	
39R-3, 64-66	465.55	Cz	3699.1	
39R-4, 109-111	467.36	Cx	3140.6	0.035
39R-4, 109-111	467.36	Cy	3251.6	
39R-4, 109-111	467.36	Cz	3159.4	
39R-5, 84-86	468.52	Mx	3703.8	
40R-1, 39-41	471.90	Cx	4323.3	0.022
40R-1, 39-41	471.90	Cz	4228.7	
40R-1, 39-41	471.90	Cy	4244.3	
40R-2, 126-128	474.16	Cx	4080.8	0.003
40R-2, 126-128	474.16	Cz	4070.6	
40R-2, 126-128	474.16	Cy	4081.1	
40R-3, 55-57	474.86	Mx	3684.7	
40R-4, 118-120	476.99	Cx	3740.9	0.006
40R-4, 118-120	476.99	Cz	3756.7	
40R-4, 118-120	476.99	Cy	3763.2	
40R-5, 49-51	477.80	Cx	4050.8	0.011
40R-5, 49-51	477.80	Cz	4065.8	
40R-5, 49-51	477.80	Cy	4020.4	
41R-1, 29-31	481.40	_x	4102.7	
41R-2, 9-11	482.71	_x	4118.6	
41R-3, 9-11	483.74	Cx	3740.5	0.022
41R-3, 9-11	483.74	Cz	3688.6	
41R-3, 9-11	483.74	Cy	3659.4	
41R-4, 134-136	486.47	Mx	3630.5	
41R-5, 11-13	486.73	Cx	3669.6	0.014
41R-5, 11-13	486.73	Cz	3722.0	
41R-5, 11-13	486.73	Cy	3704.8	
41R-6, 69-71	488.75	_x	4254.1	
41R-7, 99-101	490.11	_x	4125.9	
42R-1, 9-11	490.80	_x	3756.5	
42R-1, 29-31	491.00	_x	3748.9	
42R-1, 59-61	491.30	Cx	3804.4	0.011
42R-1, 59-61	491.30	Cy	3797.1	
42R-1, 59-61	491.30	Cz	3762.6	
42R-2, 1-3	492.22	_x	4195.6	
42R-2, 19-21	492.40	_x	3985.0	
42R-2, 29-31	492.50	_x	4036.3	
42R-2, 29-31	492.50	_x	4087.4	
42R-2, 39-41	492.60	_x	3989.5	
42R-3, 14-16	493.85	Mx	3751.1	
42R-4, 17-19	495.38	_x	3902.6	
42R-5, 13-15	496.38	Cx	3894.0	0.016
42R-5, 13-15	496.38	Cx	3850.5	
42R-5, 13-15	496.38	Cz	3833.5	
42R-5, 29-31	496.54	_x	3825.7	
42R-5, 39-41	496.64	_x	3759.9	
42R-5, 49-51	496.74	_x	4026.2	
42R-6, 59-61	498.01	_x	4163.5	
42R-6, 69-71	498.11	_x	4055.0	
42R-6, 79-81	498.21	_x	3973.0	
42R-6, 95-97	498.37	_x	3875.0	
42R-6, 99-101	498.41	_x	3838.7	
42R-7, 6-8	498.98	Cx	3963.6	0.009
42R-7, 6-8	498.98	Cy	3955.6	
42R-7, 6-8	498.98	Cz	3926.3	
42R-7, 134-136	500.26	_x	3834.9	
42R-7, 144-146	500.36	_x	3619.7	
43R-1, 9-11	500.40	_x	3417.5	
43R-1, 39-41	500.70	_x	3311.5	
43R-1, 59-61	500.90	_x	3388.8	
43R-1, 143-145	501.74	Cx	3152.7	0.027
43R-1, 143-145	501.74	Cy	3159.2	
43R-1, 143-145	501.74	Cz	3073.7	
43R-2, 9-11	501.90	_x	3374.6	
43R-2, 29-31	502.10	_x	3337.2	
43R-3, 118-120	503.92	Cx	3564.8	0.024
43R-3, 118-120	503.92	Cy	3652.0	
43R-3, 118-120	503.92	Cz	3641.8	
43R-4, 84-86	505.08	_x	3838.8	
43R-5, 1-3	505.30	_x	3329.0	
43R-5, 19-21	505.48	_x	3507.4	
43R-5, 39-41	505.68	_x	3461.0	
43R-5, 59-61	505.88	_x	3760.6	
43R-5, 79-81	506.08	_x	3709.6	
43R-6, 125-127	508.04	Cx	3469.7	0.035
43R-6, 125-127	508.04	Cy	3592.1	
43R-6, 125-127	508.04	Cz	3571.9	
43R-7, 19-21	508.44	_x	3556.8	
43R-7, 39-41	508.64	_x	3407.8	
43R-7, 69-71	508.94	_x	3489.4	
43R-7, 89-91	509.14	_x	4147.2	
43R-7, 99-101	509.24	_x	4154.5	
43R-7, 109-111	509.34	_x	4134.2	
44R-1, 23-25	510.14	Cx	4041.6	0.040
44R-1, 23-25	510.14	Cy	4167.9	
44R-1, 23-25	510.14	Cz	4207.1	
44R-2, 54-56	511.97	Cx	4154.8	0.060
44R-2, 54-56	511.97	Cy	3916.1	
44R-2, 54-56	511.97	Cz	3916.6	
44R-3, 98-100	513.74	Mx	4174.6	
44R-4, 19-21	514.29	_x	3874.8	
44R-4, 39-41	514.49	_x	3931.0	
44R-4, 59-61	514.69	_x	3878.6	
44R-5, 79-81	516.00	_x	3988.9	
44R-5, 99-101	516.20	_x	4091.6	
44R-5, 119-121	516.40	_x	4085.5	
44R-6, 55-57	517.06	Cx	4108.8	0.018
44R-6, 55-57	517.06	Cy	4132.2	
44R-6, 55-57	517.06	Cz	4183.0	
44R-7, 39-41	518.29	_x	4133.2	
44R-7, 59-61	518.49	_x	4090.4	
44R-7, 79-81	518.69	_x	4153.4	
44R-8, 60-62	519.30	Cx	4144.9	0.031
44R-8, 60-62	519.30	Cy	4255.1	
44R-8, 60-62	519.30	Cz	4277.3	
45R-1, 109-111	520.60	Cx	4174.8	0.016
45R-1, 109-111	520.60	Cy	4243.2	
45R-1, 109-111	520.60	Cz	4236.9	
45R-2, 82-84	521.48	Cx	3939.7	0.067
45R-2, 82-84	521.48	Cy	4111.0	
45R-2, 82-84	521.48	Cz	4212.0	
45R-4, 64-66	524.10	Mx	3786.7	
45R-5, 11-13	524.94	Cx	3831.1	0.030
45R-5, 11-13	524.94	Cy	3941.5	
45R-5, 11-13	524.94	Cz	3949.9	
45R-6, 57-59	526.70	Cx	3925.5	0.048
45R-6, 57-59	526.70	Cy	4120.3	
45R-6, 57-59	526.70	Cz	4094.4	
46R-1, 69-71	529.90	_x	3579.4	

Notes: x = into the core, y = across the core face, z = along the core. _ = uncut split core, C = cut sample, M = minicore. This table is also available in **ASCII format.**

Table T11. Thermal conductivity values, Hole 1184.

Core, section, interval (cm)	Depth (mbsf)	Thermal conductivity (W/[m·K])
192-1184A-		
2R-2, 75-77	136.65	1.073
3R-3, 75-77	147.75	1.168
3R-5, 75-77	150.75	1.083
4R-3, 75-77	157.45	1.106
4R-6, 75-77	161.95	1.110
5R-1, 75-77	164.05	0.922
5R-3, 75-77	167.05	1.320
6R-1, 75-77	173.65	1.083
6R-3, 75-77	176.65	1.144
7R-2, 75-77	184.75	1.130
7R-5, 75-77	189.25	1.303
8R-1, 75-77	192.55	1.146
8R-4, 75-77	197.05	1.079
8R-7, 75-77	201.05	1.046
11R-1, 68-70	207.08	1.088
11R-3, 66-68	209.72	1.244
12R-1, 48-50	211.38	1.299
12R-2, 68-70	213.08	1.224
12R-4, 125-127	216.49	1.180
13R-2, 90-92	222.74	1.173
13R-4, 16-18	224.74	1.266
14R-3, 17-19	233.01	1.222
14R-6, 5-7	236.99	1.213
15R-1, 20-22	239.80	1.181
16R-2, 12-14	246.02	1.220
16R-4, 30-32	248.79	1.265
17R-1, 47-49	249.67	1.262
17R-2, 10-12	250.69	1.254
17R-5, 125-127	256.03	1.211
18R-4, 80-82	263.62	1.262
19R-2, 80-82	270.11	1.186
19R-4, 90-92	272.56	1.229
19R-7, 100-102	276.84	1.238
20R-1, 50-52	278.60	1.209
20R-3, 65-67	281.56	1.191
21R-3, 108-110	291.73	1.243
21R-6, 10-12	294.28	1.188
22R-2, 38-40	298.48	1.253
22R-6, 103-105	304.31	1.271
24R-4, 125-127	321.02	1.119
24R-7, 40-42	324.30	1.108
25R-2, 30-32	327.93	1.124
25R-5, 40-42	331.09	1.168
26R-3, 117-119	339.74	1.130
26R-6, 10-12	342.97	1.167
27R-2, 140-142	348.51	1.178
27R-4, 140-142	351.48	1.202
28R-3, 10-12	358.19	1.180
28R-6, 10-12	362.66	1.172
29R-1, 138-140	366.38	1.138
30R-2, 138-140	377.58	1.130
30R-4, 12-14	379.32	1.157
31R-1, 30-32	384.70	1.173
31R-7, 30-32	392.62	1.151
32R-3, 30-32	396.83	1.163
32R-3, 31-33	396.84	1.169
32R-7, 10-12	402.65	1.134
33R-2, 80-82	405.99	1.175
33R-5, 140-142	410.40	1.164
34R-2, 110-112	415.84	1.182
34R-6, 110-112	421.15	1.211
35R-2, 100-102	425.55	1.211
35R-7, 10-12	431.26	1.253
36R-2, 120-122	435.54	1.165
36R-5, 140-142	439.80	1.124
37R-1, 16-18	442.76	1.192
37R-3, 20-22	445.32	1.149
38R-2, 132-134	455.14	1.178
39R-3, 80-82	465.70	1.164
40R-2, 80-82	473.69	1.114
41R-2, 30-32	482.91	1.132
41R-7, 90-92	490.01	1.133
42R-2, 60-62	492.80	1.141
42R-4, 10-12	495.30	1.068
42R-7, 140-142	500.31	1.103
43R-3, 135-137	504.08	1.134
44R-2, 45-47	511.87	1.089
45R-6, 68-70	526.80	1.121
46R-1, 70-72	529.90	1.260

Note: This table is also available in **ASCII format.**